SEARCH FOR THE STANDARD MODEL HIGGS BOSON IN ITS ASSOCIATED PRODUCTION WITH A W VECTOR BOSON IN $p\bar{p}$ COLLISIONS AT $\sqrt{s} = 1.96$TEV

By

Hatim H. Hegab

Master of Science in Physics
Cairo University
Cairo, Egypt
July, 2006

Submitted to the Faculty of the
Graduate College of
Oklahoma State University
in partial fulfillment of
the requirements for
the Degree of
DOCTOR OF PHILOSOPHY
May, 2013

SEARCH FOR THE STANDARD MODEL HIGGS BOSON IN ITS ASSOCIATED PRODUCTION WITH A W VECTOR BOSON IN $p\bar{p}$ COLLISIONS AT $\sqrt{s} = 1.96$TEV

Dissertation Approved:

Dr. Flera Rizatdinova

Advisor/Chair

Dr. Alexander Khanov

Dr. John Mintmire

Dr. Lionel Raff

ACKNOWLEDGMENTS

My present status in life, with this Ph.D. theses included, is the result of will, efforts and hard work of my beloved parents. My late father Professor Hegab A. Hegab was my first teacher of science. It was him who encouraged me to draw a plant cell after he prepared me a sample and asked me to see it under his microscope. He taught me also how to read science and think about nature. How does it work? And why this way? If I at all have achieved anything in my life, it is because of his teachings and guidance. My mother taught me how to add numbers when I was 4, and she deserves a special acknowledgment for her love and support that I had received during my work in this theses.

Comes next is my adviser, Flera Rizatdinova. She has always been a source of inspiration and I gained a lot of experience working for her. Many things I learned from Flera, things that would definitely help me in my future career.

I also would like to thank Kenneth Herner, from Fermilab, who has always been there for help while I was taking my first steps at the DØ collaboration, at Fermilab. Kenneth was always there when I needed guidance, help and support. He introduced me to the nuts and bolts of the coding and programming skills needed for such a huge work and was always there to discuss my results with me. many times I have taken hours of his time asking him my usual two questions, how? and why? He used to kindly give me the answers I needed to go on.

A number of people at the DØ collaboration have had helped me with their times, advices or assistance with some parts of this work. Among them I would like to thank Yuji

Acknowledgments reflect the views of the author and are not endorsed by committee members or Oklahoma State University

Enari, Mike Cooke, Ryuji Yamada, Chun Xu, Ashish Kumar, S. greder, Dmitri Smirnov, Satish Desai and Andres Tanasijczukand. I also would like to extend my gratitude to Suneel Dutt who has been of great help during my last year at the DØ experiment.

I also would like to extend my gratitude to Alexander Khanov, John Mintmire and Lionel Raff for kindly accepting to serve in my Ph.D. committee. Thank you all.

A special, and warm "thank you" should also go to every member in the Department of Physics, at Oklahoma State University, and I want to specially thank Susan, Sandra and Tamra at the office of the Department of Physics, for all the work they do and the support they give to every graduate student at the department. They made my time at OSU very easy.

My deepest gratitude should also go to my mother, my brothers *Mohammad* and *Waleed*, and to my sister, *Hanan*, for all the love and encouragement I had from them during every single step in this work. I couldn't have done it without your love.

Finally I would like to thank my wife *Marmar* who gave me all the love and support I needed (and she still does) during this work. Her patience and encouragement were essential for my smooth sailing through the Ph.D program. My kids *Basma*, *Mohammad* and the lovely little *Jenna* had the most profound influence on me during this work. Your presence in my life is all I needed to keep going through and to overcome all the troubles I met on my way. I would not have gone through this long path and tackle all the obstacles I faced without you. Thank you.

Acknowledgements reflect the views of the author and are not endorsed by committee members or Oklahoma State University

To My First Teacher of Mathematics

My Mother

&

To My First Teacher of Science

My Father

Name: Hatim Hegab

Date of Degree: May, 2014

Title of Study: SEARCH FOR STANDARD MODEL HIGGS BOSON IN ITS ASSOCIATED PRODUCTION WITH A W VECTOR BOSON IN $p\bar{p}$ COLLISIONS AT $\sqrt{s} = 1.96$ TeV

Major Field: PHYSICS

Abstract: In this dissertation, results from a search for the Standard Model (SM) Higgs boson is shown. The SM is the theoretical framework which describes particles of matter and force carrier gauge bosons. To solve the mass problem in the SM, the Higgs mechanism was introduced in 1963. The Higgs mechanism causes an electroweak symmetry breaking and a new massive scalar boson was postulated. This particle is the Higgs boson. A search for the Higgs boson has been ongoing at the Tevatron where protons and antiprotons were allowed to collide at a center-of-mass energy of 1.96 TeV. For a low mass Higgs, that is a Higgs with a mass lower than 135 GeV, the dominant decay mode is Higgs to a pair of b-quarks ($H \rightarrow b\bar{b}$). This work concentrated on a Higgs whose mass is in the range of 100 150 GeV, with a W vector boson produced with the Higgs boson. The final state chosen is the one which contains a lepton a neutrino and a pair of b-quarks. This study used data provided by the DZERO experiment. Results presented here are the outcome of analyzing 5.3 fb^{-1} of data from RunII period. The analysis used different techniques to increase the sensitivity of the study. Data were subdivided based on lepton flavor, number of jets in sample, jets identified as b-jets and dates of collected data. A multivariate analysis technique based on boosted decision trees were used to separate signal from background processes, physical and instrumental. A good agreement between data and simulated events was observed.

An observed (expected) upper limit of 4.5 (4.8) for a Higgs of mass 115 GeV was set on the ratio of the Higgs production to its decay branching ratio at the 95% confidence level.

TABLE OF CONTENTS

LIST OF TABLES

Table Page

LIST OF FIGURES

Figure Page

CHAPTER 1

INTRODUCTION

Particle physics is the science which concerns itself with predicting, discovering and studying the most fundamental building blocks of our universe. A particle is said to be *fundamental* if it has no internal constituents; we hypothesize that everything in the universe can be understood in terms of these particles and their interactions with each other. Theoretically, it should be possible to Model even macroscopic objects in terms of their constituent particles, but usually such Models are prohibitively complicated or mathematically intractable. Thus, particle physics is used to predict the behavior of smaller physical systems containing a relatively small number of particles interacting over distances smaller than the size of an atomic nucleus. These fundamental particles are described in section (section 1.1).

The dynamics of these fundamental particles is governed by a quantum field theory known as the *Standard Model* (SM), described in section 1.2. The SM is arguably one of the most successful theories in modern physics, and one can claim in modern science. The SM has successfully predicted the existence of both the Z and $W^{\pm}$ bosons and the *top* quark, all were required by the local symmetries that are at the heart of our understanding of particle physics. The SM has been quite remarkable that almost every result from collider experiments has been in very good agreement with the SM. One should mention that some astrophysical observations and the discovery of neutrino oscillations provide evidence that the SM does not have the final word in the realm of particle physics.

The only SM particle that has yet to be discovered is the Higgs boson[1], which is essential

[1]Latest results from CERN, the European Center for Nuclear Research, announced a discovery of a particle that looks more and more like "a" Higgs boson (see section 1.3.)

to the Standard Model's explanation to the nonzero weak boson and fermion masses. Had the Higgs boson been not found (observed) the Standard Model would have been excluded and this would have lead to physics beyond the Standard Model. Already, CERN has announced[2] an observation of a particle that is now believed to be *a* Higgs boson. Many of the characteristics of this newly discovered particle are similar to the ones predicted (calculated) by the Standard Model[3] but it has not yet been officially confirmed to be *the* SM Higgs boson. On the other hand, discovering *a* Higgs boson would be yet another addition to the Standard Model's wreath. Further studies of the properties of the Higgs boson could also point the way toward a more complete particle theory.

For the Higgs boson to be discovered and studied, a rather extreme experimental conditions are required to produce them. Very high energy densities are required for the production of the Higgs boson, a task which requires the largest and most powerful colliders in the world. The research described in this dissertation is an analysis of proton-antiproton collisions produced in the Tevatron collider at Fermlab[4], with a center-of-mass energy of 1.96 TeV. Large, complex, and sophisticated detectors are needed for precise measurement of the products of these collisions, and equally complex and sophisticated data processing and analysis techniques are required to record and analyze signals produced by such detectors. This work depended on data that was collected with the DØ[5] detector, one of two large, multipurpose detectors surrounding collision points at the Tevatron. Chapter 2 describes the experimental apparatus used to accelerate protons and antiproton at Fermilab's particle accelerator, the Tevatron, and the DØ detector used to collect the data.

A very promising, and sensitive, signature for light Higgs searches is the associated production with a heavy $W^{\pm}$ or Z boson. The signature of leptonic $W^{\pm}$ or Z boson decays can be used to select interesting events. The presence of Higgs bosons can be determined by

[2] On July 2012.

[3] And they are also similar to ones calculated by some of the extensions postulated to the SM theory.

[4] Fermi National Accelerator Laboratory; Batavia, IL, USA.

[5] Pronounced D-Zero.

looking for their decay into $b\bar{b}$ pairs. For this work, the associated production of a Higgs boson with a vector boson W, $q\bar{q} \to WH \to l\nu b\bar{b}$, was chosen.

In chapter 3, I describe the algorithms used to transform raw detector signals into measurements of particle kinematics, along with methods by which different types of particles are identified. Chapter 4 describes how simulated data is obtained from Monte Carlo techniques. Finally, all of these ingredients are brought together in a search for associated production of Higgs and W bosons, presented in chapter 5. Sophisticated multivariate techniques are used to maximize our sensitivity to the Higgs signal while accepting as many potential signal events as possible. As no significant excess is observed in the data, we extract upper limits on WH production by comparing the observed data to the simulated signals and background.

1.1 Fundamental Particles

particles currently hypothesized to be the fundamental building blocks of the universe are presented in this section. All of these particles *except* the Higgs boson have been directly detected in one or more experiments, and experimental results thus far are consistent with each of these particles being truly fundamental, that is, not composite. Many of these particles are virtual particles, that is, unstable (e.g. the μ or τ leptons) or cannot be observed in an isolated state (e.g. the quarks and gluons). The word particle is also used to refer to the quanta from which we build variations in the fundamental dynamic fields of the universe.

The Standard Model theory cannot describe all natural phenomena, most notably, gravity is entirely absent from the theory, but fortunately the effect of gravity is generally negligible in the small-scale physical systems we study. Also missing from the Standard Model theory are explanations for astrophysical dark matter and neutrino oscillations. These phenomena strongly suggest that the Standard Model is incomplete, and there are ongoing experimental and theoretical efforts to extend the Standard Model to include these phenomena. The search for the last undiscovered SM particle, the Higgs boson, may help to rule out some

hypothetical SM extensions and to indicate better the path toward a more complete theory of fundamental particles.

1.1.1 Fermions

Fermions are particles that have an intrinsic angular momentum, or *spin*, of half-integer multiples of $\hbar$ that make up ordinary matter. Another equivalent definition is that they are the quanta of fields that change sign under spatial rotations of 2π radians. As a result, fermions obey the Pauli exclusion principle, and thus systems of identical fermions are described by Fermi-Dirac statistics[6]. Fermions can be further classified into *leptons* and *quarks*. In the Standard Model, all fundamental particles are of spin $\frac{1}{2}$, so they transform according to the fundamental representation of the spatial rotation group $SU(2)$. The Standard Model is a *chiral* theory, so left- and right-handed fermions are treated separately, they transform as Weyl spinors under the restricted Lorentz group omitting discrete parity (P) and time-reversal (T) symmetries. Table 1.1 shows all know fermions along with their masses in GeV units and the forces felt by them.

leptons

Leptons are fermions that do not interact via the strong force, they interact only via the electroweak force. There are six leptons, and are arranged in three families; the first family contains the electron, a fundamental component of all atomic matter in the universe and the electron neutrino; the second family contains the muon (μ), the muon neutrino (ν_μ), and the third family contains the tau (τ) and the tau neutrino (ν_τ). Both muons and taus are identical to the electron in every respect except their masses. The muon is more than 200 times more massive than the electron, and the tau is almost 17 times as massive as the muon. The muon and tau lepton are unstable[7] and they decay to particles of smaller mass

[6]This is why they are called fermions.

[7]The electron is stable.

Fermions								
	Quarks				Leptons			
Family	Name	charge	Mass(GeV)	Forces	Name	charge	Mass(GeV)	Forces
1	u	+2/3	1.5 - 3.3$\times 10^{-3}$	S,E,W	ν_e	0	≈ 0	W
	d	-1/3	3.5 - 6.0$\times 10^{-3}$	S,E,W	e	-1	5.11×10^{-4}	E,W
2	c	+2/3	1.27	S,E,W	ν_μ	0	≈ 0	W
	s	-1/3	0.104	S,E,W	μ	-1	0.105	E,W
3	t	+2/3	171.2	S,E,W	ν_τ	0	≈ 0	W
	b	-1/3	4.2	S,E,W	τ	-1	1.77	E,W

Table 1.1: List of the set of known fermions. Included are their electromagnetic charges, masses, what forces they feel. S is the strong force, E is the electromagnetic part of the electroweak force, and W is the weak part of the electroweak force. Fermions are also grouped in their three generations, or families.

via weak nuclear interactions. With a lifetime of ≈ 2.2 μs, muons decay almost entirely into an electron, an anti-electron-neutrino, and a muon neutrino ($\mu \rightarrow e\bar{\nu}_e\nu_\mu$). The large mass of the tau makes many other decay channels (modes) kinematically available, which decreases its lifetime to almost 0.3 ps. Each of the three families of leptons contains left-handed (ℓ_L) and right-handed (ℓ_R) leptons with charge -1 and an electrically neutral left-handed neutrino ν_L. The neutrino is masseless, as nonzero neutrino mass would require the existence of right handed neutrinos. Recent observation of neutrino flavor oscillations [4,5] points to the existence of a neutrino mass, indicating that right-handed neutrinos may exist although no direct experimental evidence exists for such neutrinos so far. Because chirality and helicity are the same for massless particles but not for particles with mass, massive neutrinos cannot be easily accommodated in the Standard Model. Together with astrophysical evidence supporting the existence of dark matter [6] and dark energy [7, 8] this is one of the indications for physics beyond the Standard Model. For the purpose of my research, one can safely ignore any small but nonzero neutrino mass, as it is not expected

that it may affect Higgs production at the Tevatron.

Quarks

Quarks (and anti-quarks) carry a $\pm 2/3$ or $\mp 1/3$ electric charge, have masses ranging from less than 1 GeV up to ≈ 173 GeV, and interact via the strong nuclear interaction and the electroweak interaction. There are six quarks and they are arranged in three families (generations): the up (u) and the down (d) quarks first family, the charm (c) and the strange (s) quarks second family and the top (t) and the bottom (b) quarks third family. Table 1.1 lists these quarks, showing their families, their masses and their charges. Quarks form composite particles known as *hadrons*. Hadrons are either *mesons*, consisting of one quark and one anti-quark, or baryons, consisting of three quarks (or three anti-quarks for anti-baryons), the best known of which are the proton and neutron. The strong nuclear force *confines* quarks inside hadrons. If a quark is to be removed from a hadron, the force coupling the quark to that hadron increases, similar to stretching of a strip of rubber. Eventually, it is energetically plausible for the rubber band to break, which leads to two non-stretchable strips, representing two hadrons. Therefore any attempt we do to remove a quark from a hadron, this quark will be confined in a new hadron. Quark masses range over five orders of magnitude. The top quark is the most massive, being famously as heavy as a gold nucleus. Such a large mass makes the top quark unique as the only quark that is not a constituent of hadrons: its mean lifetime is significantly less than the time required for hadronization. Because of this, the mass of the top quark can be precisely measured at high-energy collider experiments such as DØ.

1.1.2 Bosons

Bosons are integer spin (in terms of $\hbar$) particles that mediate interactions between particles (both fermions and other bosons). Equivalently, they are the quanta of fields invariant under spatial rotations of 2π radians. As a result, bosons do not obey the Pauli exclusion

Bosons			
Name	charge	Mass (GeV)	Force Mediated
g	0	0	S
γ	0	0	E
$W^{\pm}$	± 1	80.4	W
Z	0	91.2	W
H	0	$\approx$125.6	Couples to all particles with masses

Table 1.2: Set of SM bosons. shown are their electromagnetic charges, masses and what forces they mediate. S is the strong force, E is the electromagnetic part of the electroweak force, and W is the weak part of the electroweak force. The Higgs boson does not mediate any of the known forces, but it couples to all massive particles to give them their masses.

principle, and thus systems of identical bosons are described by Bose-Einstein statistics[8]. Bosons in the Standard Model have spins of either 0 or 1. Spin-1 bosons transform according to the representation of the spatial group $SO(3)$ and as four-vectors under Lorentz transformations. The Spin-0 field, known as the Higgs field, transforms as a scalar under rotations and Lorentz boosts. Table 1.2 shows the fundamental bosons in the Standard Model. The gluon G is actually 8 gluons which mediate the strong nuclear interaction that binds quarks into hadrons and hadrons into nuclei. The W and Z bosons mediate the weak nuclear interaction which helps β-decay and other phenomena. The last boson in the table is the Higgs boson, H. The Higgs boson is the massive spinless particle that is predicted by the Higgs mechanism of electroweak symmetry breaking, which provides mass to the W and Z bosons.

[8]This is why they are called bosons.

1.2 The Standard Model

Standard Model is the theoretical framework used to describe the high energy particle physics. It emerged as the effective field theory up to at least the TeV scale. It combines the strong and electroweak forces into a framework that governs all interactions of elementary particles. It does not incorporate gravity, but gravity is so weak relative to the other forces that it plays no role at the subatomic level. Below we discuss the details of the Standard Model and its phenomenology.

1.2.1 Electroweak Interaction

The electroweak interaction as the Standard Model itself is described by a gauge theory. The corresponding symmetry group is the combination of $SU(2)_L$ and $U(1)_Y$. The index L denotes that only left handed fermions interact weakly. Left handed fermions can be represented as doublet of the weak isospin $|\vec{T}| = \frac{1}{2}$ with eigenvalues $T_3 = \frac{1}{2}$. Right handed fermions are in contrast singlet states with $|\vec{T}| = T_3 = 0$.

Just as Q generates the group $U(1)_{EM}$, the group $U(1)_Y$ is generated by the hypercharge Y which can be calculated using the Gell-Mann-Nishijma relation.

$$Q = T_3 + \frac{Y}{2} \tag{1.1}$$

The hypercharge is the same for all particles with the same multiplet.

The Lagrangian $\mathcal{L}_{EW}$ has to be invariant under transformations of the group $SU(2)_L \otimes U(1)_Y$, therefore one obtains an isotriplet of vector fields $W^i_\nu (i = 1, 2, 3)$ coupled with the strength g to the weak isospin. Additionally one obtains a single vector field B_μ coupling with g' to the weak hypercharge. Therefore the Lagrangian is given by

$$\mathcal{L}_{EW} = \bar{\Psi}\gamma_\mu D^\mu \Psi - \frac{1}{4}[\mathbf{W}_{\mu\nu}\mathbf{W}^{\mu\nu} + B_{\mu\nu}B^{\mu\nu}] \tag{1.2}$$

where D_μ is the covariant derivative

$$D_\mu = i\partial_\mu - g\mathbf{T}.\mathbf{W}_\nu + g'YB_\nu \tag{1.3}$$

And the field tensors are given by

$$\mathbf{W}_{\mu\nu} = \partial_\mu \mathbf{W}_\nu - \partial_\mu \mathbf{W}_\nu - g\mathbf{W}_\mu \mathbf{W}_\nu, \tag{1.4}$$

$$B_{\mu\nu} = \partial_\mu B_\nu - \partial_\nu B_\mu \tag{1.5}$$

The two neutral fields mix in such a way that the physical state, the mass eigenstates, are

$$A_\mu = B\mu \cos\theta_W + W_\nu^3 \sin\theta_W \qquad \text{massless} \tag{1.6}$$

$$Z_\mu = -B\mu \sin\theta_W + W_\nu^3 \cos\theta_W \qquad \text{massive} \tag{1.7}$$

here θ_W is the Weinberg or weak mixing angle. It has been measured to be $\sin^2\theta_W = 0.231$ [9]. The two remaining fields W_μ^1 and W_μ^2 are mixing as well, forming the charged gauge boson:

$$W^\pm = \frac{1}{2}(W_\mu^1 \mp W_\mu^2) \tag{1.8}$$

The fields A_μ and Z_μ can be identified with the photon and the Z boson. These fields couple to both, left and right handed fermions contrary to the charged gauge bosons $W^\pm$ which couple only to the left handed fermions, such as particles with $|\vec{T}| \neq 0$. Due to the fact that the photon field couples with strength e to charged fermions and by writing out the neutral current interaction, one can show that:

$$g \sin\theta_W = g' \cos\theta_W = e. \tag{1.9}$$

The coupling of the Z^0 boson is given by

$$-i\frac{g}{\cos\theta_W}\gamma^\mu \frac{1}{2}(c_v^f - c_A^f \gamma^5) \tag{1.10}$$

here c_v^f and c_A^f represent the vector and axial couplings, respectively:

$$c_v^f = T_3^f - s\sin^2\theta_W Q_f \tag{1.11}$$

$$c_A^f = T_3^f \tag{1.12}$$

The vertex of the charged bosons is described by:

$$-i\frac{g}{\sqrt{2}}\gamma^{\mu}\frac{1}{2}(1-\gamma^{5}) \tag{1.13}$$

Because particles of interest, e.g leptons, quarks and likewise the gauge bosons Z^0, $W^{\pm}$ are not massless the symmetry has to be broken and the particles acquire mass.

1.2.2 Strong Interaction

The strong interaction is described by *Quantum Chromodynamics* (QCD) is based on symmetry group $SU(3)_C$, the index C stands for 'color'. QCD interaction is described by the Lagrangian [10]

$$\mathcal{L}_{QCD} = \bar{q}\gamma_{\mu}D^{\mu}q - \mathbf{G}^{a}_{\mu\nu}\mathbf{G}^{\mu\nu}_{a} \tag{1.14}$$

and the covariant derivative by

$$D_{\mu} = i\partial_{\mu} - g_s\mathbf{T}^{a}.\mathbf{G}^{a}_{\mu}. \tag{1.15}$$

The field tensor $\mathbf{G}^{a}_{\mu\nu}$ represents:

$$\mathbf{G}^{a}_{\mu\nu} = \partial_{\mu}\mathbf{G}^{a}_{\nu} - \partial_{\nu}\mathbf{G}^{a}_{\mu} - g_s f_{abc}\mathbf{G}^{b}_{\mu}\mathbf{W}^{c}_{\nu}. \tag{1.16}$$

The coupling is represented by g_s and f_{abc} (with $a, b, c = 1 \ldots 8$) are the structure constants of the $SU(3)$ group. The color charge is ordered in color triplets. Color charges are carried by quarks and mediating particles of the strong force, the gluons. The gluons are forming a color-octet and show self-interaction because it is a non-Abelian gauge theory. This self-interaction leads to an increasing strength of the coupling with increasing distance of the color charges, therefore making it impossible to observe free quarks but only colorless states as mesons ($q\bar{q}$) and baryons (qqq). This is called *confinement*. In contrary the coupling decreases for very small distances, called *asymptotic freedom*, and can be calculated using perturbative theory.

1.3 The Higgs Mechanism

The theory of weak interaction is predicting massless gauge bosons in contrast to the theoretical observation where all gauge boson except of the photons have a substantial mass. Unfortunately the manual introduction of mass terms like $\frac{M^2}{2}\mathbf{W}_{\mu\nu}\mathbf{W}^{\mu\nu}$ to the Lagrangian $\mathcal{L}$ leads to unrenormalizable divergences, rendering the theory meaningless. The masses of particles can be generated by introducing the Higgs mechanism as opposed to putting them in by hand. Here an additional potential is added to the Lagrangian which has two minima, leading to spontaneous symmetry breaking and generating the masses of the particles[9].

The Higgs Potential

The Lagrangian shown in Eq. 1.2 remains gauge invariant when adding a potential of the form [12, 13]

$$\mathcal{L}_{Higgs} = (D_\mu \Phi)^\dagger (D^\mu \Phi)^\dagger - V(\Phi). \tag{1.17}$$

Here Φ is a 2-dimensional scalar field given by

$$\Phi(x) = \begin{pmatrix} \Phi^+ \\ \Phi^0 \end{pmatrix} = \frac{1}{\sqrt{2}} \begin{pmatrix} \Phi_1 + i\Phi_2 \\ \Phi_3 + i\Phi_4 \end{pmatrix} \tag{1.18}$$

and $V(\Phi)$ by

$$V(\Phi) = \mu^2 \Phi^\dagger \Phi + \lambda (\Phi^\dagger \Phi)^2 \tag{1.19}$$

When choosing $\lambda > 0$ and $\mu^2 < 0$ one gets two minima for the potential. These two conditions satisfy:

$$\Phi^\dagger \Phi = \frac{1}{2}\left(\Phi_1^2 + \Phi_2^2 + \Phi_3^2 + \Phi_4^2\right) = -\frac{\mu^2}{2}\lambda = \upsilon^2 \tag{1.20}$$

If we set $\Phi_1 = 0$, $\Phi_2 = 0$, $\Phi_3 = 0$ and $\Phi_4 = \upsilon$ the vacuum expectation value is given by

$$\langle \Phi \rangle = \frac{1}{\sqrt{2}} \begin{pmatrix} 0 \\ \upsilon \end{pmatrix}, \tag{1.21}$$

[9] For a review of Higgs Physics one can read [11]

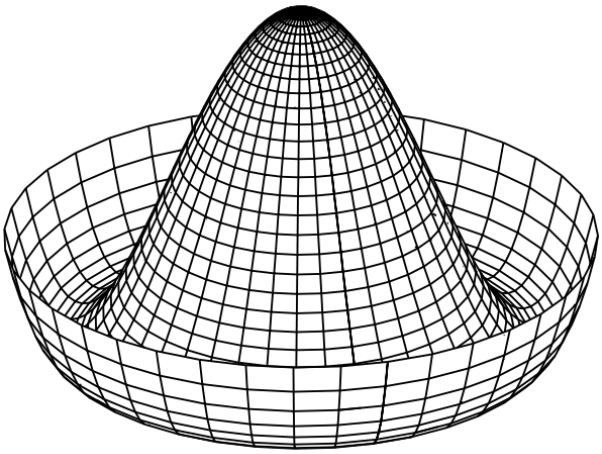

Figure 1.1: An example of a Higgs potential of a scalar field.

Perturbative (approximate) calculations should involve expressions around the classical minimum, $\Phi = \pm\upsilon$ and so one can write

$$\Phi = \frac{1}{\sqrt{2}} \begin{pmatrix} 0 \\ \upsilon + h(x) \end{pmatrix} \tag{1.22}$$

The Higgs particle is interpreted as a space-time dependent radial fluctuation $h(x)$ of the field Φ near vacuum configuration. Due to the local gauge invariance each point satisfies Eq. 1.22 because rotations of the isospin can performed at each of this points. The only field remaining is the Higgs field $h(x)$. The Lagrangian, expressed in terms of the vacuum expectation value υ and the physical state $h(x)$ describes a scalar particle with the mass $m_H = 2\lambda\nu$

$$\mathcal{L} = \frac{1}{2}\partial_\mu\partial^\nu h - \lambda\upsilon^2 h^2 - \lambda\upsilon h^3 - \frac{\lambda}{4}h^4. \tag{1.23}$$

The scalar particle that is described in Eq. 1.23 is referred to as the *Standard Model Higgs boson*. This is the only component left in Eq. 1.18 of a neutral state after electroweak symmetry breaking. The other three components are the longitudinally polarized components of the weak vector boson. This boson carries electric charge and its coupling is proportional to fermions and heavy gauge bosons masses.

Masses of the Gauge Bosons

In the SM Lagrangian, the mass terms are given by representations like $\frac{1}{2}M\Psi^{\dagger}\Psi$ and therefore are quadratic in their fields. By inserting the vacuum expectation value of Eq. 1.21 into the Lagrangian Eq. 1.17 one is able to study its structure. The covariant derivative then is reduced to the form [14]

$$D_{\mu}\left\langle \Phi\right\rangle =-\left(\frac{ig}{2}\begin{pmatrix} W_{\mu}^{3} & W_{\mu}^{1}-iW_{\mu}^{2} \\ W_{\mu}^{1}+iW_{\mu}^{2} & W_{\mu}^{3} \end{pmatrix}+\frac{ig'}{2}B_{\mu}\right)\frac{2}{\sqrt{2}}\begin{pmatrix} 0 \\ \upsilon \end{pmatrix} \tag{1.24}$$

using this equation in the Lagrangian one obtains additional quadratic field terms from the expression $\left(D_{\mu}\left\langle \Phi\right\rangle\right)^{\dagger}\left(D_{\mu}\left\langle \Phi\right\rangle\right)$:

$$\left(D_{\mu}\left\langle \Phi\right\rangle\right)^{\dagger}\left(D_{\mu}\left\langle \Phi\right\rangle\right)=\frac{1}{8}\upsilon^{2}g^{2}\left(\left(W_{\mu}^{1}\right)^{2}+\left(W_{\mu}^{2}\right)^{2}\right)+\frac{1}{8}\upsilon^{2}\left(g'B_{\mu}-gW_{\mu}^{3}\right)^{2} \tag{1.25}$$

Using Eq. 1.6-1.9 one obtains:

$$\frac{1}{8}\upsilon^{2}g^{2}\left(\left(W_{\mu}^{1}\right)^{2}+\left(W_{\mu}^{2}\right)^{2}\right)+\frac{1}{8}\upsilon^{2}\left(g'B_{\mu}-gW_{\mu}^{3}\right)^{2}=\left(\frac{1}{2}\upsilon g\right)^{2}W_{\mu}^{+}W_{\mu}^{-\mu}+\frac{1}{4}\upsilon^{2}\left(g^{2}+g'^{2}\right)Z_{\mu}Z^{\mu} \tag{1.26}$$

The symmetry breaking leads to three additional terms with quadratic fields. These mass terms can be identified with the gauge fields W^{+}, W^{-} and Z^{0}. All gauge boson except the photon acquired mass. The photon remains massless because Φ is invariant under transformations of $U(1)_{Y}$, generated by Q.

Equation 1.26 contains the gauge boson masses:

$$M_{W}^{2}=\frac{1}{4}\upsilon^{2}g^{2},\qquad M_{Z}^{2}=\frac{1}{4}\upsilon^{2}\left(g^{2}+g'^{2}\right),\qquad M_{\gamma}^{2}=0 \tag{1.27}$$

Using Eq. 1.6 and Eq. 1.7 one can show that the W and Z mass are connected via the following relation

$$\cos\theta_{W}=\frac{M_{W}}{M_{Z}} \tag{1.28}$$

which is in very good agreement with experimental results [9]. The vacuum expectation value υ of the Higgs potential can be derived from the Fermi constant: $G_{F}=1.667\times10^{-5}$

GeV^{-2}

$$v^2 = 4\frac{M_W^2}{g^2} = \frac{1}{\sqrt{2}G_F} \approx (250\text{GeV})^2 \tag{1.29}$$

1.4 Higgs Boson Searches at the Tevatron and LHC

Powerful, High energy density colliders are needed to produce the Higgs boson for experimental observation and thus a verification of the Higgs mechanism. Unfortunately, the mass of the Higgs boson is not predicted by theory and thus theoretical limits on the Higgs mass had to be calculated.

1.4.1 Theoretical Limits on the Higgs Boson Mass

The Standard Model Higgs boson mass is linked to the energy scale where the validity of the Standard Model is expected to fail. Below that scale, the Standard Model is a successful effective field theory. Above that scale the Standard Model is expected to be a subset of a more general theory that gives origin to a wealth of new physics. As a result of this link we are able to connect the Higgs boson mass to the scale of new physics Λ.

Triviality and Vacuum Stability

The Higgs' quartic coupling has to be finite at high energy scales, this is called *triviality*. In the scalar sector of the Standard Model the quartic coupling is

$$\lambda = \frac{m_H^2}{2\nu^2} \tag{1.30}$$

Where λ depends on the effective energy scale Q. Using Eq. 1.30 one sees that $\lambda(Q)$ becomes infinite for $\lambda \to \infty$[10] This behavior is shown in Fig. 1.2 [15]. Assuming the Standard Model to be valid and there is no new physics exists up to the *curt-off* or *Planck-Energy* scale ($\lambda \sim 10^{19}$ GeV), the approximate upper bound on the Higgs boson mass is [16]

$$m_H < 160\text{GeV} \tag{1.31}$$

[10]This condition is called Landau pole.

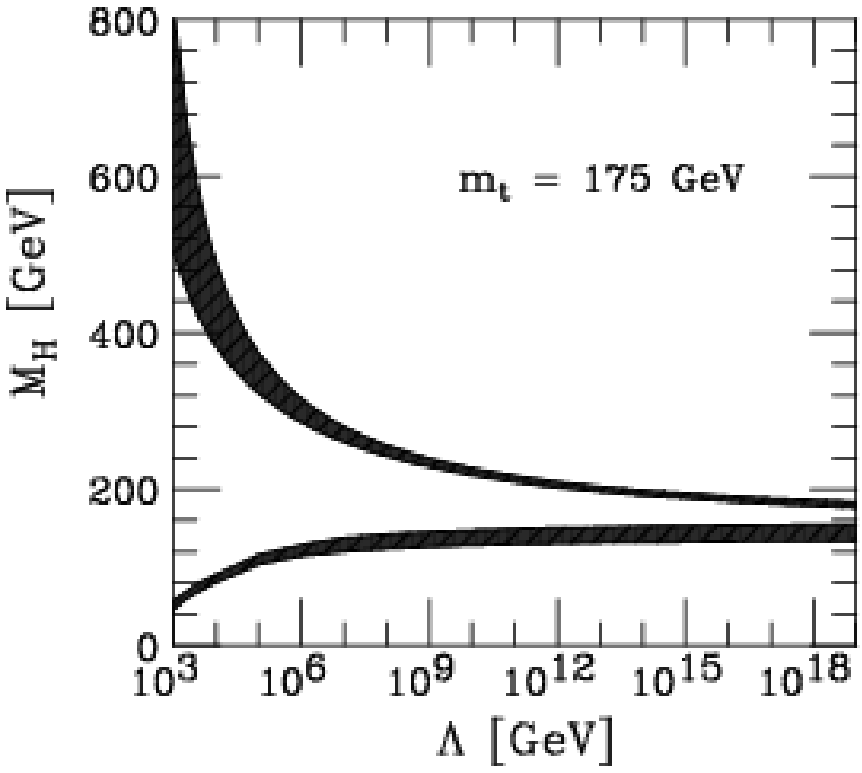

Figure 1.2: The triviality (upper) bound and the vacuum stability (lower) bound on the Higgs boson mass as a function of the New Physics cut-off scale Λ for a top quark mass $m_t = 175$ GeV and $\alpha_s(M_Z) = 0.118 \pm 0.002$; the allowed region lies between the bands and the colored/shaded bands illustrate the impact of various uncertainties.

Another bound on the Higgs mass can be derived from the top quark Yukawa coupling which causes the scalar self-coupling to decrease and becomes negative if the Higgs mass is too low. This would cause the value of the effective potential to become negative and to drop lower than the Standard Model vacuum [17]. This is equivalent to requiring that λ remains positive at all energy scales Λ, $\Lambda > 0$ because if λ becomes negative the potential has no state of minimum energy and the vacuum is not stable any more. If, as we assumed earlier, the Standard Model is valid up to scales of $\sim 10^{16}$ GeV one obtains [18]:

$$m_H(\text{GeV}) = 130 + 2(m_t - 170) \tag{1.32}$$

which limits the mass range available for the Higgs boson to be between $\sim 120- \sim 160$ GeV. This is exactly the mass range preferred by the EW precision measurements.

1.5 Direct Higgs Searches

There are many free parameters in the electroweak theory, all of which must be determined by experiment. In fact, various experiments in particle physics have succeeded in measuring all but one of these parameters. For instance, the Higgs vacuum expectation value is related to the Fermi constant G_F via this relation:

$$\upsilon^2 = \sqrt{2}G_F, \tag{1.33}$$

Where $G_F = \sqrt{2}g_W^2/(8m_W^2)$. The muon lifetime is inversely related to G_F^2, as a result determining the muon decay experimentally, and as precisely as possible, we know that $\upsilon \approx 246$GeV [19]. The weak mixing angle θ_W is well-constrained, too, as measurement of the Z boson mass and other weak neutral currents properties are in agreement with $\sin^2\theta_W \approx 0.23$ [20]. The only free parameter in the EW theory that is still loosely constrained is the mass of the Higgs boson.

1.5.1 Results from LEP

First experimental limit on the mass of the Higgs boson came from the Large Electron Positron (LEP) collider at CERN[11]. During the data taking period from 1989 to 2000 LEP was able to obtain a lower limit on the mass of the Higgs boson at $m_H > 114.4$ GeV at 95% confidence level (C.L) [21].

1.5.2 Tevatron Results

For almost two decades the Tevatron has searched for the Tevatron through its two major experiments, CDF and DØLatest results from each collaboration is given below and the

[11] *http://public.web.cern.ch/public/en/Research/LEPExp-en.html*

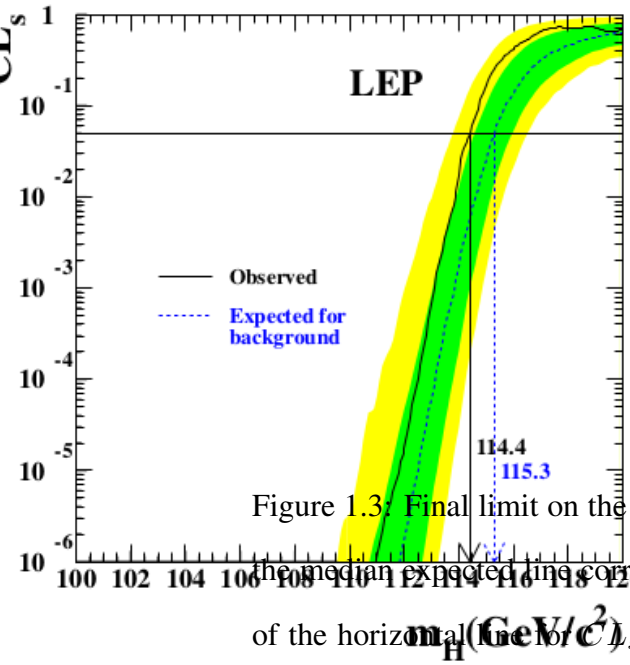

Figure 1.3: Final limit on the Higgs boson mass. The dark and light shaded bands around the median expected line correspond to 68% and 95% probability bands. The intersection of the horizontal line for $CL_s = 0.05$ with the observed curve is used to define the 95% confidence level lower bound on the mass of the Standard Model Higgs Boson.

final "combined" result from the Tevatron[12] follows.

Results From The CDF Experiment

CDF presented [22] a combination of searches for the standard model Higgs boson using their full Run II[13] data set, which corresponds to an integrated luminosity of 9.45–10.0 fb^{-1} collected from $\sqrt{s} = 1.96$ TeV $p\bar{p}$ collisions at the Fermilab Tevatron. Depending on the production mode, Higgs boson decays to W^+W^-, ZZ, $b\bar{b}$, $\tau^+\tau^-$, and $\gamma\gamma$ were examined. CDF searched for a Higgs boson with masses (m_H) in the range 90–200 GeV. In the absence of a signal and based on combined search sensitivity, CDF excluded at the

[12] That is combining the two experiments' results together.

[13] 2001-Sept. 2011

95% credibility level the mass regions $90 < m_H < 94$ GeV/c^2, $96 < m_H < 106$ GeV, and $153 < m_H < 175$ GeV. The observed exclusion regions are $90 < m_H < 102$ GeV and $149 < m_H < 172$ GeV. A moderate excess of signal-like events relative to the background expectation at the level of 2.0 standard deviations was present in the data for the $m_H = 125$ GeV search hypothesis. Finally, for the hypothesis of a new particle with mass 125 GeV, CDF could constrain the coupling strengths of the new particle to $W^{\pm}$ bosons, Z bosons, and fermions. Fig. 1.4 shows the resulting observed upper bound on the signal scale factor R_{95} for potential m_H values between 90 GeV and 200 GeV. The median expected limit in the presence of no signal, R_{95}^{med}, is shown by the dark dashed line, while the shaded regions indicate the limit fluctuation ranges at the level of one and two standard deviations. The lighter dashed line shows the broad excess in the limits that would be expected if a SM Higgs boson with $m_H = 125$ GeV were present in the data. We exclude at the 95% credibility level (C.L.) the SM Higgs boson within the mass ranges $90 < m_H < 102$ GeV and $149 < m_H < 172$ GeV. In the absence of a signal, we expect to exclude the regions $90 < m_H < 94$ GeV, $96 < m_H < 106$ GeV, and $153 < m_H < 175$ GeV.

Results From The DØ Experiment

DØ collaboration performed a combination of their searches for standard model Higgs boson production in $p\bar{p}$ collisions using all data recorded by the DØ detector at the Fermilab Tevatron Collider at a center of mass energy of $\sqrt{s} = 1.96$ TeV [23]. The different production and decay channels have been analyzed separately, with integrated luminosities of up to 9.7 fb^{-1} and for Higgs boson masses in the interval $90 \leq m_H \leq 200$ GeV. A combination of these final states to achieve optimal sensitivity to the production of the Higgs boson was preformed. DØ result excludes a standard model Higgs boson at 95% C.L. in the ranges $90 < m_H < 101$ GeV and $157 < m_H < 178$ GeV, with an expected exclusion of $155 < m_H < 175$ GeV. In the range $120 < m_H < 145$ GeV, the data exhibit an excess over the expected background of up to two standard deviations, consistent with

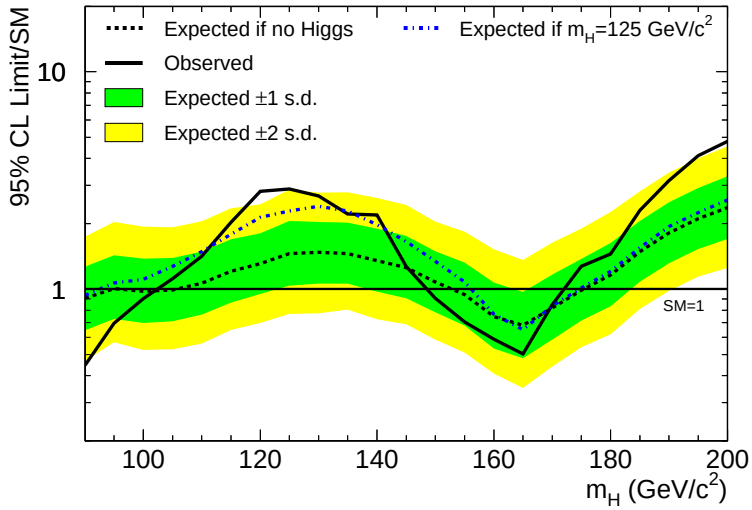

Figure 1.4: Observed and expected (median, for the background-only hypothesis) 95% C.L. upper limits on SM Higgs boson production as a function of the Higgs boson mass for the combination of CDF searches. The limits are expressed as multiples of the SM prediction for test masses in 5 GeV steps from 90 to 200 GeV. The points are connected with straight lines for improved readability. The bands indicate the 68% and 95% probability regions where the limits can fluctuate, in the absence of signal. The lighter dashed line indicates mean expected limits in the presence of a SM Higgs boson with $m_H = 125$ GeV.

the presence of a standard model Higgs boson of mass 125 GeV. Figure 1.5 shows the expected and observed upper limits on σ_H at 95% C.L. relative to the SM, for the mass region $90 \leq m_H \leq 200$ GeV, for all analyses combined. We exclude the SM Higgs boson at 95% C.L. in the mass ranges $90 < m_H < 101$ GeV and $157 < m_H < 178$ GeV. Our expected exclusion range is $155 < m_H < 175$ GeV.

1.5.3 Combined Higgs Boson Studies at The Tevatron

To increase its sensitivity to the Higgs boson, the Tevatron combines the searches of its two experiments CDF and DØ for the Standard Model Higgs boson with mass in the range

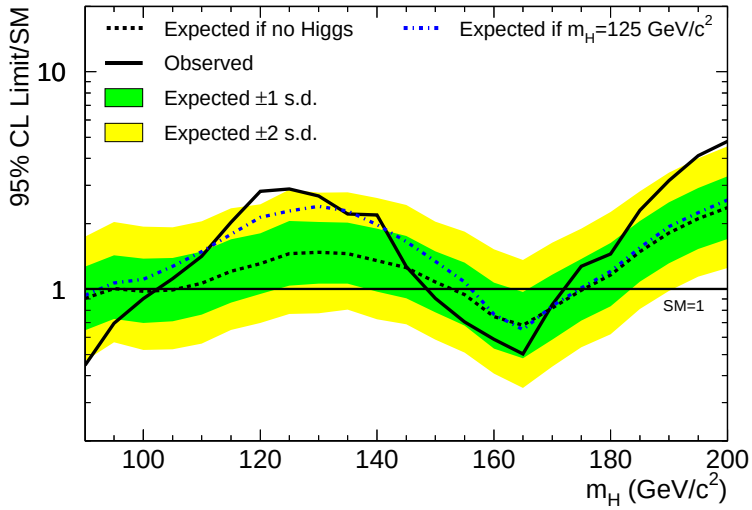

Figure 1.5: Expected (median) and observed ratios for the upper limits of the cross section σ_H at 95% C.L. relative to the SM values for all analyses combined for the range $90 \leq m_H \leq 200$ GeV. The shaded bands correspond to the regions enclosing ± 1 and ± 2 s.d. fluctuations of the background, respectively. The long-dashed line represents the expectation if a $m_H = 125$ GeV Higgs boson were present in the data with the SM cross section.

90–200 GeV. It considers a Higgs boson produced through different production modes[14] at the Tevatron and with the decay modes $H \to b\bar{b}$, $H \to WW$, $H \to ZZ$, $H \to \tau\tau$ and $H \to \gamma\gamma$. The data corresponds to integrated luminosities of up to 10 fb^{-1} and were collected at the Fermilab Tevatron in $p\bar{p}$ collisions at $\sqrt{s} = 1.96$ TeV. Latest results from the Tevatron [24] showed that it could observe a significant excess of events in the mass range between 115 and 140 GeV. The local significance corresponds to 3.1 standard deviations at $m_H = 125$ GeV, consistent with the mass of the Higgs boson observed at the LHC. The Tevatron also separately combines searches for $H \to b\bar{b}$, $H \to WW$, $H \to \tau\tau$ and $H \to \gamma\gamma$[15]. The Tevatron observed signal strengths in all channels, are consistent with the presence of a standard model Higgs boson with a mass of 125 GeV. Figure 1.6 shows a

[14] gluon-gluon fusion, vector boson fusion and associated production processes.

[15] The channels sensitive to the Higgs boson at the LHC.

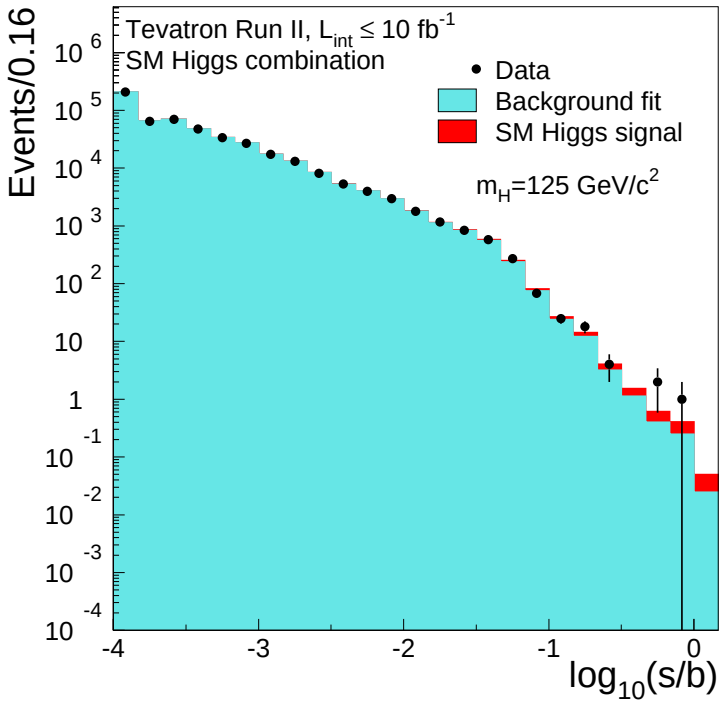

Figure 1.6: Distribution of $\log_{10}(s/b)$, for the data from all contributing Higgs boson search channels from CDF and DØ for $m_H = 125$ GeV. The data are shown with points, and the expected signal is shown stacked on top of the backgrounds, which are fit to the data within their systematic uncertainties. The error bars shown on the data correspond in each bin to the square root of the observed data count. Underflows and overflows are collected into the leftmost and rightmost bins, respectively.

summary of all the data collected by the experiments in the various final states, ordered by the value of signal-to-noise (the variable on the x axis). In each bin (which has a definite value of expected signal fraction) the light-blue background is dominant and the red signal component is undetectable until we go to the rightmost bins, which have an expected signal fraction large enough to make a difference. The mass assumed here is 125 GeV, the value measured by the LHC experiments. Data points at the far right are in agreement with the blue+red histogram (which is the signal hypothesis, also called "null hypothesis".)

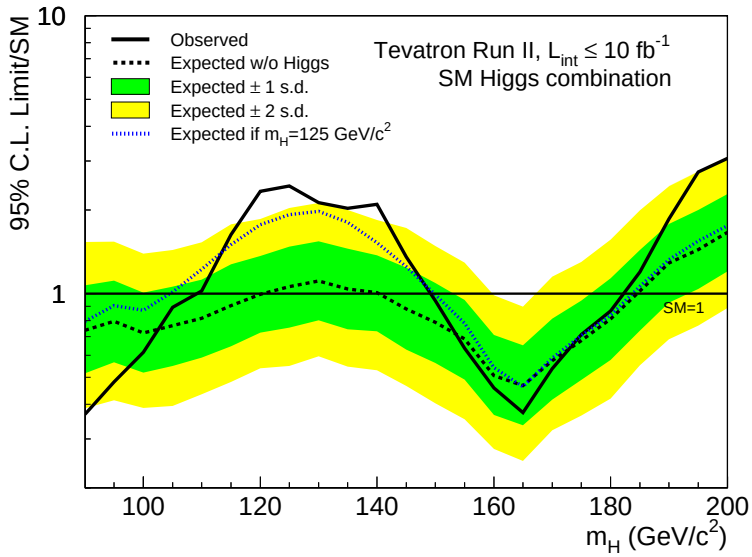

Figure 1.7: Observed and median expected (for the background-only hypothesis) 95% C.L. Bayesian upper production limits expressed as multiples of the SM cross section as a function of Higgs boson mass for the combined CDF and DØ searches in all decay modes. The dark- and light- shaded bands indicate, respectively, the one and two s.d probability regions in which the limits are expected to fluctuate in the absence of signal. The blue short-dashed line shows median expected limits assuming the SM Higgs boson is present at $m_H = 125$ GeV.

1.5.4 Latest Results From The LHC

The *Large Hadron Collider* or the *LHC* is the highest energy density hadron collider in the world. It started colliding protons together on Nov. 2010. During its successful work in the last two year, the LHC was able to collect data that is almost equivalent to all data collected by the Tevatron. On July 2011 the two major experiments at the LHC, ATLAS and CMS announced an observation of a boson that is similar in its characteristics to the Higgs boson. Latest results announced by both experiments show that the boson discovered is in almost every respect *a* Higgs boson. It remains to show whether the discovered boson is *the* Standard Model Higgs boson or one of the "Higgses"[16] predicted by any of the theoretical

[16]Supersymmetry, for instance, predicts the existence of five different Higgs bosons.

expansion to the Standard Model[17].

Results From ATLAS and CMS Experiments

Both ATLAS and CMS Collaborations, the two large experiments at the LHC, announced on July 2012 an observation of a new boson which is thought to be the Higgs boson. Whether this is the Higgs boson expected by the Standard Model of particle physics or some "Higgs-like boson" befitting a different theoretical model remains to be confirmed. To tell the difference, all the new boson properties must be checked. Some of these properties include how often this boson decays into different types of particles, and determine its spin and parity. At the LHC there are five decay channels available to the Higgs boson, $H \to \gamma\gamma$, $H \to WW$, $H \to ZZ$, $H \to b\bar{b}$ and $H \to \tau\tau$ in well defined decay widths[18]. Both the presence of and the rate at which each of these decay modes should be studied to confirm the identity of the newly discovered boson. With more data available, Both ATLAS and CMS were able to measure both the parity and the spin of the new boson and they were found to be in good agreement with a spin-0 (scalar particle) of a positive parity, exactly as *a* Higgs boson should be.

[17]LHC press release is here `http://www.interactions.org/cms/?pid=1032641`

[18]Proportions.

CHAPTER 2

Experimental Apparatus

Data used in this analysis were taken at the DØ detector, one of two general-purpose detectors at the Fermilab Tevatron. In this chapter I give an overview of the accelerator complex and the Tevatron followed by a description of the DØ detector.

2.1 The Accelerator and The Tevatron

The Tevatron is the centerpiece of the hadron collider physics program at Fermi National Accelerator Laboratory, in Batavia, Illinois. The Tevatron is a proton antiproton, $p\bar{p}$, collider that operates at a center-of-mass energy of 1.96 TeV.

2.1.1 The Accelerators

A broad range of particle physics research has been carried out at the Tevatron, including the discovery of the *top* quark. A major physics goal for the Tevatron was to search for the Higgs boson at its two colliding detectors, CDF and DØ. Both protons and antiprotons are created and accelerated with a complex chain of accelerators. An overview of these accelerators is given in Fig. 2.1 [25]. Proton sources are produced in the Booster by stripping electrons off negative hydrogen ions from the Linac. Anti-protons are accumulated from a target station where a target is bombarded by proton beams from the Main Injector. Both beams, then, are accelerated and finally injected to a tevatron ring, in which protons and antiprotons, both, are accelerated up to 980 GeV and are brought to collide with each other at the heart of both CDF and DØ detectors. Protons are also used in some fixed target experiments such as MINOS and MiniBooNE. In what follows I shall give a brief summaries

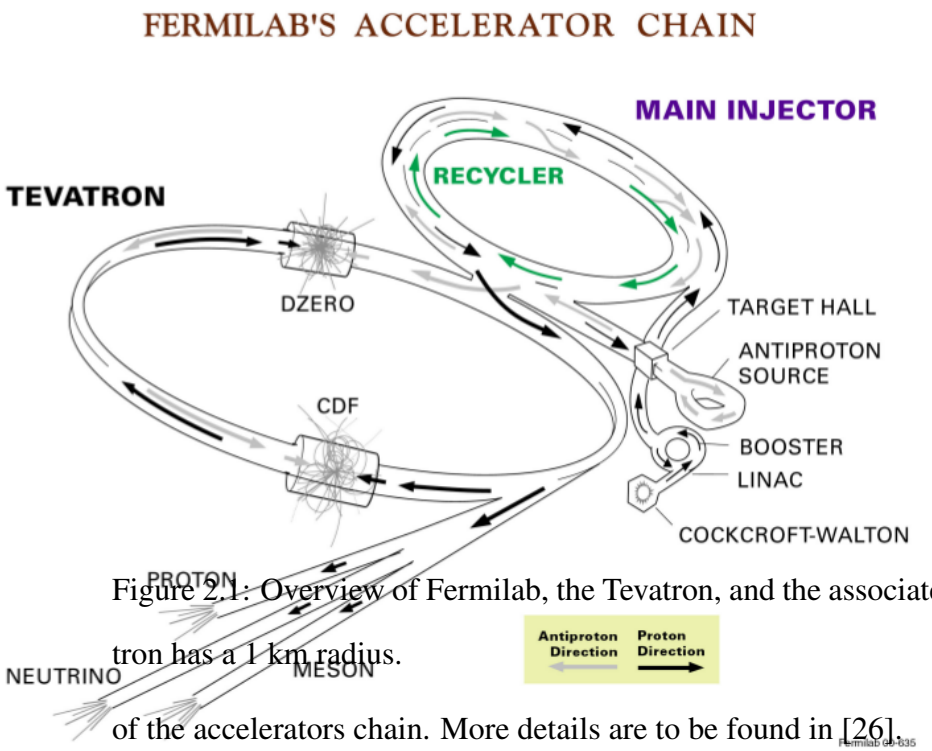

Figure 2.1: Overview of Fermilab, the Tevatron, and the associated accelerators. The Tevatron has a 1 km radius.

of the accelerators chain. More details are to be found in [26].

Particle beams starts from negative hydrogen ions accelerated by the Cockroft-Walton accelerator. Hydrogen ions H^- are produced using a magnetron surface plasma source [27], as is shown in Fig. 2.2. Hydrogen ions H^- are extracted through the anode aperture and then accelerated to 18 KeV through the extractor plate. Hydrogen ions will them enter the Cockroft-Walton accelerator, which utilizes static electric fields to accelerate charged particles. The Fermilab Cockroft-Walton accelerator has a total output voltage of 750 HV, thus H^- ions are accelerated up to 750 KeV through the Cockcroft-Walton accelerator and passed to the Linac accelerator.

At the Linac the 750 KeV H^- ions are accelerated up to an energy of 400 MeV. Linac consists of two sections, the drift tube Linac and the side coupled cavity Linac. The drift

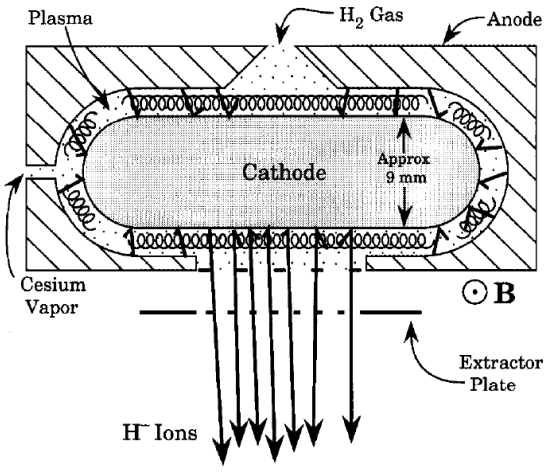

Figure 2.2: Basic configuration of the magnetron surface plasma source.

tube Linac is a line of drift tubes radially centered in five cylindrical RF tanks. These are shown in Fig. 2.3. RF tanks resonate at 201.24 MHz and are able to accelerate hydrogen ion beams to an energy of 116 MeV. The side coupled cavity Linac has seven RF tanks similar to those in the drift tube Linac but designed to be more efficient. The RF tanks of the side coupled cavity resonate at 805 MHz and thus accelerate the beams every fourth RF cycle. Beams in the Linac are just bunches of particles which are focused or defocused with a quadrupole magnets. After reaching an energy of 400 MeV, the ion beam is transferred to the Booster. The Booster is the first circular accelerator, a rapid cycling

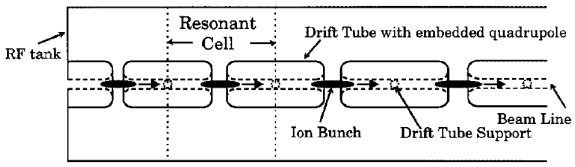

Figure 2.3: simplified top view of Alvarez drift tube linac. A RF tank contains $n + 1$ resonant cells. Each cell is filled with a bunch of particles. The particles are alternatively focused and defocused using quadrupole magnets embedded within the drift tubes. The bunches of particles are always accelerated in the gap between drift tubes while they are shielded in the drift tubes from the field of RF tank.

synchrotron, where protons are accelerated from 400 MeV to 8 GeV. It consists of a series

of magnets arranged around a circle with a circumference of about 475 m. Contrary to the magnets in the Main Injector, all Booster magnet are so-called combined function magnets, which bend the beam and focus it either horizontally or vertically (horizontal defocusing). The usage of alternating gradients to keep the proton bunches tightly constrained inside the vacuum chamber of the beam pipe is usually referred to as strong focusing and it is very similar to alternating concave and convex optical lenses.

The 8 GeV protons from the Booster are transferred to the Main Injector, another synchrotron with a circumference of roughly 3.3 km, more than half the circumference of the Tevatron and about seven times that of the Booster. The tunnel of the Main Injector houses two separate rings: the Main Injector (the lower ring), which can perform a multitude of operations and the Recycler (the upper ring), a storage ring for 8 GeV antiprotons. Since recycling is too time consuming and the achieved efficiency is low, the Recycler is used only to store antiprotons, in order to unload the antiproton accumulator. The Recycler beam pipe is equipped with permanent magnets, making it more robust against e.g. power failures, to store 8 GeV antiprotons. The Main Injector beam line makes use of separate large dipole magnets populating the ring segments to bend the beam, while special focusing/defocusing quadrupole magnets are utilized to keep the beam restricted to the beam pipe. The beam does not form a continuous stream, but it is bunched. Since the Main Injector is much larger than the Booster, 84 bunches are required to fill all the available RF slots (or buckets) around the circumference of the Main Injector; the total sum of the bunches, i.e. all available buckets, constitutes a batch. The LINAC and the Booster together form the proton source, or what is called the pre-accelerator.

The Main Injector accepts 8 GeV protons from the Booster, or 8 GeV antiprotons from the Anti-proton Source, and accelerates the 8 GeV protons to either 120 GeV or 150 GeV depending on their destination. The Main Injector and the Tevatron ring were designed to allow simultaneous operation. If the Main Injector is used to inject protons or antiprotons into the Tevatron, its final beam energy is 150 GeV; if it is used to supply protons for pro-

duction of antiprotons during a physics store in the Tevatron, which lasts typically around 24 hours, the Main Injector will continuously accelerate protons from 8 to 120 GeV. These are then delivered to fixed target experiments and to the antiproton source.

Furthermore, the 150 GeV proton and antiproton bunches delivered to the Tevatron must be super-bunches, more intense than any individual bunch that can be accelerated by the Booster. To meet this requirement, the Main injector coalesces 7 to 11 Booster bunches into one super bunch, before transferring them to the Tevatron.

The antiprotons are produced and stored with a series of apparatus including the fixed target, the Debuncher, the Accumulator and the Recycler. The 120 GeV proton beam from the Main Injector is directed and focused to strike the nickel alloy target, from which all sorts of secondary particles are produced. A lithium lens is used to collect the 8 GeV antiprotons from the spray, as shown in Fig. 2.4. A dipole magnet is added to select the momentum of the particles. The efficiency of antiproton production is very low with typically 15 antiprotons produced for every one million protons striking the target. Anti-proton are then con-

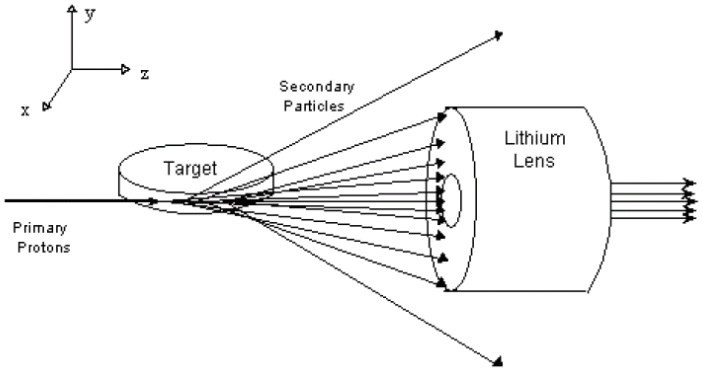

Figure 2.4: The lithium lens used to collect antiprotons from the secondary particles originated from the target.

veyed to the Debuncher, which is a triangular synchrotron used to reduce high momentum spreads of antiprotons off the target. This process is done using a method called *stochastic cooling*. One signal from the circulating antiprotons on one side of the ring is picked as an indication of of deviation from the ideal orbit, while the correction resulting form this

signal is applied to the antiproton beam on the other side of the ring to push it back to the ideal orbit. The Accumulator is the second synchrotron housed in the same tunnel with the Debuncher. Once the accumulation is complete[1], the antiproton beams are directed to Main Injector. The Recycler is housed right below the Main Injector ring and designed as a storage of antiprotons to allow higher stacking efficiency of the Accumulator. For cooling, both stochastic cooling and electron cooling systems are used. The accumulated antiproton beams are transferred to the Main Injector and then the Tevatron ring.

2.1.2 The Tevatron

The Tevatron is the main accelerator at Fermilab. At the Tevatron protons and antiprotons are both accelerated to 980 GeV and are made to collide at its two collision points, B0 where the CDF detector is located and D0 where the DØ detector is. The Tevatron has a circumference of approximately 6.2 km. With the help of cryogenically cooled superconducting magnets, the magnetic field at the Tevatron can reach up to ≈ 4 Tesla. Liquid helium at ≈ 4 K are used to keep the superconducting magnets running.

Proton beams with 36 bunches from the Main Injector are fed into the Tevatron at 150 GeV one bunch at a time. In the same orbital path but in an opposite direction, antiproton beams also with 36 bunches are inject at the same energy as the proton beam into the Tevatron. Each bunch is separated from the other typically by 396 ns. both beams[2] are accelerated from 150 GeV to 980 GeV, each. The two beams are then collimated and squeezed to collide via crossing each other path in the center of both CDF and DØ detectors.

[1] A process that takes more than 12 hours.

[2] Protons and Anti-protons.

2.1.3 Cross Section and Luminosity

Cross Section, σ

The production rate of (a) particular physical process(es) characterizes the colliding performance of the two beams. This production rate is defined as

$$\mathcal{R} = \sigma\mathcal{L} \tag{2.1}$$

where σ is the cross section and $\mathcal{L}$ is the luminosity.

In particle physics, the cross section σ is a mathematical quantity that expresses the likelihood of the occurrence of a certain effective interaction between particles. This mathematical quantity is derived from the classical picture of collisions and hence is in unit of geometrical area. Therefore, the cross section of a certain interaction is directly proportional to the occurrence probability of a certain physical process per unit flux. As an example, the NLO[3] calculations show that the cross section of WH (with $m_H = 125$ GeV) production at the Tevatron, $\sigma(p\bar{p} \to WH)$ to be 0.1855 pb [28].

Luminosity, $\mathcal{L}$

The luminosity describes the interaction of two beams in terms of particle numbers per unit area per unit time. The luminosity accounts for the effect of beam structure on the frequency of collisions. The number of $p\bar{p}$-collisions depends on numerous aspects of the p and $\bar{p}$ beams such as the number of bunches at the collision point, the number of protons (antiprotons) per bunch, and the extent of the bunches[4]. The luminosity is defined as

$$\mathcal{L} = \frac{fnN_pN_{\bar{p}}}{2\pi(\sigma_p^2 + \sigma_{\bar{p}}^2)} F(\frac{\sigma_l}{\beta^*}) \tag{2.2}$$

where N_p and $N_{\bar{p}}$ are the numbers of particles per bunches per beam (36), f is the orbital frequency of the beam, and both σ_p and $\sigma_{\bar{p}}$ are the transverse Gaussian widths of the beams

[3]Next to Leading Order approximation.

[4]Transverse and longitudinal extents.

at the collision point. The form factor $F(\frac{\sigma_l}{\beta^*})$ is less than one and depends on the bunch extent and the length of the interaction region [26]. Instantaneous luminosity is measured in terms of $\text{cm}^{-2}\text{s}^{-1}$ and it changes over time, but the integrated luminosity, $\mathcal{L}_{int}$ is what concerns us more because it is used to calculate the expected number of events for a particular process. Thus if $\mathcal{L}_{int} = \int_{t_0}^{t_0+\Delta t} \mathcal{L} dt$ is the integrated luminosity, then the number of events of a particular process can be found from

$$\mathcal{N} = \mathcal{L}_{int} \times \sigma_{\text{process}} \tag{2.3}$$

2.2 The Upgraded DØ Detector

When both protons and antiprotons collide, they mostly scatter at small angles with respect to the beam line and these events are ignored in my search for the Standard Model Higgs boson. Collisions in which the proton (antiproton) have a *hard scattering*, in which a constituent of a proton annihilates with a constituent of antiproton, are the ones that produce any number of other particles with transverse momenta. If the theory of the Standard Model is the answer to the mass problem, then occasionally this type of collisions should produce a Higgs boson. Constituents of protons and antiprotons are quarks and gluons, which collectively are called *partons*. Partons involved *directly* in the hard scatter are called *initial state*, and particles emerging *directly* the hard scatter are known as *final state*. Figure 2.5 shows a schematic representation of a typical collision event between a proton and an antiproton where the constituents of each particle are shown. The DØ detector is a general purpose particle detector capable of studies on various aspects of the high energy physics of $p\bar{p}$ collisions at the Tevatron. The DØ experiment program involved many topics of interest in particle physics such top quark physics, precision measurements electroweak parameters, bottom quark physics, jet production studies, the Higgs boson and new physics beyond the Standard Model. The DØ detector recorded its first collision during RunI of the Tevatron, 1992–1996 [29].

The DØ detector consists of various sub-detector systems used in identifying the secondary

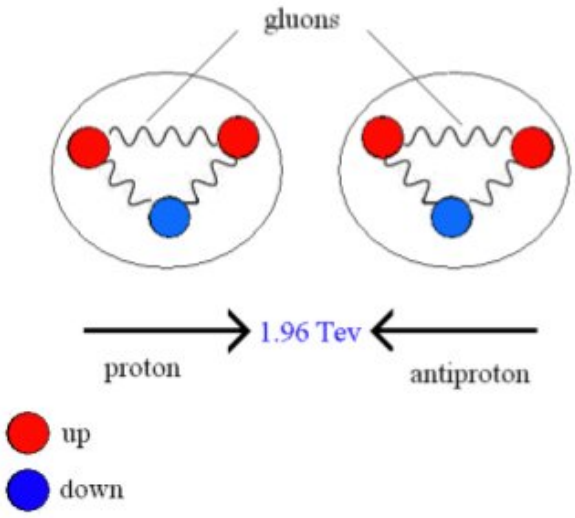

Figure 2.5: Collision between proton and antiproton. Constituents of each particle are shown

particles from $p\bar{p}$ collisions at the Tevatron. These sub-detector systems has a symmetric design of concentric cylindrical configuration centered around the collision point, like the layers of an onion. The detector consists mainly of the vertex detector, the central tracking system, the calorimeter (LAr) system, the muon spectrometer and the luminosity monitoring systems in addition to forward proton detector and sophisticated electronic readout systems [2]. Figure 2.6 shows an overview of the upgraded DØ detector. The innermost most layer of the detector is the central tracking system shown in Fig. 2.7(a). It is placed inside a solenoid magnetic field for the determination of charged particles momenta through their bending radius. The calorimeter system surrounding the central tracking system is made of copper, stainless steel filled with liquid argon (Ar) and depleted uranium. The calorimeter measures the energies of the electromagnetic particles and hadron jets. The muon system is the outermost detector. It is made of scintillator counters, drift tubes and toroid magnets. The muon detector system, as suggested by its name identifies muon particles which easily penetrate through all the inner detectors materials with no much loss in their energies. A sophisticated system of electronic readout systems are installed to collect

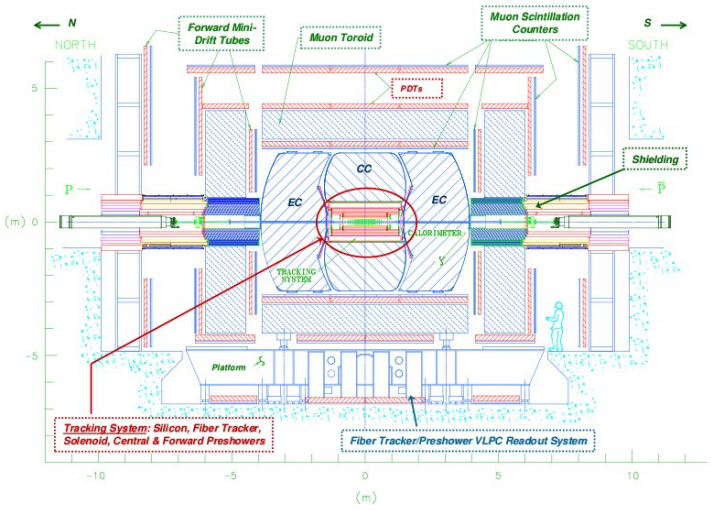

Figure 2.6: Side view of the upgraded DØ detector with major subsystems labeled [2].

signals from each detector subsystem.

2.2.1 Coordinate System

The DØ uses a right-handed coordinate system with its origin at the center of the detector. The coordinate system has a cylindrical symmetry about the beam axis, whereas particle collisions exhibit spherical symmetry about the nominal interaction point. A combination of both cylindrical and spherical coordinates, (z, θ, ϕ), is thus chosen to describe physical events at the detector. Figure 2.8 shows the coordinate system used at the DØ detector. Polar angle, θ, is defined as such that $\theta = 0$ is along the beam pipeline in the $+z$ direction, while $\theta = \pi/2$ is perpendicular to the beam pipeline. Azimuthal angle, ϕ, points away from the center of the Tevatron ring (the positive x direction). The upward direction, $\phi = \pi/2$, defines the positive y direction. The polar angle θ is usually replaced by another quantity y, called the *rapidity*, which is easier to use. The rapidity y of a particle is defined as

$$y = \frac{1}{2} ln \frac{E + p_z}{E - p_z} \tag{2.4}$$

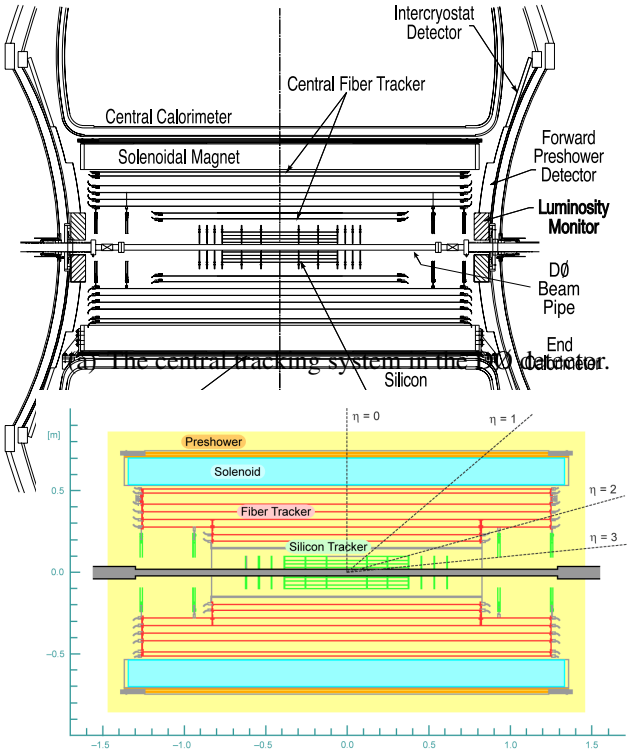

(b) Graphical representation of the central tracking system of the DØ detector. The physics pseudorapidity, η, is also shown.

Figure 2.7: The Central Tracking System.

where E and p_z are the energy and longitudinal momentum of the particle. As the energy of the particle is high enough for the particle to move at speed close to that of light, then the energy can be approximately equal to its momentum, $E \approx p$.

$$y \approx \frac{1}{2} \ln \frac{p + p\cos\theta}{p - p\cos\theta} = -\ln\left(\tan\frac{\theta}{2}\right) \equiv \eta \tag{2.5}$$

Pseudorapidity approximates the true rapidity when the mass of the particle is much smaller than its energy. In a $p\bar{p}$ experiment like DØ the beam dimensions in the plane perpendicular to the beam direction[5] are negligible compared to the beam axis (the z-axis). As a result

[5]The transverse direction.

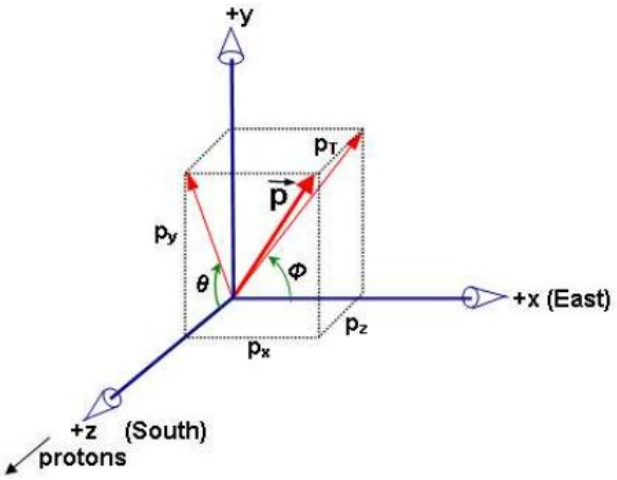

Figure 2.8: Coordinate system used at the DØ

of this structure, the true *detector pseudorapidity,* η_D which is exactly at $z = 0$ may be different from the pseudorapidity η ($\eta \neq \eta_D$). Solid angles are measured in terms of a quantity ΔR, which is defined by

$$\Delta R \equiv \sqrt{\Delta\eta^2 + \Delta\phi^2} \tag{2.6}$$

ΔR is also approximately invariant under Lorentz boosts along the z direction. The above described set of coordinates are the ones used in describing geometric and kinematic variables in my work described in this theses.

Parton-parton collisions do not occur at a fixed $\sqrt{s}$ and as a result a considerable amount of collision energy escapes the detector carried out by the nucleon remnants away down the uninstrumented beam pipe making the longitudinal boost hard to measure. Before a collision occurs, the transverse energy of the system is zero, and one can apply conservation of both energy and momentum in the transverse plane. Several variables are defined to study particles originating from the hard scattering processes in a collision in the transverse plane. Some of the particles (*i.e.*, neutrinos) escape detection and the energy carried away by them manifests itself as a net *imbalance* when we apply the conservation of energy. This imbalance is called *missing transverse energy*, $\not\!\!E_T$.

2.2.2 Tracking System

Almost all physics programs at the DØ collaboration which involves charged particles in their final states use the DØ central tracking system. The search for the Higgs boson is no exception. The DØ central tracking system measures trajectories, charge sign and momenta of the particles that pass through different components of its detectors. Elementary physics allows us to determine precisely the charge sign and the momenta of a charged particle when it passes through a magnetic field. The momentum is calculated through the radius curvature of the particle's path, $k = \frac{qB}{p}$, where B is the strength of the magnetic field, q is the charge of the particle and p is its momentum. The superconducting solenoid surrounding the tracking system is 2.7m long and produces a 2.0T uniform magnetic field [30, 31]. The entire tracking system is the closest to surround the beam pipe. It has two sub-detector components, *viz,*, the Silicon Microstrip Tracker (SMT) and the Central Fiber Tracker (CFT) as can be seen in Fig 2.7. The CFT surrounds the SMT detector system and is made of scintillating fibers. Both position and momentum of a charged particle in the central region can be determined using the CFT. The entire tracking system is able to locate the interaction vertex[6] with a resolution of 35μm along the beam line, and better than 15μm in the $r - \phi$ plane when the transverse momentum of the particle is larger than 10 GeV at $\eta = 0$. Maximum momentum resolution available is $(2 + 0.15p_T)\%$, where p_T is the transverse momentum of the particle[7].

2.2.3 Silicon Microstrip Tracker (SMT)

The SMT high precision comes from using Silicon detectors, of which the functional units are the $p - n$ junction diodes. Diodes used at the SMT are made such that one side is n-doped and the other side is p-doped. As a charged particle passes through the strips, ionization effects create electron hole pairs and cause a current pulse, which can be recorded

[6] Also called "primary vertex".

[7] In units of GeV.

by the electronic readout system. The nominal interaction point can be precisely determined with many of these strips arranged around it. The spatial resolution achieved by the SMT is of $10\mu m$ in $r-\phi$ plane and $35\mu m$ in $r-z$ direction.

Some of the requirements of the SMT system were:

- Three dimensional track reconstruction capability with transverse impact parameter resolution better than 30 μm and a good vertex resolution in the longitudinal direction.
- Radiation hard detector which can withstand the increased luminosity environment of Run II.
- Fast readout system that can be operated at 2.5 MHz bunch crossing rate.

The SMT achieved 3D tracking capabilities via its unique design of combining both barrel and disk modules. Figure 2.9(a) shows there are a total of 6 barrels with strips parallel to the beam direction and 16 disks with their strips oriented in a direction perpendicular to the beam direction. There are 3 barrels in each side of the origin[8]. Each one of these barrels consists of 4 concentric layers of Silicon wafers. Barrels are used to provide the best ϕ-related information possible and to cover the detector region of $|\eta| < 2.4$. Disks are positioned between barrels. There are 6 F-disks, which are the nearest to the detector center, and 4 H-disks, which are the farthest from the detector center. Disk modules provide better measurement of the z-direction. The tracks for large η particles are reconstructed in three dimensions primarily by the disks, while particles at small η are detected primarily by the barrels. In 2006 and during the DØ upgrade, and new layer, called layer 0 [32], was added inside the 4 barrels already in place while the farthest of the H-disks on both sides had to be removed for constructional and electronics connections reasons. One should note that the scale of the SMT is ruled by the collision region where $sigma$ in the z-direction is about 25 cm. In general, the SMT is designed to cover regions of $\eta < 3.0$, which approximately

[8]DØ geometric origin.

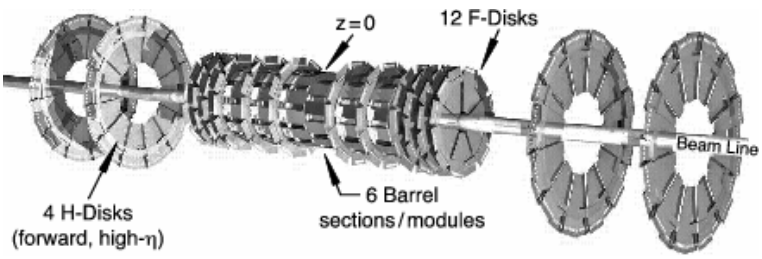

(a) A schematic diagram of the SMT.

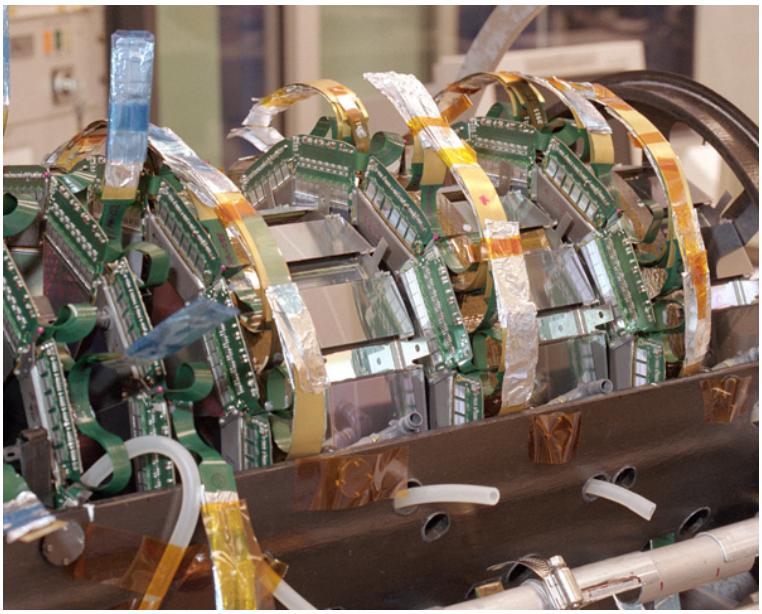

(b) SMT picture taken at the upgrade time.

Figure 2.9: The Central Tracking System [2].

covers all of the calorimeter and the muon detectors systems. More than 792,576 in total were connected and complicated electronics were in place.

2.2.4 Central Fiber Tracker (CFT)

The Central Fiber Tracker (CFT) [33] uses scintillating fibers to reconstruct charged particles tracks. It surrounds the SMT detector and extends the effective tracking volume to $\eta_D < 2.0$ as shown in Fig. 2.10. Combined hits from both the CFT and the SMT improves the overall momentum resolution. The desired impact parameter resolution cannot be achieved by either of the two detectors alone. The core materials of the scintillating fibers is polystyrene; it is doped with organic fluorescent dyes. When ionizing particles de-

posit fractions of their energies in the scintillating material, molecular excitations and rapid fluorescence decay will take place, which will emit a light of frequency ≈ 540 nm. Emitted light is then extracted via fiber waveguides and is then directed to visible light photon counters, or VLPCs. VLPCs are avalanche photo-detectors that are capable of converting light to electric signals.

The CFT consists of 8 layers of concentric carbon fiber barrels. Each layer is actually a double layers of scintillating fibers. Each barrel gives support to the axial[9] fibers which are fixed parallel to the beam pipe. Odd numbered barrels (moving from inside out) holds stereo layers of angles $\pm 3^{\circ}$. These are called stereo layers and are designated u or v. The

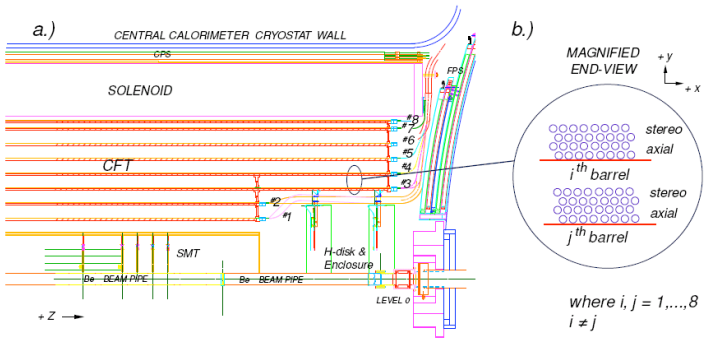

Figure 2.10: Schematic diagram of a quadrant of the DØ Run II Central Fiber Tracker showing the eight scintillating layers enclosed inside the solenoid. The SMT along with the central and forward Preshower Detectors are also shown.

axial fibers provide ϕ measurements at a certain radius, and when combined with the stereo layers information provide a measurement along the z-axis. In all, the CFT contains 78,800 readout channels and covers a radial distance from 20 cm to 50 cm. CFT can measure the transverse momentum tracks (track p_T) very well.

[9]Called axial fibers because they are along the z-axis, $i.e$ the beam axis.

2.2.5 The Solenoid

The solenoid is the magnet that is responsible of bending charged particles tracks inside either the SMT or the CFT. It provides both with a 2 Tesla magnetic field strength with either polarity along the beam-line direction. Figure 2.11 shows the solenoid magnetic field lines in the $y - z$ direction. Field strengths of both solenoidal and toroidal magnets are in unit of kiloGauss[10].

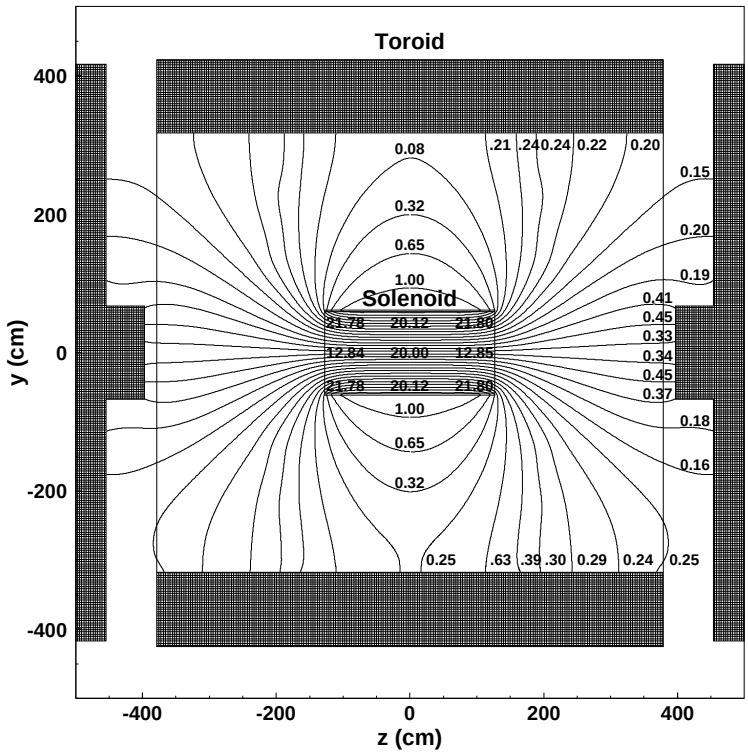

Figure 2.11: Magnetic field lines in $y - z$ plane of the DØ magnetic system [2]. Its superconducting coils carry up to 4749A current and are cooled to 4.6 K using liquid helium. The physical size is limited by the space within the calorimeters to be 2.73 m in length and 1.42 m in diameter.

[10] 1 kiloGauss = 0.1 Tesla.

2.2.6 Preshower Detectors

Preshower detectors are introduced to improve the energy measurement particularly for electrons and photons, as well as enhance the sensitivity of the tracking system. These particles, and others, may interact with the solenoid materials and thus may degrade the energy resolution measured in the calorimeters. Preshower detectors also use scintillating fibers while absorber materials are attached to initiate an electromagnetic showers. At the DØ there are two preshower detector systems, the Central Preshower Detector (CPS) which covers the detector region $\eta < 1.3$ and the Forward Preshower Detector (FPS) which covers the detector region of $1.5 < |\eta| < 2.5$. The CPS is made of 3 layers of axial and stereo fiber strips. The FPS functions similarly although its design is different. Information from the preshower system is included in Level 1 trigger system because they provide fast measurements of both energy and position measurements.

2.2.7 The Calorimeter System

The tracks of a particle can be used to determine three components of a particle's four-momentum; to measure the fourth component, energy, we use calorimeters. Also, trackers are only sensitive to charged particles, while calorimeters provide sensitivity to almost every particle type.

Energy Measurements

The calorimeter system at the DØ detector is used to measure the energy and shape of both electromagnetic (EM) and hadronic (HD) showers initiated by particles such as electrons, photons and jets. Particles are made to pass through dense materials so it can deposit most of its energy in the materials of the calorimeter. These particles are induced to create showers in these "absorbers" dense materials. The energy in the showers is then samples at different points. The calorimeter is constructed from alternating layers of heavy absorber plates and active ionization layers. Electromagnetic shower is the process in which elec-

trons or photons enter the absorber materials and develop a cascade of secondary particles. The EM and HD showers are reconstructed from their signals in the layers of the calorimeter. EM objects interact with calorimeter materials principally via either of the following processes:

- Bremstrahlung ($e \rightarrow e\gamma$)
- Electron Pair Production ($\gamma \rightarrow e^{+}e^{-}$)

The more energetic the particle is, the deeper it goes into the materials, the more secondary particles are produced while the original particle's energy decreases exponentially according to Eq. 2.7

$$E = E_{\circ}e^{-x/X_{\circ}} \tag{2.7}$$

where $E_{\circ}$ is the initial energy of the particle[11], x is the depth traveled by the particle in the detector material and $X_{\circ}$ is the radiation length. The radiation length of uranium is about 3.2 mm. A hadronic shower is almost the same except that it occurs via strong nuclear interactions and it develops over longer distances. Secondary particles in the hadronic shower process are mainly pions π^0 and $\pi^{\pm}$. The π^0 decays into two gamma pairs ($\pi^0 \rightarrow \gamma\gamma$) while $\pi^{\pm}$ interact with the absorber materials via strong forces. The strong interaction length (λ_0) for such interactions is about 10.5 cm.

Calorimeter Performance

Showers developed in the calorimeter is sampled via the active ionization medium. The energy of the original particle $E_{\circ}$ that initiate the shower is directly proportional to the total sampled energy as shown by Eq. 2.8 which shows a linear response.

$$E \propto \sum_{i=1}^{N} E_i \tag{2.8}$$

[11] Before its interaction with the detector

where i=1...N are the different sampling layers and E_i is the energy measured in each layer. By "compensating" is meant the ratio of the electromagnetic to the hadronic response (e/h) of the calorimeter is close to one. The primary sampling calorimeter in the DØ detector uses liquid argon as the active medium. Figure 2.12 shows a small-scale structure of the DØś liquid argon sampling calorimeters. The absorbers are electrically grounded while

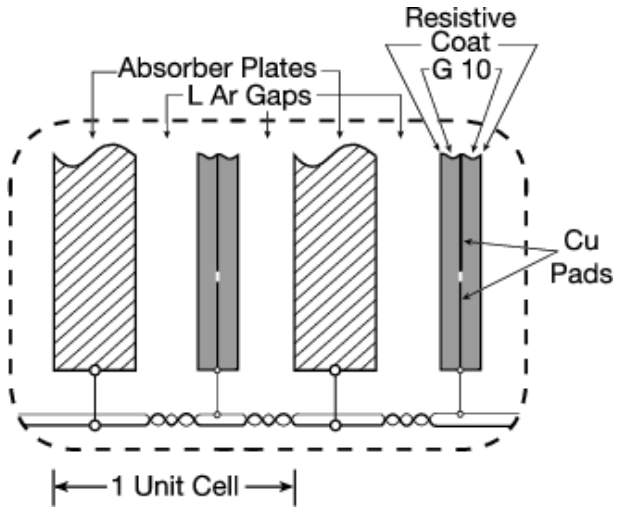

Figure 2.12: Schematic view of a unit cell for the calorimeter. A unit cell includes the absorber plate and signal board with gaps filled with liquid argon. The absorber plate is made of depleted uranium, while the signal board is a copper pad insulated with G10 insulator and coated with highly resistive epoxy.

the readout potential is kept at a positive potential of approximately 2 kV. Showers gets initiated at the absorber plate, and any secondary charged particles ionize the liquid argon, sending electrons to the readout board. This creates a pulse of current that relates directly to the energy in the shower. Considering these electrical signals from many adjacent cells, we can accurately determine the total energy that has already been deposited by the incident particle. The DØ liquid argon calorimeter consists of three parts, the central calorimeter (CC), which covers up to $|\eta| \approx 1$, and two end-cap calorimeters (EC) that extend coverage to $|\eta| \approx 4$. Each cryostat is kept at a temperature of 90 K.

The DØ calorimeter system is built into Electromagnetic Calorimeters and Hadronic Calorime-

ters which are further divided into Fine Hadronic and Coarse Hadronic calorimeters. Figure 2.13 shows that the inner Electromagnetic Calorimeters are made of 4 thinner layers with absorbers $\approx 20X_0$ in total, which allows for electron and photon absorption but not hadronic jets, which pass through them. Hadronic Calorimeters have much larger modules with absorbing materials range of $6\lambda_0$.

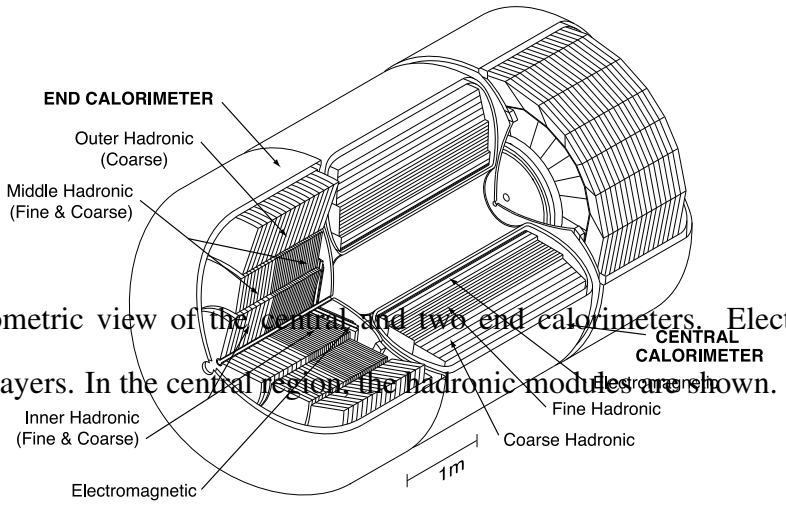

Figure 2.13: Isometric view of the central and two end calorimeters. Electromagnetic modules have 4 layers. In the central region, the hadronic modules are shown.

2.2.8 Muon Detectors

Muons are heavy compared to electrons ($m_\mu \approx 200m_e$) and as a result they suffer minimum energy loss via Bremstrahlung. Muons, therefore, can penetrate through the inner tracking systems without initiating EM showers in the calorimeter system, unlike other EM objects, and as a result muon detector systems comes as the outermost layer of the DØ detector and typically the largest of all detector systems as can be seen in Fig. 2.14. Muons primary energy loss, if their energy is above the 3.5 GeV threshold, is via ionization and excitation processes in the detectors materials themselves. A muon, with enough energy can produce a track in the inner tracking system and it can deposit a small energy amount in the calorimeter. This makes a unique signature of a muon, but muons identification

has been much improved by the muon detector system, and while the inner track could be matched simply to a hit in the muon detectors, additional matching criteria can be used to improve this method. The resolution of the muon tracker is far less efficient than those of either SMT or CFT, but an outer muon track can still provide the necessary information needed to accurately identify the inner track of a particular muon. The muon detector has also its own dedicated magnet to help bending its track for information about muon charge sign and momentum. Muons' trajectories are measured by means of *proportional drift tubes* (PDT's.) A PDT is a thin wire that is suspended in the center of a metal tube, with the wire being held at a large positive high potential relative to the tube itself. A high-energy particle that passes through the tube will cause the gas in the tube to ionize and the resulting free electrons are drifted toward the wire, a process that will cause an electrical signal (pulse). The very thin wire will produce an electric field around itself that will cause drifted electrons to accelerate causing more ionization in the gas filling the tube which will lead to a substantial signal gain. Both the particle's distance of closest approach and the longitudinal hit resolution can be inferred from the signal profile and the relative timing of the signal respectively [34]. In the central muon tracker, layer A, B and C are composed of coarse PDT's with maximum electron drift time of 500 ns. Their pseudorapidity coverage is approximately $|\eta| = 1$. In the forward region, layers A, B, C have finer segmentation which uses *mini drift tubes* (MDT's) with a maximum drift time of 60 ns. These fine segmentation are especially important in the forward region, where particles' densities are the highest. Both PDT's and MDT's are aligned to be roughly parallel to the toroidal magnetic field to optimize momentum resolution. An extra scintillating tiles are also used to provide precise timing information for muons tracks. Scintillating tiles have a response time of few nanoseconds which causes the scintillating hits to be spatially matched to PDT hits in order to associate the muon track with correct collision. Also, since the timing of each bunch crossing is precise to within nanoseconds, scintillator hits may be used to reject muons detected at unexpected times, likely originating from the beam halo or cosmic rays. For these

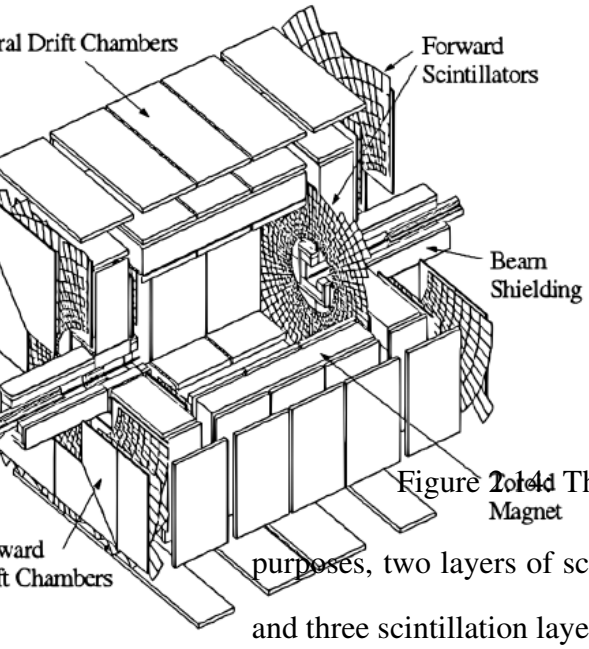

Figure 2.14 The muon system of the upgraded Run II DØ detector.

purposes, two layers of scintillating tiles are used in the central part of the muon tracker, and three scintillation layers are used in the forward region [35].

2.2.9 The Trigger System

Most of the proton-antiproton collisions taking place at the DØ result in low energy QCD processes which are of little importance in physics analysis. Collisions which create particles of interest, such as W bosons, Z bosons are most importantly the *Higgs* boson are very rare. In order to accumulate a large number of events that include any of these particles, depending on the physics analysis, saving at the same time the valuable, and expensive resources, the DØ detector is equipped with a trigger that decides whether an event should be recorded or discarded. The DØ trigger has to reduce the input rate of 2.5 MHz (given by the time between punch crossings) to 50 Hz needed for the events' reconstruction software to work.

Three distinct levels form the trigger system. Each subsequent level handles a lower rate

and can therefore examine the event in more detail. The first level, called Level 1, or L1, comprises a collection of hardware trigger elements. In L1 the 2.5 MHz input rate trigger rate is reduced to 2 kHz needed as an input rate for the second stage of triggering, Level 2, or L2. At L2, hardware engines and embedded microprocessors associated with specific sub-detectors provide information to a global processor which constructs a trigger decision based on individual objects as well as object correlations. The L2 trigger system reduces the rate by a factor of two and has an acceptance rate of roughly 1 kHz. Events which are passed by Level 1 and Level 2 are sent to the Level 3 trigger farm for real time reconstruction. Here very complex algorithms reduce the rate to 50 Hz. Events accepted by Level 3 are stored for off-line reconstruction. An over view of the DØ trigger system in shown in Fig. 2.15.

Due to improvements made to the Tevatron accelerator, the instantaneous luminosity has been increased since the start of Run II. In order to keep the acceptance rate at Level 3 trigger constant, the sets of triggers used to collect the data have to be updated accordingly.

Level 1 Trigger

This is the first level of triggering. It uses coarse information from the calorimeter, CFT, preshower detectors, and muon tracker to accept data at a rate of 2 kHz. Level 1 (L1) buffers hold enough data to allow 3.7 μs for the sub-detectors to provide the necessary information for a L1 decision, and for that decision to be made. The time necessary for readout from L1 to the level 2 trigger causes some events to be dropped immediately after every L1 accept, which places an upper limit on L1 accept rate. 2 kHz was chosen to keep this dead-time below 5%.

L1 Calorimeter Trigger (L1Cal):

It uses fast estimates of energies deposited in towers of size $\Delta\eta \times \Delta\phi = 0.2 \times 0.2$ to construct simple quantities such as total transverse energy (E_T) or the number of towers above a given $E_T$threshold. Thresholds may be applied to groups of adjacent towers to

roughly trigger on jets.

L1 Central Trace Trigger (L1CTT):

The central track trigger is designed for the ability to trigger on charged particles with $P_T > 15$ GeV/c and to find preshower clusters and match them to tracks. It reconstructs the trajectories of charged particles using fast chip data provided by the CFT (axial fibers only,) the CPS (axial strips only,) and the FPS. The CFT fibers are arranged in 4.5° trigger sectors in the transverse plane. The fiber hits from each 4.5° trigger sector are compared with approximately 20,000 predefined analytically generated track equations.

L1 Muon Trigger (L1Muon):

L1Muon triggers match hits between the various muon scintillator and PDT layers and between outer muon tracks and L1CTT tracks. Similarly, the L1CalTrk triggers match L1CaL information to L1CTT tracks. Various $p_T$thresholds may be applied to the matched objects. L1CalTrk triggers were added during the transition from RunIIa to RunIIb.

The final L1 trigger decision is is taken by a combination of information from all various L1 systems and comparing it to a set of predefined trigger terms.

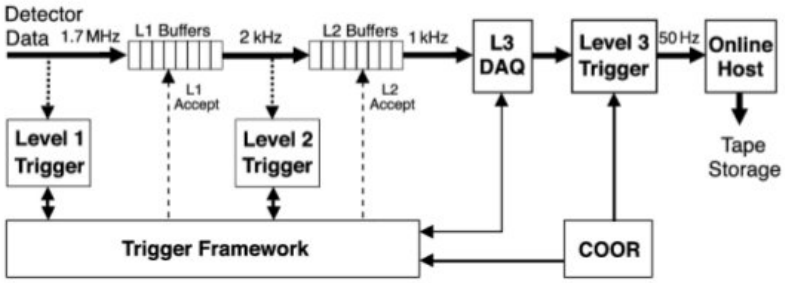

Figure 2.15: Flow of data through the DØ trigger system.

Level 2 Trigger

At the second level of triggering, the increase in decision making time over L1 allows for the use of more detailed information and more sophisticated algorithms.

L2 trigger consists of two stages, preprocessors which are specific to each sub-detector and a global processor which combines information from the different preprocessors to make a trigger decision. L2 trigger system is the first in the chain to look at events variables to create objects like muons, electrons or jets. It is at L2 that events are filtered according to correlations across the entire DØ detector. L2 filters decrease data flow by a factor of two, so the L2 accepts rate is approximately 1 kHz.

L2 Calorimeter Trigger (L2Cal):

The calorimeter preprocessor identifies the electrons/photons and jets and calculates the event $\not\!\!E_T$ to be used later by the L2 global processor. The jet algorithm operates by clustering $n \times n$ groups of calorimeter trigger towers which are centered on seed towers. Jets' seed towers are required to have $E_T > 2$ GeV. The electron, photon algorithm uses seed towers with $E_T > 1$ GeV and combines them with neighboring towers having the largest E_T. The fraction of tower energy deposited in the EM calorimeter is used to reduce the background from jets. The L2 calorimeter $\not\!\!E_T$ algorithm calculates the vector sum E_T from E_T of each trigger tower.

Central Track Trigger (L2CTT):

L2 track trigger is composed of of three preprocessors: the L2CFT which receives tracks from L1CTT, the L2STT which takes input from both SMT and L1CTT, and the L2PS which formats the L1CTT preshower clusters. Information from all three preprocessors is used in the global L2 trigger decision.

Muon Trigger (L2Muon):

It takes the L1Muon outputs and incorporates calibration information and more precise timing from scintillators.

Level 3 Trigger

Level 3 triggering system is the one that has no dedicated data path; instead it uses a subset of data to make trigger decision. L3 uses the full set of information content of each event accepted by Level 2 system.

Using a large amount of information available from L2 system, L3 trigger system makes a decision based on objects such as electrons, jets, muons that are nearly as sophisticated as those techniques used in offline analyses. For the first time, use of tracks to find primary vertices is utilized, and location provides improved calorimeter-based E_T measurements. Also available for L3 is the identification of a secondary vertex, so $b-$jets tagging can be implemented in L3 trigger system. Filters may be applied to single physics objects or to variables relating several of these objects, resulting in an acceptance rate of almost 100 kHz. Events that passes L3 trigger system are all recorded for analyses.

L3 uses a Linux farm of multiple CPU's in each farm node. Currently, the L3 farm contains 288 nodes, each with either four or eight CPU's. When an event is accepted by L2 trigger, all fragments of the event are sent from all of the detector subsystems to the same node of the Linux farm, where all of these fragments are used to furnish a complete event. Completed events then are sent to object construction and filtering algorithms with each event assigned a certain CPU and all CPU's working in parallel. Currently L3 farm can process over 1600 events simultaneously. If we assume no dead-time at L3, the 1 kHz input rate to this massively parallel system goes to a maximum decision time of more than one second.

CHAPTER 3

Events Reconstruction and Object Identification

In This chapter we discuss the details of events and physics objects reconstruction at DØ, with special emphasis on the special procedures for the three objects in the final state of this analysis: electrons, missing transverse energy $E_T$and $b-$jets.
Event reconstruction is an essential and a non-trivial first step in analyzing the data collected by the DØ detector to convert raw information provided by the detector to the objects related to the physics we are set to study. Event reconstruction can be a time-consuming process, it can take several seconds to several minutes per one event, as one must construct a variety of different physics objects out of more than million individual channels.

In this chapter, We give a concise description of the reconstruction of the objects and particles of physical interest in the $WH \rightarrow e\nu b\bar{b}$ analysis. Physics objects of interest to this analysis are tracks, primary vertices, electrons and jets.

Raw data chunks of both real data events and simulated events are processed using the DØ Offline Reconstruction Program (RECO) [36] to reconstruct the physics objects. This offline reconstruction algorithms used to identify the physics objects are described in Section 3.1

(rest of other sections should be placed here)

3.1 Offline Event Reconstruction

RECO algorithm is a collection of software that associates reconstructed objects with data chunks based on the DØ Event Data Model [37]. It is structured in hierarchical steps. Raw data chunks are unpacked first to decode raw information contained in them where is associates electronic readouts with detector components and apply specific detector calibration constants. The global tracks are reconstructed, then, and put into track chunks using the information of hits within the SMT and the CFT detectors. With tracking information available, both primary vertices and displaced secondary vertices are searched for, then they are to be associated to tracks. The final step is to combine track information with energy deposition in the calorimeter and the preshower detectors as well as with the hits in the muon chambers, to identify such physical objects as electrons, photons, muons, and jet candidates.

3.2 Tracks

Tracks, not physical objects in themselves, are important for such measurements as momentum measurements and in object identification. As an example, both electrons and photons give have the same signature in the calorimeter, but can differentiate between them if track are present for electrons. As a charged particle, when an electron traverse the layers of the central tracking system, it leaves hits that are clustered then analyzed with pattern recognition software to find tracks.

3.2.1 Track Reconstruction

A charged particle traveling through both the SMT and the CFT will probably interact with multiple channels (that is with strips in the SMT, and with fibers in the CFT) in each layer of these detectors, this will result in a cluster of hits as can be shown in Fig. 3.1 Particles traversing a scintillating fiber near the edge of its active volume result in a signal smaller

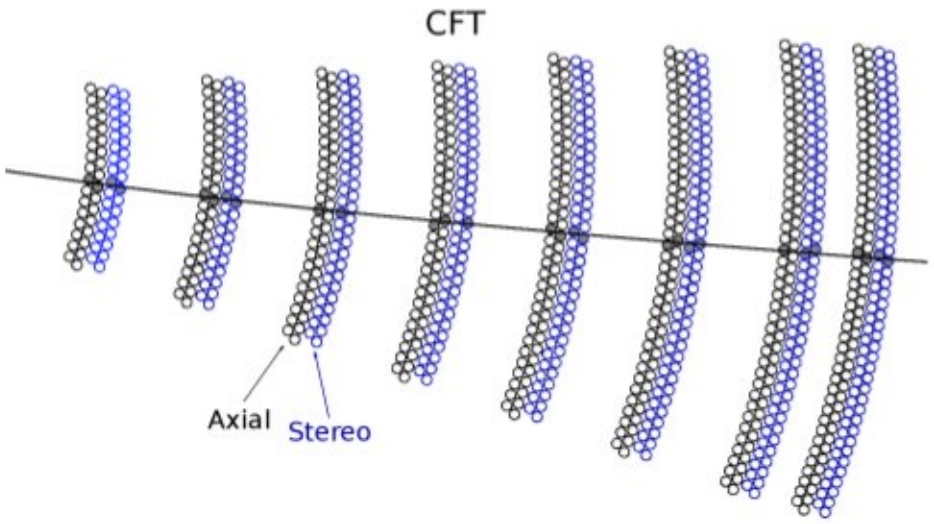

Figure 3.1: Illustration showing the clusters of hits left in each layer of the CFT from a charged particle.

than the one generated when a particle traverses through the center of the fiber or tube. In exactly the same manner, a particle moving through a silicon wafer at an oblique angle will ionize more silicon atoms than a particle at normal incidence. If a particle generates multiple hits in a single tracking layer, an interpolation between these hits is used, weighting each hit according to the charge collected by the silicon strip, the VLSP, or a drift tube. With such method, we can improve hits' resolutions beyond the physical dimensions of the detector. The information from the amount of collected charge is used to yield as precise measurements as possible.

Pattern Recognition

Pattern recognition performed on reconstructed hits yield a set of particle paths originating from the interaction region. The magnetic field is very well mapped in the tracking detectors, taking into account the fringe effects near the ends of the solenoid that create a small component in the radius direction. Both location and density of the detector materials are

mapped as well. Particles' trajectories are not a perfect helical trajectories but they are re slightly altered (and are predicted) due to these effects.

To identify tracks from a very large collection of hits, DØ uses two optimized track-finding algorithms: The first is the *alternating algorithm* (AA) [38] and last one is the *histogramming track finder* (HTF) [39]. The use of these two independent and different algorithm is essential because it is extremely important to find all of the tracks in each event to achieve maximal efficiency. Both HTF and AA excel at different phase space regions and both use different assumptions.

The first technique starts at the inner most layer of the tracking system, then it moves piecewisely (incrementally) outward (toward out layers.) The algorithm begins with a hit in an SMT F-Disk or a barrel with a second hit outer than the original one and has a difference, in the azimuthal angle, of $\Delta\phi < 0.08$. The algorithm then searches for a third hit that will be consistent with a track that has a radius of curvature, ρ, such that $\rho > 30$ cm, (which corresponds to a transverse momentum $p_T > 180$ MeV,) a distance of closest approach to the beam line of $d_\circ < 2.5$ cm, and a χ^2 fit value such that $\chi^2 < 16$. All available tracks-candidates, through the use of Kalman filter [40], will be used to construct tracks through the rest of the tracking system. Kalman filter uses a detailed mapping of the DØ detector's materials and the magnetic field used in the detector to extrapolate each track to the next layer of the tracking system. If a new hit is found within a small window around the extrapolation, then that hit will be included in the track that is being reconstructed. Missed layers are allowed by this algorithm but it stops reconstructing a track after missing three consecutive layers. An additional condition is that tracks cannot share more than 2/3 of their hits with other tracks and the hits used must fit the tracks where $\chi^2 < 16$ [41].

Tracks are also found through looking at the transverse projection of all the hits in the SMT and applying a Hough Transformation [42] to convert hits' positions in the $x \times y$ space to lines in the $\rho \times \phi$ space; where ρ is the radius of curvature of a circular path that

intersects the origin and the hits, and ϕ is the azimuthal angle from the origin to that circle at the origin. Hits from the same track intersect at one point in the $\rho \times \phi$ space. Because there exists a huge spectrum of tracks that is able to connect the interaction point with a single hit, the HTF maps the transverse coordinates of a hit in the SMT and CFT to a line in this phase space. If several hits belong to the same track, the corresponding lines should intersect at a single point (ρ, ϕ). The coordinates of this point are the transverse properties of the track responsible for these hits. Our implementation of this algorithm divides $\rho \times \phi$ space into discrete bins and fills the resultant histogram with tracking hits. Then, we identify track candidates by selecting narrow peaks in the histogram [43].

Tracks originating from decays of *long-lived* particles may not be found with the HTF method, and for these tracks, the AA outperforms the HTF. With a seed track of three SMT hits, the AA extrapolates the track outwards to the next layer and attempts to find hits within a narrow window around the extrapolation. The AA algorithm proceeds interactively through all the layers of the inner tracker, or until it counts three missed layers. The AA algorithm can also begin with a seed of three hits from the CFT. A two-dimensional Kalman filter is used to more accurately calculate the track parameters and remove those tracks with higher χ^2 values (more than 16.) The z component is calculated for each track in a manner similar to the above where then a three-dimensional Kalman filter extrapolates the tracks through the CFT. This process is again performed starting with hits in the CFT then extrapolating the tracks backward into the SMT.

3.3 Primary Vertex

The primary interaction vertex, primary vertex (PV), is a 3-D region where a proton-antiproton collision occurs. The number of collisions at this region depends on the instantaneous luminosity at which the collision occurs. For a given luminosity, the number of collision vertices per bunch crossing follows Poisson distribution. Collisions vertices locations are distributed with a width of $\sigma_r = 40$ μm in the radial direction and $\sigma_z = 28$

cm along the z-axis.

The average number of collision vertices is typically two, but due to the long Poisson tail, some bunch crossings will have more than the typical number. In bunch crossings that have an event of a physical interest, it is of great importance to find the location of the primary vertex of this event so that the momentum vectors of the resulting particles are accurately found (calculated.) other interactions' vertices that does not involve a hard scatter process are referred to as *minimum bias* (MB) interactions, particles from such vertices constitute a significant instrumental background. This background can be reduced through an accurate identification pf the PV and an association of every detected particle with the correct vertex.

3.3.1 Primary Vertex Reconstruction

Reconstruction of the PV can be done through two major passes: identifying all vertices that are consistent with $p\bar{p}$ collisions [44], then choose the vertex least consistent with the MB hypothesis [45]. At first, tracks are selected with the following criteria:

- $p_T > 0.5$ GeV;
- at least two SMT hits; and
- DCA/$\sigma_{DCA} < 5$,

Where DCA is the *distance of closest approach* of the track to the beam line, and σ_{DCA} is its associated uncertainty.

Selected tracks, and based on their z-coordinates, are to be clustered in a z-cluster. A z-cluster starts with the highest possible p_T track and then other tracks are to be added if they fulfill the $|z_{DCA} - \bar{z}| < 2$ cm condition, where $\bar{z}$ is the mean distance value of the all other tracks in the cluster. In the next iteration, the algorithm builds a different cluster around the highest possible uncluttered p_T and then the process goes on until all tracks are z-clustered

in non-overlapping, non-trivial z-clusters. At the end of the iteration processes, any trivial z-clusters that contain only one selected (chosen) track are removed.

Within each z-cluster, a Kalman fit is to be performed to locate the hard scatter vertex. If the fit χ^2 per degree of freedom $(\chi^2/n_{DF}) > 10$, then the track that contributes to the value of χ^2 is rejected. This processes continues until the condition $(\chi^2/n_{DF}) < 10$ is met, or until the z-cluster contains only one track and then gets removed. This fitting process would convert the list of z-clusters into a list of PV candidates [43].

After finding all collision vertices for a bunch crossing, it remains to choose which of them are minimum-bias interactions and which of them is the true primary vertex. Minimum-bias tracks are known to have much lower $p_T < 0.5$ GeV than tracks from hard scatter interactions. Using this fact, the probability for each track being originating from a minimum-bias interaction is calculated. Probability of all minimum-biased tracks originating from a given vertex are then multiplied to determine the minimum-bias probability for that vertex. The vertex with the lowest probability that it is a minimum-bias collision vertex is the one chosen as the primary vertex. Studies in [46] shows that the PV reconstruction efficiency is almost $\sim 100\%$ for both data and simulated events.

3.4 Electron Reconstruction and Identification

3.4.1 Reconstruction

In the detector, electrons are distinguished by their narrow showers in the electromagnetic calorimeter, with showers originating from the preshower detectors and associated with a track in the central tracking detectors [47]. Showers originating from Photons are similar to those originating from electrons, but they are not associated with any tracks. Electrons and photons are reconstructed at the DØ with the same algorithm, where the distinction between the two is made by the presence or absence of a central track or a preshower signature, respectively. Both electrons and photons are referred to collectively as "EM"-objects. Two

main approaches exist for reconstructing EM clusters: the simple cone algorithm and the nearest neighbor algorithm.

Simple Cone Algorithm

The simple cone algorithm constructs clusters of calorimeter tower within a cone of radius, R, where $\Delta R = \sqrt{\Delta\eta^2 + \Delta\phi^2} = 0.4$. The Highest EM towers are chosen as seeds for building clusters and all other adjacent towers above the threshold $E_T = 0.5$ GeV in the cone are added to the cluster if they are in the neighborhood of $\Delta\eta \times \Delta\phi = 0.3 \times 0.3$. The next step is that all towers within a cone of radius 0.4 with respect to the energy weighted axis of the original cluster are added. The energy weighted axis is re-evaluated and the steps are repeated until a stable cluster is found.

Cell Nearest Neighbor (CellNN) algorithm

Cell Nearest Neighbor (CellNN) algorithm chooses the calorimeter cell rather than towers. In each layer of the calorimeter, the cell with the highest energy deposition is chosen as the seed to be used to build the cluster. Neighboring cells are added to this seed to build the cluster in a given calorimeter layer (termed as *floor clustering*.) The third EM layer (EM3) is chosen as the global cluster, to which the other floor clusters are matched with an angular requirement [48].

3.4.2 Identification

The two algorithms described in 3.4.1 do not distinguish between electrons and photons. Distinction between the two is mainly done by looking for tracks associated with the cluster in the central tracking system [49]. Photons do not leave any tracks since they are neutral particles. For reconstructing a track that is associated with the EM cluster, a road in the region $\Delta\eta \times \Delta\phi = 0.05 \times 0.05$ is defined between the center of the EM cluster and the event's PV. Tracks with $p_T > 1.5$ GeV are chosen from within the road [50]. The existence

of One or more tracks means the particle candidate is an electron, no tracks means the particle candidate is a photon. Electrons have an $ID = -11$, positrons have an $ID = +11$ and photons have an $ID = 10$. An EM cluster identified with $|ID| = 10$ or 11 is tagged a "loose" electron. A set of criteria based on energy deposition, shower shape and track matching are developed to identify electrons. These are:

1. Electromagnetic fraction, f_{EM}
2. Isolation fraction, f_{iso}
3. Track match, χ^2
4. Seven-variable H-matrix χ^2_{HMx7} [51]
5. Electron likelihood

Electron identification studies used two samples. The signal sample was a 245 pb$^-1$ of di-electrons events ($i.e. Z \rightarrow ee.$) The background sample was obtained from 230 pb$^-1$ of EM+jet events.

Electromagnetic Fraction, f_{EM}

f_{EM} is the total energy of the cluster deposited in the EM calorimeter layers. It is calculated from:

$$f_{EM} = \frac{E_{EM}(0.2)}{E_{total}(0.4)} \tag{3.1}$$

where $E_{total}(0.4)$is calculated with a cone of radius 0.4 with both electromagnetic and hadronic calorimeters, and $E_{EM}(0.2)$ is the calculated using a radius of 0.2 using only the electromagnetic calorimeter. The electromagnetic fraction, f_{EM} is required to be more than 90%. EM showers with $f_{EM} > 0.9$ is shown in Fig. 3.2 [52].

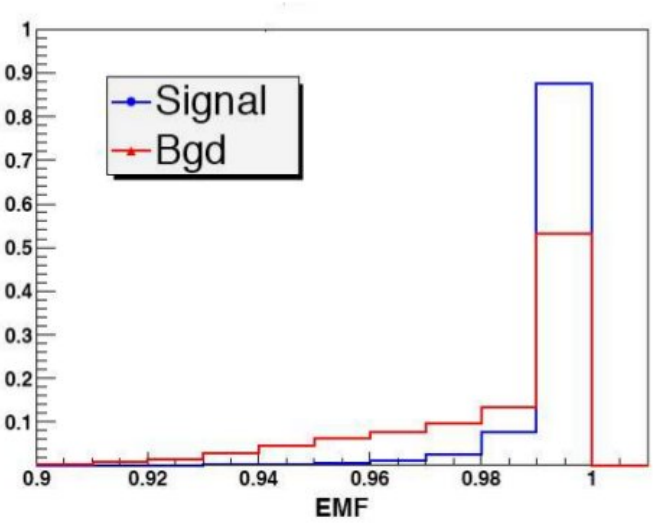

Figure 3.2: Electromagnetic fraction (f_{EM}) distribution for real electrons (in blue) and fake electrons (in red).

Isolation Fraction, f_{iso}

The isolation fraction, f_{iso}, is defined as:

$$f_{iso} = \frac{E_{total}(0.4) - E_{EM}(0.2)}{E_{EM}(0.2)} \tag{3.2}$$

f_{iso} is designed to reduce the probability that a highly collimated jet may fake an electron, since these jets may still deposit most of its energy in the electromagnetic calorimeter. The condition that $f_{iso} < 0.15$ corresponds to an energy deposition in the $\eta - \phi$ space. The isolation fraction for both signal and background are shown in Fig. 3.3 showing for good electrons, small values for f_{iso} [52].

Track match, χ^2

A track match χ^2 is calculated to determine how well a track is matched to a cluster. A candidate electron with one or more tracks is chosen and χ^2 is calculated in two distinct ways

$$\chi^2_{spatial} = (\frac{\Delta\phi}{\sigma_{\Delta\phi}})^2 + (\frac{\Delta z}{\sigma_{\Delta z}})^2 \tag{3.3}$$

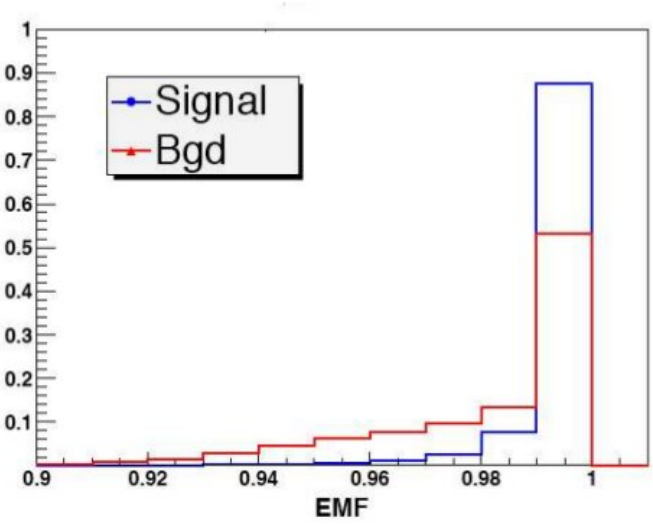

Figure 3.3: Isolation fraction (f_{EM}) distribution for real electrons (in blue) and fake electrons (in red).

$$\chi^2_{E/p} = \chi^2_{spatial} + (\frac{E_T/p_T - 1}{\sigma_{E_T/p_T}})^2 \tag{3.4}$$

where $\chi^2_{spatial}$ is the spatial track match; it uses the distance between the center of the cluster and the track. $\Delta\phi = \phi_{track} - \phi_{clus}$, and E/p track match also compares the energy, E, of the electromagnetic calorimeter to the track momentum, p. σ_X is a one standard deviation for the distribution variable X. The probability $P(\chi^2)$, is used to calculate that the probability that both track and cluster are matched. The track of the lowest χ^2 is chosen in case more than one track exist.

H-matrix χ^2

The H-matrix χ^2 [53] is used to compare between the shower shape in the cluster and the expected shower shape for an electron. The H-matrix χ^2 uses seven variables to parametrize the shower shape:

1. Fraction of shower energy in the first EM layer of the calorimeter

2. Fraction of shower energy in the second EM layer of the calorimeter

3. Fraction of shower energy in the third EM layer of the calorimeter

4. Fraction of shower energy in the fourth EM layer of the calorimeter

5. Width of the shower in the $r-\phi$ plane in the 3^{rd} EM layer

6. Logarithm of the total shower energy, $\log_{10}(E_{\text{total}})$

7. Expected width of the $z-$position of the PV, z_{vtx}/σ_{zvtx}

The expected electron shower shape is then calculated using:

$$M_{ij} = \frac{1}{N}\sum_{n=1}^{N}(x_i^n - < x_i >).(x_j^n - < x_j >) \tag{3.5}$$

where M_{ij} are the elements of the covariance matrix (**M**) The covariance matrix is derived from N MC-generated electrons using the seven variables above. The H-matrix is then define as:

$$\mathbf{H} \equiv \mathbf{M}^{-1} \tag{3.6}$$

that is the H-matrix is defined as the inverse if the covariance matrix **M**, where x_i^n is the value of i in the nth MC electron. The H-matrix is then used to build χ^2 using:

$$\chi^2_{H-\text{matrix}} = \sum_{i,j=1}^{7}(x_i^k - < x_i >)H_{ij}(x_j^k - < x_j >) \tag{3.7}$$

where x_i is the value of i for the electron candidate. Shower shapes change with different values of $|\eta|$ and as a result for each range of η a new H-matrix is constructed.

Electron likelihood

The "fake" electron term is used to refer to an electron candidate that is not a real electron. The electron likelihood [54] variable is used as a discriminator between clusters from real electrons and others from fake "no real" electrons. Thus, the use of likelihood in electron identification enhances the separation between good electrons (the signal) from the fake ones. The likelihood uses the following seven variables (as defined by Eq. 3.8):

$$\mathcal{L}_n(x) = \frac{P_{sig}(x)}{P_{sig}(x) + P_{bkg}(x)} \tag{3.8}$$

$$P_{sig}(x) = \prod_{i=1}^{7} P_{sig,i}(x_i) \tag{3.9}$$

$$\text{and} \qquad P_{bkg} = \prod_{i=1}^{7} P_{bkg,i}(x_i) \tag{3.10}$$

where x_i refer to the seven parameters:

1. Spatial track match probability, $P(\chi^2_{spatial}$

2. Calorimeter cluster E_T/p_T *per* track.

3. The distance of closest approach (DCA) of the associated track to the primary vertex.

4. The Seven-variable-H-matrix χ^2_{hmx7}.

5. EM fraction, f_{EM}

6. Sum of the p_T of all tracks, except the associated track, $\sum p_T$, in a cone of size $R = 0.4$.

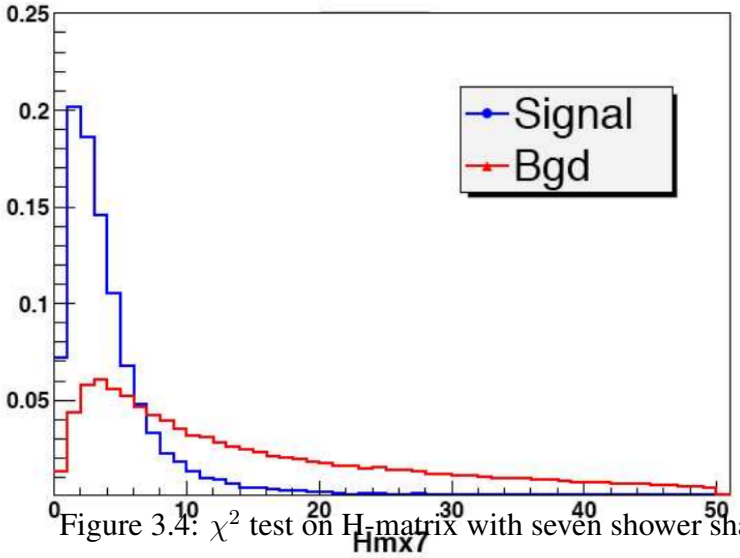

Figure 3.4: χ^2 test on H-matrix with seven shower shape variables.

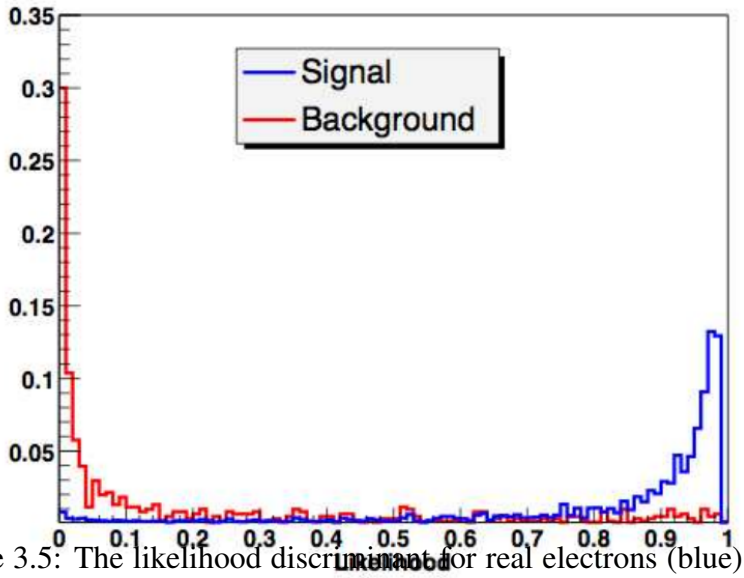

Figure 3.5: The likelihood discriminant for real electrons (blue) and that of the fake electrons (red) showing the separation. The signal peaks at value 1, while the background peaks at almost 0.

These chosen variables show a good differentiating power between real and fake electrons. As we said earlier, electrons with higher p_T tend to have a smaller DCA. Characteristics of signal-candidates are also lower values of χ^2_{hmx7} and f_{EM}. χ^2 test on H-matrix with seven shower variables is shown in Fig. 3.4. Variables six and $seven$ are track isolation variables. Good electrons (signal-candidates) have tracks that are both single and clean simultaneously. Photon conversion has two tracks that are close to each other, while jets that fake electrons usually have two or more tracks linked to the EM cluster.

Distribution of each variable is then normalized to calculate its probability distribution. Each distribution is then is either a signal, $P_{sig}(x)$, or a background, $P_{bkg}(x)$. Assuming no correlation between variables, the overall probability is defined by Eq. 3.9, that is the overall probability is simply the outcome of the product of each individual probability. The likelihood $\mathcal{L}_n$ is constructed such that $\mathcal{L}_n \sim 1$ for signal-likes and $\mathcal{L}_n \sim 0$ for background-

likes. As a result, the likelihood allows the variables to be weighted by their effectiveness in distinguishing real electrons from fake electrons. The likelihood discriminant for real and fake electrons are shown in Fig. 3.5.

A cut on the electron-likelihood, for example EM-likelihood ¿ 0.85, can then be applied to discriminate between signal and background.

3.5 Jet Reconstruction

A jet is a collimated narrow shower of energetic particles produced from the hadronization of partons (quarks or gluons) or particles decays in hadron collisions originating from the primary vertex. Jets leave tracks in the central tracking system and they deposit their energy through hadronic shower in both electromagnetic and hadronic calorimeters. At the DØ detector, jets are reconstructed using two algorithms. The DØ RunII Cone Algorithm and k_T-algorithm [55–57]. The DØ RunII Cone Algorithm is used in this analysis with a cone size $\Delta R < 0.5$. The algorithm is performed in three steps:

1. **Preclustering**:

   It starts with clustering the cells of the calorimeter into towers (calorimeter towers). These towers are in turn grouped into preclusters. Each calorimeter cell is considered a massless object with a momentum vector

   $$p^{\mu}_{cell} = (E_{cell}, \vec{p}_{cell}) \tag{3.11}$$

   where p^{μ} is the massless 4-momentum vector. The direction of the vector is that from the PV to the center of the cell. Noisy cells are discarded using another algorithm, NADA, [58,59], and the $T42$-algorithm [60–62]. Calorimeter cells in the $\Delta\eta \times \Delta\phi = 0.1 \times 0.1$ range are then built into calorimeter towers such that their corresponding 4-momentum vector is calculated from:

   $$p^{\mu}_{tower} = (E_{tower}, \vec{p}_{tower}) = \sum_{i\text{th}}^{No.ofcells} (E_i, \vec{p}_i) \tag{3.12}$$

Towers are then ordered in a descending p_T order, and those with a transverse momentum, pT, such that $p_T^{Tower} > 0.5$ GeV are considered for preclusters. In either CH or EC layers, the most energetic cell in a tower has to fulfill the condition $p_T^{Tower} - p_T^{thehighestpTcell} > 0.5$ GeV. Towers with transverse energy, p_T, such that $p_T < 0.5$ GeV, are ignored. Preclusterd towers with the highest p_T is then used as seeds for *preclustering* within a cone of radius $R = \sqrt{\Delta\eta^2 + \Delta\phi^2 = 0.5}$. Preclusters with $p_T < 1$ GeV are discarded. The procedure is repeated again with any seed towers from inside the precluster and is used to find the following precluster.

2. **Protojets**:

   Preclusters with $p_T > 1$ GeV and which have two or more energetic towers are the ones used in a list of seeds for making protojets. The seed precluster with the highest p_T is selected and then a cone of radius $\bar{R} = \sqrt{\Delta y^2 + \Delta\phi^2} = 0.5$ is constructed around the precluster; where y is the rapidity. From within the cone, towers are summed up to form a trial protojet ($p^{precluster} = \sum p^{tower}$, towers $\in R < 0.3$). Another updated cone is used and a new trial protojet is then found. A trial protojet with a $p_T(protojet) < 4$ GeV is discarded. Any seed preclusters within $\overline{R} = 0.25$ from the stable protojet is then discarded from the list of seeds and the whole procedure is then repeated with the new list of seed preclusters to find the next protojet.

3. **Merging and Splitting**:

   This is the last stage in the process of jet reconstruction. It consists of splitting or merging overlapping protojets. Any protojet that does not overlap another protojet is considered a jet. Two protojets that overlap each other are merged if they share at least half of their p_T; otherwise they are split. When merging two protojets we sum them to make a new trial protojet that is then iterated as above until a newer staple protojet is constructed. Splitting, on the other hand, is done through assigning each

of the shared towers to the closer of the two protojets. Both Merging and Splitting continue until no overlapping occurs; thus all jets are found.

3.5.1 Jet Reconstruction Requirements

Jets constructed in the above manner are required to pass further selection cuts before they are used in this analysis. The following basic set of requirements are applied to the reconstructed jets to remove any fake jets that might exist in our data set.

- To reject noise, the fraction of energy coming from cells in the EM layers of the calorimeter must be such that:

$$5\% < f_{EM} < 95\% \tag{3.13}$$

- To reduce noise due to Coarse Hadronic Calorimeter, CH, the fraction of energy deposited in these calorimeter EM cells must be such that:

$$f < 44\% \quad \text{for jets in the CC region} f < 46\% \quad \text{for jets in the EC region} \tag{3.14}$$

- If the energy of the most energetic cell in the jet is more than 10-times the energy of the next most energetic cell, the jet is *rejected*.

- The jet cannot have more then 90% of its energy in a single tower.

- Each jet is required to be a confirmed L1 trigger. The L1 trigger uses only a subset of the full data from the calorimeter that contains the 100 highest $E_T$trigger towers; where these trigger towers are $\delta\eta \times \Delta\phi = 0.2 \times 0.2$ not counting the CH layer. The L1 confirmation is defined in Eq. 3.15. Jets are required to have $L1_{conf} > 0.5$ in both CC and EC regions; and $L1_{conf} > 0.2$ in the intercryostate (ICR) region.

$$L1_{conf} = \frac{\sum_{Trigger} E_T^i}{E_T^{jet} \times (1 - CHF)} \tag{3.15}$$

Where $\sum_{Trigger} E_T^i$ is the total E_T of trigger towers inside a cone of $R = 0.5$ and E_T^{jet} is the transverse energy of the reconstructed jets. f_{CH} is the fraction of E_T^{jet} in

the coarse hadronic cells.

Jets are also required to have a transverse energy $ET > 15$ GeV in order for one to apply jet energy scale correction.

3.6 Missing Energy, E_T

The two colliding proton and antiproton beams are in almost opposite directions along the beams axis which is in the $\pm z$-direction. Their total momentum components in a plane perpendicular to the z-axis ($x-y$-plane, also called *transverse* plane) should be $zero$, and the component along the z-axis is almost negligible. For a hard scatter, momentum conservation requires the vector sum of all momenta in the final states be zero. In this analysis, the final state contains 4 particles one of them is a neutrino, ν, which goes through the detector undetected. This fact implies that the neutrino has a negligible momentum in the transverse plane, and as a result we can apply transverse momentum conservation. If the sum of the *transverse* momenta of the detected particles is significantly different from zero, this difference is then attributed to one or more particles (neutrinos) that escaped the detector without being detected. With the vector sum of transverse momenta exactly opposite to the total detected transverse momentum we define the missing transverse energy, E_T [63, 64]. Each cell in the calorimeter is assigned a 4-vector, and its energy is equal to the measured energy in the cell. The direction points from the interaction vertex to the center of the cell and is assigned a $zero$-mass. For all the cells of the calorimeter, their 4-vectors transverse components are summed up and a vector opposite in direction to this vector is constructed and called the calorimeter missing E_T. The missing transverse energy is expressed as:

$$\not\!\!\vec{E}_T^{cal} = -\sum_i \vec{E}_T^{\,i} \tag{3.16}$$

The index *i* runs over all calorimeter and ICD cells. Other related variables are:

- Scalar E_T:

  This is the scalar sum of the transverse energy of all calorimeter cells

$$S_{E_T} = \sum_i |\vec{E_T^i}| \tag{3.17}$$

- $\not\!\!E_T$projections in the x-and-y plane, $\not\!\!E_{Tx}$ and $\not\!\!E_{Ty}$

$$\not\!\!E_{Tx} = \sum_i \left(E^i_{EM} + E^i_{HAD}\right) \sin\theta_i \cos\phi_i \tag{3.18}$$

$$\not\!\!E_{Ty} = \sum_i \left(E^i_{EM} + E^i_{HAD}\right) \sin\theta_i \sin\phi_i \tag{3.19}$$

$$\not\!\!E_T = \sqrt{|\vec{\not\!\!E}_{Tx}|^2 + |\vec{\not\!\!E}_{Ty}|^2} \tag{3.20}$$

Missing $E_T$is the sum of all the energies of the calorimeter cells. Any calorimeter object that is mismeasured will lead to a change in the $E_T$by the exact amount of mismeasurement. Corrections are then made to calorimeter objects such as electrons, jets and high energy muons. After correction, the missing energy $E_T$is recalculated and the process is repeated for each mismeasured calorimeter object. Correction applied to $E_T$is calculated by

$$\vec{\not\!\!E}_{T\,corr}^{\,cal} = \vec{\not\!\!E}_{T\,uncorr}^{\,cal} + \vec{\not\!\!E}_T^{\,uncorr} + \vec{\not\!\!E}_T^{\,corr} \tag{3.21}$$

Where the uncorrected missing $E_T$is calculated from

$$\vec{\not\!\!E}_T^{\,uncorr} = -\sum_i \vec{p_i^{\,cell}} \tag{3.22}$$

and $\vec{p_i^{\,cell}}$ is the i-th cell momentum in both EM and the fine hadronic layers of the calorimeter.

3.7 Identification of b-jets; b-tagging

The primary goal of this analysis is the search for WH production with two b jets in the final state, so we focus on the identification of b-jets in the $W + 2$ and $W + 3$ jets samples.

- Introduction

  Quarks and gluons cannot be observed in a single state. Once produced they go through a process called hadronization, a process in which a quark will combine with another quark to form a hadron. In a particle detector, the experimental signature for quarks and gluons are jets. The identification of the original parton[1] is of great importance to this analysis. The process of identifying a jet as originating from a b quark is called b-tagging. A b-quark resulting from $H \rightarrow b\bar{b}$, for example, undergoes hadronization to form a b-hadron. b-hadrons have longer lifetime, of the order of $pico$-seconds, compared to other unstable hadrons. This longer lifetime gives them the chance to travel a few millimeter inside the detector before they decay into secondary particles. In addition to the PV, events with b-hadrons have a displaced secondary vertex where the b-hadron undergoes a decay. Both primary and secondary vertices and the distance traveled by the b- hadron before its decay[2] are shown in Fig. 3.6. Charged particles originating from the decay are almost of high momentum and also have large impact parameter (IP). The impact parameter is defined as the closest distance, $d_{\circ}$, to the primary vertex along its trajectory.

- Taggability

  For a jet to be identified, the jet must satisfy a certain set of minimum conditions. A jet that satisfies these conditions is called a *taggable* jet. The taggability of a jet, $\in_{taggability}$, is of value one for a jet that satisfies taggability conditions [65], and is of value zero otherwise. These conditions are:

  - A *track jet* must have tracks found within $\Delta R < 0.5$ of a seed track [66].
  - All tracks used must have at least 2 hits in the SMT.
  - The seed track must have a transverse momentum, p_T, such that $p_T > 1.0$ GeV.

[1] Quarks or gluons.

[2] Also called: *the decay length.*

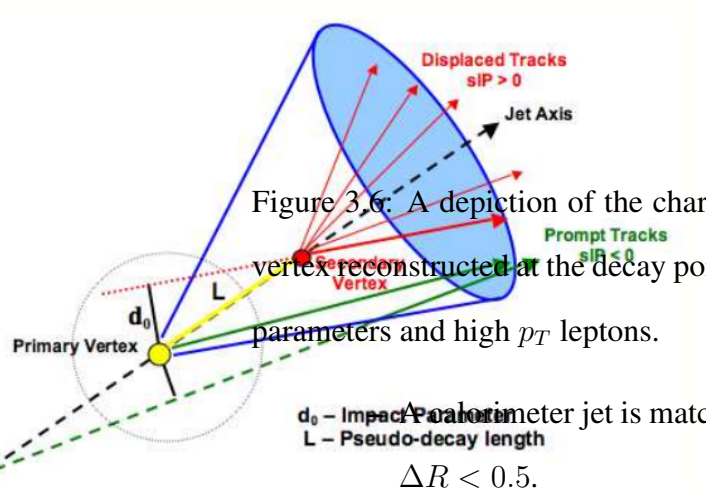

Figure 3.6: A depiction of the characteristics of a b-jet: (1) with the displaced secondary vertex reconstructed at the decay point of a b-hadron; (2) displaced tracks with large impact parameters and high p_T leptons.

A calorimeter jet is matched to a track jet within a cone of radius, ΔR such that $\Delta R < 0.5$.

3.7.1 b-tagging Methods

$b-$tagging algorithms are reconstructed such that they use the characteristics associated with the heavy $b-$hadrons decays. These algorithms are discussed as follows

- Secondary Vertex Tagging

  The SVT algorithm identifies $b-$jets through reconstructing the displaced vertex at which the $b-$hadron decays. There are three main procedures this algorithm follows

  * Removal of the V_0 vertices: These are the ones produced by other long

lived particles other than $b-$hadrons, particles such as K_s^0, Λ or electrons originating from a photon conversion. These vertices contain *two track vertices* that can lead to a jet being misidentified as a $b-$jet. The V_0 removal procedure explicitly removes these jets. The removal procedure takes place by comparing the masses of the two tracks vertices to the known masses of the other heavy long-lived particles we need to remove.

* Track-jet finding: At least two tracks with their IP significance[3], $IP/\sigma_{IP} > 3$, is greater than three, and at least there should be 7 CFT hits to fit the secondary vertex. The decay length of the secondary vertex is required to satisfy the condition $\|\vec{L}_{xy}\|/\sigma_{\vec{L}_{xy}}\|\| > 5$, that is, it's significance should be more than five.

* Jets within the cone matched to the secondary vertex:

  The jet within $\Delta R < 5$ is matched to the corresponding secondary vertex and then it is identified as a $b-$jet. The average $b-$tagging efficiency is 38.9% and the fake rate is estimated to be $\sim 0.47\%$.

– Counting Singed Impact Parameter (CSIP) Tagging:

  The impact parameter is a signed quantity. This sing is assigned with respect to a given jet axis. An impact parameter is positive if the track crosses the jet axis in front of the primary vertex, that is toward the jet. An impact parameter is considered negative if the track crosses the jet from behind the primary vertex, that is away from the jet. This is shown in Fig. 3.7. The CSIP tagger [67] combines the number of tracks and their impact parameter significances to tag the jets. Jets containing two or more tracks with an impact parameter significance $IP/\sigma_{IP} > 3$ or three tracks or more with $IP/\sigma_{IP} > 2$ are considered to be $b-$jets. The average $b-$tagging efficiency on data is $(23 \pm 1)\%$.

– Jet Lifetime Probability (JLIP) Tagging:

[3]Significance is defined as the measurement of a quantity divided by its error.

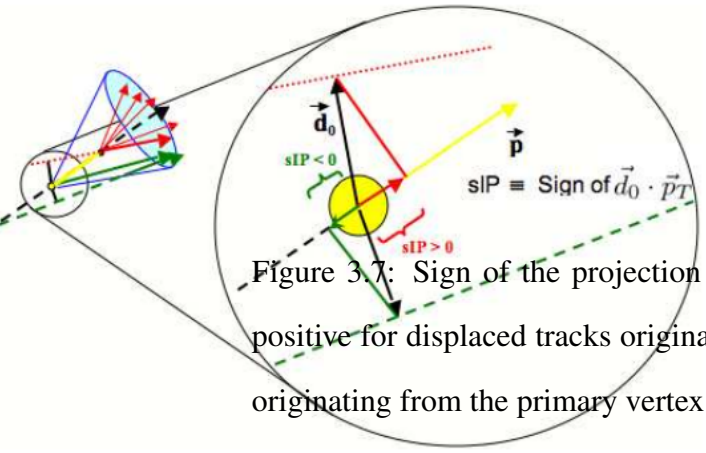

Figure 3.7: Sign of the projection of impact parameter d_0 on the jet axis (i.e., $\vec{d}_0.\vec{p}_T$ is positive for displaced tracks originating from the secondary vertex and negative for tracks originating from the primary vertex.

The Jet lifetime Probability [68] Tagger uses the impact parameters of tracks in a jet to build a probability P_{jet}, that calculates the probability that all tracks in the jet come from the primary vertex. This probability, P_{jet}, is calculated from

$$P_{jet} = \Pi. \sum_{i=0}^{N_{trk}-1} \frac{(-\ln \Pi)^i}{i!} \tag{3.23}$$

where Π is the product of all probabilities, P_{trk} for all tracks of the jet, which represent the probability of a track originating from a primary vertex, as

$$P_{trk} = \frac{\int_{s_0}^{\infty} R(s)ds}{\int_0^{\infty} R(s)ds} \,. \tag{3.24}$$

$R(s)$ in Eq. 3.24 is called the resolution function and it is determined by fitting the negative impact parameter using a sum of four Gaussian functions. For light jets, the probabilities P_{jet} is of uniform values that lie between 0 and 1, while those for b/c jets have their maximum probabilities at very small values, close to 0. At the DØ experiment, a set of 6 working points corresponding to cutoff values ranging from 0.001 to 0.004 is used to select $b-$jets. The $b-$tagging efficiency with a cut off value of 0.02 can reach up to $\sim 60\%$ with a corresponding

fake rate of only 2%.

– Soft Lepton Tagging (SLT):

This tagger identifies $b-$jets via the existence of a muon inside the jets. $b-$hadrons decay almost into $c-$hadrons that further decay semi-leptonically into a muon and another particle, ($b \to \mu X$). Also, $b-$hadrons decay semi-leptonically such that $b \to c \to \mu X$ with a branching ratio of 10.95%. As a result almost 20% of the $b-$ hadrons in this analysis decay into a muon, that is, almost 20 % of $b-$jets are associated with muon. Light hadrons, on the other side cannot decay into a muon (i.e. semi-leptonically) or have a lifetime that is able to make them pass through the detector before decaying. Thus, a jet originating from a $b-$quark can be identified using the existence of a muon within its associated jet. In the SLT, a jet is considered a tagged jet if a muon can be associated with a jet in a cone of radius $\Delta R < 0.5$.

– Neural Network (NN) Tagging:

The DØ Neural Network (NN) $b-$tagger [69] combines all the powerful variables from all the algorithms discussed above. That is, it combines the SVT, CSIP, and the JLIP algorithms in addition to more other variables to be used as discriminant variables to discriminate $b-$jets from other lighter jets. These variables are shown in table 3.1. Five of these variables are derived from the SVT, while the rest of them are derived from both CSIP and JLIP. The set of optimized NN variables are shown in table 3.2. The neural network seven points of the set of nodes and the one output node corresponds to the seven input variables and the one output of the neural network (NN). The number of hidden nodes are set to be 24. The training process of the neural network is performed on $b\bar{b}$ and other $q\bar{q}$ samples. The output of the NN discrimination process makes a continuous distribution between 0 and 1. Light jets appear to have small values around 0 while $b-$jets tends to accumulate around 1 as shown in Fig. 3.8.

Parameter	Value
NN Structure	$7:24:1:1$
Jet input selection cuts (failure results in NN output of 0)	$SVT_{SL}\ DLS > 2.5$ or $JLIP\ Prob < 0.02$ or $CSIP\ Comb > 8$
Number of training epochs	400
Number of b jets used in training (after jet selection cuts)	$389,109\ (312,549)$
Number of fake jets used in training (after jet selection cuts)	$1,672,879\ (331,751)$

Table 3.1: NN parameters. [1]

For the choice of the operation points, a set of 12 points are evaluated to classify the performance of the NN tagger. Each operation point was chosen to correspond to a cutoff value used to identify a $b-$jet. This is shown in table 3.3. The NN tagger achieves a very good performance gain over the JLIP tagger. The increase in efficiency is up to 50% for a fixed fake rate. The fake rates are also reduced using NN over JLIP by roughly $20-30\%$ for a fixed signal efficiency. This fact is illustrated in Fig. 3.9

3.7.2 Tag Rate Function

The probabilities for the NN algorithm to identify, or tag, a $b-$jet, a $c-$jet or a light jet ($l-$jet) are measured using data and are generally called *Tag Rate Functions, (TRFs),* which comprise of TRF_b, TRF_c and TRF_l respectively. The probability that a jet is identified in

Rank	Variable	Description
1	$SVT_{SL}\ DLS$	Decay length significance of the secondary vertex
2	$CSIP\ Comb$	Weighted combination of the tracks' IP significance
3	$JLIP\ Prob$	Probability that the jet originates from the primary vertex
4	$SVT_{SL}\ \chi^2_{dof}$	Chi square per degree of freedom of the secondary vertex
5	$SVT_L\ N_{Tracks}$	Number of tracks used to reconstruct the secondary vertex
6	$SVT_{SL}\ Mass$	Mass of the secondary vertex
7	$SVT_{SL}\ Num$	Number of secondary vertex found in the jet

Table 3.2: The Neural Network input variables ranked in order of b-jet discrimination power. [1]

an event is calculated from

$$P_{jet}(\vec{x}) = \epsilon_{taggability} \times TRF(\vec{x}) \tag{3.25}$$

where $\epsilon_{taggability} \in \{0, 1\}$ is the taggability of the jet and $TRF(\vec{x})$ is the tag rate function. The above equation can be used to calculate the total probability of a subset of jets in an event are tagged. The equation of the probability of one/two jets out of $N-$jets being tagged is given by

$$\begin{aligned} P_1tag(\vec{x}) &= \sum_{i=1}^{N} P_{tag}(\vec{x}_i)\Pi^N_{i\neq j}(1 - P_{tag}(\vec{x}_j) \\ P_2tag(\vec{x}) &= \sum_{i=1}^{N} P_{tag}(\vec{x}_i) \sum_{j\neq i}^{N} \Pi^N_{i\neq j}(1 - P_{tag}(\vec{x}_j)P_{tag}(\vec{x}_j)\Pi^N_{k\neq i\neq j}(1 - P_{tag}(\vec{x}_k) \end{aligned} \tag{3.26}$$

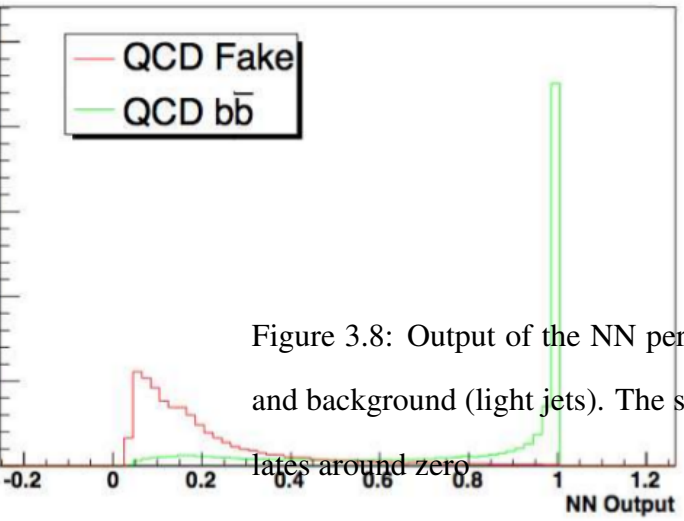

Figure 3.8: Output of the NN performance showing a separation between signal ($b-$jets) and background (light jets). The signal peaks closer to one while the background accumulates around zero.

where $P_1tag(\vec{x})$ is the probability of tagging one jet and $P_2tag(\vec{x})$ is the probability of tagging two jets.

Tag rate functions are determined when measuring the performance of the NN tagger. Use of a system of 8 equations, System, is used, which include the efficiency of the tagging into the equation. Due to the overestimation of the tracking quality in the simulated events compared to samples of data, the efficiencies of the $b-$tagging are also over estimated by a factor that can go up to $\sim 20\%$. To estimate the tagging differences between data and simulated samples (Monte Carlo Samples) $\epsilon^{MC}_{(b\to\mu)}$ is also measured, where the scale factors are measured using $b \to \mu$ samples. The ratio of these two efficiencies is a scale factor (SF) which provides a measure of the changes in tagging rate. It is given by

$$SF_{b\to\mu} = \frac{\epsilon^{data}_{b\to\mu}}{\epsilon^{MC}_{b\to\mu}} \tag{3.27}$$

and

$$TRF^b(p_T, \eta) = \epsilon^{MC}_b \times SF_{b\to\mu} \tag{3.28}$$

Operating Point	L6	L5	L4	L3	L2	Loose
NN Output	> 0.1	> 0.15	> 0.2	> 0.25	> 0.325	> 0.45
$b-$**jet efficiency**	77%	74.9%	72.2%	69.6%	65.9%	60.8%
Fake Rate	11.1%	8.16%	6.06%	4.66%	3.28%	2.02%
Systematic Error	1.67%	1.58%	1.47%	1.31%	1.29%	1.37%

Operating Point	oldLoose	Medium	Tight	VeryTight	UltraTight	MegaTight
NN Output	> 0.5	> 0.65	> 0.775	> 0.85	> 0.9	> 0.925
$b-$**jet efficiency**	59.3%	53.7%	47.6%	43.3%	39.5%	37.1%
Fake Rate	1.68%	0.958%	0.546%	0.343%	0.226%	0.169%
Systematic Error	1.45%	1.34%	1.52%	1.51%	1.33%	1.43%

Table 3.3: The different NN-tagger operating points, with their associated NN output cut value, $b-$jet efficiency, light jet mis-identification, and systematic error for jets in the central region of the calorimeter ($|\eta| < 1.2$). [1]

Similarly, one may define an inclusive $c-$jet TRF by including and another SF for the relative $c-$jet to $b-$jet efficiency in simulated MC samples

$$TRF^c(p_T, \eta) = TRF^b(p_T, \eta) \times \frac{\epsilon^{MC}_{c\to INC}}{\epsilon^{MC}_{b\to INC}} \tag{3.29}$$

Where $TRF^b(p_T, \eta)$ means that the TRFs are parametrized as a function of jet p_T and the detector pseudorapidity for each operation point as shown in Fig 3.10 and Fig 3.11 In the analysis, a jet is identified as a *good* jet and is taggable only it is matched to a track jet within $\Delta R = 0.5$, where it is reconstructed with a seed track such that its transverse momentum, p_T, is larger than 1 GeV and must have 2 or more tracks where each has a transverse momentum of p_T larger than 0.5 GeV and satisfying $|dca_{xy}| < 0.2$ cm and $|dca_z| < 0.4$ cm. The taggability is defined as

$$Taggability = \frac{Taggable \;\&\&\; Good}{Good}\,. \tag{3.30}$$

In RunIIb data taking, the luminosity is higher than ever at the Tevatron and more jets that are non-taggable that comes from the minimum bias events make the taggability more and

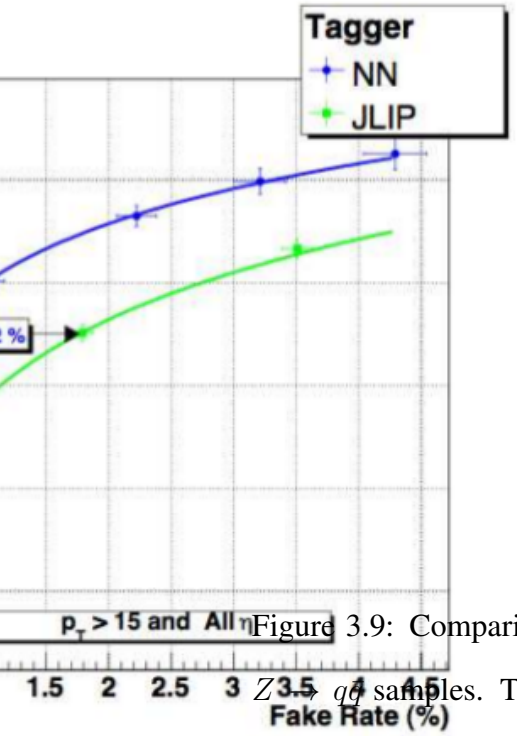

Figure 3.9: Comparison of the performance of NN and JLIP taggers using $Z \rightarrow b\bar{b}$ and $Z \rightarrow q\bar{q}$ samples. The errors represent the full statistical and systematic uncertainties in the samples. The NN tagger has smaller uncertainty on the $b-$tagging efficiency, but larger uncertainty on the fake rate lower operating points.

more depending on the instantaneous luminosity. As a result, taggability was defined for RunIIb as

$$Taggability = \frac{Taggable \;\&\&\; Good \;\&\&\; N_{trk} \geq 2}{Good \;\&\&\; N_{trk} \geq 2} \tag{3.31}$$

where

- N_{trk} is number of tracks on the jets
- $p_T > 0.5$ GeV
- $|dca_{xy}| < 0.5$cm

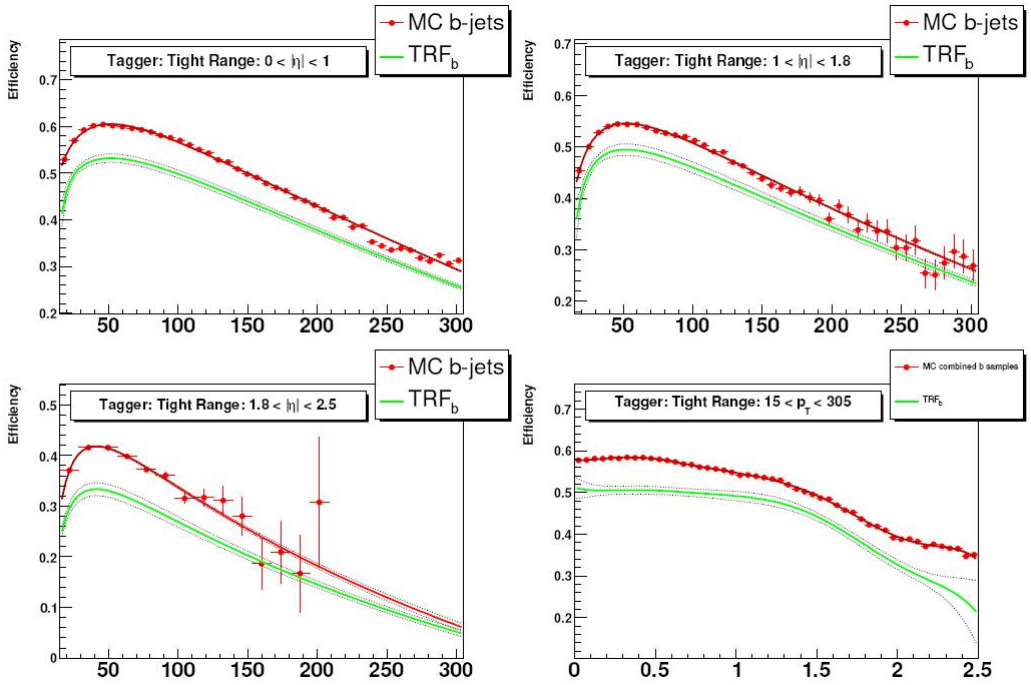

Figure 3.10: b-tagging efficiency as a function of p_T or η for the Tight operation point of the NN b-jet tagger. It is determined on Run IIb datasets (red for MC and green for data) in the CC, ICR and EC region respectively. The TRFb on data is obtained by multiplying the MC b-jet tagging efficiency by the scale factor. The dotted black lines are the fit errors dominated by the scale factor fit errors. [1]

- $dca_z < 1.0$cm
- $|\Delta z| < 2.0$cm

In the analysis, the NN-tagger is used with the jets of MC events. Therefore, the TSF and the efficiency of the tagging scale factor are used with the simulated MC samples to correct the difference.

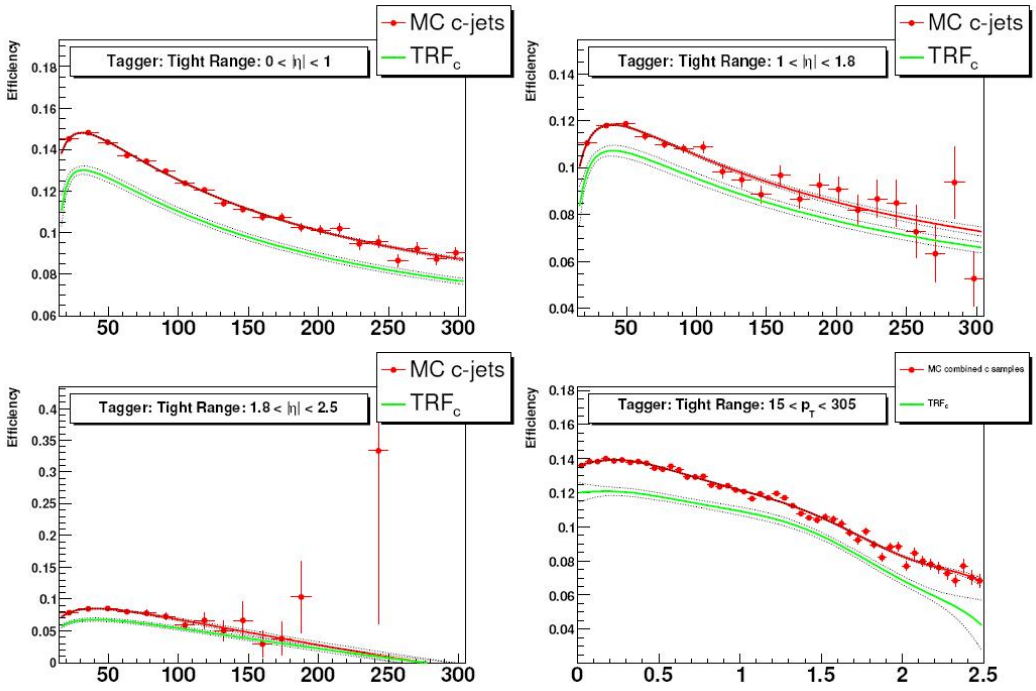

Figure 3.11: c jet tagging efficiency as a function of p_T or η for the Tight operation point of the NN tagger. It is determined on Run IIb datasets (red for MC and green for data) in the CC, ICR and EC region respectively. The TRFc on data is obtained by multiplying the b-jet tagging efficiency by the c/b scale factor. The dotted black lines are the fit errors dominated by the scale factor fit errors. [1]

CHAPTER 4

Events Selection and Processes Modeling in the WH Analysis

4.1 Overview

The WH production is one of the most sensitive channels for the search of a low-mass Higgs boson by looking for its signature in the $WH \rightarrow l\nu q\bar{q}$ decay mode. The W decay mode, $W \rightarrow l\nu$, is three times smaller than the W decay mode, $W \rightarrow q\bar{q}$, which is the dominant W decay mode. Background from QCD processes are significantly lowered; which leaves the leptonic decay mode of the W boson along with the decay of the Higgs boson, H, the most cleaner signature of the Higgs boson in the DØ detector. The considerably large branching ratio from the $b\bar{b}$ decay mode, in the mass range under consideration in this analysis, is also of an important role.

The even signature (also, event topology) which corresponds to the the WH channel consists of a one isolated high transverse momentum lepton (that is either an electron, e, or a muon, μ), a large missing transverse energy that corresponds to the escaping neutrino (both constitute the signature of the existence of the leptonic W boson decay) and two or three jets (to be tagged later) that correspond to the resonant decay of the Higgs boson. The invariant mass of the two jets is reconstructed in order to reconstruct the candidate Higgs boson mass. Channels which contain three jets allow for the selection of events that may contain an additional gluon radiation, are not selected in the dominant channel with exactly two jets in the final state.

In this chapter, we will describe the analysis strategy that has been used in this work. We shall give the details of the criteria used in the selection process of selecting events that correspond to the associated production of the Higgs boson, H with a W boson in their

$l\nu b\bar{b}$ final state. For this analysis to have high sensitivity to the Higgs boson, it was important to have the maximum acceptance for the WH signal and have as much as possible a good background rejection. Generators used to generate both the signal and background processes have their own deficiencies and therefore a correction is to be applied to their simulation output. Instrumental backgrounds cannot be simulated with the current set of available generators and therefore they are modeled through some data-driven techniques. Finally, in order to identify the jets as jets originating from $b-$quarks, the NN $b-$tagger is used in this work to select those jets.

For this analysis to run smoothly and efficiently, an efficient piece of software, aka *"framework"* has been developed and maintained for analyzing data used in this work. Most of the work of the analysis presented here, in this document, depend heavily on this framework (software) which was used at many steps of this analysis. It was used in:

- Data to Simulation comparisons to verify that data is both correctly and accurately described by the simulation.
- Correction Derivation for residual simulation modeling
- Multivariate Analysis Techniques (MVA) trainings
- Production of final histograms for results extraction

All histograms produced by this framework and used here, in this work, use the same color legend. This color legend is shown in Fig. 4.1.

4.2 Analysis Work Flow

Monte Carlo simulation generators are used in simulating background processes and in detector simulation. Then, each data and MC sample is grouped in a *requestID* These samples are then processed with the Common Analysis Format Environment, CAFe, which is used to run a set of selection requests for a certain analysis. Results are then grouped in

Figure 4.1: *Legend for the data-vs-MC plots used in this analysis. Backgrounds from Zjj, Zcc and Zbb are included in Wjj, Wcc and Wbb respectively. QCD represents backgrounds from multijets backgrounds.*

medium-sized files in what is called ROOT format.

4.2.1 The ROOT System

ROOT is a multipurpose software used in the field of high energy physics analysis. the ROOT system provides a set of Object Oriented frameworks with all the functionality needed to handle and analyze large amounts of data in a very efficient way. Having the data defined as a set of objects, specialized storage methods are used to get direct access to the separate attributes of the selected objects, without having to handle the bulk of the data. Included in the ROOT system are histograms methods in an arbitrary number of dimensions, curve fitting, function evaluation, minimization, graphics and visualization classes to allow the easy setup of an analysis system that can query and process the data interactively or in batch mode.

4.3 Data and Monte Carlo Samples used in the WH Analysis

Data and Monte Carlo obtained by the DØ detector are skimmed and produced in a format common to the DØ collaboration. In the WH analysis, both EMinclusive and MUinclusive skims are used for electron and muon data/MC respectively. At least one electron (muon) is required. A logical OR selection criterion is used for such selection processes.
Data used in this analysis were taken at two different periods:

- RunIIa dataset

  It was taken between April 2002 until 2006 shutdown. The complete data are combined into one predefined dataset for the electron and one dataset for the muon inclusive samples:

  a. CSG_CAF_EMinclusive_PASS3_p18.14.00

  b. CSG_CAF_MUinclusive_PASS3_p18.13.01

- RunIIb dataset

  It was taken between June 2006 and June 2009. The RunIIb data used here, in this work, are divided into two main periods:

  – RunIIb-1 dataset

    It was taken from June 2006 to August 2007.

    The datasets for the RunIIb-1 CSG skims are:

    * CSG_CAF_EMinclusive_PASS2_p21.10.00
    * CSG_CAF_MUinclusive_PASS2_p21.10.00

    for the electron and muon channels respectively. The CAF trees are generated with DØ production release p21.10.00.

  – RunIIb-2 dataset

    It was taken from October 2007 to June 2009.

    The datasets for the CSG RunIIb-2 EMinclusive skim are:

* CSG_CAF_EMinclusive_PASS4_p21.10.00_p20.12.00
* CSG_CAF_EMinclusive_PASS4_p21.10.00_p20.12.01
* CSG_CAF_EMinclusive_PASS4_p21.10.00_p20.12.02
* CSG_CAF_EMinclusive_PASS4_p21.10.00_p20.12.04
* CSG_CAF_EMinclusive_PASS4_p21.12.00_p20.12.05_allfix

The datasets for the CSG RunIIb-2 MUinclusive skim are:

* CSG_CAF_MUinclusive_PASS4_p21.10.00_p20.12.00
* CSG_CAF_MUinclusive_PASS4_p21.10.00_p20.12.01
* CSG_CAF_MUinclusive_PASS4_p21.10.00_p20.12.02
* CSG_CAF_MUinclusive_PASS4_p21.10.00_p20.12.04
* CSG_CAF_MUinclusive_PASS4_p21.12.00_p20.12.05_allfix

These data are reconstructed using d0reco versions p20.12.00-p20.12.05, and the CAF trees generated with DØ production releases p21.10.00 and p21.12.00.

Important detector and trigger updates have been made between RunIIa and RunIIb [70, 71].

4.4 Monte Carlo Samples and Monte Carlo Generators

Physical processes of the Standard Model that share the same final state as the WH signal and which might be included in samples used for this analysis, after applying all cuts and selection rules, are considered. These processes are generated using Monte Carlo Generators. Only one exception exists; that is, the multijets background which is determined from data. Processes which have two leptons and two jets in the final state, such as $Zjj \rightarrow l^+l^-jj$ or the purely leptonic decay of $t\bar{t}$, are also considered in case a lepton escapes reconstruction or is outside the acceptance region of the DØ detector. In this analysis, the WH signal is

simulated for different mass values because the Higgs mass is treated as a free parameter in this analysis.

Processes considered in this analysis are:

- W/Z + light jets.

  This is the dominant background before we apply the $b-$tagging. The W and Z bosons can both decay leptonically into either one or two leptons in association with light jets. These light jets originate from light partons such as $u-$, $d-$, or $s-$quarks.

- W/Z + heavy jets.

  These heavy jets originate from $c-$ or $b-$quarks. This is the dominant background after we apply $b-$ tagging.

- $t\bar{t}$

  Top pair production from strong interactions is a major source of background for the WH signal. The $t-$quark has a decay branching ratio of 100% into a $b-$quark and W boson, which can then decay leptonically into a charged lepton and a corresponding neutrino. This may lead to any of the following cases:

  - $t\bar{t} \rightarrow bbWW \rightarrow bbll + \not{E}_T$
  - $t\bar{t} \rightarrow bbWW \rightarrow bbjjl\nu$
  - $t\bar{t} \rightarrow bbWW \rightarrow bbjjjj$

  Only the first of these three configurations are used in this analysis.

- Single top Production.

  This processes include the following configurations:

  - Single-top s-channel $tb \rightarrow e\nu b\bar{b}$
  - Single-top s-channel $tb \rightarrow \mu\nu b\bar{b}$
  - Single-top s-channel $tb \rightarrow \tau\nu b\bar{b}$

  - Single-top t-channel $tqb \to e\nu bqb$
  - Single-top t-channel $tqb \to \mu\nu bqb$
  - Single-top t-channel $tqb \to \tau\nu bqb$

- Diboson Production.

  If a pair of WW, WZ or ZZ bosons are produced, then their final state may include a configuration in which we may have one or two charged leptons and two jets. The final state of the WZ diboson production is denoted as an irreducible background because it is very close in its configuration to the WH one.

- The WH signal. The signal has been simulated for several mass points (different values for the mass of the Higgs boson). Simulated signals corresponding to masses of 100 to 150 GeV were produced in steps of 5 GeV.

- ZH signal.

  This channel, when we have $ZH \to l^+l^-b\bar{b}$ and one of the lepton is misconfiguration will also contribute to the signal.

The above physics processes have not been produced with different Monte Carlo generators. In the following we shall give a brief introduction to these generators.

ALPGEN

`ALPGEN` is a matrix element calculator that uses the tree-level approximation in its work. It is used for $2 \to N$ processes where $N \leq 6$. `ALPGEN` does not handle neither the showering nor handronization. After the generation of the final state partons, another generator, `PYTHIA` is used for such operations.

CompHEP/CalcHEP

`CompHEP` is matrix element generator that uses NLO approximation in its calculations. `CompHEP` computes cross sections and distributions with many particles in the final state.

Calculations are of good value when the number of the final states is 4, although it can be used for up to 6 particles in the final state.

The author have helped in the debugging and the developing of some of the tools used in CompHEP/CalcHEP. Among his contribution he wrote the scripts needed to calculate the cross section of a certain physical process for different values of a certain parameter for two different models in the code, MSSM and NMSSM. The author also helped improve the Mathematica output of the code for further work with the multipurpose mathematical package Mathematica. Particles' Symbolic representations were changed upon a suggestion from the author to the particles and model original author.

PYTHIA

PYTHIA is an event generator that calculates the Feynman diagrams at the tree level. It can also be used for calculations at the Leading Order perturbation theory, (LO). PYTHIA uses the parton shower model to simulate higher multiplicity final states with a parton emission dealt with as a probabilistic process which occurs with a given probability. The hadronization process is modeled with a phenomenological "String Model" [72]. PYTHIA is interfaced with leading order parton distribution function CTEQ6L [73, 74].

Cross sections and Table of Events

Some physical processes' cross-sections used in this work were calculated at the Leading Order (LO) approximation in the the perturbation theory. Some others were calculated at the Next-to-Leading Order (NLO) higher approximation in the perturbation theory. In order to correct for the LO cross sections to match those calculated at the NLO order, a factor, K, was used as multiplicative term to cross-sections given from ALPGEN. Factor K is defined from the following equation:

$$K = \frac{\sigma^{NLO}}{\sigma^{LO}} \tag{4.1}$$

Table 4.4 shows the number of generated events and the their corresponding corrective K factors. The WH and diboson simulated samples have been produced with the Monte-

Sample	K Factor
$W+$ light jets	1.3
$Z+$ light jets	1.3
$W + c\bar{c}$	1.3 $\times$ 1.47
$W + b\bar{b}$	1.3 $\times$ 1.47
$Z + c\bar{c}$	1.3 $\times$ 1.67
$Z + b\bar{b}$	1.3 $\times$ 1.52

Table 4.1: *K factors for $W+$ jets and $Z+$ jets*

Carlo (MC) event generator PYTHIA making use of the leading order parton distribution functions CTEQ6L. The number of generated events (passing the data quality criteria) and their corresponding cross sections are given in Tables 4.4 and 4.4. The $t\bar{t}$ and $W+$ jets, $Z+$ jets events have been generated with the matrix element generator ALPGEN, interfaced to PYTHIA for subsequent parton shower and hadronization. The number of generated events (passing the data quality criteria) and their corresponding cross sections are given in Tables 4.4, 4.4, 4.4 and 4.4. The single-top sample was produced using CompHep as shown in Table 4.4. Cross sections used in the analysis are calculated at Next-to-Leading Order (NLO), (NNLO for $t\bar{t}$). The cross sections on WH/ZH come from Ref. [75]. All ALPGEN $W/Z+$jets , W+$b\bar{b}$ and W+$c\bar{c}$ have undergone a process of heavy-flavor (HF) skimming; that is, additional heavy-flavored partons generated by PYTHIA have been removed so as not to double-count events. Specifically, W+jj ($j = u, d, s$; "light jet") samples are skimmed to remove W+$c\bar{c}$ and W+$b\bar{b}$ events, W+$c\bar{c}$ samples are not skimmed, and W+$b\bar{b}$ samples are skimmed to remove W+$c\bar{c}$ events.

Process		# events in RunIIa	# events in RunIIb	$\sigma(\times\text{BR})$[pb]
	$m_H = 100\,\text{GeV}$	194715	320322	0.0251
	$m_H = 105\,\text{GeV}$	193580	293813	0.0209
	$m_H = 110\,\text{GeV}$	199080	316140	0.0173
	$m_H = 115\,\text{GeV}$	196937	279087	0.0141
	$m_H = 120\,\text{GeV}$	194767	321634	0.0112
$HW \to b\bar{b} + \ell\nu$	$m_H = 125\,\text{GeV}$	193882	278550	0.0087
	$m_H = 130\,\text{GeV}$	193045	553407	0.0065
	$m_H = 135\,\text{GeV}$	193795	460095	0.0047
	$m_H = 140\,\text{GeV}$	197115	495718	0.0032
	$m_H = 145\,\text{GeV}$	195850	446339	0.0021
	$m_H = 150\,\text{GeV}$	194676	320201	0.0013
	$m_H = 100\,\text{GeV}$	394432	319375	0.0046
	$m_H = 105\,\text{GeV}$	403338	279205	0.00384
	$m_H = 110\,\text{GeV}$	396185	320038	0.00320
	$m_H = 115\,\text{GeV}$	400115	279468	0.00263
	$m_H = 120\,\text{GeV}$	404973	322296	0.00212
$HZ \to b\bar{b} + \ell\ell$	$m_H = 125\,\text{GeV}$	388415	279466	0.00166
	$m_H = 130\,\text{GeV}$	385764	321965	0.00125
	$m_H = 135\,\text{GeV}$	387729	279647	0.00091
	$m_H = 140\,\text{GeV}$	376238	320005	0.000637
	$m_H = 145\,\text{GeV}$	387119	279310	0.000410
	$m_H = 150\,\text{GeV}$	387219	316756	0.000249

Table 4.2: *List of simulated signal processes, along with the number of events for both RunIIa and RunIIb datasets and their cross section times branching ratio, for one lepton flavor. The generator used is* `PYTHIA`.

Process	# events of RunIIa	# events of RunIIb	$\sigma\times$BR[pb]
WW inclusive	1905k	709.9k	1.03×11.6
WZ inclusive	1059k	632.3k	1.06×3.25
ZZ inclusive	590.6k	540.3k	1.33

Table 4.3: *List of simulated di-boson processes, along with the number of events and their cross section times branching ratio. The generator used is* `PYTHIA`.

Process		# events in RunIIa	# events in RunIIb	$\sigma(\times$BR$)$[pb]
$t\bar{t} \to b\bar{b} + \ell^+\nu\ell'^-\bar{\nu}_{\ell'}$	$+0$ light parton	1516107	749642	1.43×0.352
	$+1$ light parton	492647	452177	1.43×0.143
	$+2$ light partons	288992	281453	1.43×0.0713
$t\bar{t} \to b\bar{b} + 2j + \ell\nu$	$+0$ light parton	771271	777068	1.43×1.414
	$+1$ light parton	492647	457782	1.43 × 0.57
	$+2$ light partons	288992	321166	1.43×0.283
Single-top s-channel	($tb \to e\nu b\bar{b}$)	290262	247517	0.99×0.112
Single-top s-channel	($tb \to \mu\nu b\bar{b}$)	287994	225286	0.99×0.11
Single-top s-channel	($tb \to \tau\nu b\bar{b}$)	287991	248722	0.99×0.117
Single-top t-channel	($tqb \to e\nu bqb$)	290262	272573	0.99×0.243
Single-top t-channel	($tqb \to \mu\nu bqb$)	287994	273354	0.99×0.239
Single-top t-channel	($tqb \to \tau\nu bqb$)	289106	246552	0.99×0.254

Table 4.4: *List of simulated $t\bar{t}$ and single-top processes, along with the number of events (RunIIa and RunIIb) and the K-factor times cross section times branching ratio, where ℓ = e, τ or μ.*

Process		# events in RunIIa	# events in RunIIb	$\sigma(\times\text{BR})$[pb]
$Wjj \to \ell\nu$	$+0$ light parton	12.5M	46.4M	4.52k
	$+1$ light parton	18.9M	19.9M	1.28k
	$+2$ light partons	13.3M	18.1M	300
	$+3$ light partons	3.5M	3.75M	70.7
	$+4$ light partons	2.5M	2.6M	16.2
	$+5$ light partons	781k	2.0M	4.9
$Wb\bar{b} \to \ell\nu b\bar{b}$	$+0$ light parton	1.4M	1.1M	9.3
	$+1$ light parton	667k	782k	4.1
	$+2$ light partons	249k	524k	1.6
	$+3$ light partons	377k	413k	0.75
$Wc\bar{c} \to \ell\nu c\bar{c}$	$+0$ light parton	1.2M	934k	23.3
	$+1$ light parton		739k	13.9
	$+2$ light partons	342k	554k	5.57
	$+3$ light partons	446k	470k	2.4

Table 4.5: *List of simulated signal processes, along with the number of events for both RunIIa and RunIIb datasets and their cross section times branching ratio, for one lepton flavor. The generator used is* `PYTHIA`.

Process		# events in RunIIa	# events in RunIIb	$\sigma(\times\text{BR})$[pb]
	+ 0 light parton	577k	1.9M	337
$Zjj \to ee$	+ 1 light parton	479k	956k	40.0
15-75 GeV	+ 2 light partons	191k	549k	9.74
	+ 3 light partons	96k	536k	2.67
	+ 0 light parton	3.0M	1.2M	133
$Zjj \to ee$	+ 1 light parton	1.9M	567k	40.1
75-130 GeV	+ 2 light partons	982k	268k	9.8
	+ 3 light partons	988k	127k	3.2
	+ 0 light parton	295k	352k	0.89
$Zjj \to ee$	+ 1 light parton	192k	179k	0.38
130-250 GeV	+ 2 light partons	98k	160k	0.10
	+ 3 light partons	98k	300k	0.03
	+ 0 light parton	577k	1.7M	344
$Zjj \to \mu\mu$	+ 1 light parton	483k	570k	40.1
15-75 GeV	+ 2 light partons	192k	275k	9.66
	+ 3 light partons	96k	268k	2.74
	+ 0 light parton	3.0M	1.5M	134
$Zjj \to \mu\mu$	+ 1 light parton	2.0M	604k	41.4
75-130 GeV	+ 2 light partons	1.1M	401k	9.71
	+ 3 light partons	1.1M	146k	3.15
	+ 0 light parton	484k	351k	0.89
$Zjj \to \mu\mu$	+ 1 light parton	391k	170k	0.36
130-250 GeV	+ 2 light partons	298k	160k	0.10
	+ 3 light partons	299k	142k	0.03
	+ 0 light parton	2.9M	1.5M	131
$Zjj \to \tau\tau$	+ 1 light parton	2.0M	528k	40.3
75-130 GeV	+ 2 light partons	963k	274k	9.81
	+ 3 light partons	978k	174k	3.0
	+ 0 light parton	288k	359k	0.92
$Zjj \to \tau\tau$	+ 1 light parton	194k	171k	0.38
130-250 GeV	+ 2 light partons	97k	162k	0.10
	+ 3 light partons	100k	158k	0.03

Table 4.6: *List of simulated $Z+$ light jets processes, along with the number of events and cross section times branching ratio (the light partons are requested to have $p_T > 8$ GeV and $|\eta| < 5$). Generators used are* `ALPGEN + PYTHIA`.

Process		# events in RunIIa	# events in RunIIb	$\sigma(\times\text{BR})$[pb]
$Zb\bar{b} \to ee + b\bar{b}$	+ 0 light parton	201k	196k	0.40
	+ 1 light parton	101k	93k	0.17
	+ 2 light partons	50k	44k	0.11
$Zc\bar{c} \to ee + c\bar{c}$	+ 0 light parton	202k	182k	0.90
	+ 1 light parton	105k	89k	0.51
	+ 2 light partons	49k	47k	0.29
$Zb\bar{b} \to \mu\mu + b\bar{b}$	+ 0 light parton	194k	206k	0.42
	+ 1 light parton	99k	96k	0.20
	+ 2 light partons	50k	45k	0.10
$Zc\bar{c} \to \mu\mu + c\bar{c}$	+ 0 light parton	194k	194k	0.93
	+ 1 light parton	102k	93k	0.55
	+ 2 light partons	51k	51k	0.28
$Zb\bar{b} \to \tau\tau + b\bar{b}$	+ 0 light parton	202k	193k	0.42
	+ 1 light parton	101k	98.2k	0.20
	+ 2 light partons	50k	44k	0.10
$Zc\bar{c} \to \tau\tau + c\bar{c}$	+ 0 light parton	196k	260k	0.90
	+ 1 light parton	97k	101k	0.49
	+ 2 light partons	48k	51k	0.30

Table 4.7: *List of simulated $Z+$ heavy jets processes, along with the number of events and cross section times branching ratio. Generators used are* `ALPGEN + PYTHIA`.

4.5 Luminosity and Triggers

The luminosity corresponding to the data is calculated using the `lm_access` package [76] provided by the Luminosity-ID group. The RunIIa dataset has an integrated luminosity of 1.04 (1.08) fb^{-1} for the electron (muon) channel; the RunIIb-1 dataset has 1.20 (1.20) fb^{-1}, and the RunIIb-2 dataset has 3.08 (3.08) fb^{-1} after requiring data quality and removing bad luminosity blocks from the luminosity system.

The total integrated luminosity is 5.32 fb^{-1} and 5.36 fb^{-1} for the electron and muon channels, respectively. The uncertainty on the measured luminosity is $6.1\,\%$ [77]. This uncertainty is fully correlated across the MC-estimated background samples when it is taken into account during the limit extraction.

4.5.1 Triggers used for the Electron Channel

In the electron channel analysis we use the logical OR of the Single EM and EM+JET trigger suites. Lists of RunIIa Single EM triggers, RunIIb Single EM triggers and EM+JET triggers can be found in the internal note of this analysis [78]. These trigger terms are fired by events having a good EM object. Therefore the trigger efficiency of these terms can be modeled by the leading EM object.

The efficiencies are measured by the Trigger Study Group (TSG), using a tag-and-probe method on the $Z \rightarrow ee$ sample. A detailed description of the trigger efficiency measurement for EM+JET triggers can be found in [79], [80] and [81]. The event weight applied to simulated samples is calculated through measuring the trigger efficiencies as a function of p_T and η_{det}, and the prescale of each trigger term while normalizing the integrated luminosity of each trigger list by using the `caf_trigger` package [82]. When applying trigger efficiency corrections, trigger terms are matched with the leading electron candidate in the analysis. Table 4.8 lists the unprescaled triggers chosen for each run epoch or trigger list range.

List	Trigger	Luminosity pb^{-1}
v8	EM15_2JT15	23.35
v9	EM15_2JT15	24.73
v10	EM15_2JT15	9.81
v11	EM15_2JT15	63.40
v12	E1_SHT15_2J20	227.35
v13a	E1_SHT15_2J_J25	55.22
v13b	E1_SHT15_2J_J30	298.21
v14	E1_SHT15_2J_J25	333.57
RunIIa		Sub Total 1035.64
v15.0-V15.5	JT_125_L3J125	534.5
v15.5-V15.9	JT_125_L3J125	693.8
v15.9-V16.0	JT_125_L3J125	397.3
v16.0-V16.23	JT_125_L3J125	2656.1
RunIIb		Sub Total 4281.68
		Total 5317.32

Table 4.8: *Reconstructed luminosity for the RunIIa + RunIIb-1 + RunIIb-2 dataset per trigger epoch for normalizable unprescaled triggers in the electron channel.*

4.5.2 Triggers used in the Muon Channel

In order to increase acceptance in the muon channel, for which the trigger efficiency of the OR of single-muon triggers is approximately 70%, we do not require any explicit trigger in the muon analysis. The validity of this procedure has been established on RunIIa data [83] and was also verified on RunIIb. The single muon triggers for each trigger epoch are listed in table. 4.9. Due to the changes in the trigger list between RunIIa and RunIIb [1] as well as the effects from the higher instantaneous luminosity in RunIIb it is necessary to slightly modify the procedure for [2] estimating the trigger efficiency.

The analysis was performed through the full preselection stage using single muon triggers only. Using the difference between the inclusive-trigger data and single muon only data we derive a correction factor for the MC intended to take into account the non-single muon trigger contribution to the data:

$$P_{corr} = \frac{(Data - QCD)_{incl} - (Data - QCD)_{single\mu}}{MC_{incl}} \tag{4.2}$$

where MC_{incl} refers to the Monte Carlo with the trigger probability set to 1. The correction in H_T and in muon η_{det} variables, for $|\eta_{det}| < 1.6$ was parametrized. Here H_T is the scalar sum over all jets' transverse momenta; P_T^{jet}. In RunIIb, single muon triggers for $|\eta_{det}| > 1.6$ were not used. For each MC event, the trigger probability was set to be:

$$P_{trig} = P_{corr}(H_T, \eta_{det}) + P_{single\mu} \tag{4.3}$$

where $P_{single\mu}$ is the probability for a given event to fire a single muon trigger, obtained from the *caf_trigger* package. We further require that $P_{trig} \leq 1$ in each event. If we calculate $P_{trig} > 1$ for an event we force P_{corr} to be $1 - P_{single\mu}$ so that $P_{corr} + P_{single\mu}$ never exceeds unity. We use the inclusive trigger approach for both RunIIa and RunIIb for

[1] In RunIIb the trigger mix includes a higher fraction of multijet, missing ET+jet, and muon+jet triggers relative to RunIIa

[2] We will apply a similar trigger correction to the RunIIa dataset based on the SuperOR trigger correction during review (currently no trigger correction applied).

the remainder of the analysis. Fig. 4.2 shows the trigger correction as a function of H_T for RunIIb dataset.

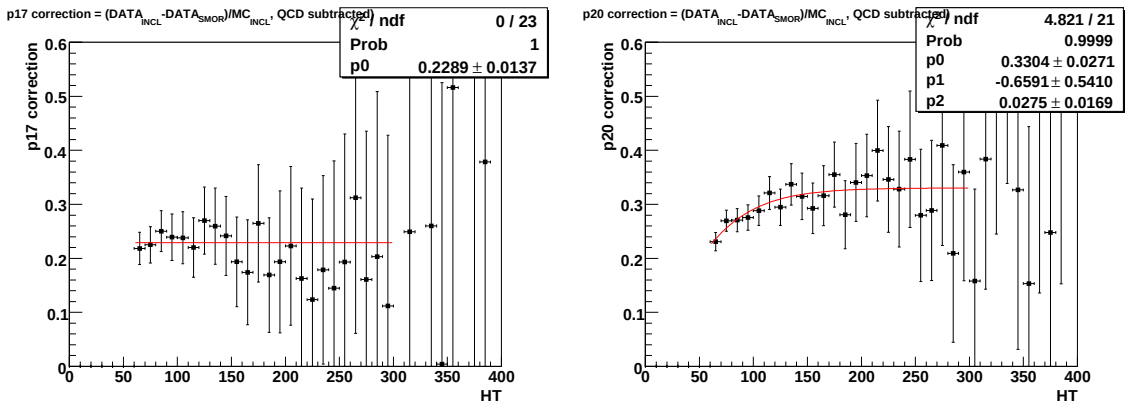

Figure 4.2: *Trigger correction, P_{corr} in Eq. 4.2, for RunIIa (RunIIa - left) and RunIIb (RunIIb - right). In RunIIb we parametrize the RunIIb correction with a* $\tanh$ *function.*

4.6 Event Selection

To simplify datasets combination and to allow for the use of the same multivariate technique, the same preselection criteria were applied to both the RunIIa and RunIIb datasets. The preselection stage consists of the following criteria:

- Exactly one electron (muon) with transverse momentum $p_T > 15$ GeV within a pseudorapidity range of $|\eta| < 1.1$ or $1.5 < |\eta| < 2.5$ for electrons and $|\eta| < 1.6$ for muons. Additional lepton flavor-specific requirements were also applied;
- $\not\!\!E_T > 20$ GeV;
- A primary vertex with at least 3 associated tracks and $|z| < 40$ cm;
- exactly two or three jets with $p_T > 20$ GeV after jet energy scale correction with ICD hot cell removal, (only in runIIa data) and $|\eta| < 2.5$;
- A 2-dimensional '"triangular" cut $M_W^T > 40 - 0.5\,\not\!\!E_T$ is applied to reduce the QCD background;

period	Trigger term
v8-11/v12	MUW_A_L2M3_TRK10, MU_W_L2M5_TRK10, MUW_W_L2M3_TRK10, MU_W_L2M0_TRK3, MU_W_L2M3_TRK10, MUW_W_L2M5_TRK10, MU_W_L2M0_TRK10
v13	MUH1_TK12_TLM12,MUH1_TK12, MUH1_LM15, MUH1_TK10, MUH2_LM3_TK12, MUH2_LM6_TK12,MUH2_LM10_TK12, MUH2_LM15, MUH3_LM3_TK10, MUH3_LM6_TK12, MUH3_LM15, MUH4_LM15, MUH4_TK10, MUH5_LM15, MUH6_TK12_TLM12, MUH6_LM15, MUH6_TK10, MUH7_TK12, MUH7_LM15, MUH7_TK10
v14	MUH1_TK12_TLM12, MUH8_TK12_TLM12, MUH1_ILM15, MUH1_ITLM10, MUH8_ILM15, MUH8_ITLM10, MUH5_LM15, MUH6_TK12_TLM12, MUH7_TK12, MUH7_LM15
v15	MUHI1_ITLM10, MUHI1_TK12_TLM12, MUHI1_ILM15, MUHI2_ITLM10, MUHI2_TK12_TLM12, MUHI2_ILM15, MUHI3_ITLM10, MUHI3_TK12_TLM12, MUHI3_ILM15
v16	MUHI1_ITLM10, MUHI2_ITLM10, MUHI1_ILM10, MUHI2_ILM10, MUHI1_TLM12, MUHI2_TLM12, MUHI1_MM10, MUHI2_MM10, MUHI1_TMM10, MUHI2_TMM10

Table 4.9: *List of single-muon triggers used in the analysis. Triggers belonging to a given trigger range have been OR-conjugated.*

- The total scalar sum of transverse momenta of jets (H_T) must exceed 60 GeV (80 GeV in the 3-jet case). This cut helps in
  - Ensure that events lie above trigger "turn-on";
  - Reduce the contribution of low p_T QCD events;
  - Increases the intrinsic sensitivity of the analysis based on the ration $\frac{S}{\sqrt{S+B}}$;
- For the electron region, the ICR region is excluded (1.1–1.5 in η_{det}).

Detector simulation for MC is not perfectly modeled and corrections are to be considered for simulation of each physical object we have in this analysis. Each correction will be discussed in its proper section.

4.6.1 Electron and Muon Selection

In our study, the chosen final state contains one isolated lepton, l, that can be either an electron or a muon. The lepton originates as a decay product of the W boson (with an accompanying lepton) produced in association with a Higgs boson. The W boson branching ratio of its decay into a pair of jets is approximately 90% yet choosing the leptonic decay of the W boson will help in reducing the multijet backgrounds that are considered a huge hindrance for such an analysis of this high degree of sensitivity. Muon and electron channels are analyzed separately; both are required to have a transverse momentum, $p_T > 15$ GeV.

Electron Selection

Electrons are calorimetric objects and are reconstructed with the electromagnetic (EM) section of the calorimeter. As a result this channel has a larger multijet contribution originating from jets and photons misidentified as electrons.

Since the calorimeter consists of two different zones, namely the central calorimeter (CC) and endcap calorimeter sections (EC), we analyze electron data separately in the detector

rapidity range of $|\eta_{det}| < 1.1$ (CC electron sample) and $1.5 < |\eta_{det}| < 2.5$ (EC electron sample). Events in the electron channel are required to contain one electron with $p_T > 15$ GeV in the CC or EC. Electrons that pass the kinematic selections are further required to satisfy more stringent identification criteria:

- For the CC region we require an electron to pass the MEDIUM selection criteria provided by the EMID group [84]

    1. fractional energy in EM calorimeter over the total, $f_{EM} = \frac{E_{EM}(0.2)}{E_{tot}(0.4)} > 0.97$, where $E_{tot}(0.4)$ and $E_{EM}(0.2)$ are the energies inside cone size 0.4 and 0.2, for the sum of hadronic and EM sections, and for EM section alone, respectively.
    2. isolation fraction, $f_{iso} = \frac{E_{tot}(0.4)-E_{EM}(0.2)}{E_{EM}(0.2)} < 0.07$,
    3. the seven-parameter electron shower shape variable, $\chi^2_{HM7} < 25$[3],
    4. electron likelihood LHood8 > 0.2

- For the EC region, the "loose" EC electron sample is defined in a similar manner, but using the top_tight selection criteria provided by the EMID group.

    1. fractional energy in EM calorimeter over the total, $f_{EM} = \frac{E_{EM}(0.2)}{E_{tot}(0.4)} > 0.9$, where $E_{tot}(0.4)$ and $E_{EM}(0.2)$ are the energies inside cone size 0.4 and 0.2, for the sum of hadronic and EM sections, and for EM section alone, respectively.
    2. isolation fraction, $f_{iso} = \frac{E_{tot}(0.4)-E_{EM}(0.2)}{E_{EM}(0.2)} < 0.15$,
    3. seven-parameter electron shower shape variable, $\chi^2_{HM7} < 50$,
    4. electron likelihood > 0.85.

Electrons passing these requirements are considered "tight" for the purposes of determining the QCD background.

[3]The 7 likelihood variables are: spatial track match χ^2 probability, E_T/p_T, H-matrix7, EMF, distance of closest approach to primary vertex, number of tracks in 0.05 cone, total p_T of tracks in 0.4 cone around candidate track.

The "loose" EC electron sample is defined in a similar manner, but using the top_loose selection criteria provided by the EMID group.

In order to minimize backgrounds that contain two isolated leptons in the final state, such as those coming from Z and $t\bar{t}$ production, the candidate event is required to contain no isolated muons[4] with $p_T^{\mu} > 15$ GeV, and no additional electrons with $p_T^{e} > 15$ GeV that satisfy the loose electron (i.e. without likelihood) criteria.

We exclude the gap situated between the central and the endcap calorimeter in the pseudo-rapidity range of $1.1 < |\eta_{det}| < 1.5$ (the intercryostate region, ICR).

Muon Selection

Muons are reconstructed using information of two independent subdetector systems which are the muon detector and the central tracker. Muon identification is based on a track in the muon system, referred to as local track. Muons are required to have hits in all layers of the muon system inside and outside the toroid. The superior spatial resolution of the central tracker is used to improve the accuracy of the muon's kinematic properties and to confirm that the muon originated from the primary vertex.

The muon candidates are required to fulfill the following criteria:

- *medium* quality as defined by the RunIIa and RunIIb muon ID certification criteria [85, 86].

- Muon type (quality) *nseg* $= +3$, signifying matching muon segments from A and BC layers, as well as a central track match (see below). This requirement rejects about ten percent of high transverse momentum muons, mainly in the bottom region of the detector where no full muon coverage in the A and BC layers is available.

- Veto against cosmic muons: scintillator hits timing requirement in A and BC layers of $|t_A| < 10\,\text{ns}$ and $|t_{BC}| < 10\,\text{ns}$.

[4] MediumNseg3, Medium track, Isolation of DR with 0.5

- a central track match of quality *trackmedium* [86] is required.

Muons coming from the leptonic decay of W bosons tend to be isolated from jets, while muons originating from semi-leptonic decays of heavy flavored hadrons are typically non-isolated due to jet fragmentation of the partial hadronic decay. We define a loose isolation criterion based on the spatial separation between a muon and jets in the geometrical plane spanned by the pseudorapidity η and the azimuthal angle φ. The distance between two objects in this plane is defined by the standard ΔR definition.
The "loose" muon sample, used to estimate the QCD background, is defined as the sample of events passing the event selection cuts and having one muon satisfying the identification, track quality, and loose isolation criterion described above. The "tight" muon sample, used as the signal sample in this analysis, requires the additional isolation criteria (*NPTight*).

The distributions of the energy, p_T, η and φ of the electrons (muons) for the $W+2$ jets events are shown in Fig. 4.3 (Fig. 4.4.) These distributions are described by the sum of the simulation and the QCD background derived from the data.

4.6.2 Primary Vertex Selection

All collisions are to be collected from the central part of the detector, where the SMT covers the whole interaction area. This criterion is essential to ensure that the analyzed collisions are chosen from within the collider acceptance area. The $z-$coordinate of reconstructed primary vertices is required to satisfy the condition $|PV_z| < 40$ cm.

4.6.3 Missing Transverse Energy, $\not\!\!E_T$

To account for the neutrino from the decaying W boson in our search channel, we require a minimum of $20\,\text{GeV}$ of missing transverse energy $\not\!\!E_T$ in the final state. This is because the neutrino does not interact with the detector and thus it escapes the detector undetected leaving behind an imbalance in the of energy in the transverse plane to the $p\bar{p}$ beam. /

Figure 4.3: *Lepton p_T, lepton η, lepton φ, lepton E, $\not\!\!E_T$ and M_T^W for the eletron channel in RunIIb dataset of the $W+$ 2 jets events. The legend of the plots can be found in page. 84.*

Figure 4.4: *Lepton p_T, lepton η, lepton φ, lepton E, $\not\!\!E_T$ and M_T^W for the muon channel in RunIIb dataset of the $W+$ 2 jets events. The legend of the plots can be found in page. 84.*

E_T undergoes the kinematic cut of $\not\!\!E_T > 20$ GeV. $\not\!\!E_T$ is corrected for the presence of any muons. All corrections to electrons, muons and jets are propagated into $\not\!\!E_T$. Fig. 4.3 (Fig. 4.4) shows the $\not\!\!E_T$ for the electron (muon) in RunIIb dataset.

4.6.4 W Boson Transverse Mass, M_W^T

The transverse momentum and transverse mass $m_T = \sqrt{m^2 + p_T^2}$ of the W boson can be reconstructed from the lepton and missing transverse energy kinematics. Fig. 4.3 (Fig. 4.4 shows the W boson transverse mass for the electron (muon) channel. Agreement in shape and amplitude is observed between data and simulation. In the transverse mass distribution the QCD background becomes more important for values above roughly 35 GeV. This is due to the selection cuts of 15 GeV in transverse momentum of the muon candidate and 20 GeV on $\not\!\!E_T$. The events passing the two kinematic cuts, concentrate at low "W" transverse masses [87].

4.6.5 Jets Selection

For this analysis, we searched for the Higgs boson in the mass range of $114.4 \leq m_H < 150 GeV$. In this mass range the Standard Model predict that the Higgs boson decays dominantly in a $b\bar{b}$ pair, that is a 2-jets final state. One can recover events with an additional jet radiated from an initial/final state radiation (ISR/FSR.) After fulfilling the identification requirements and applying the corresponding corrections, jets are to satisfy the following requirements:

- $p_T > 20$ GeV
- $|\eta_{det}| < 2.5$
- All jets must be vertex confirmed[5].

[5]To further improve data/MC agreement in the RunIIb part of the analysis (which becomes important due to the higher luminosity), vertex confirmation is required for a jet to be selected.

Fig. 4.5 (Fig. 4.6 shows the distribution of p_T, η and the φ for both the leading and the second leading jets, for the electron (muon) channel respectively.

Figure 4.5: *Leading and second leading jets' p_T, η, and φ for the eletron channel in RunIIb dataset of the $W+$ 2 jets events. The legend of the plots can be found in page. 84.*

Template normalization

We apply the unbinned Matrix Method in order to form a multijet template. We normalize the template by performing a χ^2 minimization fit to the W boson transverse mass (m_T) distribution at preselection. While determining the QCD template normalization factor, we vary the W+jet normalization so that the total number of estimated events matches the number of data events observed at preselection. Separate multijet normalization factors are

Figure 4.6: *Leading and second leading jets' p_T, η, and φ for the muon channel in RunIIb dataset of the $W+$ 2 jets events. The legend of the plots can be found in page. 84.*

determined for both the loose and tight lepton ID operating points at preselection. These normalization factors remain fixed for the rest of the analysis.

Triangular Cut

Even though a multi- dimensional fake rate is applied in the QCD background estimation, it is difficult to get a good description at low $\not\!\!E_T$ and low M_W^T because of mis-measurements on $\not\!\!E_T$. These events have low $\not\!\!E_T$ and low M_W^T and the lepton and $\not\!\!E_T$ have the same direction. Therefore we exclude this region by applying a triangle cut:

$$M_W^T > 40 - 0.5 \times \not\!\!E_T \tag{4.4}$$

. since a straight cut on a single distribution is not the most efficient method to get rid of this background. The 2-dimensional ratio of (data/WH MC) with a loose electron on M_W^T vs $\not\!\!E_T$ and the triangle cut are shown in Fig. 4.7(b). It indicates a reasonably rejected low S/N region. Here the loose data and the WH simulation are used as QCD background sample and signal sample.

4.6.6 Analysis Orthogonality

Several channels has been used to search for the Higgs boson at the DØ Tevatron. Some of these channels may have the same topology as the our analysis (the WH analysis.) As a result, avoidance of counting the same event twice in two analyses is an important condition for the search of the Higgs boson. All channels must be "orthogonal"[6] to each other. To insure orthogonality, a set of different cuts are applied to remove events selected from the $ZH \rightarrow \ell\ell b\bar{b}$ and $X + H \rightarrow \tau\tau jj$ analyses. Events that contain two isolated leptons in the final state (from Z or $t\bar{t}$ are rejected. In the electron channel, events with an additional muons with $p_T > 15$ GeV are rejected. Similarly, in the muon channel, events with a loose electron are discarded.

[6]That is, no events are shared between different channels.

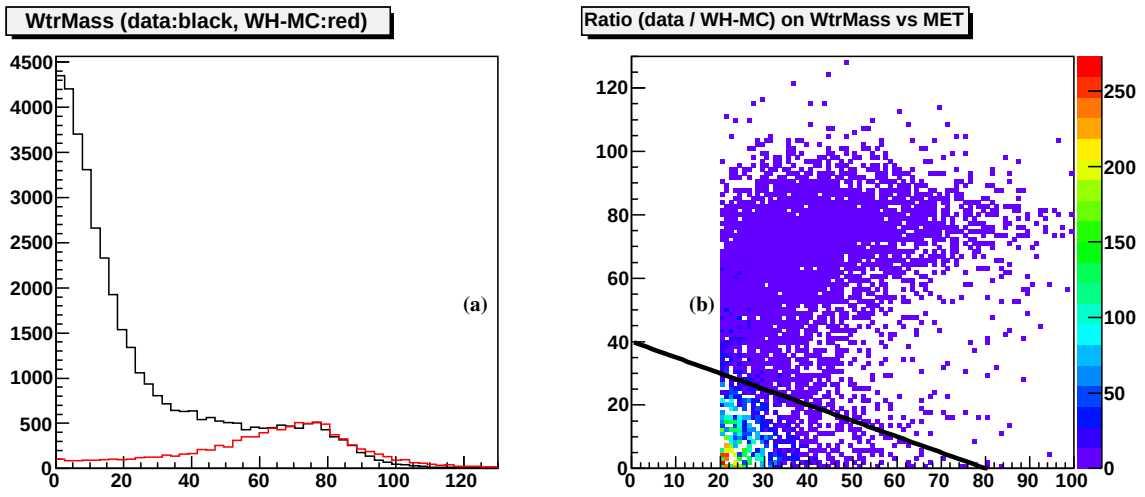

Figure 4.7: *(a) M_W^T using loose electron on data (black) as QCD sample, and WH MC (red) as real W sample. (b) 2D ratio plot of data / WH MC on the (M_W^T,$\not\!\!E_T$ plane. The QCD (multijet) events are distributed along low $\not\!\!E_T$ and low M_W^T and can therefore be eliminated by a triangle cut of $M_W^T > -0.5\ \not\!\!E_T + 40$ as shown by the black line. The WH MC is normalized on the W peak.*

Tau Veto

Some hadronic tau candidates may pass the $X + H \rightarrow \tau\tau jj$ selection. These taus are vetoed. Tau candidates can be any of a three DØ taus [88]. Requirements for each type are:

- Type 1 $E_T > 10$ GeV, $p_T > 7$ GeV, $\frac{E_T}{p_T} > 0.5$, $NN_\tau > 0.9$
- Type 2 $E_T > 10$ GeV, $p_T > 5$ GeV, $NN_\tau > 0.9$
- Type 3 $E_T > 15$ GeV, $p_T > 7$ GeV, $\sum_{trk} p_T^{trk} > 15$ GeV, $NN_\tau > 0.95$

Where NN_τ is the tau NN identification number.

Vetoing tau is applied to both electron and muon channels.

$ZH \rightarrow \ell\ell b\bar{b}$ Veto

The $ZH \rightarrow \ell\ell b\bar{b}$ channel contains two leptons. These leptons are either and electron/positron or a muon/anti-muon pairs. Our channel has only one lepton in its final state ($WH \rightarrow$

$l\nu_l b\bar{b}$). As a result and in order to ensure orthogonality, we have the following two cases:

- $ZH \to eeb\bar{b}$

  WH events are required to no have an additional electron with $p_T > 15$ GeV that fulfills the loose electron criteria.

- $ZH \to \mu\mu b\bar{b}$

  Events with two loose track-matched muons with $p_T > 10$ GeV are discarded.

Other vetoes are also applied to discard events that contains electrons from the ICR regions, such that the ICR electron greater than 5 GeV is vetoed.

4.7 Estimation of Multijet Background

4.7.1 QCD modeling strategy

QCD background is the background from multijet events. QCD background is determined by forming a template sample that models the kinematics of multijet events and then scaling that template at preselection in order to properly estimate the number of multijet events that pass our selection. The template is created by reweighting individual events in data based on the Matrix Method strategy. In the Matrix Method, the following pair of equations are solved simultaneously in order to estimate the number of QCD events:

$$N_L = N_\ell + N_{QCD}, \qquad N_T = \varepsilon_\ell N_\ell + f_j N_{QCD}, \tag{4.5}$$

where N_L (N_T) is the number of events in data with a lepton that passes a loose (tight) identification (ID) requirement, N_ℓ (N_{QCD}) is the number of real lepton events (misidentified QCD events) in that data, ε_ℓ is the efficiency for a real lepton that passes the loose ID requirement to subsequently pass the tight ID requirement, and f_j is the rate at which a jet that has been misidentified as a lepton that passes the loose ID requirement subsequently passes the tight ID requirement. Solving this system of equations for the number of QCD

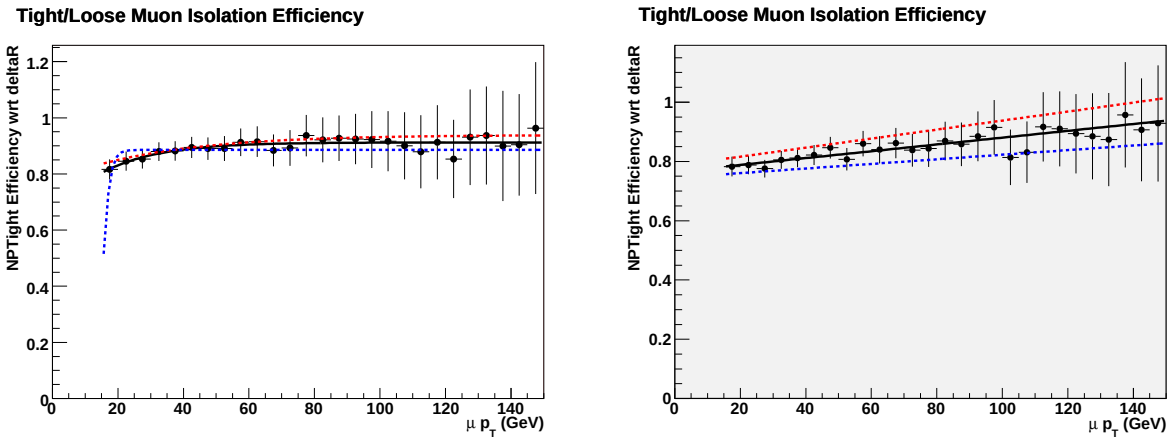

Figure 4.8: *Muon efficiency parameterization, as a function of muon p_T, for RunIIa (left) and RunIIb (right).*

events in the tight sample yields:

$$N_{QCD}^{T} = \frac{f_j}{\varepsilon_\ell - f_j}(\varepsilon_\ell N_L - N_T) \tag{4.6}$$

This method is designed to work on a binned data sample, where N_L and N_T can be counted, and constant ε_ℓ and f_j are used. For an electron, the efficiency, ε_e, is parametrized one-dimensionally in bins of electron p_T, while the efficiency for muons, ε_μ, is parametrized as a function of muon p_T (see Figure 4.8). The lepton efficiency rates are determined in data by studying a sample of $Z \to \ell\ell$ events. Fig. 4.9 shows the muon fake rate separately for RunIIa and RunIIb data, with separate treatment above and below $\Delta\phi(\not\!\!E_T\,, \mu) = \pi/2$. These fake rates are applied to both 2- and 3-jet events.

4.7.2 Lepton fake rates

The fake rate f_j for jets to fake electrons is determined as a function of electron p_T in events with $5 < \not\!\!E_T < 15$ GeV that otherwise match the signal preselection criteria, without the triangle cut. Separate parametrization in p_T are determined for several two-dimensional bins of $|\eta_{CAL}|$ and $\Delta\phi(\not\!\!E_T\,, e)$. Muon fake rates are determined based on a similarly modified preselection sample, and are determined in bins of η and $\Delta\phi(\not\!\!E_T\,, \mu)$. For electrons

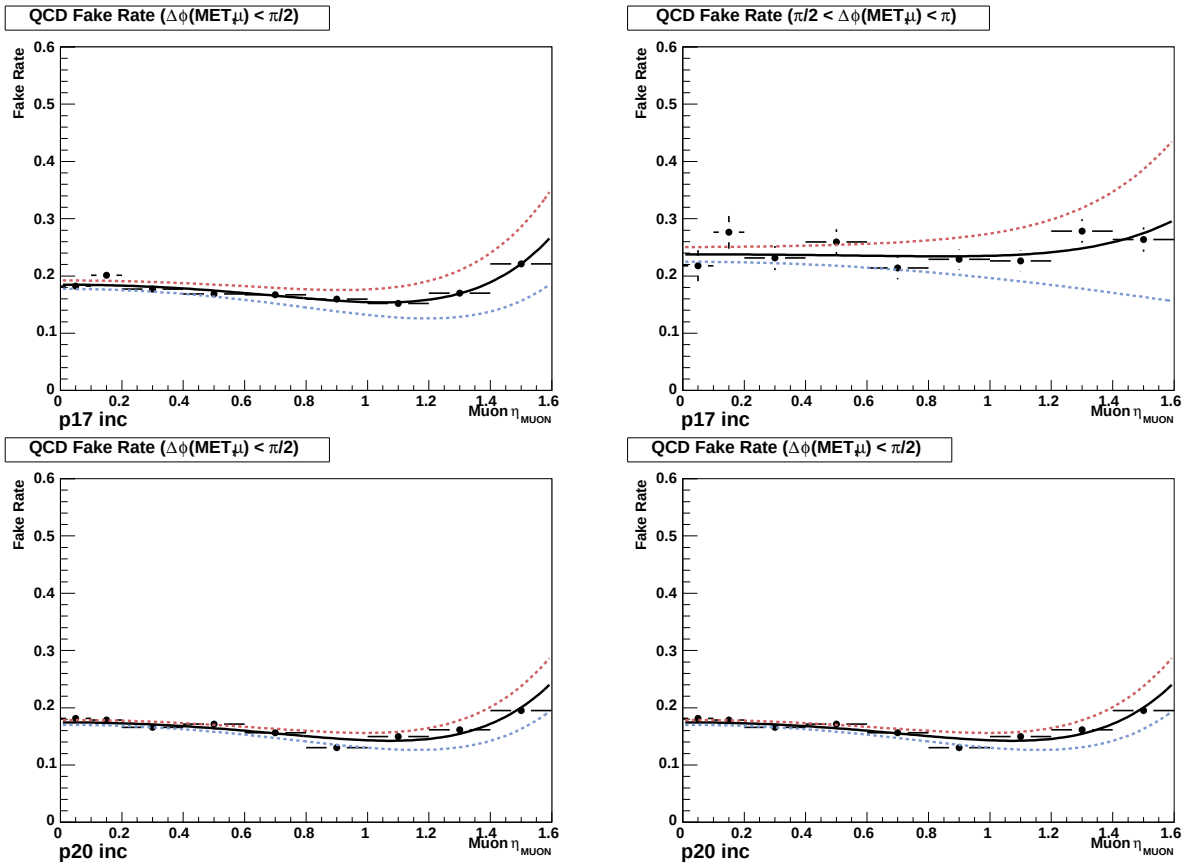

Figure 4.9: *Muon fake rate ratios in data as a function of muon $|\eta_{det}|$, including parametrized fit functions, when applicable. Plots on the left show data with $\Delta\phi(\not\!\!E_T\,,\mu) < \pi/2$, while plots on the right are $> \pi/2$. Data from RunIIa appear in the top row and RunIIb in the bottom row.*

and muons, the fake rate for a given kinematic range is determined by the loose:tight ratio of MC-subtracted data events:

$$f_{QCD} = \frac{N_T - MC_T}{N_L - MC_L}, \tag{4.7}$$

where N_L (N_T) is the number of data events in the QCD estimation sample with a reconstructed loose (tight) lepton and MC_L (MC_T) is the total MC estimation of the number of events with real loose (tight) leptons in them. Figure 4.10 shows the resultant fit for each of these bins. Figure 4.11 shows the QCD fake rate for electrons in RunIIb 2-jet events as a function of $e\ p_T$ for each bin in $|\eta_{CAL}|$ vs. $\Delta\phi(\not\!\!E_T\,, e)$. each individual parametrized function overlaid on the corresponding data, with uncertainty bands. To check against the multijet background description, Fig. 4.12 shows the distribution of $\Delta\varphi(\ell, \not\!\!E_T\,)$ for both electron and muon channels in the 2-jets channels.

4.7.3 Jet Properties

The jets used in this analysis are RunII cone type jets with a radius of $R = 0.5$ identified following the CALGO/Jet-id recommendations. The jet multiplicities and properties may be distorted by the presence of so-called "noise" jets which are reduced by the jet-ID criteria. Noise jets are either created by fake energy in the calorimeter (electronics malfunction in some region of the calorimeter), or they are real low energy jets which collect sufficient fake energy to pass the energy threshold cuts. Since distinguishing between these two cases on an event by event basis is not trivial, the CALGO/Jet-ID group has developed a set of ID cuts which classify the jets as "good" or "bad". The energy of "bad" jets is not corrected and this decreases their influence on the event kinematics. A subset of the bad jets consists of noise jets, i.e. jets which fail the L1 criteria. The following cuts ensure that the jet energy distribution in the various layers of the calorimeter is reasonable and that the jets are not built from spurious energy deposits:

- Energy fraction in the EM layers of a jet is required to be $0.05 < EMF < 0.95$.

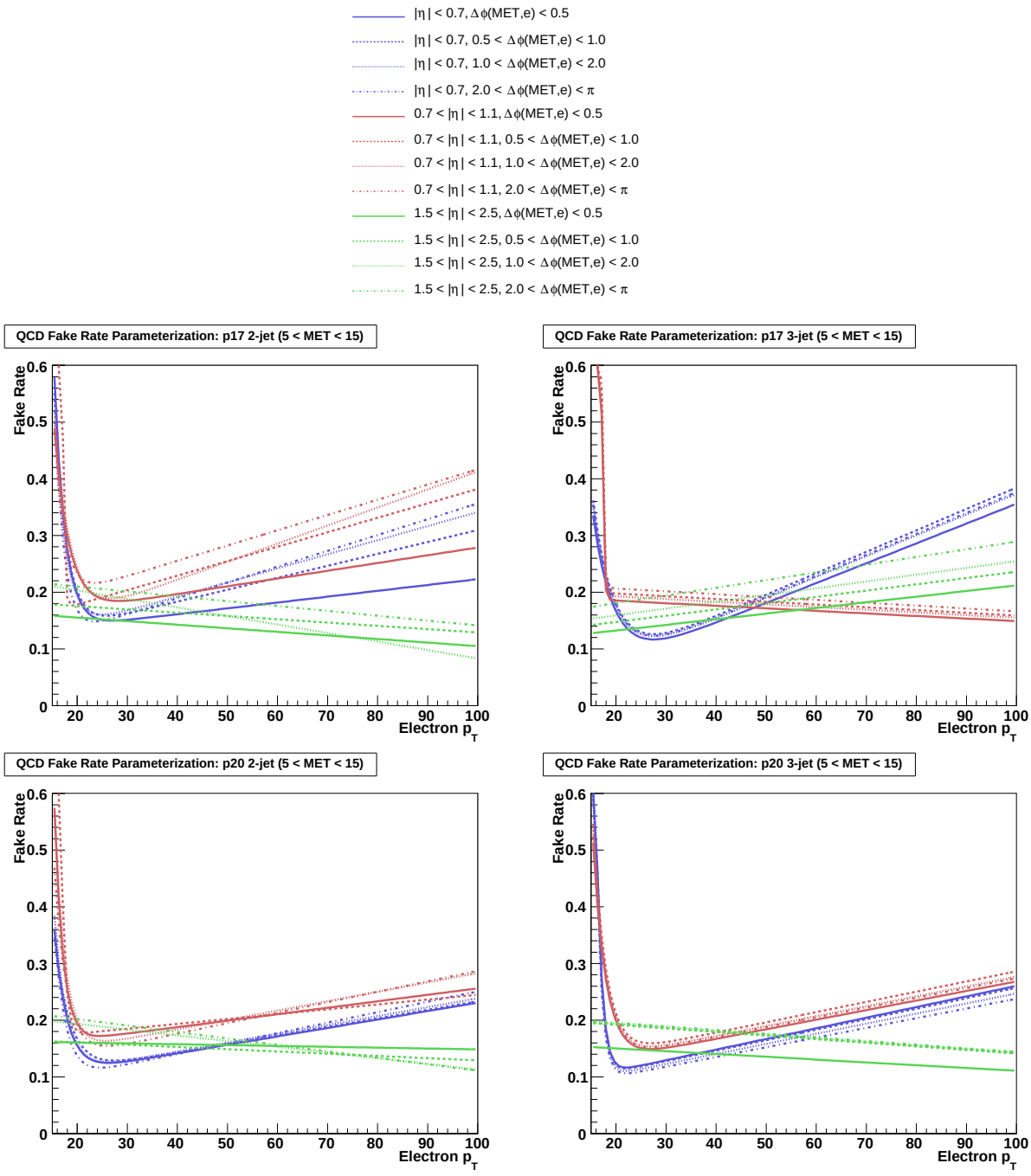

Figure 4.10: *The electron fake rate in 2-jet (left) and 3-jet (right) events for RunIIa (top) and RunIIb (bottom) as a function of* e p_T *for each bin in* $|\eta_{CAL}|$ *vs.* $\Delta\phi(\not\!\!E_T, e)$.

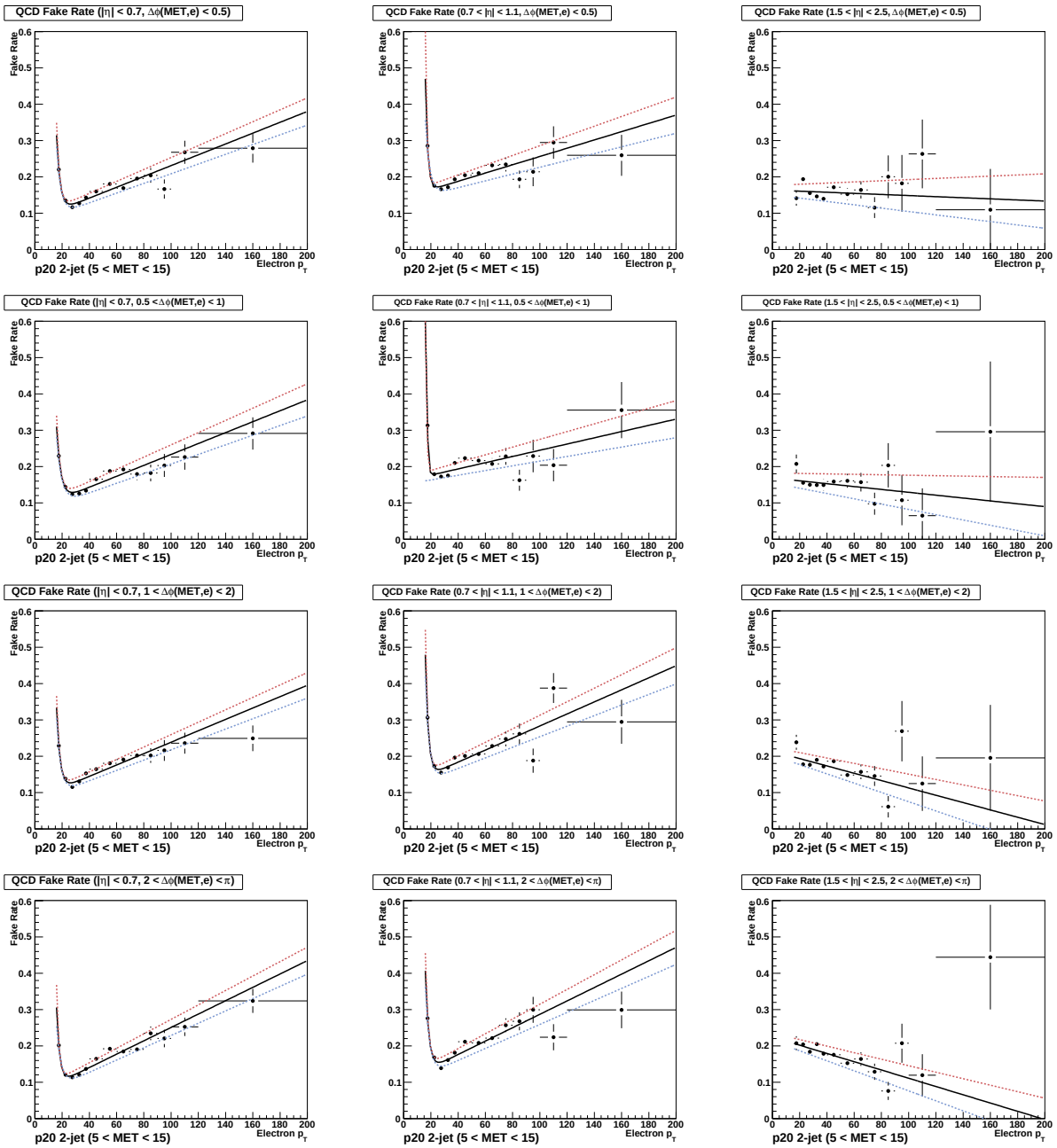

Figure 4.11: *The QCD fake rate for electrons in RunIIb 2-jet events as a function of* e p_T *for each bin in* $|\eta_{CAL}|$ *vs.* $\Delta\phi(\not\!\!E_T\,, e)$. *The red dashed curve represents the* $+1\sigma$ *variation of the fit and the blue curve represents the* -1σ *variation.*

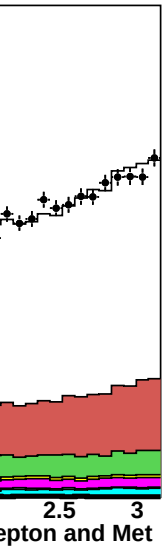

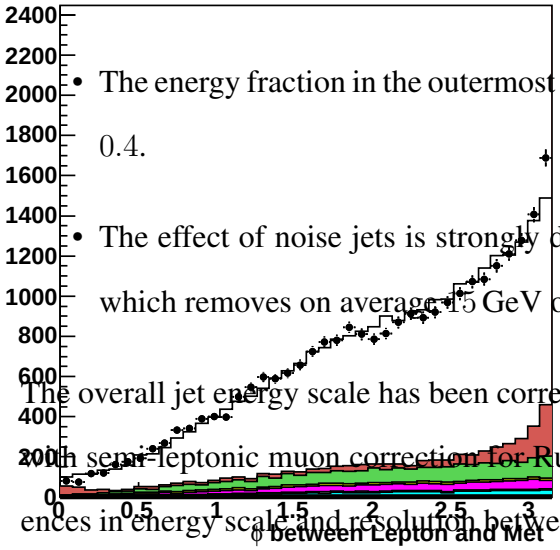

Figure 4.12: *Left:* $\Delta\phi(e, \not\!\!E_T)$. *Right:* $\Delta\phi(\mu, \not\!\!E_T)$.

- The energy fraction in the outermost layer (coarse hadronic) is required to be $CHF < 0.4$.
- The effect of noise jets is strongly diminished by the use of the T42 algorithm [89] which removes on average 1.5 GeV of noise per event [90].

The overall jet energy scale has been corrected using the p17 final JES version (p18-br-11) with semi-leptonic muon correction for RunIIa data, and p20 JES for RunIIb data. Differences in energy scale and resolution between data and MC have been further reduced using the JSSR algorithm [91]. JES and JSSR correct jets with a minimal transverse momentum of 6 GeV. We apply Jet Shifting to all MC samples, and use the Uniform Remapping option on signal, $t\bar{t}$, single top, and diboson samples. The difference in efficiency of the jet-ID cuts between data and simulation is quantified by the overall jet reconstruction efficiency scale factor. This scale factor has been studied in the Top and Higgs groups on data and simulation corresponding to a similar final state used in this analysis. This scale factor has been parametrized as a function of jet p_T and $|\eta_{det}|$. It is very close to to 1 (greater than 97.5%).

Jets in the simulation are rejected with a probability equal to one minus the scale factor. The jet reconstruction efficiency reaches a plateau at higher p_T therefore it has small influence on the WH signal since the average p_T of the leading and second jet originating from a 115 GeV Higgs after the selection cuts, are ~ 80 and ~ 40 GeV respectively. To further improve data/MC agreement in the p20 part of the analysis (which becomes important due to the higher luminosity), vertex confirmation is required for a jet to be selected. The criteria of a jet to be vertex confirmed are for the jet to have at least two tracks with $p_T > 0.5$ GeV, $SMThits >= 0$, $DCA_{xy} < 0.5$, $DCA_z < 1.0$ and $dZ < 2.0$ cm. This ensures that the jet originates from the primary vertex (i.e. it has at least two tracks connected to the primary vertex). For MC, vertex confirmed scale factors, provided by the JetID group, are applied using random removal (default setting in the VPlusJets framework).

4.8 Reweighting

4.8.1 VJets reweighting

As stated before in Section 4.4, both $W+$ jets and $Z+$ jets are among the crucial backgrounds of this analysis. Both processes are simulated with the `ALPGEN` generator.These samples are overlayed with zero bias events such that generated events are the closest possible to data from the DØ detector. However, these zero bias events were not collected with the same luminosity spectrum used for the data; this may result in small difference between data and MC simulated events. Also, comparing other MC generators, one finds differences in shapes [3, 41]. By default, standard p_T^W and p_T^Z corrections are already added to the DØ analyses to correct the physics modeling of soft radiation [92–94]. These correction, yet, don't seem to correct the shape problem. In order to correct shape differences, reweighting functions are derived and used to regenerate the difference between MC samples and the DØ data.

The common reweightings implemented in the VJets framework (version 3.5.0) for the z

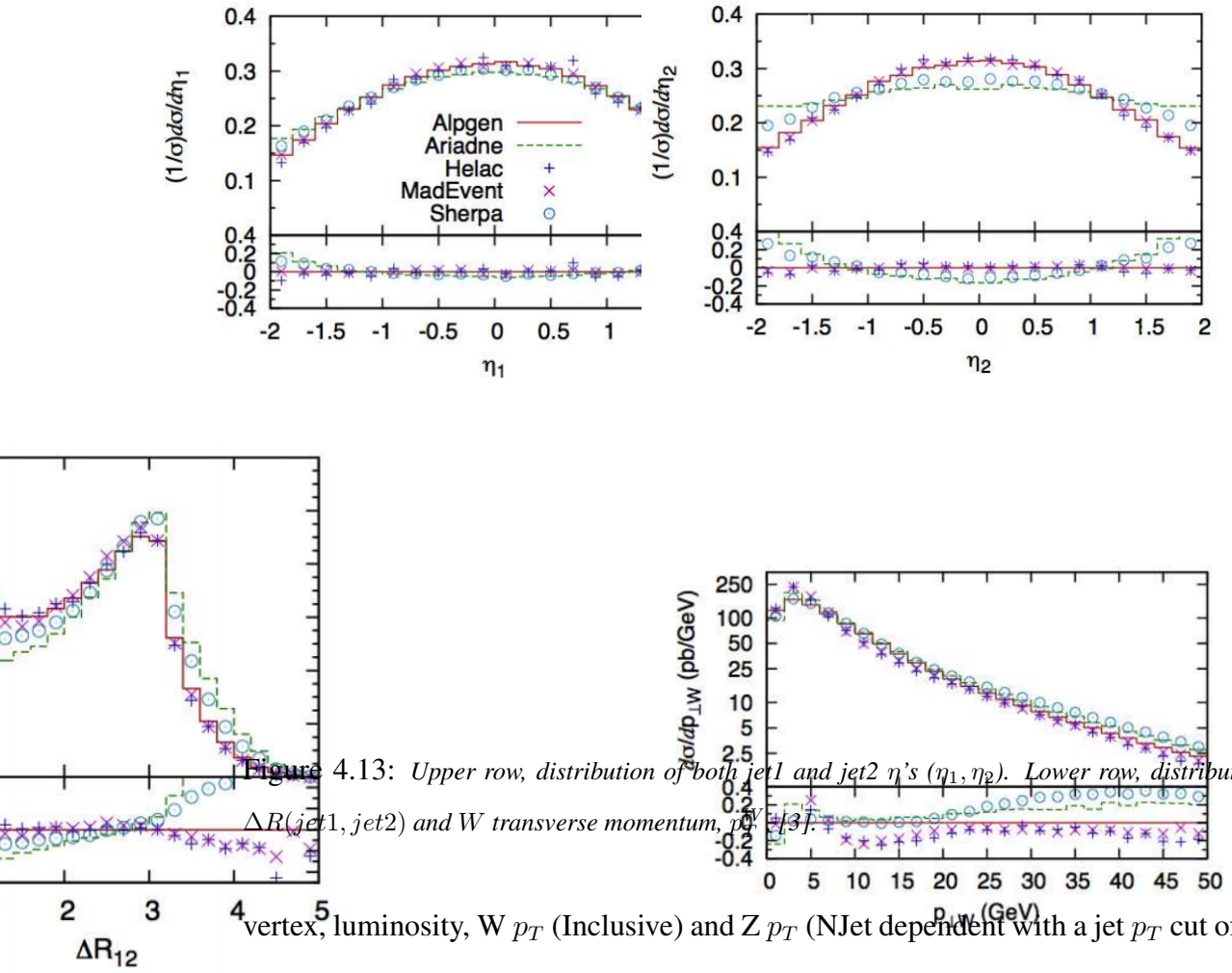

Figure 4.13: *Upper row, distribution of both jet1 and jet2 η's (η_1, η_2). Lower row, distribution of both $\Delta R(jet1, jet2)$ and W transverse momentum, p_T^W [3].*

vertex, luminosity, W p_T (Inclusive) and Z p_T (NJet dependent with a jet p_T cut of 20 GeV) distributions are applied in this analysis. Fig. 4.13 shows comparison plots for η^{jet1}, η^{jet2}, $\Delta R(jet1, jet2)$ and p_T^W.

4.8.2 Reweighting on `Alpgen` W+jets and Z+jets samples

To account for mismodeling in `ALPGEN` MC samples, we reweight the W+jets and Z+jets MC samples for both RunIIa and RunIIb in the electron and muon channel. All light and heavy flavor W/Z+jets samples are reweighted using the same functions. We derive our

reweighting functions from the ratio of background-subtracted data to the ALPGEN W+jets and Z+jets MC samples. The subtracted backgrounds include QCD, top, single-top and diboson MC events.

In the ICD region of the detector ($0.8 < |\eta_{det}| < 1.4$) we see a "horn" effect in the η_{det} distributions of the leading and second leading jet of the event (in RunIIb only, this is the only reweighting exclusively applied to RunIIb). We compensate this effect by applying constant factors $W_{\eta_{j1ICD_{north}}}$, $W_{\eta_{j1ICD_{south}}}$, $W_{\eta_{j2ICD_{north}}}$, and $W_{\eta_{j2ICD_{south}}}$, listed below, to the corresponding ICD regions of the jet.

To reproduce the shapes observed in data, we further derive a reweighting function for the lepton η distribution with a second order polynomial, $W_{\eta_{lepton}}$, and reweighting functions for the η distributions of the leading and second leading jet with fourth order polynomials, $W_{\eta_{j1}}$ and $W_{\eta_{j2}}$, listed below.

We also see a discrepancy in the shape of the ΔR and $W\,p_T$ distributions. These two variables show a strong correlation, therefore we derive a 2D reweighting function $W_{WpT} * W_{Delta\,R}$ on the ratio of W+jets data (meaning all other backgrounds have been subtracted) to W+jets MC in the ΔR – $W\,p_T$ plane (see Fig. 4.15 (a)–(c)). Both functions are then applied to the W+jets MC sample. The ΔR function is also applied to the Z+jets MC sample conserving the event yield for this sample.

See Figs. 4.14–4.15 for plots of all reweighting functions applied in this analysis.

In each figure, the black curve represents the nominal reweighting function, while the red and blue dashed curves represent $\pm 1\sigma$ variations on the fit function. These variations are based on selecting the parameter that affects the shape of the fit function the most (the highest order polynomial term for most fits; the slope of the sigmoid turn-on for Wp_T), varying that by one full σ based on the uncertainty of the fit, and varying the other fit parameters by the appropriate amount based on the covariance matrix of the fit. The functions

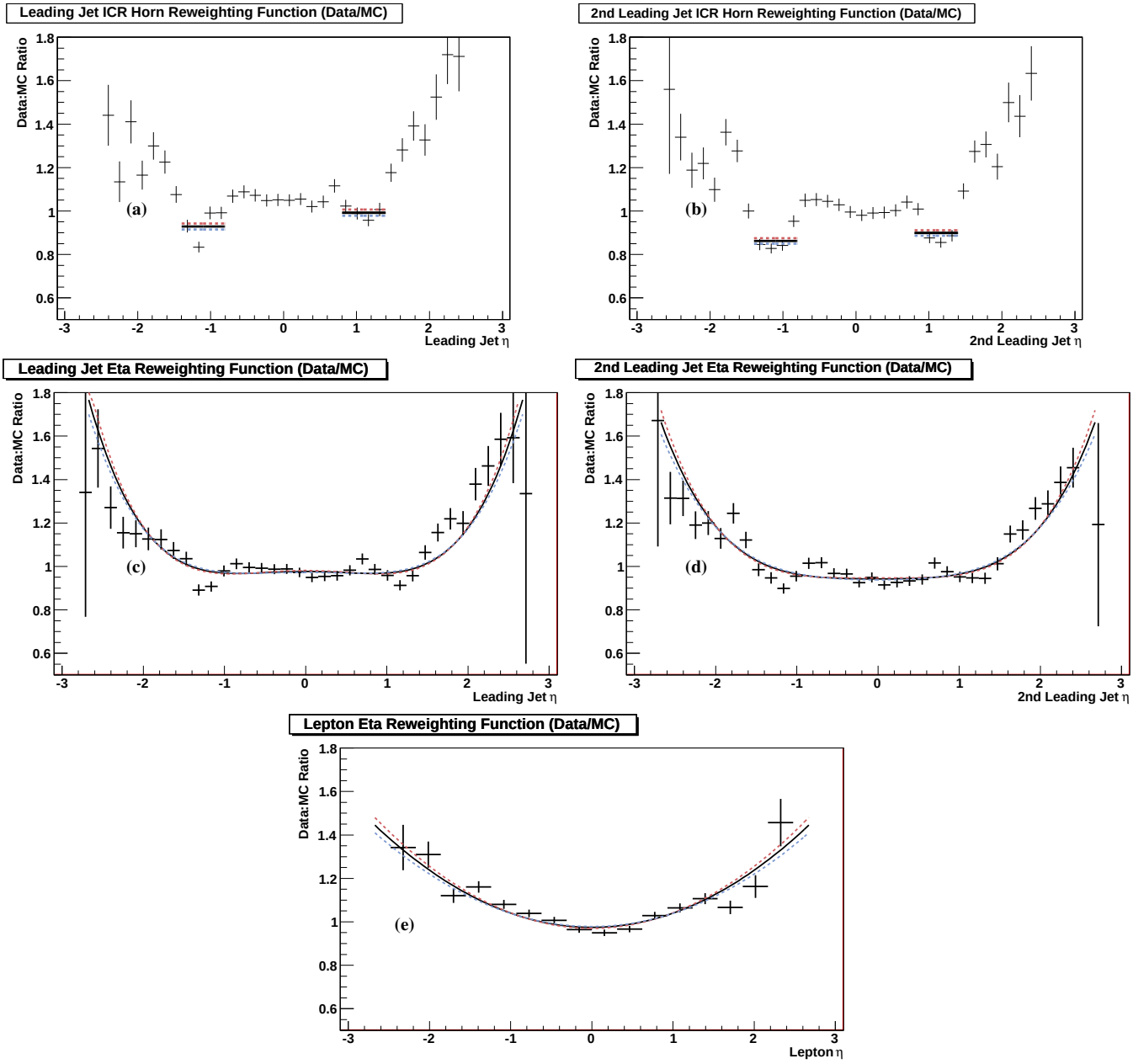

Figure 4.14: *Reweighting functions applied to correct for the horns in the ICR region in η_{det} of the leading jet (a) and the second leading jet (b), constant factors are used for these correction; the mismodeling of η in the leading jet (c) and the second leading jet (d), fourth order polynomials are used in these cases; and the mismodeling of η of the lepton (e), a second order polynomial is used for the correction function. The black curve is the nominal reweighting function, while the red and blue dashed curves are systematic variations.*

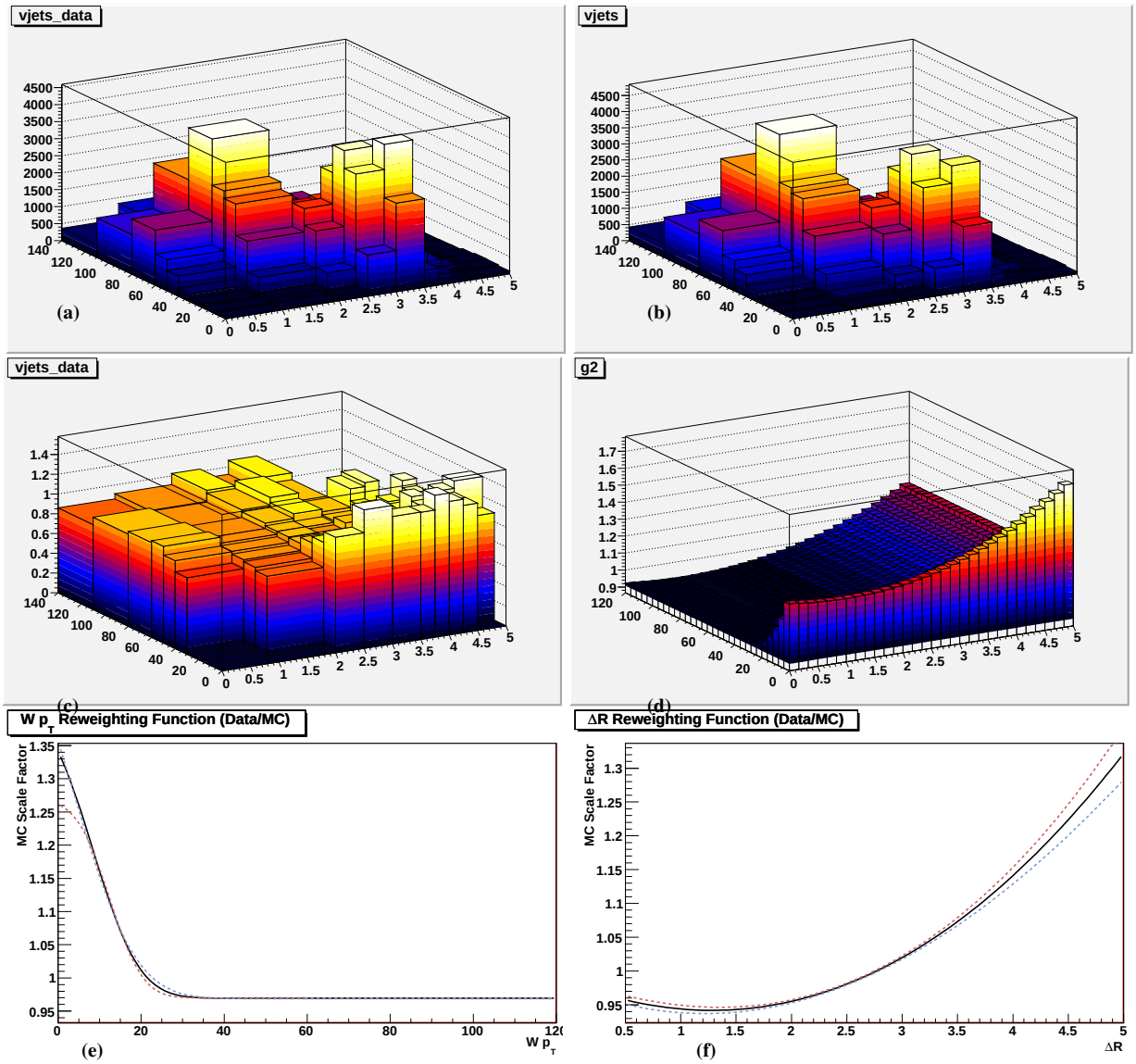

Figure 4.15: *2D (simultaneous) reweighting of ΔR and $W\ p_T$. (a) shows the distribution of W+jets data (meaning all other MC backgrounds have been subtracted) in the ΔR – $W\ p_T$ plane, (b) shows the distribution for W+jets MC, (c) shows their ratio, (d) shows the 2D fit function applied to reweight the ratio plot. (e) shows the 1D $W\ p_T$ reweighting function (obtained from the 2D fit) that we apply to the W+jets MC sample only, (f) shows the 1D ΔR reweighting function (obtained from the 2D fit) that we apply to the W+jets and Z+jets MC samples (conserving the event yield for the Z+jets MC sample).*

are defined as

$$
\begin{aligned}
W_{\eta_{j1ICD_{south}}} &= 0.928472 \\
W_{\eta_{j1ICD_{north}}} &= 0.992236 \\
W_{\eta_{j2ICD_{south}}} &= 0.862120 \\
W_{\eta_{j2ICD_{north}}} &= 0.899186 \\
W_{\eta_{lepton}} &= 0.97426 + 0.0658797\ \eta^2_{lepton} \\
W_{\eta_{j1}} &= 0.976774 - 0.0262889\ \eta^2_{j1} + 0.0191657\ \eta^4_{j1} \\
W_{\eta_{j2}} &= 0.942693 - 0.004809\ \eta^2_{j2} + 0.018491\ \eta^4_{j2} \\
W_{Delta\,R} &= 4.3822 - 0.255443\ \Delta R + 0.085197\ \Delta R^2 - 0.00630133\ \Delta R^3 \\
W_{WpT} &= 0.215941 + 0.0538577\ (1 + Erf((W_{pT} - 7.96332)/(\sqrt{2} * (-8.97439))))
\end{aligned}
$$

4.9 Experimental K-factors, and HF scale factors for W+jet and Z+jet

The simulated background processes are absolutely normalized to the SM prediction of their cross section except for the ALPGEN W+jets samples. W+jets samples are normalized to data before applying b-tagging. The final normalization is set in conjunction with the scaling of the QCD background template, as described in Section 4.6.5. The experimental K-factor K^{exp}_{LF} for the W+jets processes is defined as

$$K^{exp}_{LF} = \frac{N_{data} - N_{SM} - N_{QCD}}{N_{W+jet}}. \tag{4.8}$$

where N_{SM} is the number of Standard Model expected events with proper isolated lepton identification but without the W+jets contribution, and N_{QCD} is the number of standard model events with isolated lepton mis-identification, estimated from data. The K^{exp}_{LF} for e (μ) from each data set is summarized in Table. 4.10, and is $\sim$ 1.1 (1.1) for RunIIa and $\sim$ 1.0 (1.0) for Run IIb. All these numbers are consistent with their average of 1.0, given the uncertainty which is of the order of 10%, and which originates from lepton characteristics (lepton trigger, lepton efficiency, QCD background, other indirect effects linked to the the

lepton, like the $\not\!\!E_T$ requirement which is corrected with the lepton energy). The cross section for the heavy flavor processes are obtained by multiplying the Wbb, Wcc, Zbb and Zcc ALPGEN cross sections by K_{LF}^{exp} and by the Heavy Flavor (s_{HF}) factor which is derived from data. With these conventions, the experimental K-factor for heavy flavor is given by $K_{HF}^{exp} = s_{HF} \times K_{LF}^{exp}$. The S_{HF} factor is determined on each orthogonal sample, the tagged sample (denoted by $'$) and the anti-tagged sample (denoted by $''$) by the following equation:

$$S_{HF} = \frac{(Data' - X') * W'' - (Data'' - X'') * W'}{(Data'' - X'') * B' - (Data' - X') * B''} \tag{4.9}$$

where $W(B)$ is the number of events in the $W + nlp$ ($Wbb + nlp$ and $Wcc + nlp$) sample, and X is the number of events in the MC background sample except W+jets (i.e. $t\bar{t}$, single top and dibosons). For the purposes of verifying that the MC describes the data well, we calculate and apply a S_{HF} factor to use while making plots. We use all channels to derive the S_{HF} factor we use in our plots and obtain 1.00, which we apply to the heavy flavor samples (Wbb, Wcc, Zbb and Zcc). While all plots in this note use this predetermined value of S_{HF}, we set S_{HF} to 1.0 and allow it to vary within its 20% uncertainty band during the limit setting procedure itself. With all these corrections applied, a good agreement between

	channel	2 jet	3 jet
RunIIa	Electron	1.07 $\pm$ 0.01	1.17 $\pm$ 0.03
	Muon	1.14 $\pm$ 0.01	1.31 $\pm$ 0.03
RunIIb	Electron	0.98 $\pm$ 0.01	1.05 $\pm$ 0.01
	Muon	1.04 $\pm$ 0.01	1.13 $\pm$ 0.01

Table 4.10: *The experimental K_{LF}^{exp} factors for each sample, taking into account the theoretical K-factor of 1.3. Errors are statistical only. The total uncorrelated systematic uncertainty between the e and μ determinations is approximately 7-8%, based on trigger (3-4% e, 5% μ) and lepton ID (3% e, 4% RunIIa μ, 2% RunIIb μ) uncertainties.*

data and MC simulations was achieved as can seen from both Fig. 4.3 and Fig. 4.4. Also, with these corrections, the W boson distributions can be, then, reconstructed, such as its

	Electron	muon
RunIIa	0.78 ± 0.09	0.99 ± 0.11
RunIIb	1.14 ± 0.06	1.02 ± 0.06

Table 4.11: *The S_{HF} heavy flavor factor in 0tag sample, applied on top of the theoretical heavy flavor K-factor (1.47 for $W+$ jet). The error is only data statistical errors is considered. Luminosity weighted average is 1.00.*

transverse mass, M_W^T. Figs. 4.5, 4.6 show the distributions related to both the leading and the second leading jets. The Dijet invariant mass can be calculated from

$$M_{jj} = \sqrt{(E^{j_1} + E^{j_2})^2 - (p_x^{j_1} + p_x^{j_2})^2 - (p_y^{j_1} + p_y^{j_2})^2 - (p_z^{j_1} + p_z^{j_2})^2} \tag{4.10}$$

Some of the variables that can reconstructed using the information from the two jets are shown in Figs. 4.16, 4.17 With the selection process and the corrections added to the analysis, a good agreement between data and simulated MC events is achieved. Tables 4.12 and 4.13 show the number of events lost at each stage of our analysis as cuts are applied for data and for estimated signal ($m_H = 115$ GeV). Tables 4.14 and 4.15 show the event yields after applying the selection rules and the MC W/Z+Jets corrections for RunIIa and RunIIb respectively, for both the electron and the muon channels. Tables 4.16 and 4.17 shows the event yields for the $W+$ 3 jets for RunIIa and RunIIb, respectively and for both the electron and the muon channels. The above tables summarizes our data and events yields before applying any restrictions on the type of jet in the final state. We can notice that the electron yield is always higher than the muon yield, this is due to the following

- The loss of acceptance from the "phi hole"
- In the electron channel, the pseudorapidity coverage is smaller

One also notices that the rate of multijet events is a little higher in the electron case than it is in the muon case. This is due to the fat that photons can add a potential objects to the

Figure 4.16: *Dijet mass, M_{jj}, Dijet mass transverse momentum, $p_T(j,j)$, and the scalar sum of the transverse momenta of jets, H_T are shown in the upper row. $\Delta\varphi(j,j)$, $\Delta\eta(j,j)$, and $\Delta R(j,j)$ for the two leading jets are shown in the bottom row for the electron channel in RunIIb dataset of the $W+$ 2 jets events. The legend of the plots can be found in page. 84.*

Figure 4.17: *Dijet mass, M_{jj}, Dijet mass transverse momentum, $p_T(j,j)$, and the scalar sum of the transverse momenta of jets, H_T are shown in the upper row. $\Delta\varphi(j,j)$, $\Delta\eta(j,j)$, and $\Delta R(j,j)$ for the two leading jets are shown in the bottom row for the muon channel in RunIIb dataset of the $W+$ 2 jets events. The legend of the plots can be found in page. 84.*

	RunIIa		RunIIb	
Cut	Data	Signal	Data	Signal
SAM definition	72589360	—	672888263	—
Loose e (skim)	21767359	8.19	82160197	33.88
Tight e	2472818	7.28	7771993	27.89
2 or 3 "good" jets	116393	6.13	331114	21.05
2^{nd} lepton veto	114616	6.13	326274	21.00
Triangle cut	37759	5.60	108237	19.34
$\not\!\!E_T$	25400	5.28	66854	18.26
Lepton η	25400	5.28	66854	18.26
H_T	17489	5.03	49299	17.51
PV_Z	16044	4.56	47226	16.54

Table 4.12: Events surviving at each stage of selection for the RunIIa and RunIIb electron channels. The signal column represents the estimated number of events produced by a standard model Higgs boson with $m_H = 115$ GeV. Note that "good" jets refer to standard DØ *good jets* that pass L1 trigger confirmation. In RunIIb data, a "good jet" must also satisfy vertex confirmation.

	RunIIa		RunIIb	
Cut	Data	Signal	Data	Signal
SAM definition	30100306	—	126728321	—
Loose μ (skim)	2817581	4.94	7735373	16.23
Tight μ	1563066	4.37	3927626	13.21
2 or 3 "good" jets	50934	4.25	97933	11.53
2^{nd} lepton veto	50934	4.25	97933	11.53
Triangle cut	26835	3.90	56096	10.53
$\not\!\!E_T$	23211	3.71	48963	10.05
Lepton η ¡ 1.6	23211	3.71	43452	10.05
H_T	15900	3.55	31791	9.63
PV_Z	14313	3.19	30202	9.02

Table 4.13: Events surviving at each stage of selection for the RunIIa and RunIIb muon channels. The signal column represents the estimated number of events produced by a standard model Higgs boson with $m_H = 115$ GeV. Note that "good" jets refer to standard DØ *good jets* that pass L1 trigger confirmation. In RunIIb data, a "good jet" must also satisfy vertex confirmation.

	$W(e)+2$ jets	$W(\mu)+2$ jets
WH	3.01 $\pm$ 0.33	2.45 $\pm$ 0.27
WW	266.45 $\pm$ 29.31	222.96 $\pm$ 24.53
WZ	43.96 $\pm$ 4.84	37.14 $\pm$ 4.09
ZZ	2.43 $\pm$ 0.27	2.14 $\pm$ 0.24
$Wb\bar{b}$	358.68 $\pm$ 71.74	316.62 $\pm$ 63.32
$Zb\bar{b}$	16.84 $\pm$ 3.37	8.93 $\pm$ 1.79
$Wc\bar{c}$	856.02 $\pm$ 171.20	771.01 $\pm$ 154.20
$Zc\bar{c}$	30.84 $\pm$ 6.17	21.37 $\pm$ 4.27
$t\bar{t}$	126.57 $\pm$ 17.72	80.29 $\pm$ 11.24
Single top	62.13 $\pm$ 8.08	52.35 $\pm$ 6.81
QCD Multijet	2048.58 $\pm$ 184.37	457.19 $\pm$ 41.15
$W+$ jets (light)	8225.6 $\pm$ 740.30	7406.36 $\pm$ 666.57
$Z+$ jets (light)	373.89 $\pm$ 33.65	178.64 $\pm$ 16.08
Total expectation	12412.00 (n.t.d.)	9555.00 (n.t.d.)
Observed Events	12412	9555

Table 4.14: *Summary table for the $W(e)$ and $W(\mu)$ + 2 jet final state in RunIIa. Observed events in data are compared to the expected number of $W+$ 2 jets before we apply the b-tagging. Expectation originates from the simulation of WH (with $m_H = 115$ GeV), dibosons (WW, WZ, ZZ, labeled WZ in the table), $Wb\bar{b}$ production, top production ($t\bar{t}$ and single-top), QCD multijet background and "$W+$ jet" production, which contains light and c quarks. All Z processes are included in the corresponding W categories. "n.t.d." stands for "normalized to data".*

	$W(e)+2$ jets	$W(\mu)+2$ jets
WH	10.66 $\pm$ 1.17	8.18 $\pm$ 0.90
WW	819.06 $\pm$ 90.10	628.50 $\pm$ 69.14
WZ	134.36 $\pm$ 14.78	107.17 $\pm$ 11.79
ZZ	5.03 $\pm$ 0.55	7.95 $\pm$ 0.88
$Wb\bar{b}$	1099.18 $\pm$ 219.84	963.55 $\pm$ 192.71
$Zb\bar{b}$	31.25 $\pm$ 6.25	33.75 $\pm$ 6.75
$Wc\bar{c}$	2637.17 $\pm$ 527.43	2035.37 $\pm$ 407.07
$Zc\bar{c}$	60.86 $\pm$ 12.17	73.94 $\pm$ 14.79
$t\bar{t}$	496.90 $\pm$ 69.57	336.94 $\pm$ 47.17
Single top	196.40 $\pm$ 25.53	165.66 $\pm$ 21.54
QCD Multijet	8319.60 $\pm$ 748.76	1477.89 $\pm$ 133.01
$W+$ jets (light)	23416.9 $\pm$ 2107.52	20357.1 $\pm$ 1832.14
$Z+$ jets (light)	496.15 $\pm$ 44.65	615.15 $\pm$ 55.36
Total expectation	37712.90 (n.t.d.)	26803.00 (n.t.d.)
Observed Events	37713	26803

Table 4.15: *Summary table for the $W(e)$ and $W(\mu)$ + 2 jet final state in RunIIb. See caption for Table 4.14.*

	$W(e)+3$ jets	$W(\mu)+3$ jets
WH	0.68 $\pm$ 0.08	0.58 $\pm$ 0.07
WW	60.13 $\pm$ 6.61	52.53 $\pm$ 5.7
WZ	10.95 $\pm$ 1.20	9.13 $\pm$ 1.00
ZZ	1.55 $\pm$ 0.17	0.60 $\pm$ 0.08
$Wb\bar{b}$	94.5 $\pm$ 18.90	89.63 $\pm$ 17.93
$Zb\bar{b}$	6.53 $\pm$ 1.31	3.01 $\pm$ 0.60
$Wc\bar{c}$	243.43 $\pm$ 48.69	237.63 $\pm$ 47.53
$Zc\bar{c}$	13.62 $\pm$ 2.72	6.84 $\pm$ 1.37
$t\bar{t}$	201.56 $\pm$ 28.22	151.45 $\pm$ 21.20
Single top	18.01 $\pm$ 2.34	15.48 $\pm$ 2.01
QCD Multijet	662.18 $\pm$ 59.60	132.01 $\pm$ 11.88
$W+$ jets (light)	1360.77 $\pm$ 122.47	1365.48 $\pm$ 122.89
$Z+$ jets (light)	83.77 $\pm$ 7.54	36.20 $\pm$ 3.26
Total expectation	2757.00 (n.t.d.)	2100.00 (n.t.d.)
Observed Events	2757	2100

Table 4.16: *Summary table for the $W(e)$ and $W(\mu)$ + 3 jet final state in RunIIa. See caption for Table 4.14.*

	$W(e)+2$ jets	$W(\mu)+2$ jets
WH	2.14 $\pm$ 0.24	1.68 $\pm$ 0.19
WW	176.06 $\pm$ 19.37	118.03 $\pm$ 12.98
WZ	32.84 $\pm$ 3.61	20.33 $\pm$ 2.24
ZZ	1.86 $\pm$ 0.22	1.90 $\pm$ 0.22
$Wb\bar{b}$	256.11 $\pm$ 51.22	224.08 $\pm$ 44.82
$Zb\bar{b}$	9.51 $\pm$ 1.90	9.64 $\pm$ 1.93
$Wc\bar{c}$	710.24 $\pm$ 142.05	489.05 $\pm$ 97.81
$Zc\bar{c}$	22.09 $\pm$ 4.42	19.38 $\pm$ 3.88
$t\bar{t}$	681.66 $\pm$ 95.43	518.42 $\pm$ 72.58
Single top	53.03 $\pm$ 6.89	46.48 $\pm$ 6.04
QCD Multijet	2084.97 $\pm$ 187.65	353.38 $\pm$ 31.80
$W+$ jets (light)	3458.06 $\pm$ 311.23	3112.87 $\pm$ 280.16
$Z+$ jets (light)	93.57 $\pm$ 8.42	96.44 $\pm$ 8.68
Total expectation	7580.00 (n.t.d.)	5010.00 (n.t.d.)
Observed Events	7580	5010

Table 4.17: *Summary table for the $W(e)$ and $W(\mu)$ + 3 jet final state in RunIIb. See caption for Table 4.14.*

electron channel. Another reason to this high rate of multijet is the fast that the luminosity is higher in case of RunIIb data. High luminosity will cause more jets to be produced with higher energy and this increases their probability of semi-leptonically decays which increases the rate of fake muons or photons that can be misidentified as electrons. One also notices that the signal to background ratio, S/B, is almost 1/4000 where the dominant background comes from the Wjj process, which represents approximately 2/3 of the $2-$jets sample.

Reducing the background from both multijets and $W+$ ($Z+$) light jets is the next, crucial, step.

4.10 $b-$tagging In the WH Analysis

The primary goal of this analysis is the search for WH production with two $b-$jets in the final state. With identifying both jets in the final state as originating from a $b-$quark, major contributions from $W+$ light jets, $Z+$ light jets as well as $V + c\bar{c}$ and multijet backgrounds can be reduced and a increase in the analysis sensitivity will be achieved. The remaining major contributions to the background for this analysis will come from $W + b\bar{b}$, $Z + b\bar{b}$ and $t\bar{t}$.

We define two orthogonal samples, a double-tag sample with two jets at the Old-Loose (OL) operating point (NN > 0.5) and a single-tag sample with one jet passing the Tight operating point (NN > 0.775) and no other jet passing Old Loose. The OL and Tight operating points have fake rates of about 1.5% and 0.5% , respectively, for a jet p_T of 50 GeV [95]. We find that the Tight/Old-Loose working point provides a marginally better sensitivity than the Very-Tight/L3 working point on the RunIIa data sample, but a 10% gain on the RunIIb sample. Indeed the amount of QCD is larger in the latter sample and a tighter working point rejects this more efficiently.

4.10.1 Taggability

The DØ detector is not perfectly modeled in the Monte Carlo simulation. Jets' taggability is affected by this modeling imperfection and we find that it is higher in the MC simulation that it is in data which will lead to a higher yield in the MC simulated events that it is in data. As a result, corrections to MC simulated events to match data.

In order for a jet to be tagged, it has to pass a minimum track-based criterion (called "taggability") corresponding to a match within a $\Delta R < 0.5$ cone size between a track with $p_T > 0.5$ GeV and a track-jet ($p_T > 1$ GeV, $SMThits >= 1$,$DCA_{xy} < 0.15$, $DCA_z < 0.4$). To account for tracking mismodeling in the MC we correct the MC by a scale factor to match the taggability efficiency measured in data. We have measured the taggability of jets in the $W + 2$ jet sample (data and simulation) to determine the taggability scale factor in four z-vertex regions as a function of jet transverse momentum (applied in RunIIa only because there is no p_T dependence in RunIIb) and only jet pseudorapidity as shown in Fig. 4.18-4.19 (RunIIa), and Figs. 4.20-4.21 (RunIIb). In these figures plots (a) and (b) show the derived parametrization for $-40 < z_{\text{vtx}} < -30$ cm and $-30 < z_{\text{vtx}} < 0$ cm and plots (c) and (d) show derived parametrization for $0 < z_{\text{vtx}} < 30$ cm and $30 < z_{\text{vtx}} < 40$ cm. The taggability scale factors are derived from the ratio of taggability on data to taggability on simulation. The correlation between the taggability scale factor and the bID scale factors has been verified in the b-tagged $t\bar{t}$ cross section measurement [96].

We then do a closure test by plotting the ratio of the data taggability divided by the simulated taggability corrected by the scale factor, as a function of p_T and η. If the simulation has been corrected properly in all kinematic/spatial regions, the result must be flat, at unity. The result is shown in Figs. 4.22 and 4.23, for both the electron and muon channels. The closure test fit results are summarized in Table 4.18, which shows that all closure test fits are consistent with unity within 1σ.

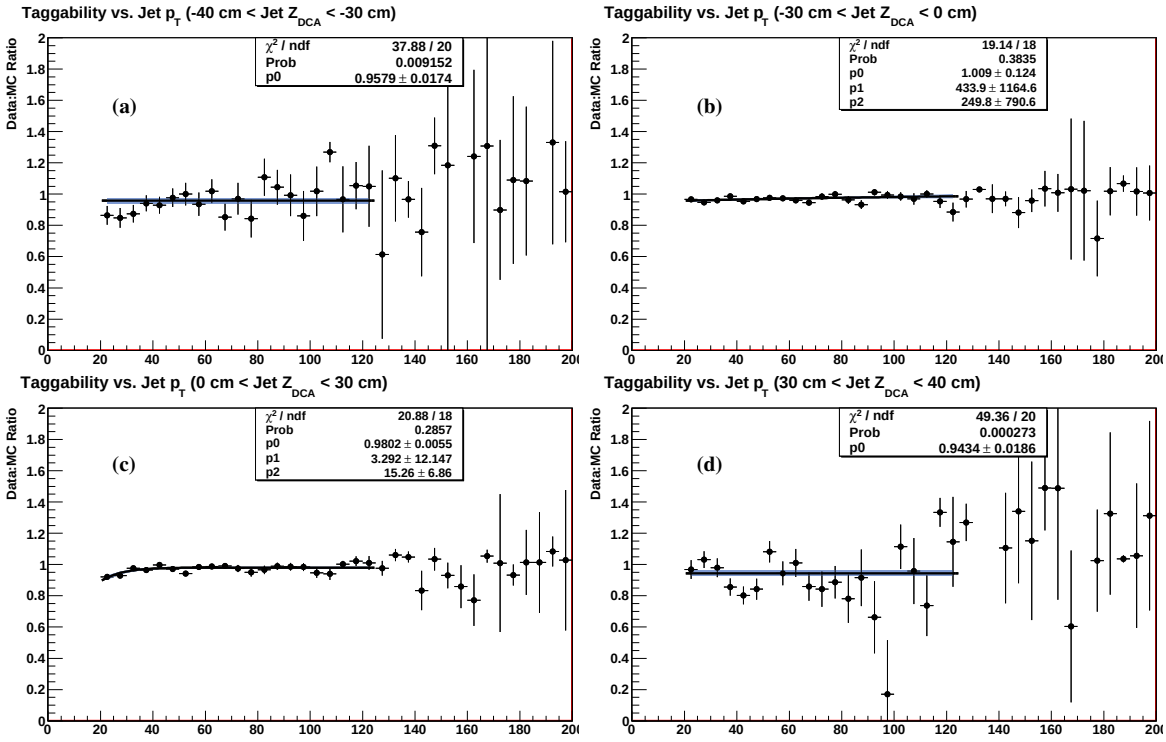

Figure 4.18: *RunIIa Jet taggability scale factors for muon channel versus transverse momentum p_T measured from the data and simulated samples of the RunIIa analysis. The parametrization of (a),(b) apply to the $-40 < z_{vtx} < -30$ cm bin and $-30 < z_{vtx} < 0$ cm bin as function of p_T^{jet}, where (c) and (d) show the scale factor as function of p_T^{jet} for the $0 < z_{vtx} < 30$ cm bin and $30 < z_{vtx} < 40$ cm , respectively. The black line represents the nominal fit and the blue band represents the $\pm 1\sigma$ uncertainty band on the fit.*

Distribution	-40 to -30 cm	-30 to 0 cm	0 to 30 cm	30 to 40 cm
RunIIa: p_T	1.002±0.035	1.012±0.013	1.003±0.013	1.031±0.039
RunIIa: η	1.000±0.036	1.010±0.010	1.001±0.013	1.023±0.039
RunIIb: p_T	1.000±0.025	1.001±0.008	1.003±0.008	1.020±0.030
RunIIb: η	1.000±0.024	1.001±0.008	1.003±0.008	1.015±0.026

Table 4.18: *Taggability closure test fit results. Column headings show the range of primary vertex z-values used for the fit. Numbers represent the result of fitting the ratio of data to taggability-modified MC to a constant, with uncertainty.*

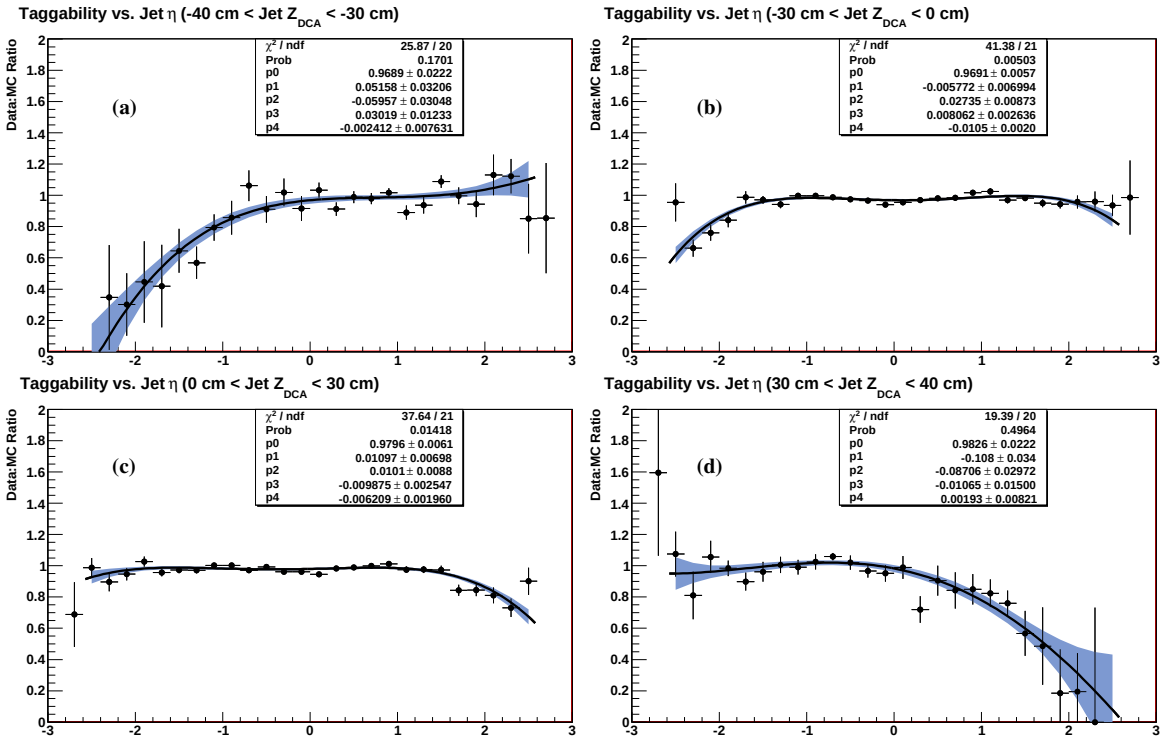

Figure 4.19: *RunIIa Jet taggability scale factors for muon channel versus eta measured from the data and simulated samples of the RunIIa analysis. The parametrizations of (a),(b) apply to the* $-40 < z_{vtx} < -30$ *cm bin and* $-30 < z_{vtx} < 0$ *cm bin as function of eta, where (c) and (d) show the scale factor as function of eta for the* $0 < z_{vtx} < 30$ *cm bin and* $30 < z_{vtx} < 40$ *cm , respectively. The black line represents the nominal fit and the blue band represents the* $\pm 1\sigma$ *uncertainty band on the fit.*

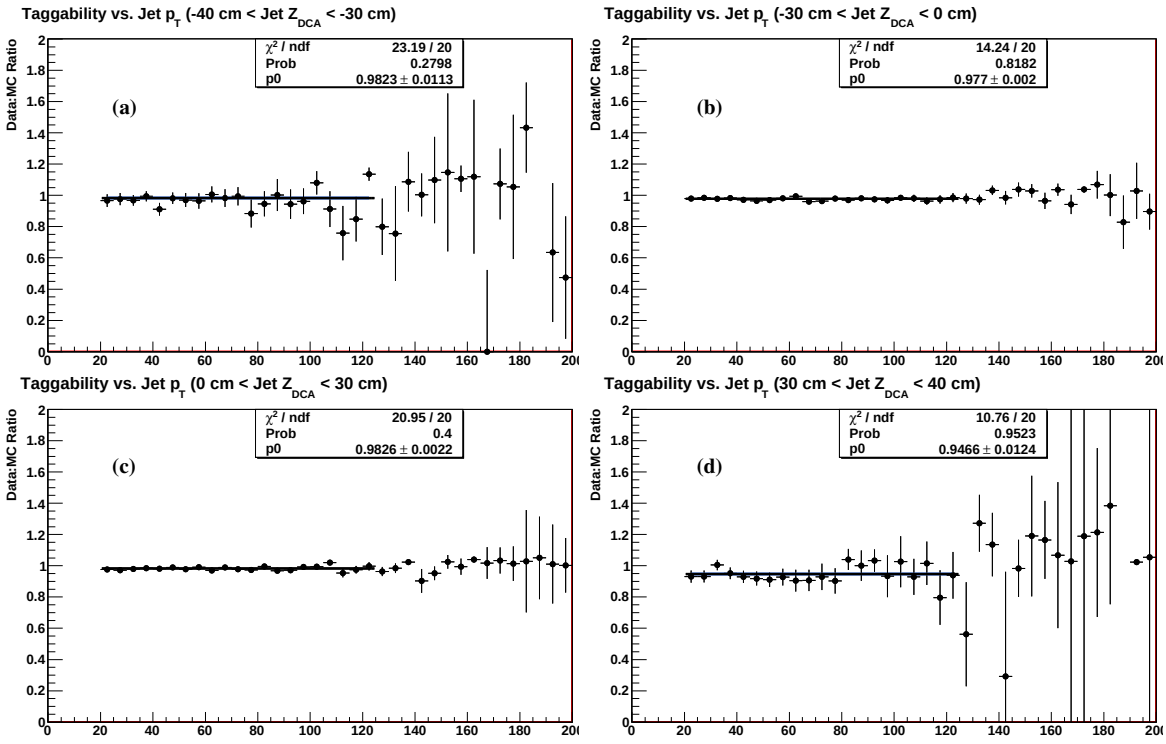

Figure 4.20: *p20 Jet taggability scale factors for muon channel versus jet transverse momentum measured from the data and simulated samples of the RunIIb analysis. The parametrizations of (a),(b),(c) and (d) apply to the* $-40 < z_{vtx} < -30$ *cm,* $-30 < z_{vtx} < 0$ *cm bin,* $0 < z_{vtx} < 30$ *cm, and* $30 < z_{vtx} < 40$ *cm bins, respectively. The black line represents the nominal fit and the blue band represents the* $\pm 1\sigma$ *uncertainty band on the fit.*

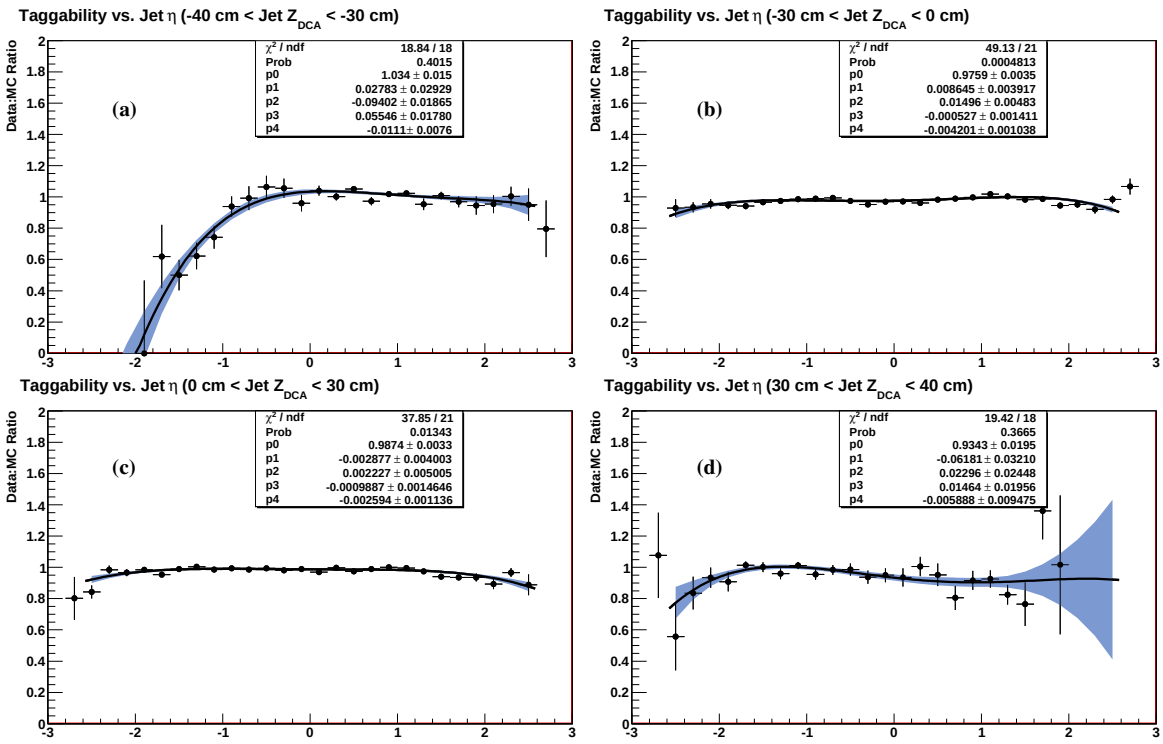

Figure 4.21: *p20 Jet taggability scale factors for muon channel versus eta measured from the data and simulated samples of the RunIIb analysis. The parametrizations of (a),(b),(c) and (d) apply to the* $-40 < z_{vtx} < -30$ *cm,* $-30 < z_{vtx} < 0$ *cm bin,* $0 < z_{vtx} < 30$ *cm, and* $30 < z_{vtx} < 40$ *cm bins, respectively. The black line represents the nominal fit and the blue band represents the* $\pm 1\sigma$ *uncertainty band on the fit.*

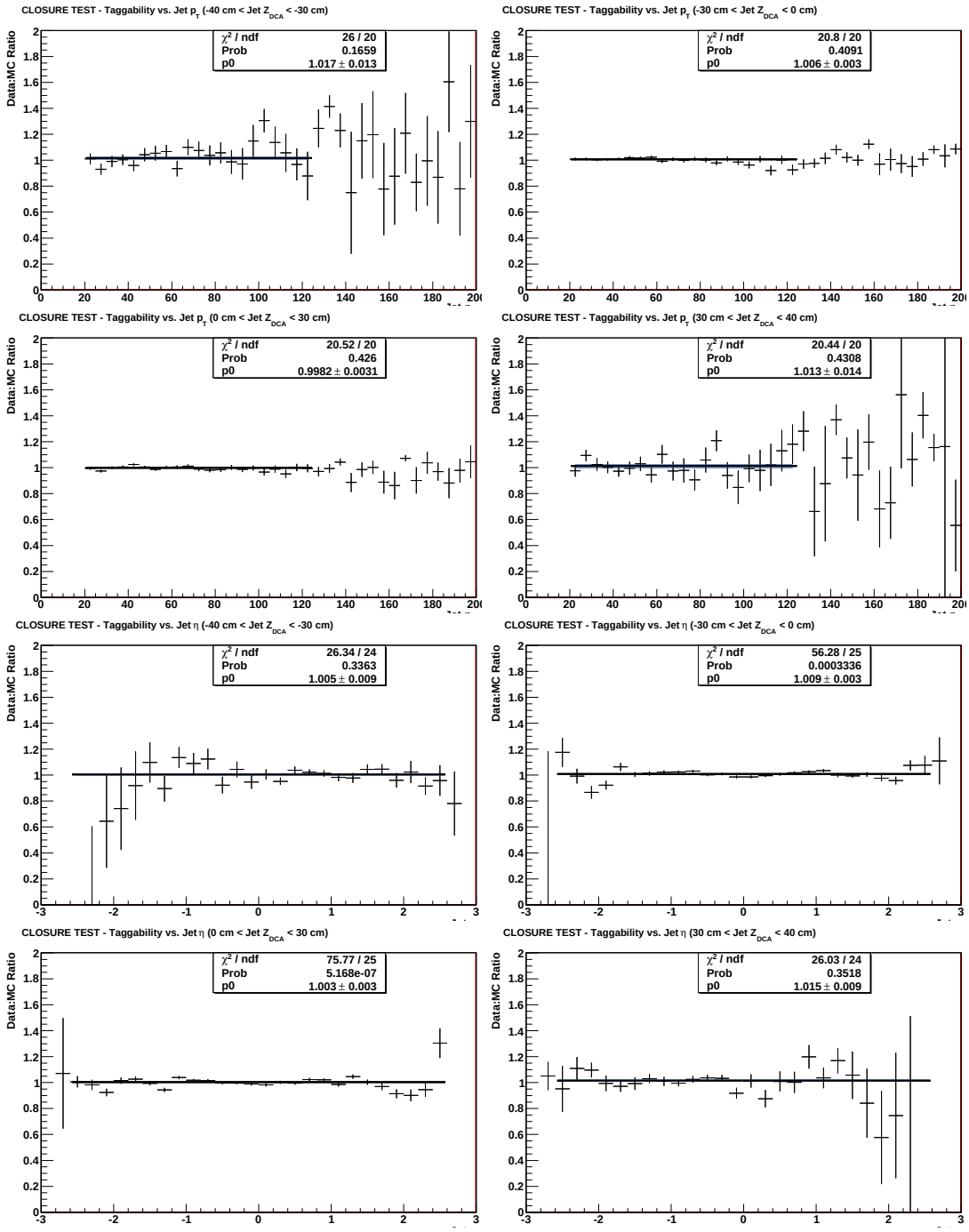

Figure 4.22: *Taggability closure test results, for p17 (top row: vs. p_T for the $-40 < z_{vtx} < -30$ cm, $-30 < z_{vtx} < 0$ cm bins; second row: vs. p_T for the $0 < z_{vtx} < 30$ cm, and $30 < z_{vtx} < 40$ cm bins; third row: vs. η for the $-40 < z_{vtx} < -30$ cm, $-30 < z_{vtx} < 0$ cm bins; fourth row: vs. η for the $0 < z_{vtx} < 30$ cm, and $30 < z_{vtx} < 40$ cm bins.) The black line represents the fit to a constant and the blue band represents the $\pm 1\sigma$ uncertainty band on the fit.*

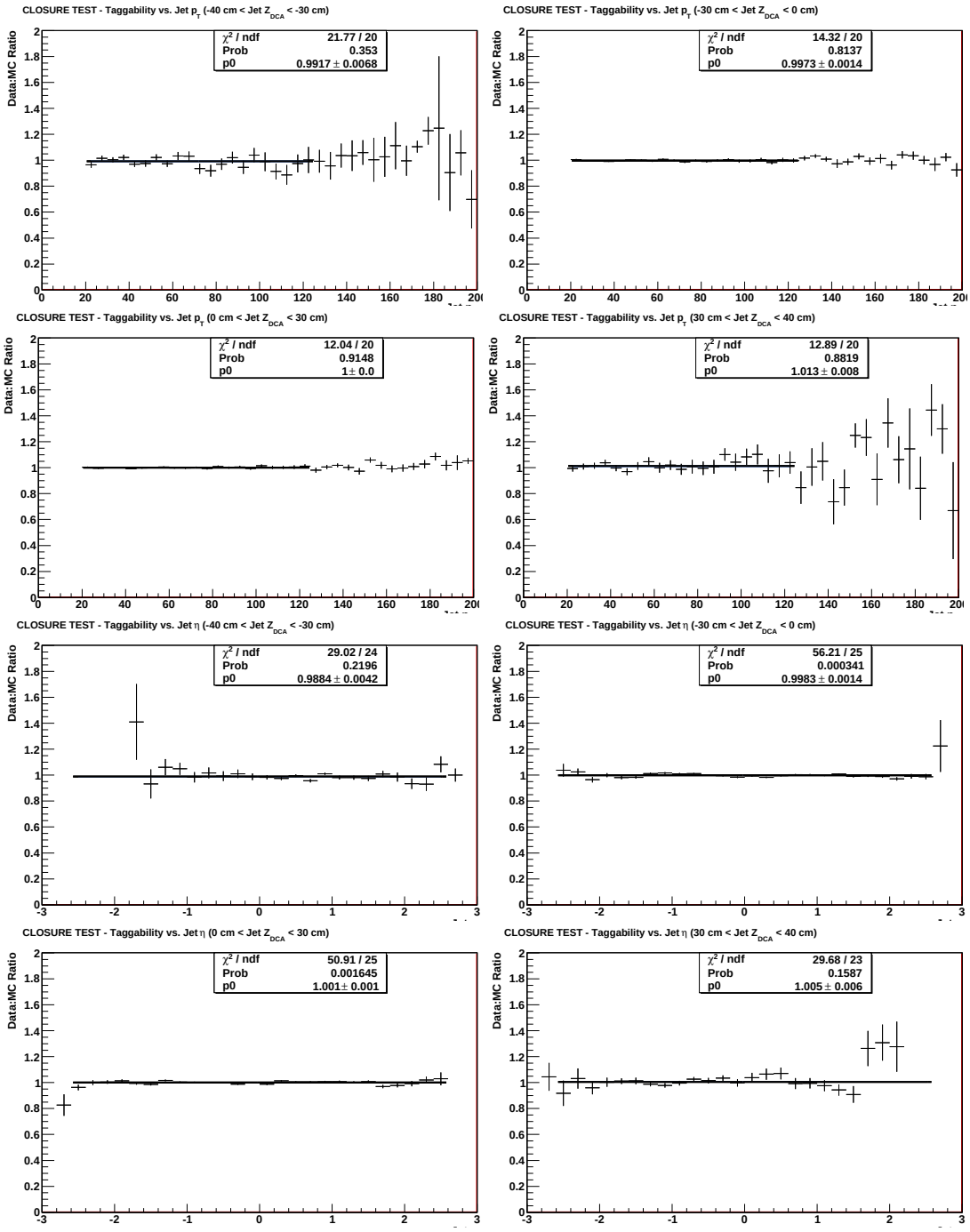

Figure 4.23: *Taggability closure test results, for p20 (top row: vs. p_T for the $-40 < z_{vtx} < -30$ cm, $-30 < z_{vtx} < 0$ cm bins; second row: vs. p_T for the $0 < z_{vtx} < 30$ cm, and $30 < z_{vtx} < 40$ cm bins; third row: vs. η for the $-40 < z_{vtx} < -30$ cm, $-30 < z_{vtx} < 0$ cm bins; fourth row: vs. η for the $0 < z_{vtx} < 30$ cm, and $30 < z_{vtx} < 40$ cm bins.) The black line represents the fit to a constant and the blue band represents the $\pm 1\sigma$ uncertainty band on the fit.*

4.10.2 MC correction on b-tagging

To correct the tagging efficiency of the simulated events, data vs. MC scale factors are applied (These scale factors are provided by the b-ID group) which depend on the kinematics of the jets.

We apply these scale factors on tagged events as follows:
The scale factor weight for double tagged events, DT_{weight} is

$$DT_{weight} = SF_{j1} \times SF_{j2} \tag{4.11}$$

where SF_{j1} and SF_{j2} are the scale factors for the leading and second leading jet, respectively, parametrized in p_T, η and jet flavor of the jet.

The scale factor weight (ST_{weight}) on the single tagged events is determined by:

$$ST_{weight} = ST_{weight}^{STevent} + ST_{weight}^{DTevent} \tag{4.12}$$

where $ST_{weight}^{STevent}$ is the event weight calculated for the single exclusively tagged event, and $ST_{weight}^{DTevent}$ is the contribution from double tagged events that can migrate (due to the scale factor) into the single tagged sample. The single tagged event weights are calculated as

$$ST_{weight}^{STevent} = SF_j \tag{4.13}$$

where SF_j is the scale factor for the tagged jet in the single tagged event. The scale factor for the other jet to migrate below the operating point of double tagged sample is given by:

$$ST_{weight}^{DTevent} = (1 - SF_{\bar{j}}^{DT}) * SF_j. \tag{4.14}$$

where SF_j is the scale factor of the single tag operating point and $SF_{\bar{j}}^{DT}$ is the scale factor for the jet with the double tagged operating point. The migration from a double tagged event to a single tagged event will happen if one jet fails to be tagged, in which case a factor of $(1 - SF_{\bar{j}}^{DT})$ from the other jet will be applied. This parametrization is valid only for the case where the double tag operating point is looser than the single tag operating point (in this analysis, OldLoose for double tag and Tight for single tag).

The total b-tagging scale factors corresponds to the product of the b-ID scale factor and the taggability scale factors.

The systematic error on b-tagging is evaluated separately on the light flavor jet scale factor and the heavy flavor jet by varying the b-tagging scale factors by $\pm$ 1σ. On average, the systematic uncertainty on bID is $\sim 5\%$ per b-tagged jet.

4.10.3 b-tagged Event Distributions

Figures 4.24 - (e) (4.25 - (μ)) (RunIIa), 4.26 - (e) (4.27 - (μ)) (RunIIb) (a) and (b) show the p_T, η, H_T and dijet mass distributions of the b-tagged jets for the $W + 2$ jet events in the electron (muon) channel, which have exactly one Tight b-tagged jet. The observed agreement in both cases indicates that the simulation, which includes all the different Standard Model processes, describes the data well. The data are compared to the sum of the simulated standard model processes added to the multijet background. The QCD background is estimated using the standard matrix method, as for the pre-tag sample.

When requiring only one b-tagged jet, the background due to $W + 2$ light quark jets, top and QCD processes is still larger than processes which have not yet been measured and which can be studied with the upgraded Tevatron: WZ, with $Z \rightarrow b\bar{b}$, and Higgs production. To improve the signal versus background ratio, we study also the events in which a second jet is b-tagged.

Figures 4.28(4.29) (RunIIa), 4.30(4.31) (RunIIb) (a) show the p_T distribution of all the double b-tagged jets from the $W + 2$ b-tagged jet events, compared to the simulated expectation.

The power of the $b-$tagger used can be notices in that the expectation from single top processes is of the same order as the Wjj processes. The Wjj process has a cross section that is 6000 times higher than that of the single top one; when starting from the pre-tag sample, the associated production of the W and light jets is reduced by a factor of 1000.
In total, approximately 19 signal events are expected after combining all channels for

$M_H = 115$ GeV.

In the $W + 2b$ jet sample, the number of observed events in the electron and muon channels are well reproduced by the sum of the Standard Model backgrounds as detailed in Table 4.19 (RunIIa), 4.21 (RunIIb). The event yields for the $W + 3$ jet events are also given in Table 4.20 (RunIIa), 4.22 (RunIIb). Our next step is to increase the discriminating

	$W(e)$ + 2 jets (1 b jet)	$W(e)$+ 2 jets (2 b jets)	$W(\mu)$+ 2 jets (1 b jet)	$W(\mu)$+ 2 jets (2 b jets)
WH	1.25 ± 0.14	0.73 ± 0.08	1.02 ± 0.11	0.62 ± 0.07
WW	13.35 ± 1.47	0.36 ± 0.12	10.50 ± 1.16	0.21 ± 0.22
WZ	4.79 ± 0.53	2.17 ± 0.24	3.86 ± 0.43	1.89 ± 0.21
ZZ	0.29 ± 0.07	0.07 ± 0.14	0.23 ± 0.06	0.11 ± 0.10
$Wb\bar{b}$	124.26 ± 24.85	33.59 ± 6.72	107.56 ± 21.51	29.93 ± 5.99
$Zb\bar{b}$	5.38 ± 1.08	0.63 ± 0.14	3.26 ± 0.65	0.58 ± 0.13
$Wc\bar{c}$	68.07 ± 13.61	5.31 ± 1.06	54.81 ± 10.96	4.76 ± 0.95
$Zc\bar{c}$	2.07 ± 0.42	0.04 ± 0.25	1.38 ± 0.28	0.06 ± 0.32
$t\bar{t}$	51.97 ± 7.28	20.53 ± 2.87	32.97 ± 4.62	13.37 ± 1.87
Single top	26.39 ± 3.43	6.65 ± 0.86	22.54 ± 2.93	5.50 ± 0.72
QCD Multijet	76.76 ± 6.91	5.07 ± 0.47	38.55 ± 3.47	1.74 ± 0.20
W+ jets (light)	141.73 ± 12.76	2.11 ± 0.19	122.56 ± 11.03	4.04 ± 0.38
Z+ jets (light)	4.58 ± 0.42	0.19 ± 0.28	2.83 ± 0.26	0.00 ± 0.00
Total expectation	519.62 ± 32.90	76.73 ± 7.46	401.05 ± 27.37	62.19 ± 6.41
Observed Events	479	74	400	62

Table 4.19: *Summary table for the $W(e)$ and $W(\mu)$ + 2 jet final state in RunIIa. Observed events in data are compared to the expected number of W+ 2 jet after one tight b-tag, and after 2 loose b-tag; e channel: first 2 columns, μ channel: last 2 columns. Expectation originates from the simulation of WH (with $m_H = 115$ GeV), dibosons (WW, WZ, ZZ, labeled WZ in the table), $Wb\bar{b}$ production, top production ($t\bar{t}$ and single-top), QCD multijet background and "W+ jet" production, which contains light and c quarks. All Z processes are included in the corresponding W categories.*

power of this analysis via separating the signal from the background contributions.

Figure 4.24: *Kinematic distribution on 1 b-tag sample for Electron (CC+EC) $W + 2$ jet event sample in RunIIa data set.*

Figure 4.25: *Kinematic distribution on 1 b-tag sample for Muon $W + 2$ jet event sample in RunIIa data set. The legend of the plots can be found in page. 84.*

Figure 4.26: *Kinematic distribution on 1 b-tag sample for Electron (CC+EC) $W + 2$ jet event sample in RunIIb data set. The legend of the plots can be found in page. 84.*

Figure 4.27: *Kinematic distribution on 1 b-tag sample for Muon $W + 2$ jet event sample in RunIIb data set. The legend of the plots can be found in page. 84.*

Figure 4.28: *Kinematic distribution on 2 b-tag sample for Electron (CC+EC) $W + 2$ jet event sample in RunIIa data set. The legend of the plots can be found in page. 84.*

Figure 4.29: *Kinematic distribution on 2 b-tag sample for Muon $W + 2$ jet event sample in RunIIa data set. The legend of the plots can be found in page. 84.*

Figure 4.30: *Kinematic distribution on 2 b-tag sample for Electron (CC+EC) $W + 2$ jet event sample in RunIIb data set. The legend of the plots can be found in page. 84.*

Figure 4.31: *Kinematic distribution on 2 b-tag sample for Muon $W + 2$ jet event sample in RunIIb data set. The legend of the plots can be found in page. 84.*

	$W(e)$ + 3 jets (1 b jet)	$W(e)$+ 3 jets (2 b jets)	$W(\mu)$+ 3 jets (1 b jet)	$W(\mu)$+ 3 jets (2 b jets)
WH	0.29 ± 0.03	0.09 ± 0.03	0.24 ± 0.03	0.09 ± 0.04
WW	2.91 ± 0.32	0.11 ± 0.21	3.16 ± 0.35	0.07 ± 0.41
WZ	1.18 ± 0.14	0.37 ± 0.11	0.98 ± 0.12	0.26 ± 0.10
ZZ	0.13 ± 0.10	0.02 ± 0.32	0.06 ± 0.11	0.02 ± 0.23
$Wb\bar{b}$	28.47 ± 5.69	4.69 ± 0.94	26.55 ± 5.31	3.58 ± 0.72
$Zb\bar{b}$	1.90 ± 0.38	0.26 ± 0.10	1.00 ± 0.20	0.21 ± 0.10
$Wc\bar{c}$	17.65 ± 3.53	1.42 ± 0.28	15.62 ± 3.12	1.07 ± 0.23
$Zc\bar{c}$	0.84 ± 0.18	0.01 ± 0.44	0.68 ± 0.17	0.00 ± 0.00
$t\bar{t}$	82.52 ± 11.55	22.07 ± 3.09	63.09 ± 8.83	16.97 ± 2.38
Single top	7.27 ± 0.95	1.60 ± 0.21	6.34 ± 0.82	1.40 ± 0.18
QCD Multijet	30.13 ± 2.71	1.70 ± 0.22	11.28 ± 1.02	0.63 ± 0.23
W+ jets (light)	22.29 ± 2.01	0.33 ± 0.03	21.32 ± 1.92	0.95 ± 0.09
Z+ jets (light)	1.14 ± 0.13	0.03 ± 0.44	0.78 ± 0.12	0.01 ± 0.63
Total expectation	196.43 ± 13.81	32.60 ± 3.26	150.85 ± 11.02	25.17 ± 2.52
Observed Events	178	32	137	25

Table 4.20: *Summary table for the $W(e)$ and $W(\mu)$ + 3 jet final state for RunIIa data set (for the reference). See caption of Table 4.19*

	$W(e)$ + 2 jets (1 b jet)	$W(e)$+ 2 jets (2 b jets)	$W(\mu)$+ 2 jets (1 b jet)	$W(\mu)$+ 2 jets (2 b jets)
WH	4.21 ± 0.46	2.83 ± 0.31	3.23 ± 0.36	2.32 ± 0.26
WW	48.56 ± 5.34	1.77 ± 0.26	41.76 ± 4.59	1.73 ± 0.29
WZ	15.30 ± 1.68	7.47 ± 0.82	12.67 ± 1.39	6.24 ± 0.69
ZZ	0.56 ± 0.11	0.25 ± 0.17	0.72 ± 0.11	0.22 ± 0.14
$Wb\bar{b}$	385.74 ± 77.15	117.8 ± 23.56	348.44 ± 69.69	101.54 ± 20.31
$Zb\bar{b}$	10.09 ± 2.02	2.13 ± 0.43	11.89 ± 2.38	3.05 ± 0.61
$Wc\bar{c}$	258.79 ± 51.76	22.59 ± 4.52	207 ± 41.40	22.68 ± 4.54
$Zc\bar{c}$	5.33 ± 1.07	0.83 ± 0.23	7.11 ± 1.42	0.65 ± 0.22
$t\bar{t}$	196.71 ± 27.54	84.47 ± 11.83	135.36 ± 18.95	58.69 ± 8.22
Single top	82.81 ± 10.77	25.35 ± 3.30	71.32 ± 9.27	20.76 ± 2.70
QCD Multijet	397.26 ± 35.75	39.65 ± 3.57	149.89 ± 13.49	10.00 ± 0.90
W+ jets (light)	535.17 ± 48.17	25.36 ± 2.28	457.24 ± 41.15	24.67 ± 2.22
Z+ jets (light)	15.50 ± 1.40	0.65 ± 0.44	10.42 ± 0.94	0.45 ± 0.62
Total expectation	1951.82 ± 114.69	328.31 ± 27.30	1453.81 ± 94.49	250.68 ± 22.68
Observed Events	2002	325	1435	248

Table 4.21: *Summary table for the $W(e)$ and $W(\mu)$ + 2 jet final state in RunIIb (the corresponding tables for RunIIa are given in Table 4.19). Observed events in data are compared to the expected number of W+ 2 jet after one tight b-tag, and after 2 loose b-tag; e channel: first 2 columns, μ channel: last 2 columns. Expectation originates from the simulation of WH (with $m_H = 115$ GeV), dibosons (WW, WZ, ZZ, labeled WZ in the table), $Wb\bar{b}$ production, top production ($t\bar{t}$ and single-top), QCD multijet background and "W+ jet" production, which contains light and c quarks. All Z processes are fully simulated, and included in the corresponding W categories. The processes $W(Z)b\bar{b}$ and WH are counted separately.*

	$W(e)$ + 3 jets (1 b jet)	$W(e)$+ 3 jets (2 b jets)	$W(\mu)$+ 3 jets (1 b jet)	$W(\mu)$+ 3 jets (2 b jets)
WH	0.86 ± 0.10	0.37 ± 0.05	0.69 ± 0.08	0.30 ± 0.05
WW	10.82 ± 1.19	0.00 ± 0.00	7.19 ± 0.80	0.05 ± 0.51
WZ	4.25 ± 0.47	0.95 ± 0.16	2.84 ± 0.32	0.67 ± 0.16
ZZ	0.19 ± 0.17	0.05 ± 0.35	0.18 ± 0.17	0.05 ± 0.37
$Wb\bar{b}$	78.68 ± 15.74	14.32 ± 2.86	72.93 ± 14.59	11.72 ± 2.34
$Zb\bar{b}$	2.81 ± 0.56	0.37 ± 0.15	2.74 ± 0.55	0.47 ± 0.15
$Wc\bar{c}$	64.89 ± 12.98	4.38 ± 0.88	39.68 ± 7.94	4.89 ± 0.98
$Zc\bar{c}$	1.80 ± 0.37	0.01 ± 0.50	1.79 ± 0.37	0.35 ± 0.31
$t\bar{t}$	274.84 ± 38.48	77.33 ± 10.83	212.20 ± 29.71	59.69 ± 8.36
Single top	20.93 ± 2.72	5.45 ± 0.71	19.04 ± 2.48	4.57 ± 0.59
QCD Multijet	109.62 ± 9.87	7.36 ± 0.67	34.52 ± 3.11	2.99 ± 0.28
W+ jets (light)	88.56 ± 7.97	7.18 ± 0.66	74.49 ± 6.70	3.55 ± 0.35
Z+ jets (light)	0.29 ± 0.36	0.00 ± 0.00	1.46 ± 0.29	0.00 ± 0.00
Total expectation	657.70 ± 45.48	117.41 ± 11.30	469.05 ± 34.94	89.01 ± 8.77
Observed Events	671	125	477	119

Table 4.22: *Summary table for the $W(e)$ and $W(\mu)$ + 3 jet final state for RunIIb. (the corresponding tables for RunIIa are given in Table 4.20). See caption of Table 4.21*

CHAPTER 5

Multivariate Analysis Techniques: Decision Trees

A multivariate analysis technique (MVA), namely the neural network, has already been used in a previous published results for the WH analysis. With the amount of data available for this version of the analysis, decision was taken to use the another MVA technique, the Boosted Decision Trees technique.

A *decision tree* is a multivariate technique which can be used to classify observations [97, 98]. In this work, the term decision trees refers to what is more specifically known as *classification trees*, and this separation technique is used to separate the Higgs signal from the vast amount of background physical processes [99].

In this chapter, we shall give an overview of decision trees and motivates behind why and how they can be used in experimental particle physics.

5.1 Why Use Decision Trees

5.1.1 Standard Decision Trees

A decision tree is a tree in which each internal node represents a choice between a number of alternatives, and each terminal node is marked by a classification. Decision trees are potentially powerful predictors and provide an explicit concept description for a dataset. In practice, decision tree learning is one of the most popular technique in classification because it is fast and produce models with reasonable performance.

Associated Higgs production is a very rare process. After applying the event selection described in the previous chapter, the signal to background ratio is still very high and the

signal excess still smaller than the uncertainty on the background prediction. In this case an observation of the associated Higgs production, or an inference of an evidence of such a process would require a more efficient separation of signal from background.

Applying more cuts to the discriminating variables to enhance the signal to background ratio will cause some of the very rare signal to be cut from the data sample under consideration, with every cut we apply to the data sample.

In the MVA technique, the separation power of several variables $\vec{x}$ are combined into a single discriminate $D(\vec{x})$. With more separating variables available to the discriminate, $D(\vec{x})$, a better separation between the signal and background can be achieved. The signal significance can then be evaluated by either applying a selection criterion on $D(\vec{x})$, or, by integrating over the full discriminant distribution.

Multivariate analysis techniques, such as Matrix Elements has been used before (WH analysis with 1.2 fb^{-1} of data) but due to the larger amount of data available now for this analysis and the lack of huge, dedicated, computer resources for such method, ME has become a less appealing approach for the sought for separation.

Neural Network (NN) is also one of the MVA techniques that has been used for the WH analysis, but, again, NN performance becomes more and more unstable with more data available to the analysis. Also, with every NN can work with approximately 7-10 separating variables, and the more variables added to the Network, the more degraded the performance becomes.

In this work, we have used the boosted decision trees as a multivariate technique to find a discriminant $D(\vec{x})$ that monotonically increases with the increase in the probability of an event being a signal.

5.2 Decision Trees

5.2.1 Introduction

With the accumulation of data in many fields of science, data mining and pattern recognition has evolved to help in analyzing these vast amount of data. Much of the work done in this field was made by Breiman *et al.* who developed the *Classification and Regression Trees* [97]. Several methods was invented to improve the performance of the classifiers algorithms via creating several sets (ensembles, or, forests) of decision trees in the 1990s. Boosting was among these algorithms, and it is the one used in our analysis.

Decision trees are used in many areas of science, technology, medicine and financial analysis. In experimental particle physics, decision trees have rarely been used until recently, with the new generation of colliders pouring more and more data to be analyzed, mostly in search for very rare and hard to observe signals. The two main applications in Experimental particle physics are the particle identification (PID) and the separation of a physical process signal from a huge and vast background that is almost identical to the signal being sought for. Examples for a PID application is the identification of a jet being originating from a $b-$ jet or from a hadronic decay of a τ lepton from ordinary QCD jets. Boosted Decision Trees (BDT) are now used by both the CDF and the DØ international groups at the Fermilab Tevatron in their search for rare physical processes, including the Higgs boson. The observation of Single-Top production at the DØ was done with the help of the BDT technique.

5.2.2 The Working of a Decision Tree

A two branches tree, is a tree in which each node, that is a forking point, can have up to two sub-nodes (daughter nodes.) The *root node*, the first node in the tree and is typically the identifier number 1 ($t = q$) in the tree. The two sub-nodes will be assigned identifiers IDs $2t$ and $2t + 1$ respectively. Each of these sub-nodes will have their own two sub-

nodes (sub-sub-nodes) if the sub-nodes are not terminal nodes, that is if they have their own daughter nodes. A sub-node that is not a terminal node (i.e. has no daughter nodes) is called an *internal node.* An example of such a tree is shown in Figure 5.1. Terminal nodes are called leaves. A decision tree can have $n-$leaves that can be used to classify the

Figure 5.1: *A tree with each of its nodes assigned an identifier number t.*

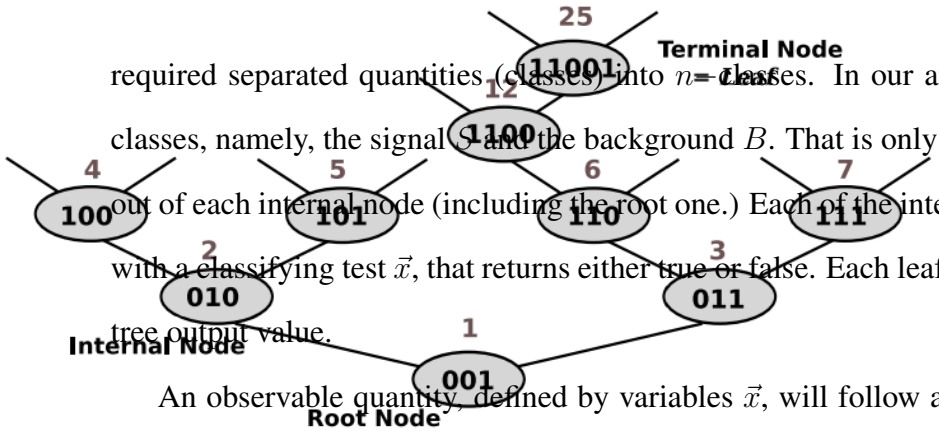

required separated quantities (classes) into $n-$classes. In our analysis, we only use two classes, namely, the signal S and the background B. That is only two branches are forking out of each internal node (including the root one.) Each of the internal nodes are associated with a classifying test $\vec{x}$, that returns either true or false. Each leaf has an assigned decision tree output value.

An observable quantity, defined by variables $\vec{x}$, will follow a certain path through the decision (classifying) tree depending on the output of the tests in each node. In the end, each observation will end up at a leaf and each leaf will have a classification number from the decision tree for this leaf. A simple decision tree is shown in Figure 5.2.

5.2.3 Advantages of using Decision Trees

The biggest advantage of using a decision tree against the cut-based analysis is that events which fail a certain individual criterion (cut) can be used again by the algorithm to apply

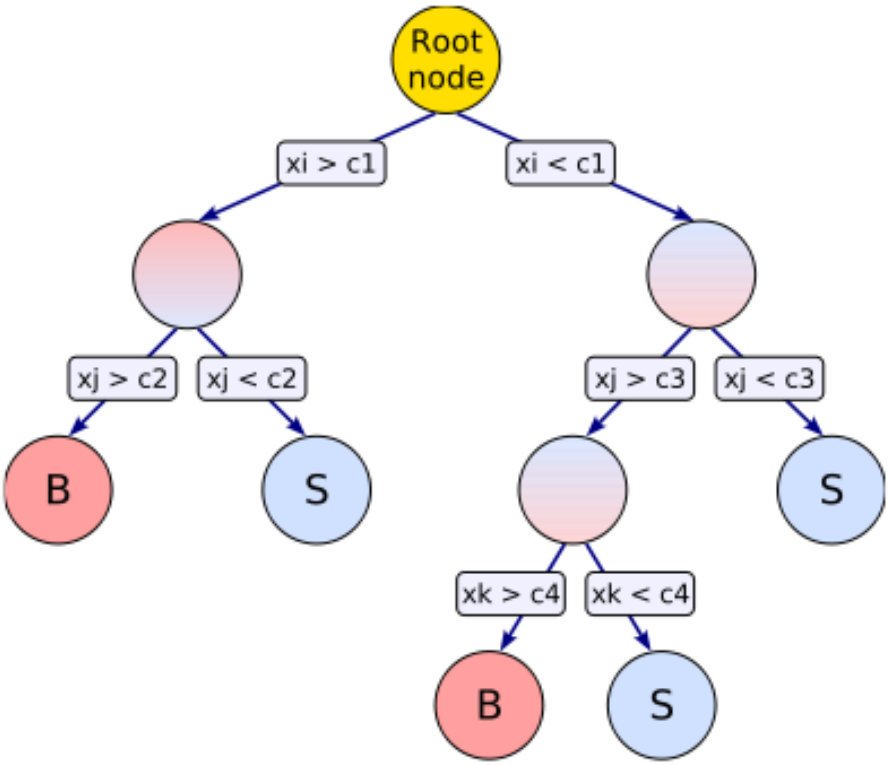

Figure 5.2: *A representation of a simple decision tree. Nodes are shown with their associated tests used as splitting criterion in blue. Green leaves are the terminal nodes with their purity values. All nodes should continue to be split to finally become leaves.*

certain other separation criteria, which might succeed in classifying this event with these other criteria.

Compared with other MVA techniques, Decision Trees are:

- Decision Trees are easy structure to read. This makes it easier to understand the internal working of the algorithm and question why a certain event (or a subset of events) have been classified as signal (background)
- The learning process is fast compared with other MVA techniques (neural networks, for example)
- Use of discrete input variables is done directly, no internal calculations are needed
- Unlike the neural network, for instance, decision trees can use more and more vari-

ables effectively, while adding more variables to neural networks may lead to a lower performance for its output(s). Actually adding more variables to a neural network may cause more "noise" in its output which degrades its ability to be used as a classifier.

5.2.4 Limitations of Decision Trees

Limitations to the performance of decision trees include

- Instability of the tree structure with the learning sample composition
- lower optimum performance on non-linear data
- The nature of the output. each leaf has its own purity number.
- Tuning the variables used in the training process might be a hard task at first.

These limitations can be overcome if one creates many different trees and takes the average of their outputs. This will result in a smooth combined discriminant made from all these different trees. With this method one will lose the easiness of knowing why events have been classified the way that had. It also may affect the fastness of the learning and the separation process, but compared with neural networks, for example, decision trees' performance is still superior.

5.3 Decision Trees Training Process

Decision trees *training* process, also called *learning, building, growing* process starts with a training sample $\mathcal{L}$ with N known signal and background events. Each event $\jmath$ has a weight w_j and a list of variables $\vec{x}$ and label $y_j \in S, B$. As a result we can write this as $\mathcal{L} = (w_1, \vec{x_1}, y_1), \cdots, (w_N, \vec{x_N}, y_N)$.

The number of weighted signals events, *s*, is

$$s = \sum_{\mathcal{L}} w_j \times I(y_j = S) \tag{5.1}$$

and the number of weighted background events, *b*, is

$$b = \sum_{\mathcal{L}} w_j \times I(y_j = B) \tag{5.2}$$

where *I* (condition) is 1 is the condition is true, and is 0 if the condition is false. s and b correspond to the expected number of signal and background events, respectively.

The following list [99] outlines the steps required to create a decision tree from $\mathcal{L}$

1. Normalize the learning sample such that the weighted sums of signal and background become the same ($s = b$):

$$\sum_{\mathcal{L}} w_j \times I(y_j = S) = \sum_{\mathcal{L}} w_j \times I(y_j = B) \tag{5.3}$$

   This step is an optional step.

2. Create a root node with all events in the learning (training) sample: $\mathcal{L}_\infty = \mathcal{L}$. The root node has an index t.

3. The node becomes a leaf if any of the stopping conditions is met. The algorithm gets aborted.

4. $\forall$ variable, $\vec{x}$, we find the splitting value that gives the best signal-to-background separation possible. If no split is found that improves the separation, the node turns into a leaf.

5. The variable and split value giving the best separation are selected, and the events $\mathcal{L}_\sqcup$ in the node are divided into two sub-samples $\mathcal{L}_{\in\sqcup}$ and $\mathcal{L}_{\in\sqcup+\infty}$ depending on whether they pass or fail the splitting criterion.

6. Apply the algorithm recursively from Step 3 until all remaining nodes have been turned into leaves.

Now each leaf is assigned an output value, usually the signal purity, p_l, defined by

$$p_l = \frac{s_l}{s_l + b_l} \tag{5.4}$$

s_l (b_l) is the weighted sum of the signal (background events which reach the leaf. A leaf l is deemed a signal or background depending on whether the purity p_t is greater or smaller than a parameter called the purity limit, p_{limit}.

Different impurity measures are defined in literature, The two most commonly used are the Gini Index [100] and the cross Entropy Index [97] defined by

$$\text{Gini Index:} \frac{sb}{s+b} \tag{5.5}$$

and

$$\text{Cross Entropy Index:} -s\log\frac{s}{s+b} - b\log\frac{b}{s+b} \tag{5.6}$$

Other indexes have been developed and used as impurity measures.

5.4 Forests of Decision Trees

A decision tree is rarely powerful enough to achieve a good separation between signal and background. The tree produces a set of signal-dominated regions. These regions, however, often fail to capture a non-linear structure of data. The mediocre predictive power of single decision tree can be greatly enhanced by combining classifiers - few algorithms are used to grow decision trees and combine them into a stronger classifier have been created. In this section We shall discuss to of them, Bagging and Boosting. Both methods work by training many classifiers, that is, decision trees, on variants of the original training data set.

5.4.1 Boosting

A boosting algorithm enhances weights of misclassified events and reduces weights of correctly classified events and trains a new classifier on the reweighted sample. The output of the new classifier is then used to re-evaluate fractions of correctly classified and misclassified events and update the event weights accordingly. After training is complete, events

of this approach, has been shown to produce a high-quality robust training mechanism. Application of "Adaptive Boosting" to HEP has been explored in [100, 101].

5.4.2 Bagging

Bagging algorithm [102] do not weight events. Instead, they train new classifiers on bootstrap replicas of the training set. Each bootstrap replica [103] is obtained by sampling with replacement from the original training set, with the size if each replica equal to that of the original set. After training is complete, events are classified by the majority vote of the trained classifier. For successful application of the bagging algorithm, the underlying classifier must be sensitive to small changes in the training data. Otherwise all trained classifiers will be similar, and the performance of the single classifier will not be improved. This condition is satisfied by the decision tree with fine terminal nodes. Because of the small node size, each decision tree is significantly over-trained; if the tree used just by itself, its predictive power on a test data set would be quite poor. However, because the final decision is made by the majority vote of all the trees, the algorithm delivers a high predictive power.

Various kinds of boosting and bagging algorithms have been compared in the statistics literature. Neither of these two approaches has a clear advantage over the other. On average, boosting seems to provide a better predictive power. Bagging tends to perform better in the presence of routine with respect to the chosen figure of merit.

5.5 Improving Sensitivity With Random Forests

Sensitivity improvement studies have been conducted in the WH analysis and the Random Forest technique has been used in this analysis. Different software provide this technique, among them are the `StatPatternRecognition` or *SPR* [101, 104] and the `Toolkit for Multivariate Data Analysis` or *TMVA* [105]. The Random Forest technique has been successfully used for the observation of the first evidence of Diboson pro-

duction (WW, WZ, ZZ) in the $l\nu jj$ final state at the DØ [106]. It has also been successfully used in the first observation of Single-Top production [107]

5.6 Selection of Input Variables and Training

Variable Selection

The previous analysis in this channel used a seven-variable neural network trained against Wbb and signal. In the Random Forest we use twenty variables, including all seven neural network training variables. The full list of variables is:

- p_{T}, leading jet
- p_{T}, sub-leading jet
- E_j Energy of the sub-leading jet
- $\Delta R(j_1, j_2)$, ΔR between jets
- $\Delta\phi(j_1, j_2)$, $\Delta\varphi$ between jets
- $\Delta\varphi(j_1, l)$, $\Delta\varphi$ between lepton and leading jet
- p_{T}(dijet system), dijet invariant mass
- p_{T}(ℓ-$\not\!\!E_T$ system), p_T of W candidate.
- $\Delta\phi(\ell, j_1)$), $\Delta\varphi$ between lepton and leading jet.
- $\not\!\!E_T$, missing transverse energy.
- $\mathcal{A}$, Aplanarity.
- $\sqrt{\hat{s}}$, invariant mass of the neutrino-lepton-dijet system
- ΔR(dijet system,$\ell - \nu$ system)

- lepton-$\not\!\!E_T$ transverse mass
- H_{T},sum of the transverse momenta of all jets in the event
- H_{Z},sum of the z-momenta of all jets in the event
- $\cos\theta*$, cosine of angle between W candidate and beam direction in the zero-momentum frame [108]. Angle $\theta*$ is the angle between the u-quark and the W candidate in the zero-momentum frame.
- $\cos\chi$, spin correlation variables described in [108]. It is the cosine of the angle between the lepton and the rotated vectorial sum of $b-$quarks in the production plane. Angle χ is the angle between the rotated $b\bar{b}$ system in the production plane and the lepton in the W candidate rest frame

For both $\sqrt{\hat{s}}$ and $\Delta R(\ell - \not\!\!E_T)$ there are two inputs for each event, corresponding to the two solutions for the neutrino z-momentum $p_{\mathrm{Z}\nu}$, obtained by solving $p^2_{\mathrm{T}\ell}p^2_{\mathrm{Z}\nu} - p_{\mathrm{Z}\ell}(M^2_W + 2\left(p_{\mathrm{x}\ell}p_{\mathrm{x}\nu} + p_{\mathrm{y}\ell}p_{\mathrm{y}\nu}\right) + p^2_{\mathrm{T}\ell}p^2_{\mathrm{T}\nu} + p^2_{\mathrm{Z}\ell}p^2_{\mathrm{T}\nu} - \frac{1}{4}(M^2_W + 2\left(p_{\mathrm{x}\ell}p_{\mathrm{x}\nu} + p_{\mathrm{y}\ell}p_{\mathrm{y}\nu}\right)^2 = 0$. Adding the neural network output from the previous analysis as an additional input variable was also considered, but it was found that it did not improve the expected limit. The acoplanarity [109] reflects the isotropy of an event and its value ranges between 0 and 0.5. Large values correspond to spherical events; smaller values correspond to planar events. The $\cos\theta*$ and $\cos\chi$ are used to discriminate pairs of $b-$jets decaying from spin-0 or spin-1 particles. It provides discrimination between $Wb\bar{b}$ and WH processes. Both of these variables make use of the spin angular correlations observables of the particles in the final state.

Training

We train the RF separately for each mass point against all backgrounds except for QCD. We use odd-numbered events for training and even-numbered events (based on the MC event number) for testing. We also train separately on the electron and muon channels as well

as the single and double tag samples. In 2-jet events we train RunIIa and RunIIb events separately, but in the 3-jet analysis we combine them due to lower statistics. As the figure of merit (FOM) we use the Cross-Entropy, defined as $-p \ln p - (1-p)\ln(1-p)$, where p is the purity of the node, defined as the ratio of signal events to all events in the node. The three training parameters of interest are S, the maximum number of input variables per tree; n, the number of trees in the forest; and l, the minimum leaf size. The most important variable in Random Forests is typically l.

To determine the optimal training parameters for n and l we use the cross-validation technique. Cross-validation splits the training sample into N equal pieces. The first piece is used for validation while the others are used for training. The process repeats with the second piece used for validation and the others for training. This procedure is repeated for the total of N pieces. The final output is then taken as the average over all iterations. We choose the optimal parameter by optimizing the FOM. For double tag events l is typically around 150; in single tag events it is between 300 and 400 in the 2jet case. To determine the optimal number of trees we follow the same procedure as Ref. [106], using 60% of events (even-numbered) for training and 40% for testing. The final result is relatively insensitive to the choice of S. For this analysis, we choose $S = 13$. Table 5.1 lists the values of N and l for each sample.

Re-binning

The raw RF output has no protection against producing bins with insufficient statistics to properly evaluate a limit. In order to ensure that each bin in the final discriminant used to set our limits can be well described by our background models, we produce 1,000 initial bins of the RF output and then re-bin to 24 bins in such a way that each bin contains a statistically significant estimate of the data.

The current re-binning algorithm combines bins from the highest RF output down until

Sample	Single tag		Double tag	
	N	l	N	l
Single tag				
RunIIa ele 2-jet	70	1000	100	300
RunIIa mu 2-jet	70	500	200	300
RunIIb ele 2-jet	50	400	50	150
RunIIb mu 2-jet	50	300	50	150
RunIIa+RunIIb ele 3-jet	70	1500	70	850
RunIIa+RunIIb mu 3-jet	70	1500	70	750

Table 5.1: Number of trees N and minimum leaf size l for the RF training for each channel.

these conditions are satisfied:

$$\begin{aligned} \mu_B &> 0.01 \\ \mu_{S+B} &> 0.1 \\ \sigma_B/\mu_B &< 0.28 \\ \sigma_{S+B}/\mu_{S+B} &< 0.2 \end{aligned} \tag{5.7}$$

where μ_B (μ_{S+B}) is the total expected background (signal + background) yield and σ_B (σ_{S+B}) is the statistical uncertainty of that background (signal + background) expectation, calculated as $\sqrt{\Sigma w_i^2}$ over the weights, w_i, for contributing events. After the highest bin is calculated in this manner, the remaining bins in the original RF output distribution are divided equally as a function of RF output into the other 23 bins of the final discriminant.

The value of$\sigma_B/\mu_B(\sigma_{S+B}/\mu_{S+B})$ in Equation 5.7 can be understood as representing the inverse of the statistical significance of the background (signal plus background) away from zero, in standard deviations. The choice of μ_B and μ_{S+B} conditions in equation 5.7 are made to ensure that a single high statistics background sample does not dominate the choice of binning by giving a high signal-to-background ratio while maintaining a reasonable statistical understanding of the background. Our choice of re-binning parameters

introduces no bias in the final limit as shown in Figure 5.3.

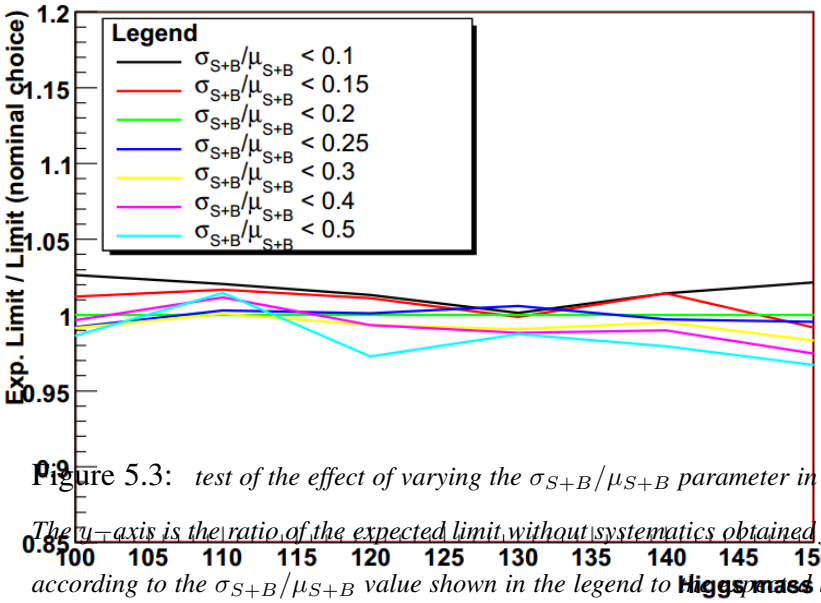

Figure 5.3: *test of the effect of varying the σ_{S+B}/μ_{S+B} parameter in the RF re-binning vs Higgs mass. The $y-$axis is the ratio of the expected limit without systematics obtained from an RF distribution re-binned according to the σ_{S+B}/μ_{S+B} value shown in the legend to the expected limit obtained from re-binning the RF distribution using the nominal σ_{S+B}/μ_{S+B} choice of* 0.2.

5.6.1 Performance

Figures 5.4 through 5.11 show the RF output for each different output channel. We find an improvement of between 7 and 13% in the expected limit relative to the previous NN result. Figure 5.12 shows the improvement in the expected limit.

(a) Run IIa **(b)**

(c) **(d)**

Figure 5.4: *Distributions for the $W+2$* **jet events (top: e-channel, bottom: μ-channel, RunIIa data) pretag level**. *The data are compared to $Wb\bar{b}$, $t\bar{t}$, W+jets and other smaller expectations. The simulated processes are normalized to the integrated luminosity of the data sample using the expected cross sections (absolute normalization) except for the $W+2$ jets sample which is normalized to data on the "pre-tag sample", taking into account all the other backgrounds. a,b) Random Forest (RF) trained on ST,DT for $W+2$ jets events in the electron channel, pretag level; c,d) RF trained on ST,DT for $W+2$ jets events in the muon channel, pretag level. The legend of the plots can be found in page. 84.*

(a) Run IIb **(b)**

(c) **(d)**

Figure 5.5: *Distributions for the $W+2$* **jet events (top: e-channel, bottom: μ-channel, RunIIb data) pretag level**. *The data are compared to $Wb\bar{b}$, $t\bar{t}$, W+jets and other smaller expectations. The simulated processes are normalized to the integrated luminosity of the data sample using the expected cross sections (absolute normalization) except for the $W+2$ jets sample which is normalized to data on the "pre-tag sample", taking into account all the other backgrounds. a,b) Random Forest (RF) trained on ST,DT for $W+2$ jets events in the electron channel, pretag level; c,d) RF trained on ST,DT for $W+2$ jets events in the muon channel, pretag level. The legend of the plots can be found in page. 84.*

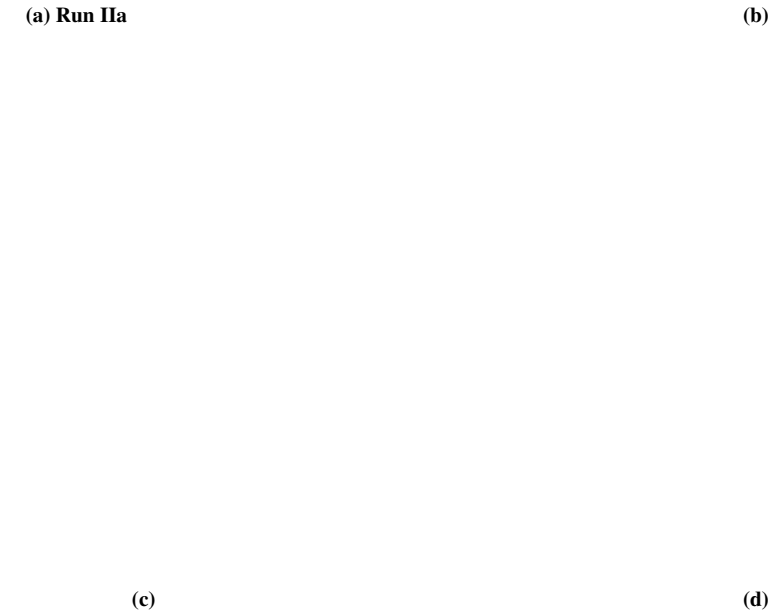

Figure 5.6: *Distributions for the $W+2$* **jets events (top: e-channel, bottom: μ-channel, RunIIa data) when one or two jets are b-tagged**. *The data are compared to $Wb\bar{b}$, $t\bar{t}$, W+jets and other smaller expectations. The simulated processes are normalized to the integrated luminosity of the data sample using the expected cross sections (absolute normalization) except for the $W+2$ jets sample which is normalized to data on the "pre-tag sample", taking into account all the other backgrounds. a,b) Random Forest (RF) trained on ST,DT for $W+2$ jets events in the electron channel with 1,2 b-tagged jets; c,d) RF trained on ST,DT for $W+2$ jets events in the muon channel with 1,2 b-tagged jets. The legend of the plots can be found in page. 84.*

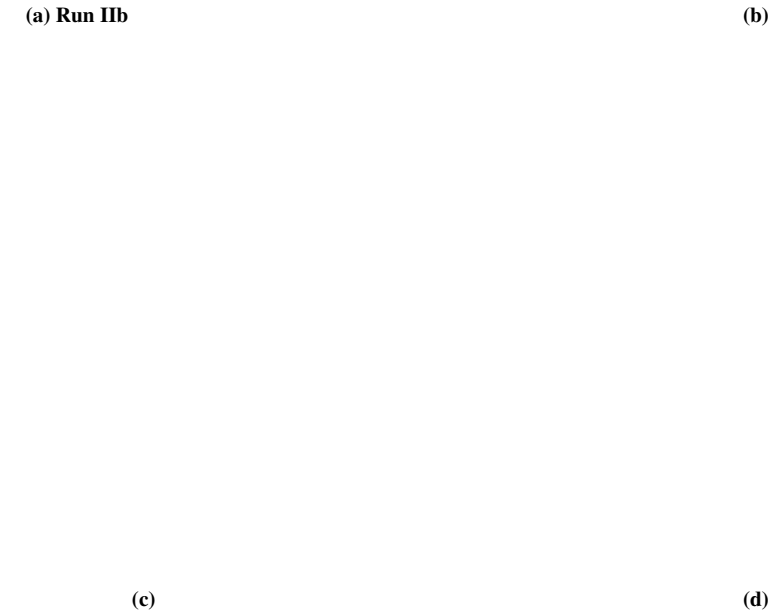

Figure 5.7: *Distributions for the $W + 2$* **jet events (top: e-channel, bottom: μ-channel, RunIIb data) when one or two jets are b-tagged**. *The data are compared to $Wb\bar{b}$, $t\bar{t}$, W+jets and other smaller expectations. The simulated processes are normalized to the integrated luminosity of the data sample using the expected cross sections (absolute normalization) except for the $W + 2$ jets sample which is normalized to data on the "pre-tag sample", taking into account all the other backgrounds. a,b) Random Forest (RF) trained on ST,DT for $W + 2$ jets events in the electron channel, pretag level; c,d) RF trained on ST,DT for $W + 2$ jets events in the muon channel, pretag level. The legend of the plots can be found in page. 84.*

(a) Run IIa

(b)

(c)

(d)

Figure 5.8: *Distributions for the $W+3$* **jet events (top: e-channel, bottom: μ-channel, RunIIa data) pretag level**. *The data are compared to $Wb\bar{b}$, $t\bar{t}$, W+jets and other smaller expectations. The simulated processes are normalized to the integrated luminosity of the data sample using the expected cross sections (absolute normalization) except for the $W+3$ jets sample which is normalized to data on the "pre-tag sample", taking into account all the other backgrounds. a,b) Random Forest (RF) trained on ST,DT for $W+3$ jets events in the electron channel, pretag level; c,d) RF trained on ST,DT for $W+3$ jets events in the muon channel, pretag level. The legend of the plots can be found in page. 84.*

(a) Run IIb **(b)**

(c) **(d)**

Figure 5.9: *Distributions for the $W+3$* **jet events (top: e-channel, bottom: μ-channel, RunIIb data) pretag level**. *The data are compared to $Wb\bar{b}$, $t\bar{t}$, W+jets and other smaller expectations. The simulated processes are normalized to the integrated luminosity of the data sample using the expected cross sections (absolute normalization) except for the $W+3$ jets sample which is normalized to data on the "pre-tag sample", taking into account all the other backgrounds. a,b) Random Forest (RF) trained on ST,DT for $W+3$ jets events in the electron channel, pretag level; c,d) RF trained on ST,DT for $W+3$ jets events in the muon channel, pretag level. The legend of the plots can be found in page. 84.*

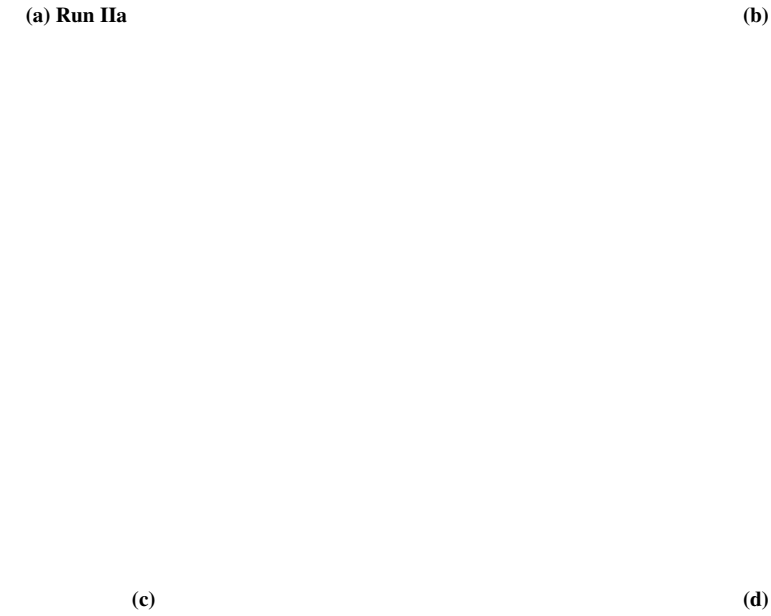

Figure 5.10: *Distributions for the $W+3$* **jets events (top: e-channel, bottom: μ-channel, RunIIa data) when one or two jets are b-tagged**. *The data are compared to $Wb\bar{b}$, $t\bar{t}$, W+jets and other smaller expectations. The simulated processes are normalized to the integrated luminosity of the data sample using the expected cross sections (absolute normalization) except for the $W+3$ jets sample which is normalized to data on the "pre-tag sample", taking into account all the other backgrounds. a,b) Random Forest (RF) trained on ST,DT for $W+3$ jets events in the electron channel with 1,2 b-tagged jets; c,d) RF trained on ST,DT for $W+3$ jets events in the muon channel with 1,2 b-tagged jets. The legend of the plots can be found in page. 84.*

Figure 5.11: *Distributions for the $W+3$* **jet events (top: e-channel, bottom: μ-channel, RunIIb data) when one or two jets are b-tagged**. *The data are compared to $Wb\bar{b}$, $t\bar{t}$, W+jets and other smaller expectations. The simulated processes are normalized to the integrated luminosity of the data sample using the expected cross sections (absolute normalization) except for the $W+3$ jets sample which is normalized to data on the "pre-tag sample", taking into account all the other backgrounds. a,b) Random Forest (RF) trained on ST,DT for $W+3$ jets events in the electron channel, pretag level; c,d) RF trained on ST,DT for $W+3$ jets events in the muon channel, pretag level. The legend of the plots can be found in page. 84.*

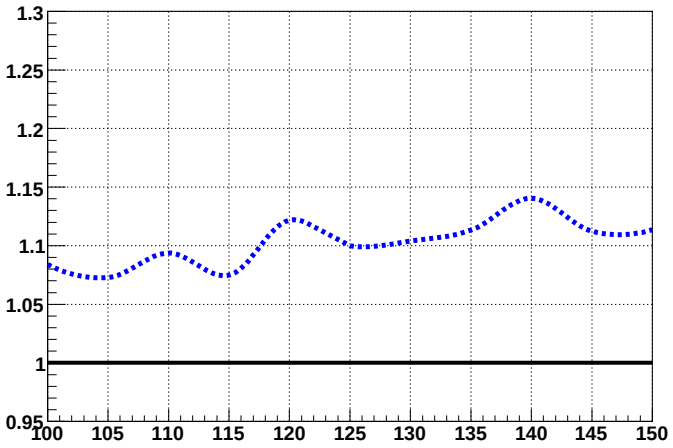

Figure 5.12: *Expected limit improvement relative to the NN-based analysis.*

CHAPTER 6

Limit Derivation and Results for the WH Analysis

From Chapter 5, the modeling of Monte Carlo simulation can be seen to be of high accuracy.However, the signal yield for the $WH \rightarrow l\nu b\bar{b}$ after applying all cuts and selection criteria is low. The signal-to-background ratio is found to be of the order of $\frac{1}{100}$ after applying $b-$tagging. To make use of all available events' information in the separation process between signal and background, a discriminant (See Chapter 5) was used based on the Random Forest technique. No excess consistent with a signal was found; as a result, we set to calculate the expected and observed limits from data, after putting together all channels in the analysis.

Limit setting procedure is based on a semi-Frequentist approach [110] used in the "Colli" software [111].

6.1 Introduction

A typical high-energy new physics search analysis is ultimately described by a final variable (or variables) chosen to be sensitive to a parameter of the search system. The result of the search are distributions of this final variable for the new physics process, one or more modeled background processes, and the observation from data. These final variable distributions become the input to statistical calculations. In general, the final variable distributions are designed to describe two distinct hypothesis that will be compared to data. The first hypothesis is intended to describe a specified new physics process (henceforth signal, using HEP jargon) in addition to the predicted background processes that are expected to comprise the majority of the data sample. This is referred to as the Test or signal-plus-

background ($S + B$) hypothesis. The second hypothesis is a subset of the first obtained by removing the signal model and is referred to as the Null or background-only hypothesis. Both are compound hypothesis and depend on a set of parameters that affect the final variable, but are not of immediate interest. Examples of such parameters are integrated luminosities, efficiencies, acceptances, and background cross sections. Referred to as nuisance parameters, the values of these ingredients are important in the extraction of limits on the parameter of interest in the new physics model, and any uncertainty in these nuisance parameters will generally degrade the sensitivity of the search to the parameter of interest.

The Collie software suite is designed to calculate statistical quantities including $p-$values for signal and background processes, limits on model parameters, and measurements of cross sections. All Higgs analyses and New Physics searches at the DØ experiment use the Collie software suit [111] [112] [113].

6.2 Calculations Method

6.2.1 Definitions

The following is a list of definitions that are needed to give a clearer idea of the concepts involved in hypothesis testing.

- **NULL Hypothesis:**

  The NULL hypothesis represents a model that is either believed to be true or is used as the basis (control) of a test. This is also commonly referred to as the *background-only* hypothesis.

- **TEST Hypothesis:**

  The TEST hypothesis is the alternative model that has been established for testing against the NULL hypothesis. For example, in a search for new physics the TEST hypothesis represents the model in which there is new physics that has a distinguishable effect. This is also commonly referred to as the signal-plus-background ($S + B$)

hypothesis.

- **Test Statistic:**

  A test statistic is a quantity derived from data sample and used to quantify the degree to which the data are consistent with the TEST and NULL hypotheses. Also referred to as an "Ordering Rule", the test statistic is used to order the outcomes of individual datum relative to one another in the two hypotheses.

- **Nuisance Parameter:**

  A nuisance parameter is a parameter of model (or hypothesis) that is unspecified but not of immediate interest to the test. For example, in a model describing the number of events counted in a particle physics experiment ($N = L \times \epsilon \times \sigma$) either the luminosity L, the efficiency ϵ, or the cross section σ could be the parameter of interest, and the remaining parameters are nuisance parameters.

- **Confidence Interval:**

  A confidence interval is an interval in the space of the parameter that is associated with a confidence level. The interpretation of the confidence level, however, depends on how probability is interpreted: relative frequency, or degree of belief.

- **Confidence Level:**

  In a Frequentist interpretation, a confidence level is a guaranteed lower bound on the fraction of intervals that contain the true value of their associated parameter. In a Bayesian approach, it is the probability, interpreted as a degree of belief, that the parameter lies within the given interval. For example, if a measurement of the luminosity of a data sample is found to have an uncertainty, it is commonly described by the region enclosing 68.3% (1σ) of the possible values of the true parameter: $L = 1000 \pm 60\text{pb}^{-1}$. In this example, the confidence interval is $940 \leq L \leq 1060$ and the confidence level is 68.3%.

- $p-$**value:**

  A $p-$ defines the probability that a test would find a result more extreme than the observed result based on a purely random sampling ($P(x \geq x_{obs})$).

COLLIE adopts a semi-Frequentist construction for the estimation of the likelihood distributions associated with a comparison of the TEST and NULL hypotheses. These probability distribution functions (PDFs) are generated numerically via the distribution of a pre-specified test statistic evaluated in a large array of data events generated via artificial pseudo-experiments (pseudo-data).

6.2.2 Sensitivity Estimator

In order to decide on which hypothesis is more favored for a given data sample, a test statistic compares likelihoods for the TEST and NULL hypotheses. By treating the two hypotheses as a Poisson counting experiment with expected numbers of signal (s) and background (b) and the observed number of data (d) we can construct a Poisson likelihood ratio:

$$Q(s,b,d) = \frac{e^{-(s+b)}(s+b)^d/d!}{e^{-b}(b)^d/d!} \tag{6.1}$$

In this equation, the values of s and b are the expected number of signal and background events from Monte Carlo templates and d is defined by either the observed data or pseudo-data used to populate the distributions of Q.

To include multiple bins and/or multiple channels, a joint likelihood can be formed by the multiplicative juncture of the probabilities:

$$Q = \prod_{i=1}^{N_{channels}} \prod_{j=1}^{N_{bins}} \frac{e^{-(s_{ij}+b_{ij})}(s_{ij}+b_{ij})^{d_{ij}}/d_{ij}!}{e^{-b_{ij}}b_{ij}^{d_{ij}}/d_{ij}!} \tag{6.2}$$

$$= \prod_{i=1}^{N_{channels}} \prod_{j=1}^{N_{bins}} e^{-(s_{ij})}(\frac{s_{ij}+b_{ij}}{b_{ij}})^{d_{ij}} \tag{6.3}$$

where the i index runs over the number of channels and the index j runs over the number of bins in each channel. By recasting the test statistic as a negative log-likelihood ratio

(NLLR) Γ a mathematically compact version can be obtained:

$$\Gamma = -2\ln(Q) \tag{6.4}$$

$$= 2 \prod_{i=1}^{N_{channels}} \prod_{j=1}^{N_{bins}} (s_{ij} - d_{ij}\ln(1 + s_{ij}/b_{ij})) \tag{6.5}$$

This test statistic has the desirable benefit of being monotonically increasing in the number of candidate data events and ensures a non-negative change in sensitivity for each additional channel and/or bin.

To have a Frequentist interpretation, many trials are repeated using pseudo-data for the TEST and NULL hypotheses. Pseudo-data can be generated via using random trials for a Poisson distribution with a mean value of d_{ij}. $d_{ij} = s_{ij} + b_{ij}$ for the TEST hypothesis and $d_{ij} = b_{ij}$ for the NULL hypothesis for a any given bin i in any channel j.

Confidence levels, thought of as the probability to observe a deviation from a measured value of the data are derived according to the chosen test statistic. Confidence levels for both hypotheses are found through the following:

$$CL_{(S+B)} = p_{(S+B)}(\Gamma \geq \Gamma_d) = \int_{\Gamma_d}^{+\infty} \frac{\partial P_{(S+B)}}{\partial \Gamma} d\Gamma \tag{6.6}$$

$$CL_B = p_B(\Gamma \geq \Gamma_d) = \int_{\Gamma_d}^{+\infty} \frac{\partial P_B}{\partial \Gamma} d\Gamma \tag{6.7}$$

An example of the Probability Distribution Functions, PDFs, and confidence levels can be seen in Figure 6.1. For bias prevention, the signal confidence level is estimated as:

$$CL_S = \frac{CL_{(S+B)}}{CL_B} \tag{6.8}$$

The estimator constructed above, then, can be defined for two cases:

1. CL_S^{exp}, which is obtained when making the assumption that the data corresponds exactly to the background-only hypothesis.

2. CL_S^{obs}, which is obtained from observation in data.

More details about the method used in the limit calculations and about the COLLIE software used can be found in [111, 112].

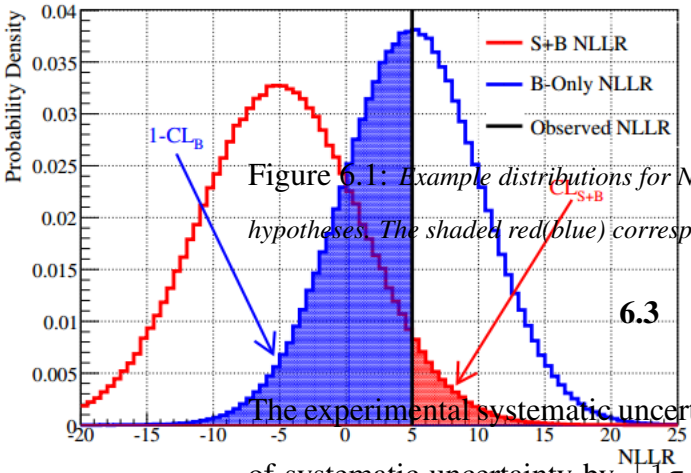

Figure 6.1: *Example distributions for NNLR test statistic evaluated for the* TEST *(red) and* NULL *(blue) hypotheses. The shaded red(blue) correspond to the values* $CL_{(S+B)}(1 - CL_B)$.

6.3 Systematic Uncertainties

The experimental systematic uncertainties are obtained by individually varying each source of systematic uncertainty by $\pm 1\sigma$ (where σ is the size of the uncertainty), re-performing a full analysis, and then taking the ratio of the obtained distribution to the nominal result (where no systematic variation has been applied). When we vary the systematics we re-normalize to data such that the total pretag background yield remains constant (i.e. the W+jets scaling factor may not be the same as in the nominal case.) In practice this implies that the W+jets yield will often move in the opposite direction to the other background processes to keep the pretag background yield constant. We take all such effects into account properly.

Each source of systematic uncertainty is studied separately for each lepton-type (e and μ) and for each jet multiplicity (2-jet and 3-jet) sample. For each systematic variation the uncertainty is presented and applied for signal and for each of the main Standard Model backgrounds separately. The QCD background is treated separately since it is derived from data. All systematic uncertainties are evaluated using the RunIIb samples and the same result is applied to both RunIIb and RunIIa except where explicitly stated otherwise.

Further details on the determination of the systematics (e.g the uncertainty arising from the uncertainty in the efficiency ratios between data and simulation, the uncertainties on the propagation of trigger, energy calibration, smearing etc.,) are described below.

6.3.1 Jet Energy Scale (JES)

We evaluate the JES systematic uncertainty using the recommended method of scaling the jet object by $\pm 1\sigma$ instead of using the nominal jet object.

6.3.2 Jet Resolution (RES) and Jet ID (EFF)

We evaluate the Jet Resolution systematic uncertainty through moving the shifting/smearing parameters up or down by 1σ and we use the resulting jet instead of the nominal jet. To evaluate the systematic error on the Jet ID, we shift the removal scale factor down 1σ (i.e. more jets will be removed than in the nominal case.) For the $+1\sigma$ Jet ID variation, we symmetrize the -1σ distribution.

6.3.3 Vertex Confirmed Jet (VCJ)

The Vertex Confirmed Jets Scale Factor which represents the probability of the random removal of the jet is shifted down by 1σ to evaluate the systematic error on this scale factor (the procedure is the same as the Jet ID systematic.) For the $+1\sigma$ variation, we symmetrize the -1σ distribution.

6.3.4 Lepton-ID

EM-ID

The EM-ID systematic for electron identification, reconstruction efficiency and energy smearing is obtained by varying by $\pm 1\sigma$ for the upward and downward systematic uncertainties. Details are available in [114].

μ ID

The MU-ID systematic has three components: uncertainty on the muon identification efficiency, uncertainty on the track reconstruction efficiency, and the uncertainty on the muon isolation efficiency. We apply separate uncertainties in the RunIIa [85] and RunIIb [86] samples.

- *Identification Efficiency uncertainty:* We apply a 0.8% uncertainty in RunIIa and a 1.2% uncertainty in RunIIb. For RunIIb we also apply an additional 2% systematic in events with muon $p_T < 20$ GeV per the recommendation of the Muon ID group.

- *Track Reconstruction Efficiency Uncertainty:* We apply a 2.3% uncertainty in RunIIa and a 1.4% uncertainty in RunIIb.

- *Isolation Efficiency Uncertainty:* We apply a 3.8% uncertainty in RunIIa and a 0.9% uncertainty in RunIIb.

6.3.5 ALPGEN reweighting

- The systematic uncertainty of the ALPGEN reweighting is estimated by comparing the nominal (reweighted) version to a version in which reweighting functions are applied that generate a reweighting effect increased or decreased by 1 σ. The reweighting in the ICD region for the leading and 2nd leading jets, as a function of η_{det}, are varied simultaneously up and down. The leading and 2nd leading jet η reweightings are also varied simultaneously. Lepton η is varied independently. For W+jet processes, the ΔR and Wp_T reweightings are varied simultaneously. For Z+jet processes, ΔR is varied separately from the Zp_T variations. Zp_T variations are taken from standard CAF tools.

- Additionally, the ALPGEN MLM parton matching is reweighted on the dijet mass. The evaluation is done in the same way as for the other ALPGEN reweightings, with

reweighting functions shifted by $\pm 1\sigma$. This reweighting is applied to W/Z+light jets only.

- The systematics related to the ALPGEN event scale (k_T and Q^2) and the underlying event modeling are also evaluated [115]. The scale uncertainty evaluated separately W/Z+light and W/Z+heavy, and the underlying uncertainty evaluated on W/Z+light, and applied to all W+jets.

Previous studies of the ratio of the data-to-background expectation at the tagged stage, where we start to see W+heavy flavor events, showed a shape dependence in the single, double and combined tag samples. These were however within with assigned systematic shape, ALPGEN, JES and JSSR uncertainties, therefore no further modeling systematic is applied to W+heavy flavor events.

6.3.6 Taggability (TAG)

The systematic uncertainty for taggability is evaluated by shifting the parametrization of the taggability Scale Factor functions up and down by 1σ.

6.3.7 B-ID

The systematic uncertainty on b-ID is evaluated by using the $\pm 1\sigma$ deviation from the Tagging scale factor (TSF). In this analysis, we are applying direct tagging to the MC, and apply a scale factor which is the ratio of the data TRF and the MC TRF. This systematic uncertainty is evaluated separately for light and for heavy flavor jets.

On average, 3% , 2.5% , 1$\sim$4% for the b-tagging efficiency per b-jet, c-jet and light-jet are observed in single tag events (double for double-tag events), respectively.

6.3.8 Parton Density Functions (PDF)

In total 40 PDF variations are considered (20 pairs of positive and negative variations). While each PDF variation can change both the cross section and the kinematic acceptance of a MC process, only the changes due to kinematic acceptance are retained as part of the PDF systematic. To do this, we determined the cross section of each process under each PDF variation, then renormalized each of these variations to match the nominal cross section for that process. This methodology retains the effect that each PDF variation has on the kinematic acceptance of a process, while avoiding double-counting the cross section uncertainties.

6.3.9 Electron and Muon trigger

In the electron channel a 2% uncertainty from the trigger efficiency derived from the data sample used in this analysis is taken, whereas in the muon channel where all triggers are used (inclusive MU trigger) a larger systematic for the normalization change is applied. To confirm that the muon trigger efficiency is 100%, we compare this result with a result triggered with the Single Muon triggers. The change in surface normalization is 2% between the inclusive MU trigger and the Single Muon trigger result. In order to check for a shape uncertainty, we build ratios for Data/MC (inclusive trigger - single mu trigger) over Data/MC (single mu trigger) and also separately the ratios Data/Data and MC/MC (inclusive)/(single mu) that show the trigger effect. We develop a fit function (sigmoid + exponential decay) in di-jet p_T for the Data/MC (inclusive trigger - single mu trigger) over Data/MC (single mu trigger) double ratio. We derive the function in the pretag sample and apply it to the ST and DT samples (on signal and all MC backgrounds) as well. Figure 6.3.9 shows the function, we apply the value of the function as a multiplicative factor on P_{corr} and take the difference with the nominal as the systematic on the muon trigger (normalization included.). The muon systematic is typically 1-3%.

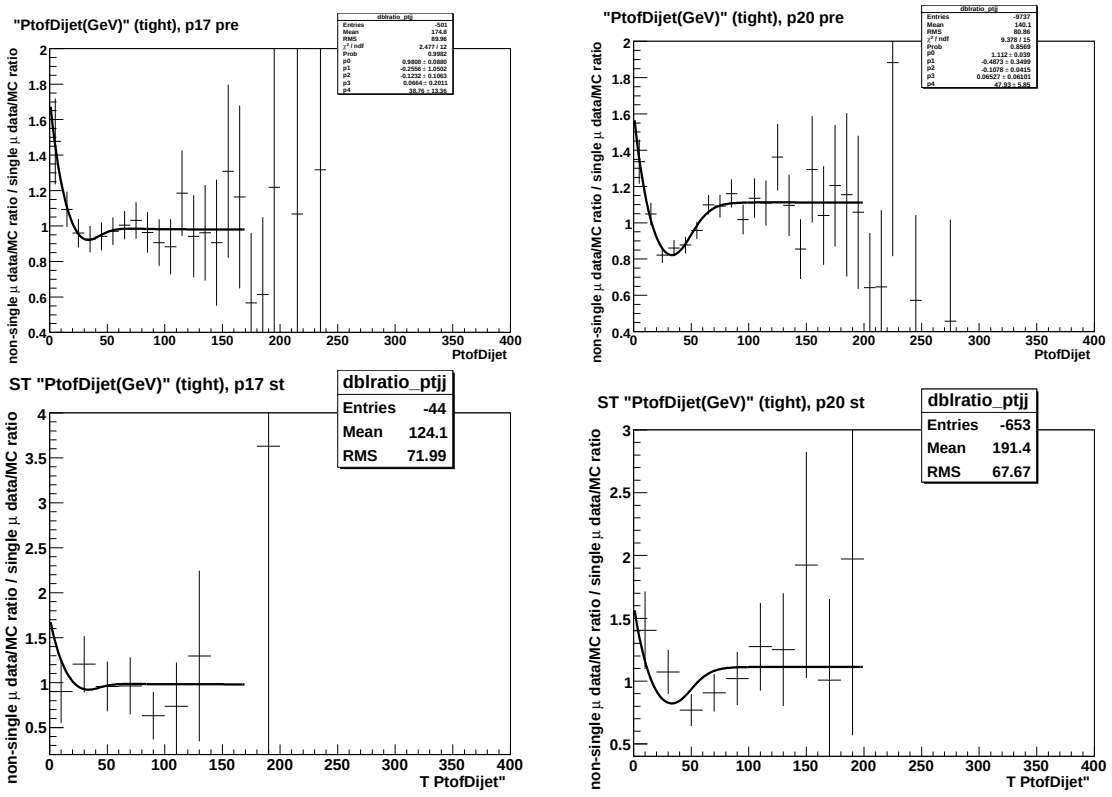

Figure 6.2: *Fit function (sigmoid + exponential) on di-jet p_T for the Data/MC (inclusive trigger - single mu trigger) over Data/MC (single mu trigger) double ratio used as the systematic uncertainty on the muon trigger. We derive the function in the pretag sample and apply it to both the ST and DT samples. Upper left: p17 pretag. Upper right: p20 pretag. Lower left: p17 single tag. Lower right: p20 single tag.*

6.3.10 QCD

The systematic uncertainty on the QCD background is estimated by varying separately the lepton efficiency and the jet fake rate by $\pm 1\sigma$. The normalization of the QCD sample is anti-correlated with the normalization of W+jet (light and heavy flavor) events, and this anti-correlation it taken into account during our limit setting procedure.

6.3.11 Cross Section Uncertainties

Overall the total experimental systematic uncertainty for WH production is approximately 6%. The luminosity uncertainty is treated separately and amounts to 6.1%. The uncertainties on the cross sections of the background processes are 10% for $t\bar{t}$ production, 10% for single-top production, 7% for WW, WZ and ZZ inclusive production [116].

We also also apply uncertainties to the K-factors applied to the W+jets samples, which directly affect the apparent cross section. We apply a 20% uncertainty on the W/Z+HF K-factor, and a 6% uncertainty on the W/Z+LF K-factor.

We shall give here a summary of the cross section's uncertainties used in this work:

1. $t\bar{t}$

   The $t\bar{t}$ cross section is calculated in NNLO to be 6.77 ± 0.42 pb for $M_t = 175$ GeV/c^2, where the uncertainty comes from the renormalization and factorization scale dependence. Including the uncertainty due to PDF, the error becomes ± 0.6 pb [117]. Finally taking into account the mass dependence, 0.22 pb per GeV/c^2 [118], for the current error of M_t measurement (± 2.3GeV/c^2 [119]), the uncertainty is $\pm 0.6 \pm 0.5$ pb. by adding the two errors in quadrature, the total uncertainty is ± 0.8 pb, which 12% relative error. In conclusion we used the value of 10% pb.

2. **Single Top**

   The single top production cross section is calculated in NLO to be 0.88 ± 0.14 pb for the $s-$channel and 1.98 ± 0.30 pb for the $t-$channel [120]. The relative uncertainties

are 16% and 15%, respectively. The value used in this work is 12%.

3. WW **or** WZ

   The W^+W^- cross section is quoted as 12.4 ± 0.8 pb [121], which is 6% relative error. This is consistent with the MCFM calculations which lead to a 5.6% error in total. The value of 7% is used for both W^+W^- and WZ. The value used in this work is 7%.

4. $Wb\bar{b}$

   The $Wb\bar{b}$ cross section is studied with MCFM with the jet p_T cut on 8 GeV/c and CTEQ5M PDF. The central value was calculated to be 1548 fb for the renormalization and factorization scale ($\equiv \mu$) of $\sqrt{M_W^2 + p_T(W)^2}$. The $W^+b\bar{b}$ cross section is 1875 fb for $\mu = M_W/2$, and 1346 fb for $\mu = 2 \times M_W$. As the uncertainty due to normalization and factorization scales, we assigned 264.5 fb ($= (1875 - 1346)/2$), which is 17.1% relative error. The uncertainty due to PDF is3.3% which is much smaller than the variation between the new and old PDF set. Adding the 17.1%, 4.0%, and 3.3% in quadrature, the total error is 20%.

5. $(W/Z)jj$

   The total normalization error for Wjj is 6% in the exclusive single tagging (EST) and 9% in the double-tagging (DT). The value used in this work is 6%.

These numbers can be summarized in Table 6.1:

Process	Cross Section Uncertainty
WH	6%
$t\bar{t}$	10%
Single Top	12%
$W/Z + jj$	6%
$W/Z + c\bar{c}, b\bar{b}$	20%
WW, WZ, ZZ	7%

Table 6.1: *Cross Section Uncertainties, derived from theory, for the WH and its background processes. The $W/Z + jj$ is derived from data. The $W/Z + c\bar{c}, b\bar{b}$ is derived from the heavy flavor scale factor, S_{HF}.*

Collie name	Explanation, see following tables for the processes to which they apply
DZero_Lumi	Part of the Luminosity uncertainty coming from Dzero
Lumi	Part of the Luminosity uncertainty correlated with CDF
EMID	EM-id, -reconstruction, -scale, -smearing and -trigger (2%) added in quadrature
JES	Jet Energy Scale uncertainties
JSSR	Jet Shifting/Smearing/Resolution uncertainties
JetID	Jet-ID uncertainties
JetID	Vertex confirmation scale factor uncertainties. Applied only to RunIIb samples.
Tagga	Taggability uncertainties.
bTag_HF	Uncertainties on data/MC TRF ratios for heavy flavor jets.
	We apply 3% per b-jet and 2.5% per c-jet.
bTag_LF	Uncertainties on data/MC TRF ratios for heavy flavor jets (1-4% per jet.)
PDF 1-20	The 20 pairs of up/down PDF uncertainties. Effects of the PDF reweighting
	on the signal cross section have been removed, leaving only shape and acceptance effects.
Bkgd_Xsec_EW	Diboson cross section uncertainty (6% .)
ALP_JTE	uncertainty on the ALPGEN jet eta reweighting. Applied only to W/Z+jets.
ALP_JTH	uncertainty on the ALPGEN jet horn reweighitng. Applied only to W/Z+jets.
ALP_DR	uncertainty on the ALPGEN ΔR reweighting. Includes the
	uncertainty on the W p_T reweighting. Applied only to W/Z+jets.
ALP_LPE	uncertainty on the ALPGEN lepton eta reweighting. Applied only to W/Z+jets.
ALP_ULE	uncertainty on the underlying event. Applied only to W/Z+jets.
ALP_SCA	uncertainty on the ALPGEN scale parameter. Applied only to W/Z+jets.
ALP_MLM	uncertainty on the MLM matching parameter. Applied only to W/Z+light jets.
ALP_ZPT	uncertainty on the Z p_T reweighting. Applied only to Z+jets.
Bkgd_Xsec_Top	$t\bar{t}$ cross section uncertainty (10% .)
Bkgd_Xsec_singletop	single top cross section uncertainty (12% .)
Bkgd_Xsec_HF	uncertainty on the heavy flavor K-factor (20%.) Applied only to $W/Z + c\bar{c}, b\bar{b}$ samples.
Bkgd_Xsec_LF	uncertainty on the W/Z+light jet cross section (6% .) Applied only to W/Z + light jet samples.
MUID	muon-id , track-reconstruction, and -isolation efficiency.
MUTrigger_WH	uncertainty on muon trigger efficiency (5%)
QCDev_fake	uncertainty on the electron QCD fake rate (epsQCD).
	Applied only to QCD and W+jets (anti-correlated.)
QCDev_eff	uncertainty on the electron QCD efficiency (epsSig).
	Applied only to QCD and W+jets (anti-correlated.)
QCDev_fake	uncertainty on the muon QCD fake rate (epsQCD).
	Applied only to QCD and W+jets (anti-correlated.)
QCDev_eff	uncertainty on the muon QCD efficiency (epsSig).
	Applied only to QCD and W+jets (anti-correlated.)

Table 6.2: *Explanations of the systematic error naming. The errors having a name starting with Bkgd apply only to the background, the other to Background and Signal, except for the last error of the table.*

	electron 2jet-1b IIa IIb	electron 2jet-2b IIa IIb	electron 3jet-1b IIa IIb	electron 3jet-2b IIa IIb	muon 2jet-1b IIa IIb	muon 2jet-2b IIa IIb	muon 3jet-1b IIa IIb	muon 3jet-2b IIa IIb
DZero_Lumi	4.6% 4.6%	4.6% 4.6%	4.6% 4.6%	4.6% 4.6%	4.6% 4.6%	4.6% 4.6%	4.6% 4.6%	4.6% 4.6%
Lumi	4.0% 4.0%	4.0% 4.0%	4.0% 4.0%	4.0% 4.0%	4.0% 4.0%	4.0% 4.0%	4.0% 4.0%	4.0% 4.0%
EMID/EMTrigger	S S	S S	S S	S S				
JES	S S	S S	S S	S S	S S	S S	S S	S S
JSSR	S S	S S	S S	S S	S S	S S	S S	S S
JetID	S S	S S	S S	S S	S S	S S	S S	S S
VCJet	S	S	S	S	S	S	S	S
Tagga	S S	S S	S S	S S	S S	S S	S S	S S
bTag_HF	S S	S S	S S	S S	S S	S S	S S	S S
bTag_LF	S S	S S	S S	S S	S S	S S	S S	S S
PDF 1-20	S S	S S	S S	S S	S S	S S	S S	S S
Bkgd_Xsec_EW	6% 6%	6% 6%	6% 6%	6% 6%	6% 6%	6% 6%	6% 6%	6% 6%
ALP_JTE	S S	S S	S S	S S	S S	S S	S S	S S
ALP_JTH	S S	S S	S S	S S	S S	S S	S S	S S
ALP_DR	S S	S S	S S	S S	S S	S S	S S	S S
ALP_LPE	S S	S S	S S	S S	S S	S S	S S	S S
ALP_ULE	S S	S S	S S	S S	S S	S S	S S	S S
ALP_SCA	S S	S S	S S	S S	S S	S S	S S	S S
ALP_MLM	S S	S S	S S	S S	S S	S S	S S	S S
ALP_ZPT	S S	S S	S S	S S	S S	S S	S S	S S
Bkgd_Xsec_Top	10% 10%	10% 10%	10% 10%	10% 10%	10% 10%	10% 10%	10% 10%	10% 10%
Bkgd_Xsec_singletop	12% 12%	12% 12%	12% 12%	12% 12%	12% 12%	12% 12%	12% 12%	12% 12%
Bkgd_Xsec_HF	20% 20%	20% 20%	20% 20%	20% 20%	20% 20%	20% 20%	20% 20%	20% 20%
Bkgd_Xsec_LF	6% 6%	6% 6%	6% 6%	6% 6%	6% 6%	6% 6%	6% 6%	6% 6%
MUID					4.5% S	4.5% S	4.5% S	4.5% S
MUTrigger_WH					5% 5%	5% 5%	5% 5%	5% 5%
Bkgd_QCDev_fake	S S	S S	S S	S S				
Bkgd_QCDev_eff	S S	S S	S S	S S				
Bkgd_QCDmv_fake					S S	S S	S S	S S
Bkgd_QCDmv_eff					S S	S S	S S	S S

Table 6.3: *Correlation across the sixteen channels of the systematics uncertainties, see next table for explanations of these uncertainties. The errors having a name starting with Bkgd apply only to the background, the other to Background and Signal, except for the last error of the table.*

6.4 Upper Limits on WH Production

No signal excess in data can be seen, after all cuts being applied. Limits on the WH production cross section $\sigma(p\bar{p} \to WH) \times BR(H \to b\bar{b}$ are set with the CL_s method derived above. For each Higgs boson mass point (Higgs masses), the 95% confidence level limits for both expected and observed results are set. Table 6.4 shows the limits obtained for both electron and muon channels and also shows the combined results for both channels, used in this analysis. Limits are given as ratios of the obtained limit to the expected Standard Model Higgs boson production cross section. The Log Likelihood Ratio LLR, over all Higgs

Electron channel Results (RunIIa+IIb combined)											
Mass (GeV)	100	105	110	115	120	125	130	135	140	145	150
Expected Limit $/\sigma_{SM}$	4.54	4.86	5.81	6.45	7.94	9.33	11.67	15.70	23.19	32.60	50.97
Observed Limit $/\sigma_{SM}$	4.53	5.36	5.09	6.49	10.40	8.90	9.53	11.69	18.63	24.13	36.28
Muon channel Results (RunIIa+IIb combined)											
Mass (GeV)	100	105	110	115	120	125	130	135	140	145	150
Expected Limit $/\sigma_{SM}$	4.88	5.21	6.00	6.88	8.54	9.98	12.74	17.29	24.26	36.25	55.04
Observed Limit $/\sigma_{SM}$	3.42	5.18	5.67	5.24	7.01	10.45	10.69	12.52	21.21	24.19	55.93
Full Combined Results											
Mass (GeV)	100	105	110	115	120	125	130	135	140	145	150
Expected Limit $/\sigma_{SM}$	3.27	3.56	4.15	4.77	5.58	6.75	8.48	11.52	16.45	23.59	36.77
Observed Limit $/\sigma_{SM}$	2.71	4.04	4.29	4.45	5.78	6.62	7.04	7.62	12.16	15.03	30.37

Table 6.4: *Expected and observed limits at 95% C.L. as a ratio to the Standard Model cross section (include all systematics with collie option of fast approximation) for all considered Higgs mass points (also known as Higgs masses). Both Electron and Muon channels are shown. The Full combined results are shown in the lower part of the table.*

boson mass points hypotheses for both Electron and Muon channels are shown in Figure 6.4 and Figure 6.4, respectively, with the their ratio of the 95% C.L. limit cross section times the branching ratio of $H \to b\bar{b}$ to the SM prediction as a function of the Higgs mass. The straight line represents the SM predicted value. The combined LLR distributions over all Higgs boson mass points hypotheses distribution as a function of the Higgs mass is

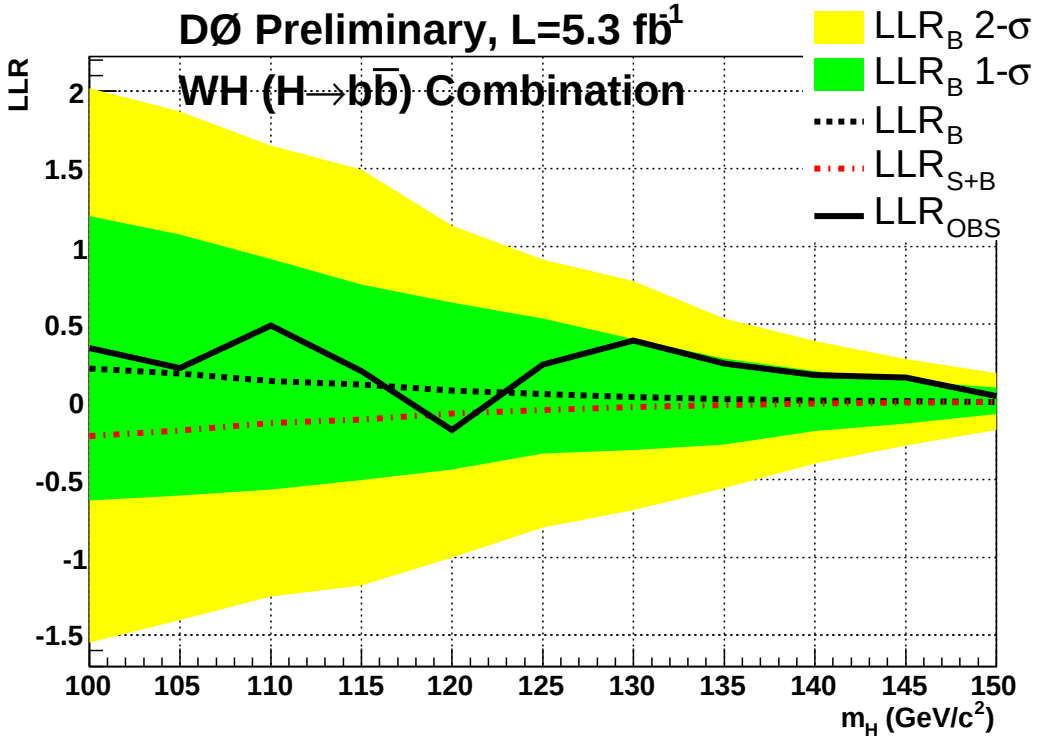

Figure 6.3: *The Log Likelihood Ratio LLR, over all Higgs boson mass points hypotheses for the Electron channel.*

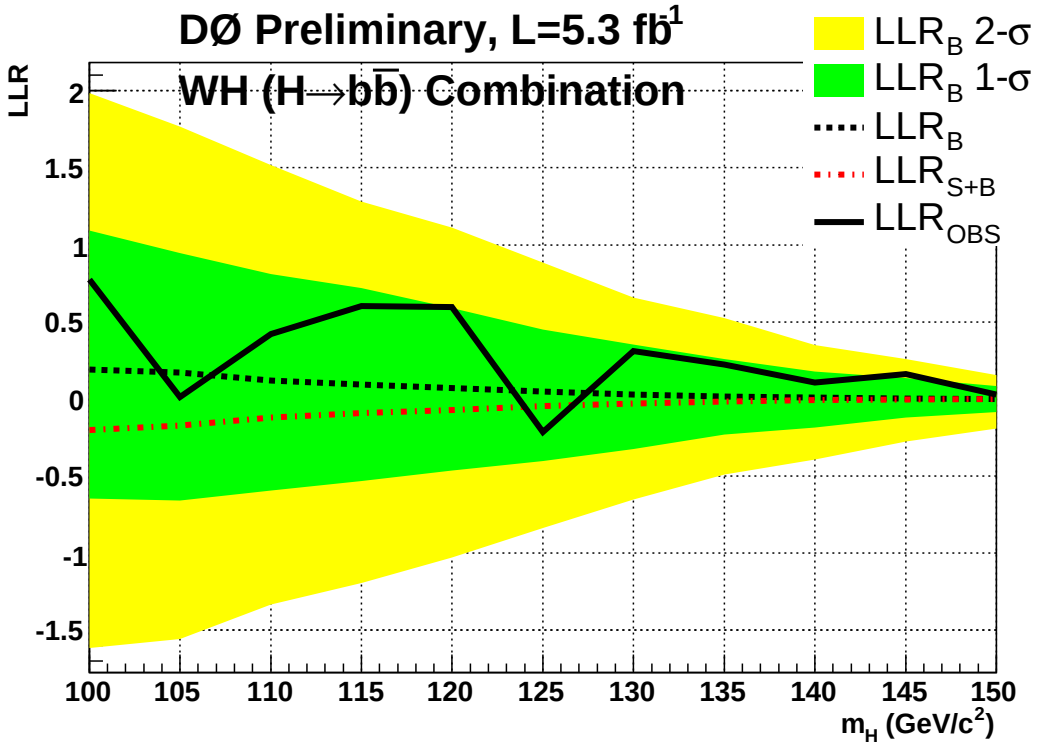

Figure 6.4: *The Log Likelihood Ratio LLR, over all Higgs boson mass points hypotheses for the Muon channel.*

shown in Figure 6.4. Table 6.5 shows the limits at 115 GeV for each analysis channel and

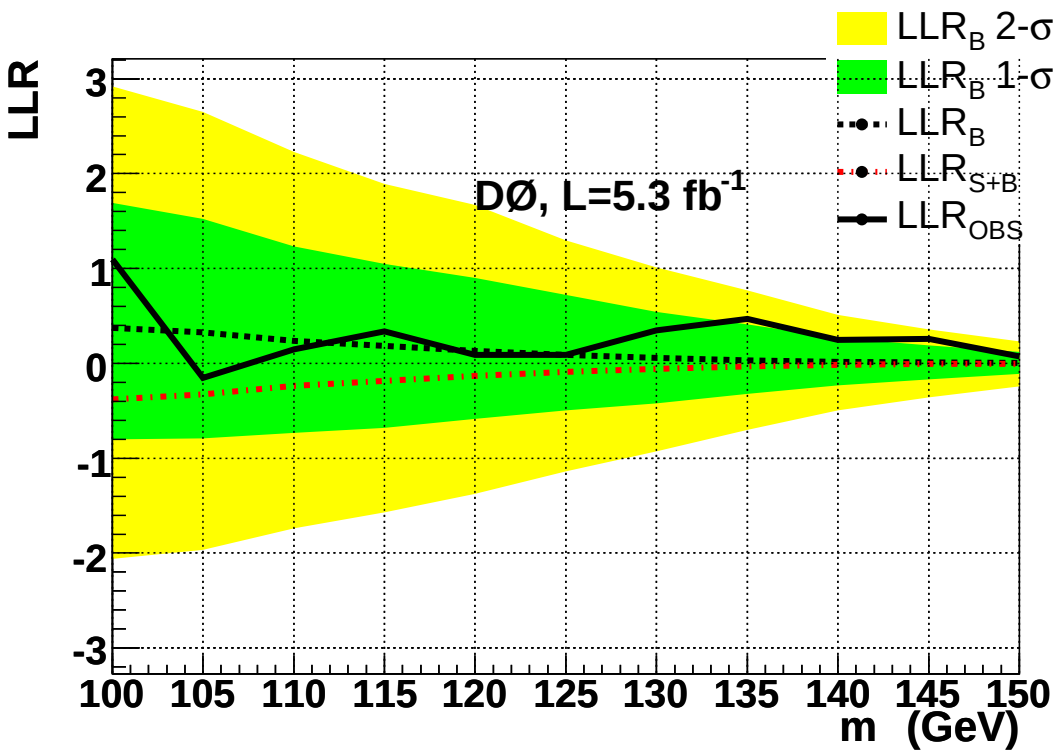

Figure 6.5: *The combined Log Likelihood Ratio, LLR, distribution over all Higgs boson mass points hypotheses as a function of the Higgs mass.*

compares them to the previous limits using the NN/di-jet mass approach. From the results above we can see that the separation between the Signal+Background and Background hypotheses is less than 1σ. As a result we see that a combination between all Higgs boson search channels in both DØ and CDF experiments of the Fermilab Tevatron is necessary to achieve the sensitivity to the Standard Model Higgs production. The limit ratio obtained for $\sigma(p\bar{p} \rightarrow WH) \times B(H \rightarrow b\bar{b}) < 0.585$ pb at 95% C.L. calculated for a Higgs of mass 115 GeV. The cross section is very small and the corresponding upper limit is 0.624 pb. The Standard Model cross section is 0.13 pb. Figure 6.4 shows the ratio of the 95% C.L. limit cross section times the branching ratio of $H \rightarrow b\bar{b}$ to the Standard Model prediction as a function of the Higgs mass for all channels combined. For a Higgs boson of mass 115 GeV, an upper limit observed (expected) is set to be 4.62 (4.94) on the ratio.

Analysis	elec. NN/m_{jj}	elec. RF	muon NN/m_{jj}	muon RF
IIa / 2 jet	13.2	12.5	12.1	11.8
IIa / 2+3	12.9	12.1	11.7	11.4
IIb / 2 jet	7.0	6.1	7.0	6.5
IIb / 2+3	6.7	5.9	6.8	6.3
IIa+b / 2 jet	6.0	5.3	6.0	5.6
IIa+b / 2+3	5.9	5.2	5.8	5.4

Analysis	$e + \mu$ NN/m_{jj}	$e + \mu$ RF
IIa / 2 jet	8.7	8.4
IIa / 2+3	8.4	8.0
IIb / 2 jet	4.9	4.4
IIb / 2+3	4.7	4.2
IIa+b / 2 jet	4.1	3.8
IIa+b / 2+3	4.0	3.7

Table 6.5: *Summary table of the current analysis: ratio of the expected limit to the standard model prediction. Numbers are given at $m_H = 115$ GeV for both channels and for the 2- and 2+3-jet samples, in the electron and muon samples for both the NN/di-jet mass approach and the RF approach. Both single- and double-tagged events are included in each CLFAST calculation. In the second table, numbers are given for the electron-muon combination.*

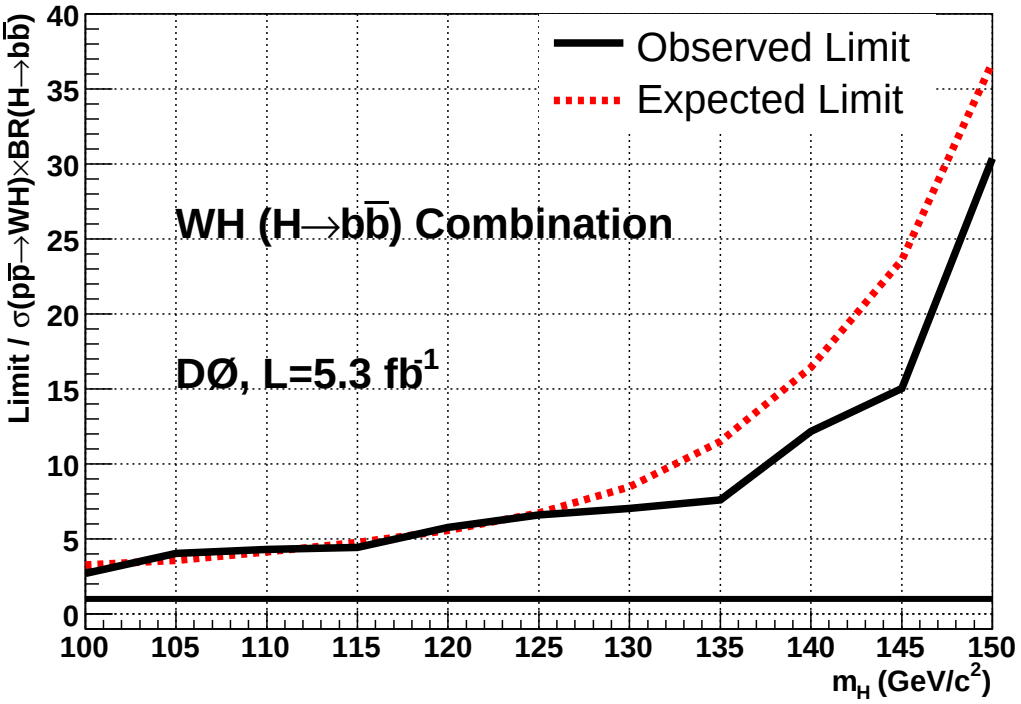

Figure 6.6: *Ratio of the* 95% *C.L. limit cross section times branching ratio limit to* $B(H \to b\bar{b})$ *to the Standard Model prediction as a function of the Higgs mass, for all channels combined. The black curve corresponds to the observed limit, obtained from data, and the red, dotted, curve is the one corresponding to the expected limit, obtained from replacing the observed data with the median background expectation. The straight line represents the Standard Model predicted value. For a Higgs boson of mass* 115 *GeV, an upper limit observed (expected) is set to be* 4.62 (4.94) *on the ratio.*

CHAPTER 7

More Data and Improvements

[1]After the publication of the first round of the results [122], the Tevatron was shut down for the last time on September, the 30^th, 2011. As a result of this shutdown, improvements to analysis techniques to gain more sensitivity has become of ultra importance to the search for the the Standard Model Higgs boson in the Tevatron's data. In this chapter another round of this analysis is shown based on [123]. Data analyzed in this part has increased to be 6.2fb^{-1}. Other improvements will be discussed. Since this analysis depends on the separation power achieved between the Higgs' signal and the background processes that mimic the signal, and because the most important variable used in the separation process is the invariant *dijet* mass, m_{jj}, some extra studies have been done to increase the discrimination power between the signal and the background using this variable. Also, a new algorithm has been developed to be used at the selection level and also to isolate as much signal as possible from the background processes, among them a new $b-$tagging algorithm has been developed to use multivariate analysis techniques. The author's contribution were to develop the training/testing codes, run the training/tests processes and to study the new TMVA toolkit [105]. After the Random Forest technique that was used before (see chapter 5) the new technique improvements, using the TMVA toolkit, were confirmed after using the new $b-$tagger developed by the collaboration. Other optimization aspects will be discussed in the following sections [110].

[1]This part is based on the D0 internal note 6154. The first round of the analysis (5.3 fb^{-1}) is based on the D0 internal note 5960

7.1 Updates in the analysis

With the publication of the 5.3 fb^{-1}, more important updates have been reviewed in order to increase the analysis sensitivity. These updates are explained below:

7.1.1 More data

By the end of the lifetime of the Tevatron, the amount of data recorded was almost 10.5 fb^{-1} as shown in Figure 7.1.1. This instance of the analysis will use only 6.2 fb^{-1} of this data[2].

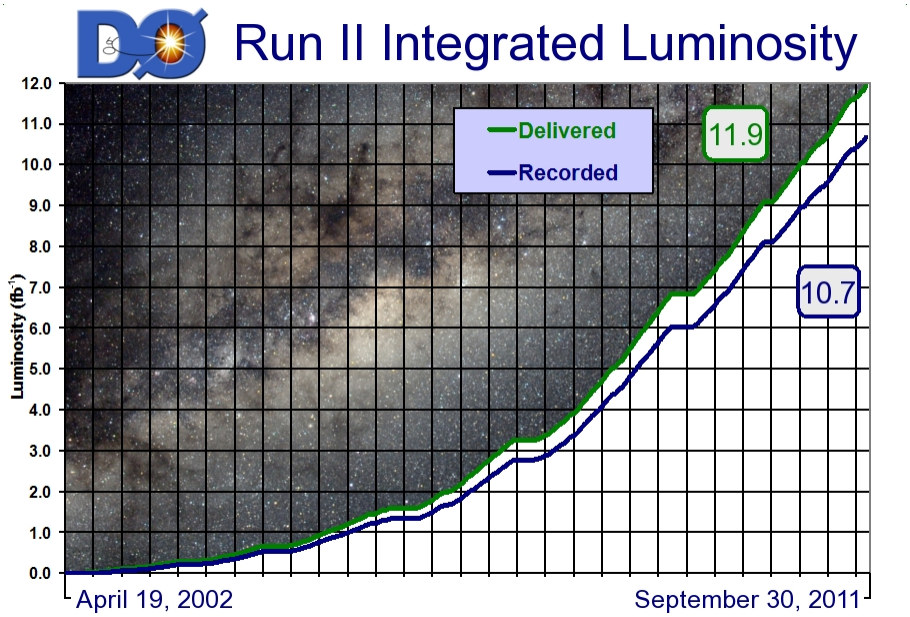

Figure 7.1: *Integrated luminosity by the end of the Tevatron lifetime.*

7.1.2 Event Selection

The preselection criteria has been updated than those used in [122]. The new preselection stage consists of the following criteria:

- Exactly one electron (muon) with transverse momentum $p_T > 15$ GeV within a pseudorapidity range of $|\eta| < 1.1$ or $1.5 < |\eta| < 2.5$ for electrons and $|\eta| < 1.6$ for

[2]This is the amount that was made ready for this round of the analysis.

muons. Additional lepton flavor-specific requirements are below.

- $\not\!\!E_T > 15$ GeV.
- A primary vertex with at least 3 associated tracks and $|z| < 60$ cm, which was 40 cm.
- exactly two or three jets with $p_T > 20$ GeV after jet energy scale correction with ICD hot cell removal, (only in runIIa data) and $|\eta| < 2.5$.
- A 2-dimensional "triangular" cut $M_W^T > 40 - 0.5\,\not\!\!E_T$ is applied to reduce the QCD background ONLY for muon, not in the electron channel. We do NOT require H_T cut any more[3], where H_T is the sum of the p_T of the jets.

We veto events with additional leptons that pass certain electron ID requirements to decrease the Z and $t\bar{t}$ dilepton backgrounds and for orthogonality to the $ZH \rightarrow \ell\ell b\bar{b}$ analysis. We also veto on hadronic τ candidates[4] and events with $e + ICRe$ or $\mu + track$ final states.

7.1.3 Multijet background suppression

Triangle cut for Muon channel:

Even though a multi dimensional fake rate is applied in the QCD background estimation, it is difficult to get a good description at low $\not\!\!E_T$ and low M_W^T because of mis-measurements on $\not\!\!E_T$. These events have low $\not\!\!E_T$ and M_W^T and the lepton and $\not\!\!E_T$ have the same direction. Therefore we exclude this region by applying a triangle cut of $M_W^T > 40 - 0.5 \times \not\!\!E_T$. Both the loose data and the WH simulation are used as QCD background sample and signal sample. The 2-dimensional ratio of (data / WH MC) with a loose electron on M_W^T vs. $\not\!\!E_T$ and the triangle cut are shown in Figure 7.2.

Multivariate discriminant for Electron channel:

[3] in the 5.3 fb^{-1} analysis, we applied the $H_T > 60(80)$ GeV cut for 2jets (3jets) case.

[4] Done by the author

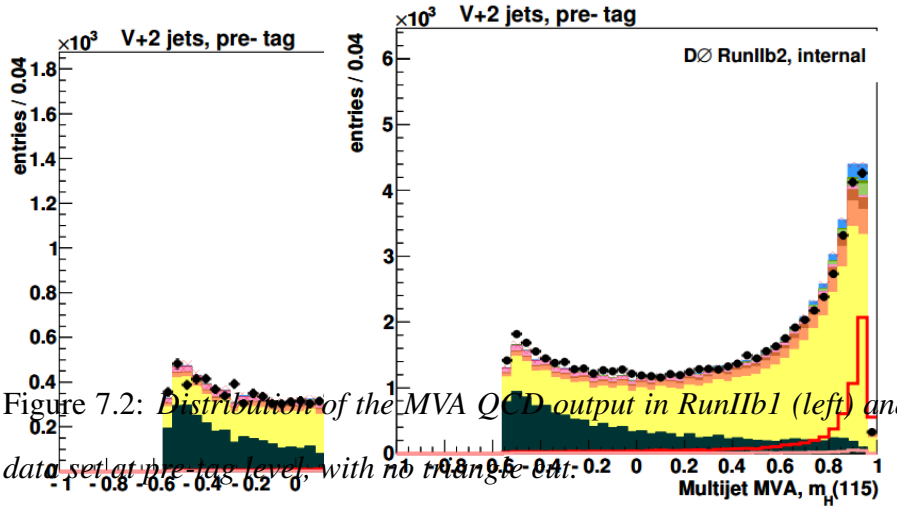

Figure 7.2: *Distribution of the MVA QCD output in RunIIb1 (left) and RunIIb2+3 (right) data set at pre-tag level, with no triangle cut.*

In order to suppress the multi-jet background while increasing the signal acceptance a boosted decision tree based multivariate analysis technique from the TMVA toolkit package is introduced to replace the triangular and the HT cuts (MVA QCD). It exploits the kinematical and topological differences between multijet and signal events.The MVAQCD output distribution is shown in Figure 7.3.

The following TMVA decision tree settings were used for the training phase:

```
NTrees=200:BoostType=Grad:Shrinkage=0.10:UseBaggedGrad:
GradBaggingFraction=0.6:SeparationType=GiniIndex:nCuts=20:
pruneMethod=CostComplexity:PruneStrength=0.50:NNodesMax=10:
IgnoreNegWeightsInTraining=True
```

The background sample is chosen from a subset of data events with a *loose but not tight* electron. The MVA QCD is trained to distinguish these events from signal ones after preselection cuts. The output of the MVA QCD for both RunIIb1 and RunIIb2 data are shown in Figure 7.2. A cut of this output of -0.8 is approximately 50% efficient for the multijet events which corresponds to a similar performance with the previously applied triangular

and HT cuts but it increases the signal acceptance by about 18%[5].

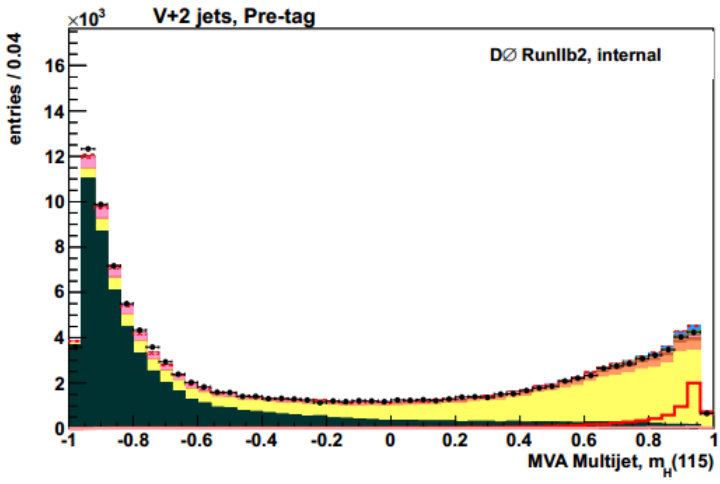

Figure 7.3: *Dijet invariant mass distributions before (left) and after (right) cut in the MVA QCD output.*

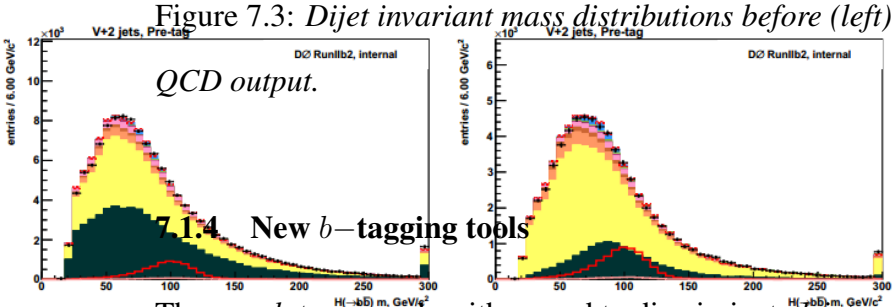

7.1.4 New $b-$tagging tools

The new b-tagging algorithm used to discriminate b jets uses the following:

- The MVA BL is used to discriminate b jets from light jets.
- The MVA BC is trained to differentiate b from c-like quarks, and could potentially help to reduce the $Wc\bar{c}$ background which is still present after the b-tagging.

[5]The value of this cut has been optimized to improve the sensitivity in the 2-tag channel. It will be optimized separately for the double and single-tag data.

- The MVA BB is built to differentiate pairs of b quarks combined in one jet from b jets induced by a single parton which is more likely to be emerging from a Higgs decay into a pair of b-quarks.

Contrary to the previous analysis, an MVA technique (Random Forests) was employed. This technique is the one that will be used in any further analyses in the DØ collaboration. A comparison between the Neural Network and the MVA technique is shown in Figure 7.1.4 Using the MVA techniques, preliminary studies has shown that an improvement of more than 20% can be achieves using the TMVA toolkit package, as shown in Figure 7.1.4. The b-tagging discrimination is used at the final discrimination stage as one of the input variables. This gives information about the jet identity and it provides a better discrimination. Figure 7.1.4 shows a comparison of the limits obtained with 2 L6 b-tagged jets with and without b-tagging discriminant. a 15% decrease in sensitivity is shown compared with the 5.3 fb^{-1} analysis results. The addition of MVA BL output of the two jets would give an enhancement in the final sensitivity in the range of 10% to 20% through the mass range of 100 GeV to 150 GeV.

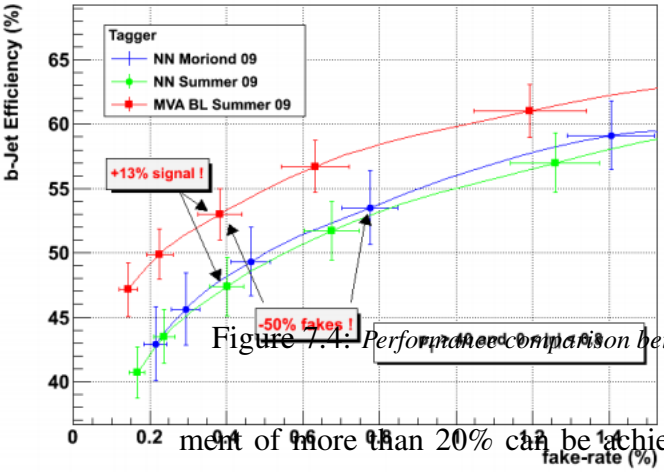

Figure 7.4: *Performance comparison between MVA BL and NN taggers for tighter operating points.*

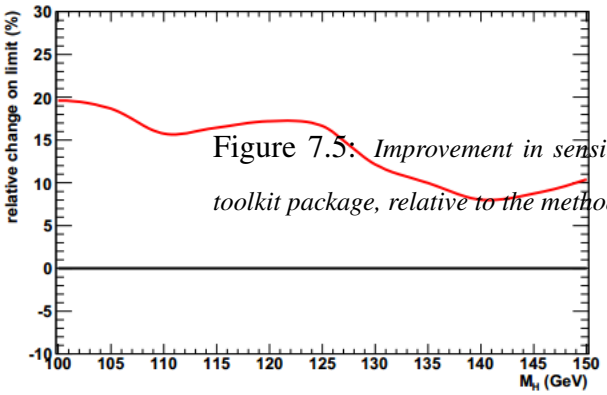

Figure 7.5: *Improvement in sensitivity using MVA technique (Boosted Decision Trees) from the TMVA toolkit package, relative to the method used in the first round of the analysis.*

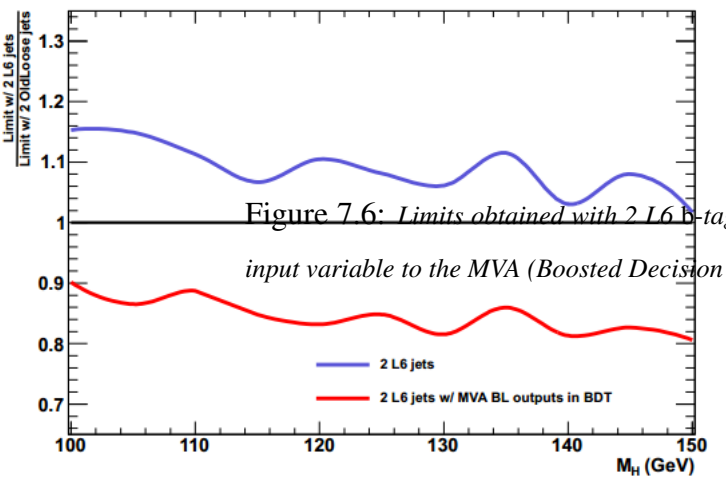

Figure 7.6: *Limits obtained with 2 L6* b*-tagged jets, with and without* b*-tagging discriminants used as an input variable to the MVA (Boosted Decision Trees) Results are compared to the 5.3 fb^{-1} analysis results.*

CHAPTER 8

The discovery of the Higgs Boson

8.1 The LHC

The LHC at CERN is considered the world largest collider. The LHC inherited this title from Fermilab Tevatron when it started circulating beams of protons for the first time on September the 10^{th} 2008. On November 2009 proton beams circulated the LHC again with the first recorded proton-proton collisions occurring 3 days later at the injection energy of 450 GeV per colliding beam.

The LHC operated at 3.5 TeV per colliding beam in 2010 and 2011 then the injected energy was increased to be 4.0 TeV per colliding beam in 2012. The LHC is also used to accelerate lead nuclei for the ALICE experiment.

Among the problem to be studied by the LHC and its experiments are:

- Are the masses of elementary particles actually generated by the Higgs mechanism via electroweak symmetry breaking? (solved)

- Is supersymmetry, an extension of the Standard Model and Poincar symmetry, realized in nature, implying that all known particles have supersymmetric partners?[1] [124]

- Are there extra dimensions, as predicted by various models based on string theory, and can we detect them?

[1]The reader may consult the author's Masters' thesis for a thorough introduction to the Minimal Supersymmetric Standard Model Theory. http://arxiv.org/abs/hep-Cph/0608168

- What is the nature of the dark matter that appears to account for 27% of the mass-energy of the universe?
- Are electroweak force and the strong nuclear force just different manifestations of one universal unified force, as predicted by various Grand Unification Theories.
- Why is the fourth fundamental force (gravity) so many orders of magnitude weaker than the other three fundamental forces? (The Hierarchy problem)
- Are there additional sources of quark flavor mixing, beyond those already predicted within the Standard Model?
- Why are there apparent violations of the symmetry between matter and antimatter? (CP violation)

The LHC is built inside a tunnel, part of it used before to host CERN's LEP electron-positron, (e^-e^+), linear collider. Approximately 1232 dipole magnets keep the beams on their circular path, while more than 392 quadrupole magnets are used to keep the beams focused at the 4 interaction points, where the two beams will cross each other. Almost a 100 tonnes of super-fluid helium 4 is used to cool down the magnets at their operating temperature of 1.9 K (-271.25 °C.) The superconducting quadrupole electromagnets used to direct the beams were build at Fermilab using the expertise of the Tevatron experts. A schematic diagram that shows the LHC and the participating experiments is shown in Figure 8.1. In the next few sections, we will concentrate on the work of the ATLAS collaboration. CMS collaboration has also, simultaneously, published their findings, in which they announced the observation of the Higgs boson [125]. Figure 8.2 shows the Higgs signal from the diphoton invariant mass distribution obtained by the CMS collaboration.

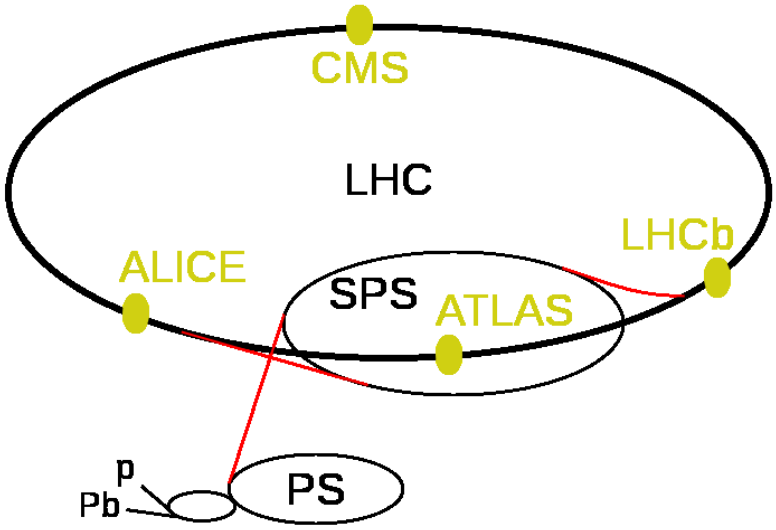

Figure 8.1: The LHC. The 4 experiments can be seen.

8.2 The ATLAS Detector

The ATLAS detector [126–129] is a multipurpose particle physics apparatus with forward-backward symmetric cylindrical geometry. The inner tracking detector (ID) consists of a silicon pixel detector, a silicon microstrip detector (SCT), and a straw-tube transition radiation tracker (TRT). The ID is surrounded by a thin superconducting solenoid which provides a 2 T magnetic field, and by high-granularity liquid-argon (LAr) sampling electromagnetic calorimetry. The electromagnetic calorimeter is divided into a central barrel (pseudorapidity[2] $|\eta| < 1.475$) and end-cap regions on either end of the detector ($1.375 < |\eta| < 2.5$ for the outer wheel and $2.5 < |\eta| < 3.2$ for the inner wheel). In the region matched to the ID ($|\eta| < 2.5$), it is radially segmented into three layers. The first layer has a fine segmentation in η to facilitate e/γ separation from π^0 and to improve the res-

[2]ATLAS uses a right-handed coordinate system with its origin at the nominal interaction point (IP) in the center of the detector, and the z-axis along the beam line. The x-axis points from the IP to the center of the LHC ring, and the y-axis points upwards. Cylindrical coordinates (r, ϕ) are used in the transverse plane, ϕ being the azimuthal angle around the beam line. Observables labeled "transverse" are projected into the $x-y$ plane. The pseudorapidity is defined in terms of the polar angle θ as $\eta = -\ln\tan(\theta/2)$.

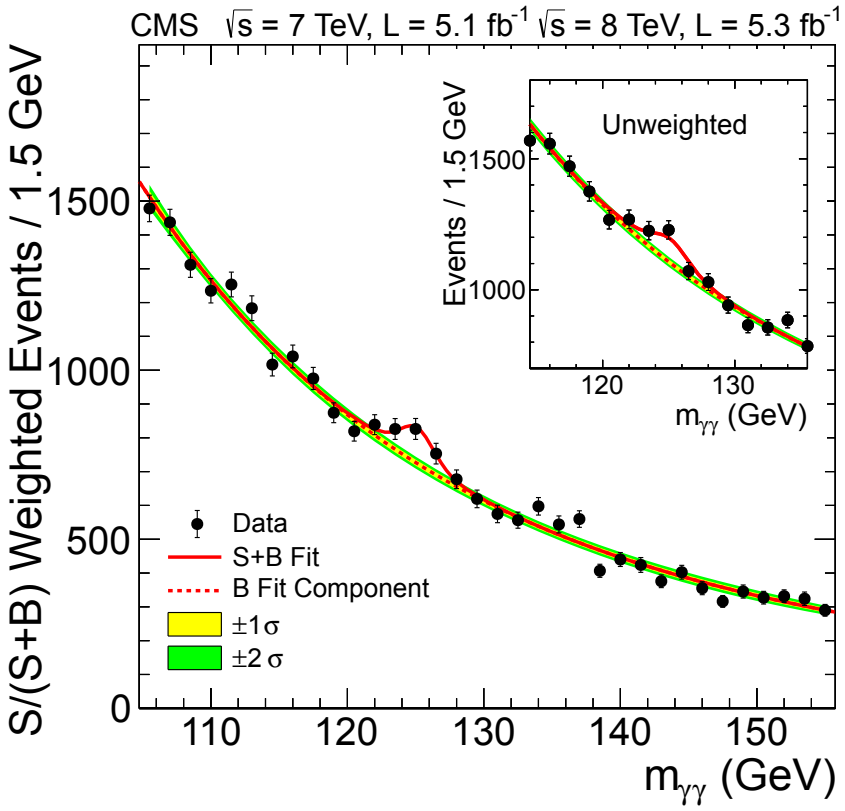

Figure 8.2: The diphoton invariant mass distribution with each event weighted by the $\frac{S}{S+B}$ value of its category. The lines represent the fitted background and signal, and the colored bands represent the ± 1 and ± 2 standard deviation uncertainties in the background estimates. The inset shows the central part of the unweighted invariant mass distribution.

olution of the shower position and direction measurements. In the region $|\eta| < 1.8$, the electromagnetic calorimeter is preceded by a presampler detector to correct for upstream energy losses. An iron-scintillator/tile calorimeter gives hadronic coverage in the central rapidity range ($|\eta| < 1.7$), while a LAr hadronic end-cap calorimeter provides coverage over $1.5 < |\eta| < 3.2$. The forward regions ($3.2 < |\eta| < 4.9$) are instrumented with LAr calorimeters for both electromagnetic and hadronic measurements. The muon spectrometer (MS) surrounds the calorimeters and consists of three large air-core superconducting magnets providing a toroidal field, each with eight coils, a system of precision tracking chambers, and fast detectors for triggering. The combination of all these systems provides

charged particle measurements together with efficient and precise lepton and photon measurements in the pseudorapidity range $|\eta| < 2.5$. Jets and $\not{E}_T$ are reconstructed using energy deposits over the full coverage of the calorimeters, $|\eta| < 4.9$.

8.2.1 Signals at the ATLAS

At the ATLAS detector the Higgs boson was discovered through the following processes:

1. $H \to ZZ^{(*)} \to 4\ell$

   The search for the SM Higgs boson through the decay $H \to ZZ^{(*)} \to 4\ell$, where $\ell = e$ or μ, provides good sensitivity over a wide mass range (110-600 GeV), largely due to the excellent momentum resolution of the ATLAS detector. For this analysis, the ATLAS collaboration searched for "a"/"the" Higgs boson candidates by selecting two pairs of isolated leptons, each of which is comprised of two leptons with the same flavour and opposite charge. The expected cross section times branching ratio for the process $H \to ZZ^{(*)} \to 4\ell$ with $m_H = 125\,GeV$ is 2.2 fb for $\sqrt{s} = 7\,TeV$ and 2.8 fb for $\sqrt{s} = 8\,TeV$.

   The expected signal significances for a Higgs boson with $m_H = 125\,GeV$ are 1.6 σ for the $7\,TeV$ data and 2.1 σ for the $8\,TeV$ data. The invariant mass distribution for the sub-leading lepton pair is shown in Figure 8.3

2. $H \to \gamma\gamma$ channel

   ATLAS search through the decay $H \to \gamma\gamma$ *considered the golden channel for ATLAS*, was performed in the mass range between 110 GeV and 150 GeV. background process for this search comes mainly from the SM diphoton production ($\gamma\gamma$.) Some contributions also come from γ+jet and jet+jet production with one or two jets misidentified as photons (γj and jj) and some other background processes come from the Drell-Yan process. The 7 TeV data was combined with those from the 8 TeV data. The distributions of the invariant mass, $m_{\gamma\gamma}$, of the diphoton events, summed

over all categories, are shown in Figure 8.4 (a) and (b). The result of a fit including a signal component fixed to $m_H = 126.5$ GeV and a background component described by a fourth-order Bernstein polynomial is superimposed.

3. $H \to WW^{(*)} \to e\nu\mu\nu$ channel

   The signature for this channel is two opposite-charge leptons with large transverse momentum and a large momentum imbalance in the event due to the escaping neutrinos. The dominant backgrounds are non-resonant WW, $t\bar{t}$, and Wt production, all of which have real W pairs in the final state.

   Figure 8.5 shows the distribution of the transverse mass after all selection criteria used by the ATLAS collaboration applied. This channel although highly sensitive was of low resolution which would have been used to confirm results obtained from the above two channels.

8.3 The Higgs Observation

A significant gain in sensitivity was obtained by the addition of the 8 TeV data for the $H \to ZZ^{(*)} \to 4\ell$, $H \to \gamma\gamma$ and $H \to WW^{(*)} \to e\nu\mu\nu$ channels as well as the improvements of the analyses of the 7 TeV data in the first two of these channels.

8.3.1 The Excluded Mass Range

The combined 95% CL exclusion limits on the production of the SM Higgs boson, expressed in terms of the signal strength parameter μ, as found by the ATLAS collaboration are shown in Figure 8.6 (a) as a function of m_H . The expected 95% CL exclusion region covers the m_H range from 110 GeV to 582 GeV. The observed 95% CL exclusion regions are 111–122 GeV and 131–559 GeV. Three mass regions are excluded at 99% CL, 113–114, 117–121 and 132–527 GeV, while the expected exclusion range at 99% CL is 113–532 GeV.

8.3.2 Observation of an Excess of Events

The ATLAS Collaboration could observe an excess of events near m_H =126 GeV in the $H \to ZZ^{(*)} \to 4\ell$ and $H \to \gamma\gamma$ channels, both of which provided fully reconstructed candidates with high resolution in invariant mass, as shown in Figures 8.8(a) and 8.8(b). These excesses are confirmed by the highly sensitive but low-resolution $H \to WW^{(*)} \to \ell\nu\ell\nu$ channel, as shown in Figure 8.8(c). The observed local p_0 values from the combination of channels, using the asymptotic approximation, are shown as a function of m_H in Figure 8.6(b) for the full mass range and in Figure 8.7 for the low mass range. The largest local significance for the combination of the 7 and 8 TeV data is found for a SM Higgs boson mass hypothesis of m_H=126.5 GeV, where it reaches $6.0\,\sigma$, with an expected value in the presence of a SM Higgs boson signal at that mass of $4.9\,\sigma$.For the 2012 data alone, the maximum local significance for the $H \to ZZ^{(*)} \to 4\ell$, $H \to \gamma\gamma$ and $H \to WW^{(*)} \to e\nu\mu\nu$ channels combined is 4.9 σ, and occurs at $m_H = 126.5$ GeV (3.8 σ expected).

The global significance of a local $5.9\,\sigma$ excess anywhere in the mass range 110–600 GeV was estimated to be approximately 5.1 σ, increasing to 5.3 σ in the range 110–150 GeV , which is approximately the mass range not excluded at the 99% CL by the LHC combined SM Higgs boson search [130].

The final result from the ATLAS Collaboration was:

> The Standard Model Higgs boson is excluded at 95% CL in the mass range 111–559 GeV, except for the narrow region 122–131 GeV. In this region, an excess of events with significance $5.9\,\sigma$, corresponding to $p_0 = 1.7 \times 10^{-9}$, is observed. The excess is driven by the two channels with the highest mass resolution, $H \to ZZ^{(*)} \to 4\ell$ and $H \to \gamma\gamma$, and the equally sensitive but low-resolution $H \to WW^{(*)} \to \ell\nu\ell\nu$ channel. Taking into account the entire mass range of the search, 110–600 GeV, the global significance of the excess is $5.1\,\sigma$, which corresponds to $p_0 = 1.7 \times 10^{-7}$.

The final result from the CMS Collaboration was:

> The search is performed in five decay modes: $\gamma\gamma$, ZZ, W^+W^-, $\tau^+\tau^-$, and $b\bar{b}$. An excess of events is observed above the expected background, with a local significance of 5.0 σ, at a mass near 125 GeV, signaling the production of a new particle. The expected local significance for a standard model Higgs boson of that mass is 5.8 σ. The global p-value in the search range of 115–130 (110–145) GeV corresponds to 4.6 σ (4.5 σ). The excess is most significant in the two decay modes with the best mass resolution, $\gamma\gamma$ and ZZ, and a fit to these signals gives a mass of $125.3 \pm 0.4(\text{stat.}) \pm 0.5(\text{syst.})$ GeV. The decay to two photons indicates that the new particle is a boson with spin different from one. The results presented here are consistent, within uncertainties, with expectations for a standard model Higgs boson.

8.4 Contribution from the Tevatron

The Tevatron was shot down for the last time on September the 30^{th} 2011. The data collected by the two collaborations, DØ and CDF is almost 10 fb^{-1} per experiment. Each experiment by itself could not verify the existence of the SM Higgs boson, but the combined result from both experiments was very interesting because the data was enough to make an announcement of an evidence of the existence of a boson produced in association with a W vector boson that decay into a pair of $b-$quarks. The announcement was made on July, 2^{nd} 2012, two days before the announcement of the observation of the Higgs boson at CERN. The evidence had a standard deviation of 3.1 σ [131]. The tevatron results are shown in Figure 8.9, Figure 8.10 and Figure 8.11.

Tevatron collaborations had served their purposes very well. A good portion of researchers at both ATLAS and CMS had their training at either DØ or CDF (and sometimes both.) New techniques developed and tested at the DØ and CDF experiments were applied directly to data collected by ATLAS and CMS. The Multivariate analyses technique, for

example, was the technique used by ATLAS and CMS for the separation between the signal and background. The Random Forest technique was the main technique used in the Higgs searches at the Tevatron. Also, as said earlier, many significant parts of the LHC were manufactures and developed by the experts and technicians at the Tevatron. Thus one would conclude that thanks to the work of thousands of people at the Tevatron and the LHC and their respective collaborations we could have one step further toward knowing more about some of the subtle mysterious questions of the universe we live in.

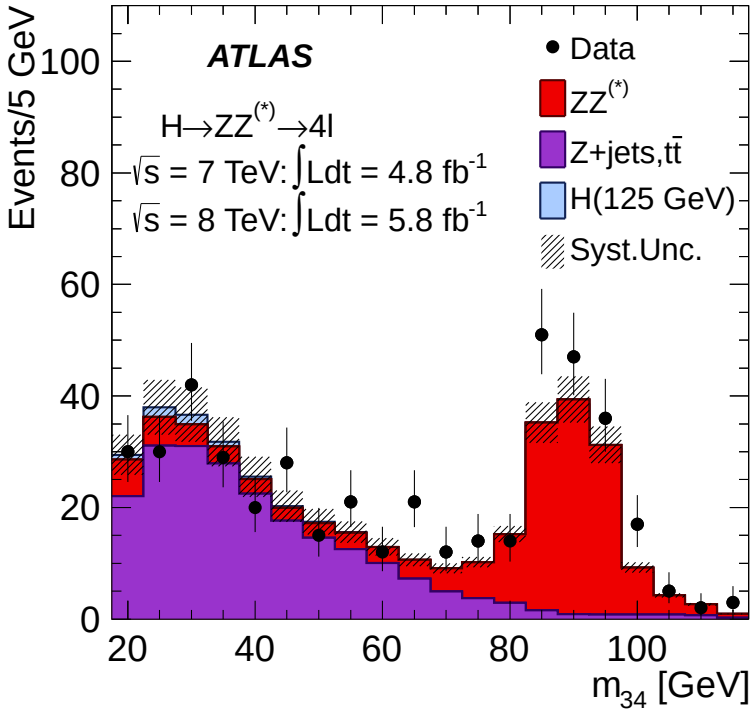

Figure 8.3: Invariant mass distribution of the sub-leading lepton pair (m_{34}) for a sample defined by the presence of a Z boson candidate and an additional same-flavor electron or muon pair, for the combination of $\sqrt{s} = 7\,TeV$ and $\sqrt{s} = 8\,TeV$ data in the entire phase-space of the analysis after the kinematic selections described in the text. Isolation and transverse impact parameter significance requirements are applied to the leading lepton pair only. The MC is normalized to the data-driven background estimations. The relatively small contribution of a SM Higgs with $m_H = 125\,GeV$ in this sample is also shown.

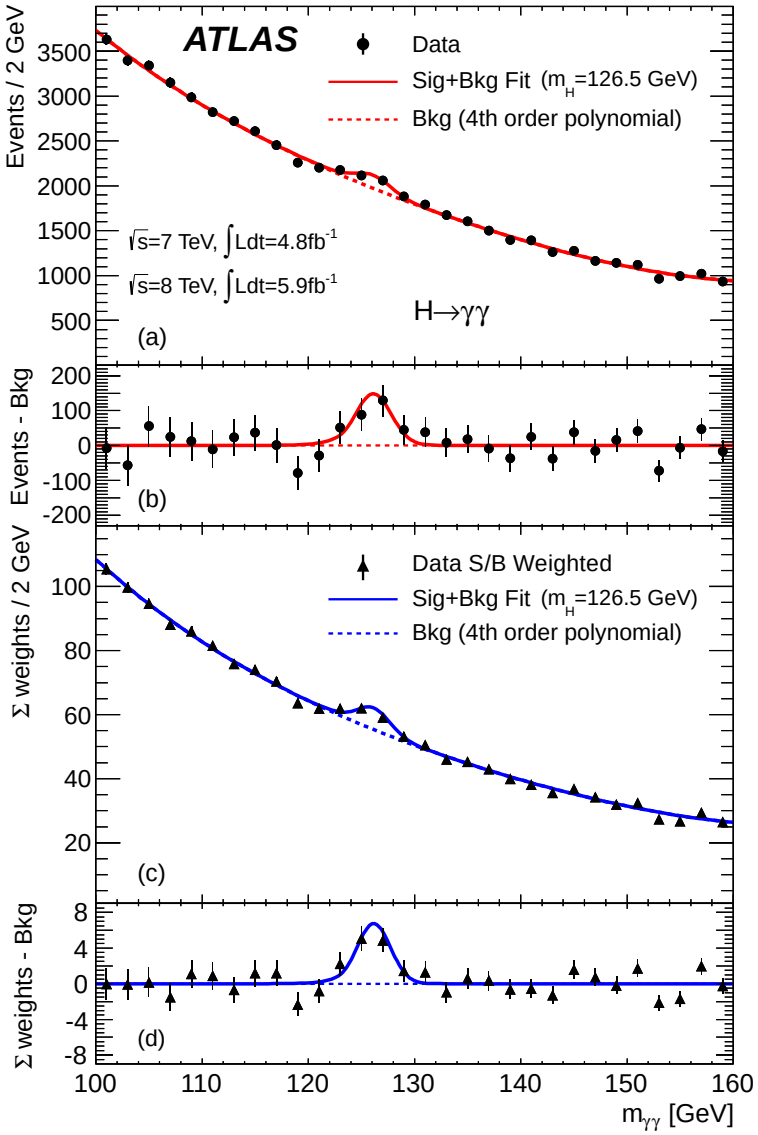

Figure 8.4: The distributions of the invariant mass of diphoton candidates after all selections for the combined 7 TeV and 8 TeV data sample. The inclusive sample is shown in (a) and a weighted version of the same sample in (c). The result of a fit to the data of the sum of a signal component fixed to $m_H = 126.5$ GeV and a background component described by a fourth-order Bernstein polynomial is superimposed. The residuals of the data and weighted data with respect to the respective fitted background component are displayed in (b) and (d)

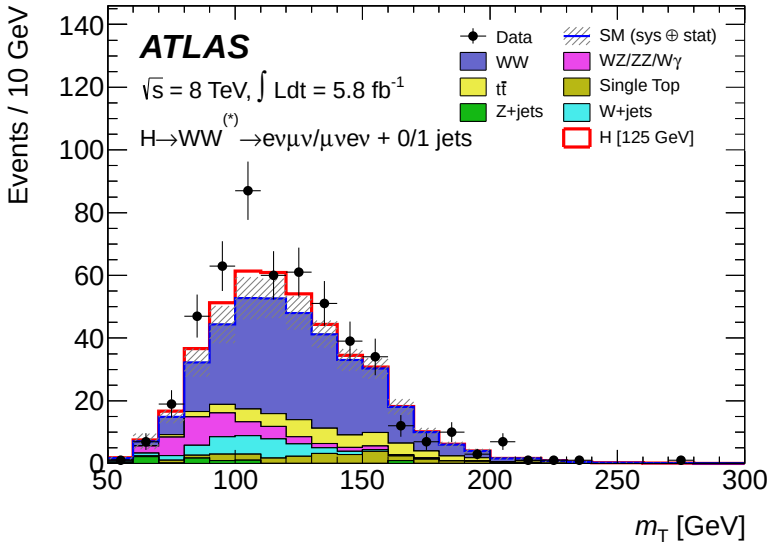

Figure 8.5: Distribution of the transverse mass, m_{T}, in the 0-jet and 1-jet analyses with both $e\mu$ and μe channels combined, for events satisfying all selection criteria. The expected signal for $m_H = 125$ GeV is shown stacked on top of the background prediction. The W+jets background is estimated from data, and WW and top background MC predictions are normalized to the data using control regions. The hashed area indicates the total uncertainty on the background prediction.

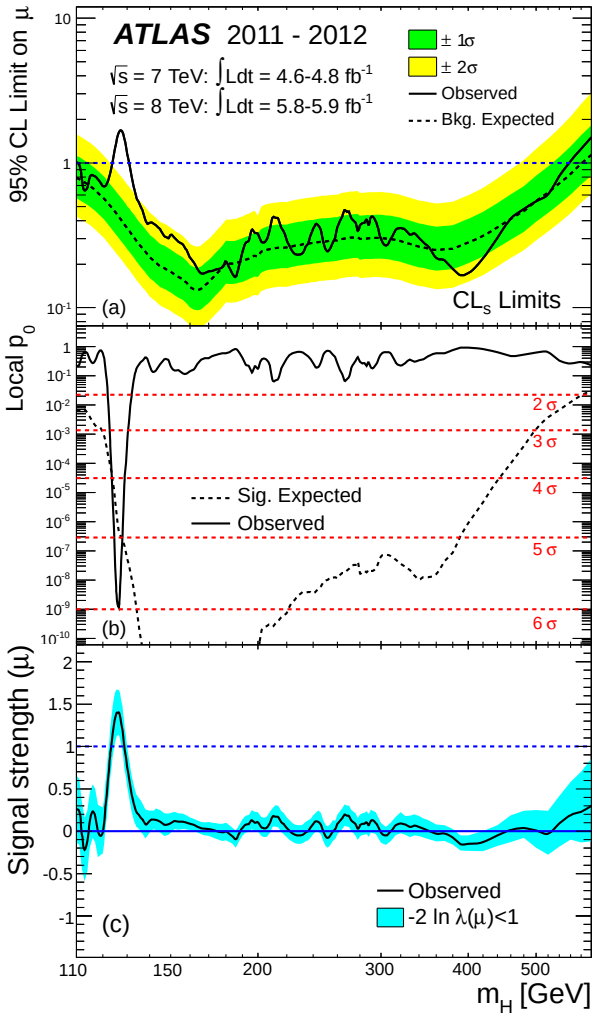

Figure 8.6: Combined search results: (a) The observed (solid) 95% CL limits on the signal strength as a function of m_H and the expectation (dashed) under the background-only hypothesis. The dark and light shaded bands show the $\pm 1\sigma$ and $\pm 2\sigma$ uncertainties on the background-only expectation. (b) The observed (solid) local p_0 as a function of m_H and the expectation (dashed) for a SM Higgs boson signal hypothesis ($\mu = 1$) at the given mass. (c) The best-fit signal strength $\hat{\mu}$ as a function of m_H . The band indicates the approximate 68% CL interval around the fitted value.

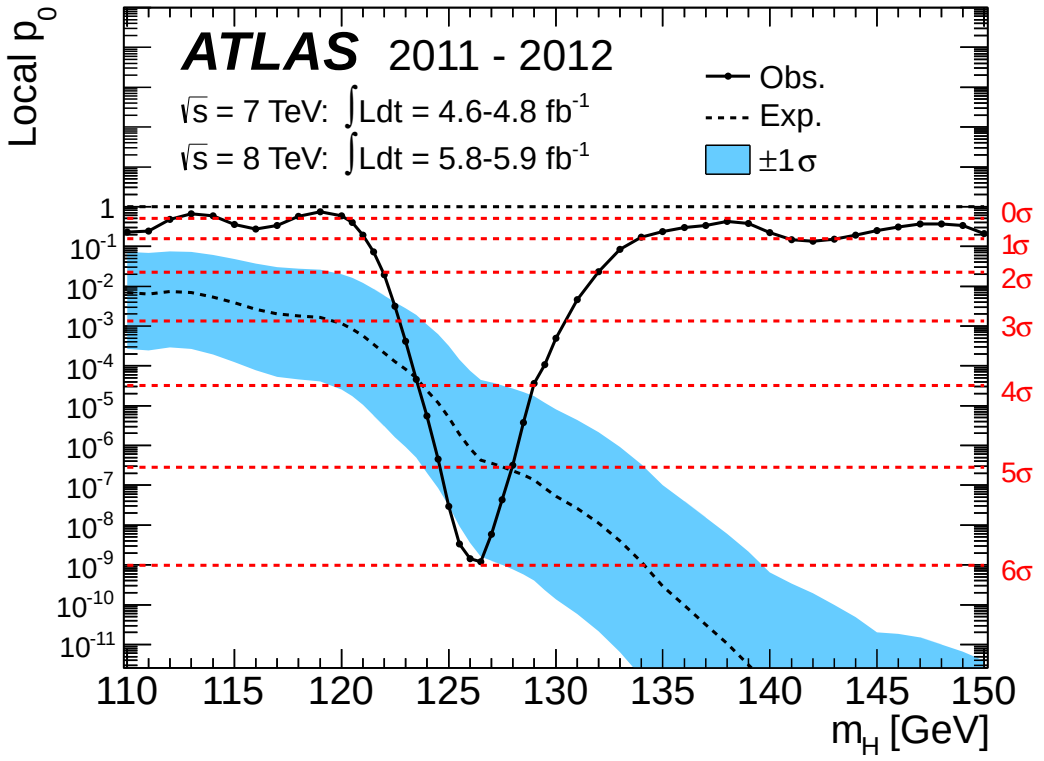

Figure 8.7: The observed (solid) local p_0 as a function of m_H in the low mass range. The dashed curve shows the expected local p_0 under the hypothesis of a SM Higgs boson signal at that mass with its $\pm 1\sigma$ band. The horizontal dashed lines indicate the p-values corresponding to significances of 1 to 6 σ.

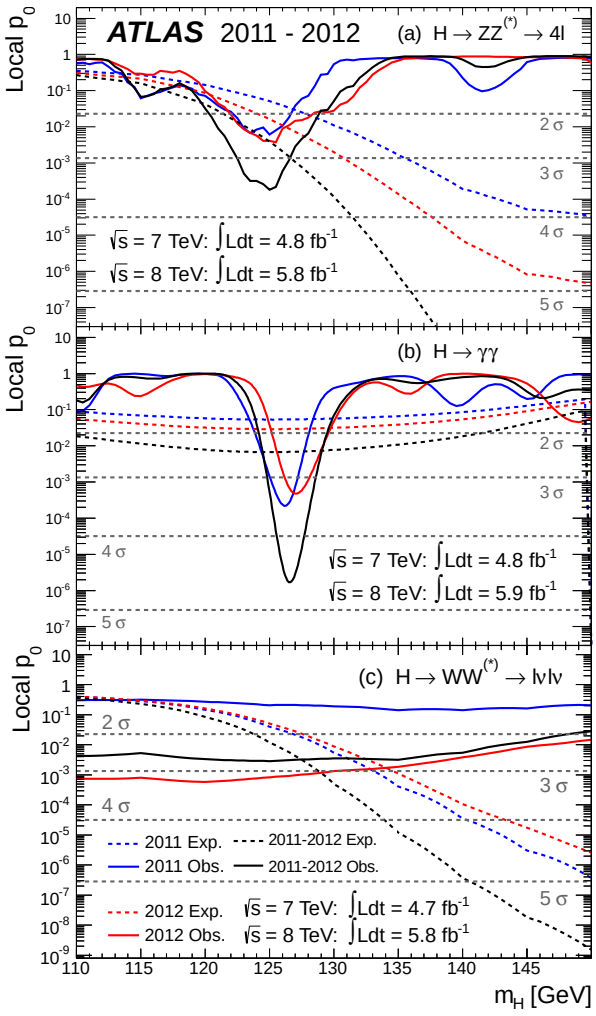

Figure 8.8: The observed local p_0 as a function of the hypothesized Higgs boson mass for the (a) $H\to ZZ^{(*)}\to 4\ell$ (b) $H\to\gamma\gamma$ and (c) $H\to WW^{(*)}\to \ell\nu\ell\nu$ channels. The dashed curves show the expected local p_0 under the hypothesis of a SM Higgs boson signal at that mass. Results are shown separately for the $\sqrt{s}=7$ TeV data, the $\sqrt{s}=8$ TeV data, and their combination (black).

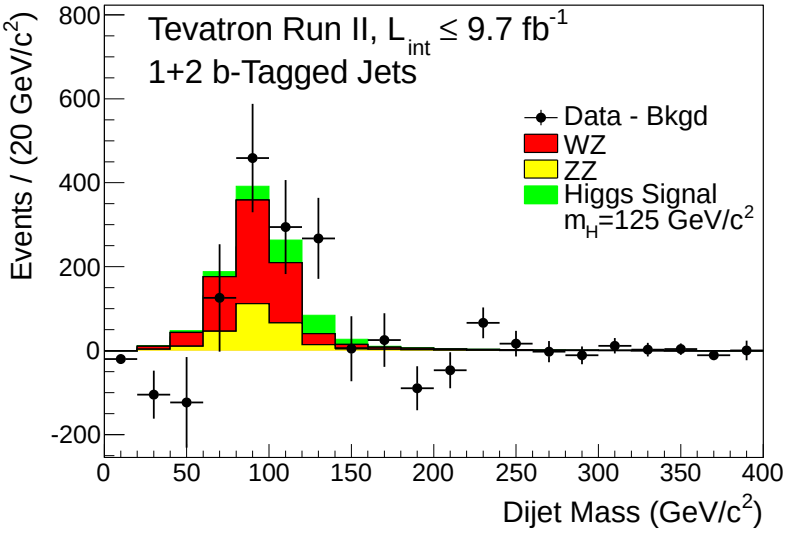

Figure 8.9: Background-subtracted distribution of the reconstructed dijet mass m_{jj}, summed over all input channels. The *VZ* signal and the background contributions are fit to the data, and the fitted background is subtracted. The fitted *VZ* and expected SM Higgs ($m_H = 125$ GeV/c^2) contributions are shown with filled histograms.

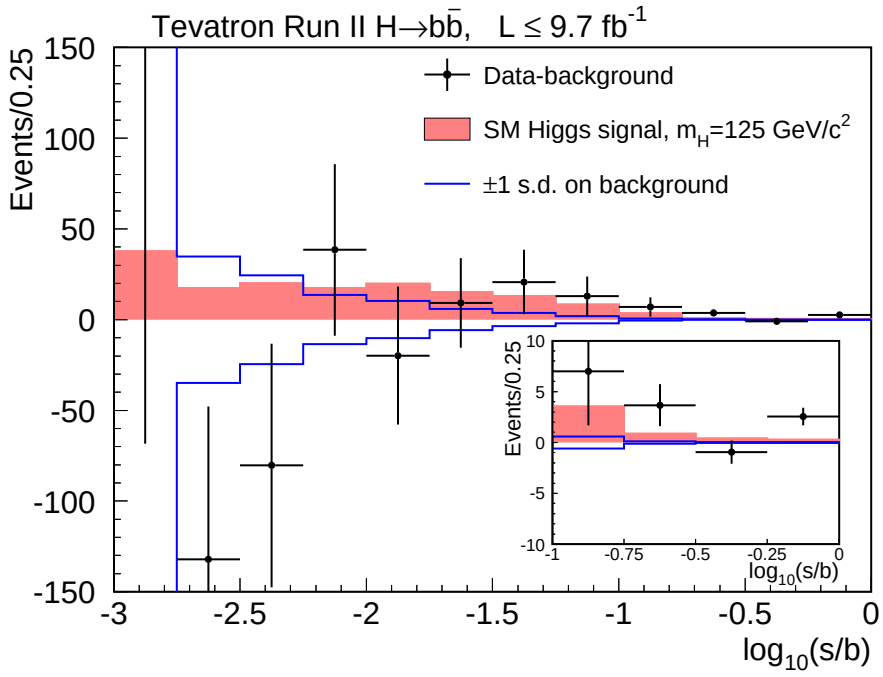

Figure 8.10: Background-subtracted distribution for the discriminant histograms, summed for bins with similar signal-to-background ratio (s/b), for the $H \to b\bar{b}$ ($m_H = 125$ GeV/c^2) search. The solid histogram shows the uncertainty on the background after the fit to the data as discussed in the text. The signal model, scaled to the SM expectation, is shown with a filled histogram. Uncertainties on the data points correspond to the square root of the sum of the expected signal and background yields in each bin.

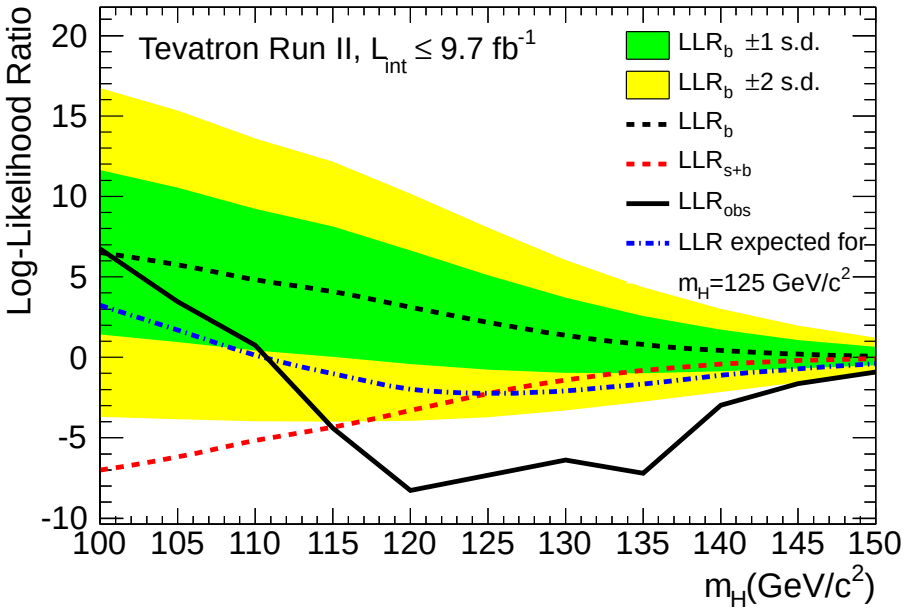

Figure 8.11: The log-likelihood ratio LLR as a function of Higgs boson mass. The dark and light-shaded bands correspond to the regions encompassing 1 s.d. and 2 s.d. fluctuations of the background, respectively. The dot-dashed line shows the median expected LLR assuming the SM Higgs boson is present at $m_H = 125$ GeV/c^2.

CHAPTER 9

Conclusion

Presented here is the search for the Standard Model Higgs boson in the channel $WH \rightarrow l\nu b\bar{b}$ using data collected by the DØ detector at Fermilab. The chosen channel is what used to be called the golden channel in the search for the Higgs boson because it is the most sensitive channel to search for the Higgs boson at the DØ detectors.

The decay of the W boson to a lepton, l and a neutrino, ν, where $l = e\text{or}\mu$ made the reconstruction of both isolated electrons and jets to be done mainly from their characteristic signature in the calorimeter. Muons (μ) were detected with the help of the muon spectrometer. Muons are known to interact weakly with matter, thus they only deposit a tiny fraction of their energy in the electromagnetic calorimeter. Neutrinos (ν), do escape the detector without being detected since they do not interact with the detector and as a result the imbalance in energy in the transverse plan was used to account for them. Measurement of all other objects present in the calorimeter were used in the calculation of the escaped transverse energy due to these neutrinos. For such measurements needed to reconstruct all objects used in this analysis, and for the measurement of particles momenta, an efficient tracking system was used. A good tracking system is important for the reconstruction of jets, muons and electrons identification.

Techniques used in this analysis were powerful enough to reach the highest possible sensitivity in the WH analysis. Identification of jets originating from a $b-$quark via was achieved using the displaced secondary vertices consistent with the presence of a $b-$hadron. Multivariate analysis techniques were used extensively to increase the discrimination power between the signal and background were also used in this analysis. These techniques were

compared with Neural Network technique that was used before and an achievement of more sensitivity was confirmed.

Monte Carlo generators were studied and a deeper knowledge were obtained about their limitations and abilities and also the effect of imperfect detector simulation. identified objects were corrected in order to account for reconstruction and identification differences in data and Monte Carlo. The instrumental background was obtained from a side-band region in data where the use of a precise method to model distribution shapes and normalization.

A good agreement between data and Monte Carlo simulation was obtained, and no signal excess was found in data. An upper observed (expected) limits (for $M_H = 125$ GeV of 0.6 pb (0.64) pb are set at 95% confidence level on the ratio of the WH cross section multiplied by the branching ratio of $H \to b\bar{b}$ to its SM prediction that represent 4.6 (4.9) times the SM expectation. The semi-frequentist approach was used to take into account systematic errors. Systematic errors were found to degrade the sensitivity by almost 20%.

Results presented here were based on an integrated luminosity of 5.3 fb^{-1} and has been published in the *Physics Letter Review* **B** as can be seen in Figure 9.1. The second round of work was based on an integrated luminosity of 6.2 fb^{-1} and was to be published in the *Physics Letter Review* **B**.

Although the search presented here did not lead to an observation of the Higgs boson at the DØ, yet the Multivariate technique used here for the first time in the search of the Standard Model Higgs boson proved to an essential analysis tool. At first it was used in the combined results from both CDF and DØ collaborations that lead to the first evidence of the existence of the Higgs boson by the Tevatron. The multivariate analysis technique was used also, later, by both ATLAS and CMS collaborations in their observation of the Standard Model Higgs boson.

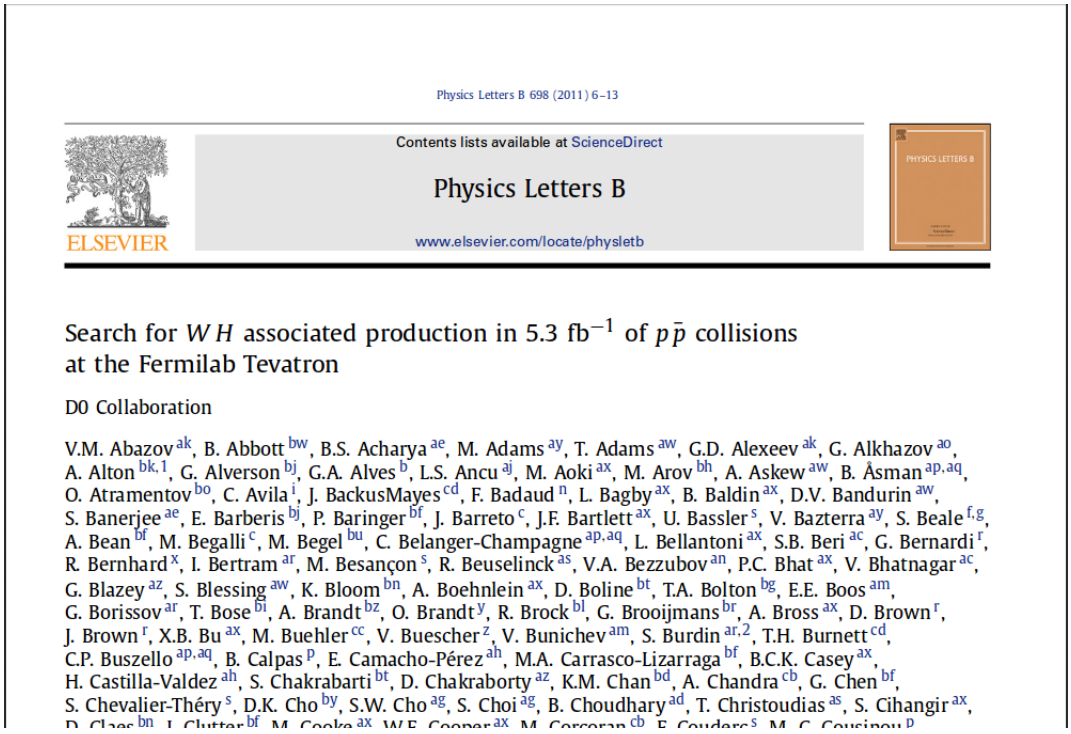

Physics Letters B 698 (2011) 6–13

Contents lists available at ScienceDirect

Physics Letters B

www.elsevier.com/locate/physletb

Search for WH associated production in 5.3 fb^{-1} of $p\bar{p}$ collisions at the Fermilab Tevatron

D0 Collaboration

V.M. Abazov[ak], B. Abbott[bw], B.S. Acharya[ae], M. Adams[ay], T. Adams[aw], G.D. Alexeev[ak], G. Alkhazov[ao], A. Alton[bk,1], G. Alverson[bj], G.A. Alves[b], L.S. Ancu[aj], M. Aoki[ax], M. Arov[bh], A. Askew[aw], B. Åsman[ap,aq], O. Atramentov[bo], C. Avila[i], J. BackusMayes[cd], F. Badaud[n], L. Bagby[ax], B. Baldin[ax], D.V. Bandurin[aw], S. Banerjee[ae], E. Barberis[bj], P. Baringer[bf], J. Barreto[c], J.F. Bartlett[ax], U. Bassler[s], V. Bazterra[ay], S. Beale[f,g], A. Bean[bf], M. Begalli[c], M. Begel[bu], C. Belanger-Champagne[ap,aq], L. Bellantoni[ax], S.B. Beri[ac], G. Bernardi[r], R. Bernhard[x], I. Bertram[ar], M. Besançon[s], R. Beuselinck[as], V.A. Bezzubov[an], P.C. Bhat[ax], V. Bhatnagar[ac], G. Blazey[az], S. Blessing[aw], K. Bloom[bn], A. Boehnlein[ax], D. Boline[bt], T.A. Bolton[bg], E.E. Boos[am], G. Borissov[ar], T. Bose[bi], A. Brandt[bz], O. Brandt[y], R. Brock[bl], G. Brooijmans[br], A. Bross[ax], D. Brown[r], J. Brown[r], X.B. Bu[ax], M. Buehler[cc], V. Buescher[z], V. Bunichev[am], S. Burdin[ar,2], T.H. Burnett[cd], C.P. Buszello[ap,aq], B. Calpas[p], E. Camacho-Pérez[ah], M.A. Carrasco-Lizarraga[bf], B.C.K. Casey[ax], H. Castilla-Valdez[ah], S. Chakrabarti[bt], D. Chakraborty[az], K.M. Chan[bd], A. Chandra[cb], G. Chen[bf], S. Chevalier-Théry[s], D.K. Cho[by], S.W. Cho[ag], S. Choi[ag], B. Choudhary[ad], T. Christoudias[as], S. Cihangir[ax], D. Claes[bn], J. Clutter[bf], M. Cooke[ax], W.E. Cooper[ax], M. Corcoran[cb], F. Couderc[s], M.-C. Cousinou[p]

Figure 9.1: Results obtained in this analysis were published in the journal Physics Letters **B.**

BIBLIOGRAPHY

[1] T. Gadfort *et al.*, "Performance of the D0 NN $b-$ tagging tool on p20 data.," *D0 Internal NOTE 5554*, 2008.

[2] A. Abazov *et al.*, "The Upgraded D0 Detector," *Nucl. Instrum. Meth.*, vol. A565, p. 463, 2006.

[3] Johan Alwall and Stefan Hoche and Frank Krauss and Nilson Lavensson and Leer Loonbald, "Comparative study of various algorithms for merging of parton showers and matrix elements in hadronic collisions.," *Eur. Phys. J.*, vol. C53:473-500, October 2008.

[4] C. W. Walter, "Experimental neutrino physics," *arXiv:hep-ex/0810.3937*, 2008.

[5] A. D. Dolgov, "Neutrinos in cosmology," *arXiv:hep-ph/0202122*, 2002.

[6] S. Lewin, "Dark matter survey," *Astropart. Phys.*, vol. 6, pp. 87–112, 1996.

[7] S. Weinberg, "Theory of dark matter," *Rev. Mod. Phys.*, vol. 61, p. 1, 1989.

[8] A. Albrecht *et al.*, "Report of the dark energy task force," *arXiv:astro-ph/0609591*, 2006.

[9] PARTICLE Data Group, "The review of particle physics," *http://pdg.lbl.gov/*, 2010.

[10] C. Quigg, *Gauge Theories of the Strong, Weak, and Electromagnetic Interactions*. Westview Press, first ed., 1983.

[11] A. Djouadi, "Higgs physics: Theory," *arXiv:1203.1252*, 2012.

[12] D. Griffiths, *Introduction to Elementary PARTICLEs*. John Wiley and Sons, Inc., second ed., 2010.

[13] A. Quadt, "Top quark physics at hadron collider," *Eur. Phys. J.*, vol. C48, pp. 835–1000, 2006.

[14] F. Halzen and A. D. Martin, *Qauarks and Leptons*. Wiley, first ed., 1984.

[15] A. Djouadi, "THE ANATOMY OF ELECTRO-WEAK SYMMETRY BREAKING. I: THE HIGGS BOSON IN THE STANDARD MODEL," *arXiv:hep-ph/0503172*, p. 65, 2005.

[16] K. Riesselmann and T. Hambye, "Matching conditions and higgs mass upper bounds revisited," *PRD , arXiv:hep-ph/9610272v2*, vol. 55, pp. 7255–7262, 1997.

[17] Higgs working group. Tevatron New Phenomina, "Combined CDF and D0 Upper Limits on Standard Model Higgs-Boson Production with up to 4.2 fb^{-1} of Data," *arXiv:hep-ex/0903.4001*, 2009.

[18] S. Dawson, "Introduction to electroweak symmetry breaking," *AIP Conf. Proc., arXiv:hep-ph/0812.219v1*, pp. 1116–1123, 2009.

[19] M. Steinhauser and T. Seidensticker, "Second order corrections to the muon lifetime and the semileptonic b decay," *Phys. Lett.*, vol. B467, p. 271, 1999.

[20] K. Nakarama *et al.*, "The review of particle physics," *J. Phys.*, vol. G37, p. 075021, 2010.

[21] ALEPH Collaboration, DELPHI Collaboration, L3 Collaboration, OPAL Collaboration and LEP Working Group for Higgs Boson Searches, "Search for the Standard Model Higgs Boson at LEP," *Phys. Lett. B*, vol. 565, p. 61, 2003.

[22] T. Aaltonen *et al.*, "Combination of Searches For The Higgs Boson Using The Full CDF Data Set," *arXiv:1301.6668*, 2013.

[23] V. M. Abazov *et al.*, "Combined Search For The Higgs Boson With The D0 Experiment," *arXiv:1303.0823*, 2013.

[24] T. Aaltonen *et al.*, "Higgs Boson Studies at The Tevatron," *arXiv:1303.6346*, 2013.

[25] D. Collaboration. `http://www-cbdnew.fnal.gov/operations.html`.

[26] D. Collaboration. `http://www-cbdnew.fnal.gov/operations/rookie_BOOKs/rBOOKs.html`.

[27] M. Schmidt, "Review of negative hydrogen ion sources," in *Linear Accelerator CONFERENCE*, (Albuquerque, MN), September 1990.

[28] J. Conway. `http://www.physics.ucdavis.edu/~conway/research/higgs/smhiggs-ctev.html`.

[29] S. Abachi *et al.*, "The D0 Detector," *Nucl. Instrum. Methods Phys. Res. Sect.*, vol. A 325, p. 393, 1993.

[30] J. Brzezniak *et al.*, "Conceptual Design of a 2 Tesla Superconducting Solenoid for the Fermilab D0 Detector Upgrade.," *FERMILAB-TM*, vol. 1886, 1994.

[31] P. Balm *et al.*, "Magnetic Field Monitors for the D0 Solenoid," *D0 Internal NOTE 3977*, 2001.

[32] R. Angstadt *et al.*, "The layer 0 inner silicon detector of the D0 experiment," *Nucl. Instrum. and Methods*, vol. 662, pp. 298–310, October 2010.

[33] D. Collaboration, "The D0 Upgrade Central Fiber Tracker Technical Design Report," *D0 Internal NOTE*, vol. 4154, 1999.

[34] B. S. Acharya *et al.*, "Technical Design Report of the Central Muon System," *D0 Internal NOTE 3365*, 1998.

[35] G. Alexeev *et al.*, "Technical Design Report for the D0 Forward Muon Tracking Detector Based on Mini-drift Tubes," *D0 Internal NOTE 3366*, 1997.

[36] D. Collaboration, "D0 offline reconstruction program.." http://www-⊂d0.fna.gov/computing/algorithms/howto/howtoreco.html.

[37] D. Collaboration, "Runii event data model.." http://www-⊂d0.fnal.gov/software/data_model/data_model.html#docs.

[38] G. Borisov, "Ordering a Chaos or Technical Details of AA Tracking,," *All D0 Meeting*, February 2000. Also available as http://www-⊂d0.fnal.gov/globaltracking/talks/20030228/talk-⊂adm-⊂030228.ps.

[39] A. Khanov, "HTF: histogramming method for finding tracks. The algorithm description,," *D0 Internal NOTE 3778*, 2000.

[40] R. Fruhwirth, "Application of Kalman Filtering to Track and Vertex Fitting," *Nucl. Inst. Methods*, vol. A262, 444, 1987.

[41] J. Haley, *First Evidence for W W and W Z Diboson Production with Semi-Leptonic Decays at a Hadron Collider*. PhD Theses, July 2009.

[42] P. V. C. Hough, "Machine Analysis of Bubble Chamber Pictures," *Proc. Int. Conf. High Energy Accelerators and Instrumentation*, March 1959.

[43] J. BackusMayes, *Search for associated production of Z and Higgs bosons in proton-antiproton collisions at 1.96 TeV.* BiblioLab, first ed., September 2011.

[44] C. Tully and A. Schwartzman, "Primary Vertex Reconstruction by means of Adaptive Vertex Fitting," *D0 Internal NOTE 4918*, 2005.

[45] A. Schwartzman and M. Narain, "Probabilistic Primary Vertex Selection," *D0 Internal NOTE 4042*, 2002.

[46] Y. Peters, A. Schwartzman, and M. Strauss, "Certification of the adaptive Primary Vertex in p17.," *D0 Internal NOTE 5192*, 2006.

[47] S. Protopopescu, "Em reconstruction algorithm," *D0 Internal Note*, 1999. Published online: `http://www-⊂d0.fnal.gov/d0dist/dist/packages/emreco/devel/doc/EMReco.ps`.

[48] L. Duflot and M. Ridel, "The CellNN AlgorithmL Cell Level Clustering in the D0 Calorimeter," *D0 Internal NOTE 3923*, 2001.

[49] V. Kausheek, *Search for associated production of W and Higgs bosons in proton-antiproton collisions at 1.96 TeV.* Not Published, first ed., February 2008.

[50] F. Beaudette and J. F. Grivaz, "Road Method: An Algorithm for the Identification of Electrons in Jets," *D0 Internal NOTE 3976*, 2002.

[51] M. Narain, "Electron Identification in the D0 Detector," *DPF 92 FERMILAB-CONF-93-054-E*, march 1993.

[52] A. Kumar and others., "Electron Likelihood Study," *D0 Internal NOTE 4796*, 2005.

[53] M. S. Anzel and J. Hayes, "Comparison of EMcert HMatrix Cuts and Efficiencies in Data and Monte Carlo," *D0 Internal NOTE 5075*, 2006.

[54] C. Schwanenberger, "Electron Likelihood Effeciency in p17," *D0 Internal NOTE 5114*, 2006.

[55] N. Hadley, "Cone Algorithm For Jet Finding.," *D0 Internal NOTE 904*, 1989.

[56] G. Blazey *et al.*, "Run II Jet Physics.," *ArXiv:hep-ex/0005012*, 2000.

[57] E. Busato and B. Andrieu, "Jet Algorithms in the D0 RunII Software: Description and Users Guide.," *D0 Internal NOTE 4457*, 2004.

[58] G. Bernardi, B. Oliver, B. Kneuteson, and M. Strovink., "NADA: A New Event by Event Hot Cell Killer.," *D0 Internal NOTE 3687*, 1999.

[59] G. Bernardi and S. Trincaz-Duvoid., "Improvement of the NADA algorithm: Hot Cells Killing in D0 RunII Data.," *D0 Internal NOTE 4057*, 2002.

[60] U. Bassler and G. Bernardi., "Towards a coherent Treatment of Calorimetric Energies: Missing Transverse Energy, Jets, EM objects and the T42 Algorithm.," *D0 Internal NOTE 4124*, 2003.

[61] G. B. J. Vlimant, U. Bassler and S. Trincaz-Duvoid., "Technical Description of The T42 Algorithm for The Calorimeter Noise Suppression.," *D0 Internal NOTE 4146*, 2003.

[62] G. Bernardi, E. Busato, and J. Vlimant., "Improvements from the T42 Algorithm on calorimeter Objects Reconstruction.," *D0 Internal NOTE 4335*, 2004.

[63] L. Swayer and A. Stone, "Missing E_TReconstruction: Variables and Methods.," *D0 Internal NOTE 3957*, 2003.

[64] S. Trincaz-Duvoid and P. Verdier, "Missing E_TReconstruction in p17.," *D0 Internal NOTE 4474*, 2004.

[65] C. Gerber, "Taggability in Pass2 p14 Data.," *D0 Internal NOTE 4995*, 2005.

[66] A. Schwartzman and M. Narain, "Track-Jet Studies using 3D Simple Jet Cone Algorithm.," *D0 Internal NOTE 3919*, 2001.

[67] R. Demina *et al.*, "b-tagging with counting signed impact parameter method.," *D0 Internal NOTE 4049*, 2002.

[68] D. Bloch *et al.*, "Update of the jlip b-tagger performance in p14/pass2 with jes 5.3," *D0 Internal NOTE 4824*, 2005.

[69] M. Anastasoaie *et al.*, "Performance of the nn b-tagging tool on p17 data.," *D0 Internal NOTE 5213*, 2007.

[70] R. Angstadt *et al.*, "The layer 0 inner silicon detector of the d0 experiment," *Nucl. Inst. Meth. A*, 2009. Published online: `http://arxiv.org/abs/0911.2522`.

[71] M. Abolins *et al.*, "Design and implementation of the new d0 level-1 calorimeter trigger," *Nucl. Inst. Meth.*, vol. A 584, 2008.

[72] B. Andersson *et al.*, "Parton fragmentation and string dynamics," *Phys. Rep.*, vol. 97, pp. 31–45, July 1983.

[73] H. Lai, "Improved parton distribution from global analysis of recent deep inelastic scattering and inclusive jet data.," *Phys. Rev. D.*, vol. D55, 1997. Available from `http://hep.pa.msu.edu/people/wkt/cteq6/cteq6pdf.html`.

[74] J. Pumplin, "New generation of parton distributions with uncertainties from global qcd analysis.," *JHEP07*, vol. 012, 2002. arXiv:hep-ph/0201195v3.

[75] T. Hahn *et al.*, "Sm and mssm higgs boson production cross sections at the tevatron and the lhc," *arXiv:hep/ph:060308v2*, 2006.

[76] FERMILAB-TM-2365, "lm_access package," November 2007.

[77] Luminosity ID Group, "Improved determination of the DØ luminosity," November 2006. DØ NOTE 5140.

[78] G. Bernardi, D. Brown, J. Brown, M. Cooke, Y. Enari, S. Greder, Hatim Hegab, K. Herner, N. Huske, J. Lellouch, J. Qian, C. Xu, "Search for WH Associated Production with 5.3 fb^{-1} of RunII Data," November 2010. DØ NOTE 5960.

[79] M. Agelou and others, "Top Trigger Efficiency Measurements and the "top_trigger" Package," July 2004. DØ NOTE 4512.

[80] L. Christofek, "Text and Trigger Tables for Publications for the Top Group," January 2006. DØ NOTE 4978.

[81] Mark Owen and Marc Hohlfeld, "Trigger Efficiencies for the OR of Single Electron Triggers in p17 Data," May 2007. DØ NOTE 5409.

[82] "caf_trigger," Published online: `http://www.phys.ualberta.ca/$\sim$kwchan/d0/caf\_trigger/readme.html`.

[83] G. Bernardi and others, "Improved Limits on WH Production using a Neural Net Algorithm with 1 fb^{-1} of Run IIa Data," September 2008. DØ NOTE 5713.

[84] O. Atramentov and others, "Electron and Photon Identification with p20 data," September 2008. DØ NOTE 5761.

[85] T. Gadford and others, "MuonID Certification for p17 Data," April 2007. DØ NOTE 5157.

[86] O. Brandt and others, "Muon Identication Certication for the Summer 2009 Extended Dataset (Run IIb-1 and -2)," March 2010. DØ NOTE 6025.

[87] Stephanie Beauceron and Gregorio Bernardi, "A Search for Wbb and WH production in ppbar collisions at 1.96 TeV (in French)," October 2004. DØ NOTE 4633.

[88] Romain Madar and Fabrice Couderc, "Tau lepton identification using MVA optimizations," April 2011. DØ NOTE 6061.

[89] J. R. Vlimant and others, "Technical description of the T42 algorithm for the calorimeter noise suppression.," April 2004. DØNOTE 4146.

[90] G. Bernardi and E. Busato and J.R. Vlimant, "Improvements from the T42 Algorithm on Calorimeter Objects Reconstruction.," November 2004. DØNOTE 4335.

[91] N. Makovec and J.-F. Grivaz, "Shifting, Smearing and Removing Simulated Jets.," March 2005. DØNOTE 4914.

[92] Daniel Boline, "Jet Multiplicity Dependent Reweithing of the Z Boson pT in p20," October 2010. DØNOTE 5569.

[93] Mansoora Shamim and Tim Bolton, "Generator Level Rewighting of pT of Z Boson.," May 2010. DØNOTE 5565.

[94] G. Husketh, "W pT Re-weighting for ASlpgen and Pythia.," March 2011. DØNOTE 5786.

[95] C.M. Anastasoaie, S.L. Robinson and T. Scanlon, "Performance of the NN b-tagging Tool on p17 Data.," September 2007. DØNOTE 5213.

[96] C. Clément and others, "Measurement of the $\mathrm{t\bar{t}}$ production cross section at $\sqrt{s} = 1.96$ TeV using lifetime tagging.," April 2006. DØNOTE 4900.

[97] L. Breiman and J. Friedman and C.J. Stone and R.A. Olsen, *Classification and Regression Trees*. Wadsworth, Stamford, Second ed., 1984.

[98] J. R. Quinlan, "Induction of Decision Trees.," *Machine Learning*, vol. 1, pp. 81–106, April 1986.

[99] Dag Gillberg, *Observation of Signle Top Quark Production*. Springer, First ed., 2011.

[100] Gini, C., "Variabilta e Mutabilita," in *Memorie di Metodologica Statistica* (Pizetti, E. and Salvemini, T., ed.), Rome: Libreria Eredi Virgilio Veschi, 1912.

[101] I. Narsky, "StatPatternRecognition: A C++ Package for Statistical Analysis of High Energy Physics Data," 2005. Published in Cornell ArXive: ArXiv:physics/0507143[physics-data-an].

[102] Breiman, L., "bagging Predictors," *Machine Learning*, vol. 26, pp. 123–140, 2006.

[103] Efron, B. and Tibshirani, R. J., *An introduction to the bootstrap*. Chapman&Hall, 1993.

[104] I. Narsky, "Optimization od Signal Significance by Bagging Decision Trees," 2005. Published in Cornell ArXive: ArXiv:physics/0507157[physics-data-an].

[105] A. Hoecker, P. Speckmayer, J. Stelzer, J. Therhaag, E. von Toerne, H. Voss, M. Backes, T. Carli, O. Cohen, A. Christov, D. Dannheim, K. Danielowski, S. Henrot-Versille, M. Jachowski, K. Kraszewski, A. Krasznahorkay Jr., M. Kruk, Y. Mahalalel, R. Ospanov, X. Prudent, A. Robert, D. Schouten, F. Tegenfeldt, A. Voigt, K. Voss, M. Wolter, A. Zemla, "TMVA - Toolkit for Multivariate Data Analysis," 2007. Published in Cornell ArXive: ArXiv:physics/0703039[physics-data-an].

[106] DØ Collaboration, "First evidence for the Diboson production in lepton plus jets decays," April 2009. DØNOTE 5544.

[107] D. Collaboration, "Observation of Single Top Quark Production with the D0 Detector," *PRL*, August 2009.

[108] Parke, S. and Veseli, S. *PRD*, vol. 60, p. 093003, 1999.

[109] Berger, V. D and Philips, J. N, *Collider Physics*. Adison-Wisley Publishing Co., First ed., 1987.

[110] Brown, J., *Search for The WH Associated Production in The $l\nu b\bar{b}$ Final State Using The DØ Detector at The Tevatron*. PhD Theses, First ed., September 2011.

[111] Fisher, W., "Collie: A Confidence Level Limit Evaluator.," April 2009. DØNOTE 5595.

[112] Read, A., "Presentation of Search Results: The CL(s) Technique.," *J. PHYS.*, vol. G 28, March 2002.

[113] Junk, T., "Confidence Level Computation For Combining Searches With Small Statistics.," *Nucl. Inst. Meth.*, vol. A 434, pp. 435–443, April 1999.

[114] Bauer, D. and Huang, J. and Zieminski, A., "Studies of Upsilon state production with the DØ detector at FNAL," JULY 2004. DØNote 4264.

[115] Fisher, W and Haley, J. and Price, D., "Studies of Alpgen parameters, corrections and associated uncertainties," April 2009. DØNote 5966.

[116] Bernardi, G. and Choi, S. and Hanagaki, K, "Cross Section Errors Used in the Higgs Searches," April 2006. DØNote 5043.

[117] Private Communications.

[118] Bonciani, R. and others *Nucl. Phys.*, vol. B 529, p. 424, 1998.

[119] T. T. E. Group, "Combination of CDF and D0 Results on the Mass of the Top Quark," *PRL*, August 2006.

[120] Harris, B. W. and others *PRD*, vol. D 66, p. 054024, 2002.

[121] Acosta, D. and others *PRL*, vol. 94, p. 211801, 2005.

[122] Abazov, V. M. and others *PL*, vol. B698, pp. 6–13, 2011.

[123] G. Bernardi, D. Brown, M. Cooke, Y. Enari, S. Greder, H. Hegab, K. Herner, F. Miconi, B. Penning, "Search for WH associated production with 6.2 fb^{-1} of RunIIb data," February 2011. DØNote 6154.

[124] Hatim Hegab, "Production of Charged and Neutral Higgs Bosons with Charginos and Neutralinos through different Propagators in the MSSM," August 2006.

[125] CMS Collaboration, "Observation of a new boson at a mass of 125 GeV with the CMS experiment at the LHC," *CERN-PH-EP/2012-220*, vol. , January 2013.

[126] ATLAS Collaboration, "Observation of a New Particle in the Search for the Standard Model Higgs Boson with the ATLAS Detector at the LHC," August 2006.

[127] A. Collaboration, "letter of intent for a general-purpose pp experiment at the large hadron collider at CERN," *CERN-LHCC-92-004*, vol. , August 1992.

[128] ATLAS Collaboration, "ATLAS Technical Proposal for a General-Purpose pp Experiment at the Large Hadron Collider at CERN," *CERN-LHCC-94-43*, vol. , September 1994.

[129] ATLAS Collaboration, "The ATLAS Experiment at the CERN Large Hadron Collider," *JINST*, vol. , September 2008.

[130] ATLAS and CMS Collaborations, "Combined Standard Model Higgs boson searches with up to 2.3 fb^{-1} of pp collisions at $\sqrt{s}$=7 TeV at the LHC," *ATLAS-CONF-2011-157, CMS-PAS-HIG-11-023*, vol. , September 2011.

[131] DØ and CDF Collaborations, "Evidence of a particle produced in association with weak bosons and decaying to a bottom-antibottom quark pair in Higgs boson searches at the Tevatron," , vol. , July 2013.